

**Shear and Anchorage Behaviour  
of  
Fire Exposed Hollow Core Slabs**



# **Shear and Anchorage Behaviour of Fire Exposed Hollow Core Slabs**

## **Proefschrift**

ter verkrijging van de graad van doctor  
aan de Technische Universiteit Delft,  
op gezag van de Rector Magnificus prof.dr.ir. J.T. Fokkema,  
voorzitter van het College voor Promoties,  
in het openbaar te verdedigigen,

op maandag 5 April 2004 om 15:30 uur

door

**Joris Harko Herman FELLINGER**

civil ingenieur  
geboren te Didam

Dit proefschrift is goedgekeurd door de promotoren:

**Prof. ir. J.W.B. Stark**

**Prof. dr. ir. J.C. Walraven**

Samenstelling promotiecommissie:

Rector Magnificus,	voorzitter
Prof. ir. J.W.B. Stark	Technische Universiteit Delft, promotor
prof. dr. ir. J.C. Walraven	Technische Universiteit Delft, promotor
Prof. ir. H.W. Bennenk	Technische Universiteit Eindhoven
Prof. dr. ir. M. Fontana	Eidgenössige Technische Hochschule Zürich
Prof. dr. ir. L. Taerwe	Universiteit Gent
ir. J.A. Den Uijl	Technische Universiteit Delft
ir. L. Twilt	TNO Bouw

Cover: Crack pattern of the side view of a hollow core slab after 20 minutes of fire exposure as obtained in a fire test and with a finite element simulation.

*Published and distributed by: DUP Science*

DUP Science is an imprint of  
Delft University Press  
PO Box 98  
2600 MG Delft  
The Netherlands  
Telephone: +31 15 2785678  
Telefax: +31 15 2785706  
E-mail: [info@library.tudelft.nl](mailto:info@library.tudelft.nl)

ISBN 90-407-2482-2

Keywords: Fire resistance, concrete, hollow core slabs, shear, anchorage

Copyright © 2004 by Joris H.H. Fellingner

All rights reserved. No part of the material protected by this copyright notice may be reproduced or utilised in any form or by any means, electronic or mechanical, including photocopying, recording or by any other information storage and retrieval system, without written permission from the publisher: Delft University Press.

Printed in The Netherlands.

# Acknowledgements

With respect to the funding, the financial support by the Technology foundation STW is gratefully acknowledged. In addition, the financial support by the BFBN (Bond van Fabrikanten van Betonproducten in Nederland), and BmS (Bouwen met Staal) is highly appreciated. Also TNO is thanked for the financial support, for the flexible way I was allowed to finalise my Ph.D. and for the facilities that I could use during all the years of my study.

I'm very grateful to my guidance team that has added quality and direction to the thesis by the fruitful discussions during the years and their thorough review of the manuscript. Moreover, they all have supported me unconditionally during the entire study which kept me motivated. In particular, I'd like to express my special thanks to Prof. Jan Stark, without whom the project never would have started nor finished, as he was the driving force behind the initiation of the project and as he kept the project always on the right track with his excellent helicopter view; Prof. Joost Walraven for the challenging scientific discussions we had and his extensive overview of the concrete research area as well as for the much enjoyed tennis games we played; Prof. Wim Bennenk for his stimulating and very supportive role bringing science and the concrete industry together; Joop Den Uijl who made the basis of the bond model and the calibration tests that form a central part of my thesis and was my conscience in the field of anchorage of strands; and last but not least Leen Twilt for the way he supported me from the very beginning in getting the project started to the end with his help in the development of the fire tests and the way he facilitated my study at TNO.

Also, the contributions to the research made by Rein Sagel, Ralph Hamerlinck, Arnold van Acker, Jan Brekelmans, Jan de Wit, Gerry Klösters, Ronald Klein Holte and Aad van Paassen are kindly appreciated.

Furthermore, I wish to express my gratitude to my colleagues from TNO for their assistance in testing, notably Ton Eekhout, Paul Wolve, Ron van Zwet, Jaap Ruijsbroek, Gé Bol, Edward Vergouwen and Peter van de Leur. I'm also grateful for the assistance in the preparation of the test specimens by Arjen van Rhijn from the Stevin laboratory of the TU Delft. For the support in running FE simulations, special thanks is given to Wiltze Pieter Kikstra and Arno Wolthers who were always willing to provide direct support for another obscure error in DIANA even though the errors were mostly introduced by my own extensions to the FE programme.

I'd like to end with a special thanks to my colleagues Kees Both and Arnoud Breunese for playing my daily sparring partner in my struggle for dissertation. And last but not least I want to thank Mrs. Lea Tiwon-Klaassen as she has made life at work so much easier and more enjoyable.



# Summary

Hollow core (HC) slabs are made of precast concrete with pretensioned strands. These slabs are popular as floor structures in offices and housing. At ambient conditions, the load bearing capacity can be dominated by four different failure modes, i.e. flexure, anchorage, shear compression and shear tension. As the economic production process does not allow for the inclusion of mild reinforcement, the slabs rely on the tensile strength of concrete for the shear and anchorage capacity.

When exposed to a fire, the HC slabs have to maintain their load bearing and separating function for a certain time in order to facilitate the fire fighting actions and to provide sufficient time for the users of the building to escape and for rescue teams to search the building. Current design codes consider only flexural failure, while fire tests carried out in the past showed that the other failure modes can dominate the fire behaviour as well. As a result, design codes might overestimate the actual performance of fire exposed HC slabs. However, the experiments might represent a worst case compared to the practice. At least, fatalities caused by a premature collapse of fire exposed HC slabs, have never been reported up to the author's knowledge. Because there is a lack of fundamental understanding of the shear and anchorage behaviour, an optimum design between safety and economics can yet not be achieved.

The objective of the research presented in this thesis is to gain a basic understanding of the shear and anchorage behaviour of fire exposed HC slabs and to develop FE models to predict this behaviour. With the models, design measures to improve the behaviour can be evaluated.

The field of application is limited to HC slabs in accordance with the European product standard prEN 1168 [1197], exposed to standard fire conditions and simply supported on rigid supports like walls. The results are on the safe side for HC slabs with restraining support conditions.

In chapter 2, the literature on HC slabs at ambient and fire conditions is reviewed. At ambient conditions, the failure modes can accurately be described with existing formulations. These formulations can satisfactorily be used to determine the load level in fire tests. From the reviewed fire tests, no distinction could be made between shear and anchorage failure, requiring new tests. The shear or anchorage capacity decreases rapidly in the early stage of fire exposure although the scatter is high. The decrease is attributed to the thermal expansion that causes damage. Axial restraint at the supports improves the fire resistance significantly. Higher slabs are more vulnerable to such a failure than lower slabs.

The FE models need to take the actual constitutive behaviour into account in order to predict this damage. Therefore, existing constitutive models are assessed in chapter 3. Concrete stress-strain relations at high temperature are highly non-linear. The bond of the strands is strongly affected by the splitting cracks in the concrete cover. Therefore, the FE models need to account for the confining action of the concrete cover.

Chapter 4 presents 27 full scale fire tests that were carried out on single HC units and mainly on double ribs sawn out of HC units. The test set up of the standard shear test was used. In the double rib specimens the deformations of the webs of each rib were observed. Furthermore, the

temperature field was measured and the slip of each strand.

Vertical cracks in the web were observed in all tests after 14-16 minutes of fire exposure, even if the slab was partially axially restrained. Splitting cracks and horizontal cracks through the webs at the smallest web thickness developed between 20-22 minutes, depending on the geometry of the cross section of the HC slab and the positions of the strands in the cross section. The slip increased rapidly in all tests up to some 15 mm at the onset of failure in specimens of 4 m.

Shear and anchorage failure can be distinguished. Due to the cracks in the webs, no distinction between shear tension and shear compression can be made. Due to the splitting cracks, the bond of the strands is reduced and the anchorage capacity can be provided by the cracking moment capacity rather than the pull out capacity at some stage of the fire. The load level has a negligible effect on the slip and the cracks, but a large effect on the time to failure. The capacity decreases rapidly in the first hour, hereafter the decrease of the shear and anchorage capacity is small.

On the basis of the literature review and the full scale tests, the shear and anchorage behaviour of fire exposed HC slabs was modelled with two 2D FE models as presented in chapter 5. The first model of the cross section of the HC slabs is used to determine the development of splitting and horizontal cracks and the confining response of the concrete cover to radial expansion of the strands. A newly developed bond model assumes that the slip and a change in the axial steel strain causes this radial expansion. The confining response is transferred to a bond yield strength through a friction analogy that is used as input for the second FE model of the entire slab. This model is used to calculate the vertical cracks in the webs, the slip of the strands and the actual failure behaviour. Both 2D models use a newly developed temperature dependent constitutive model for concrete that takes into account thermal expansion, transient creep, cracking, and plasticity. The behaviour in compression depends also on the loading history.

In chapter 6, the parameters of the bond model and the concrete model were successfully calibrated. For that purpose small scale calibration tests were carried out at elevated temperatures in a specially developed test set up. The main parameters were calibrated within a narrow range, i.e. the tensile strength and the fracture energy of concrete and the friction coefficient of the bond interface.

With the calibrated model parameters, FE models were successfully validated in chapter 7 against the fire tests of chapter 4. All crack patterns, the slip development and the failure modes can satisfactorily be predicted with the models. Also at ambient conditions, shear and anchorage failure and the introduction of the prestress can adequately be described.

With a sensitivity study in chapter 8, it was shown that a low thermal expansion of concrete and a high fracture energy improve the shear and anchorage behaviour of fire exposed HC slabs. Both parameters are determined by the type of aggregate. A high friction coefficient of the strands also improves the behaviour. Restraining support conditions improve the behaviour as well, but it is recommended not to rely on it as the actual amount of restraint in practice is unknown.

When the load level with respect to shear and anchorage failure is a sufficiently low, these failure modes can be avoided. As the FE models are too complex for daily engineering use, it is recommended to determine for each HC slab on the market this load level through a parameter study with the models and to use this load level as a safe lower bound in practice.

# Samenvatting

Kanaalplaten zijn gemaakt van geprefabriceerd beton met strengen van voorgerekt staal. Deze platen zijn populair als vloerconstructies in woningen en kantoorgebouwen. Bij kamertemperatuur kan de vloer bezwijken op 4 verschillende manieren: op buiging, verankering, afschuifbuigbreuk en afschuiftrekbreuk. Door het economische productieproces kan geen gewone wapening worden toegevoegd, waardoor de afschuif- en verankeringscapaciteit afhangen van de trekstrekte van beton.

Tijdens brand moeten kanaalplaatvloeren hun dragende en scheidende functie gedurende enige tijd behouden opdat aanwezigen kunnen vluchten en de brandweer het gebouw kan doorzoeken en de brand kan beheersen. In de vigerende voorschriften wordt alleen getoetst op bezwijken op buiging terwijl brandproeven hebben aangetoond dat de andere bezwijkvormen maatgevend kunnen zijn. Hierdoor wordt de brandwerendheid van de vloeren in de regelgeving overschat hoewel deze proeven mogelijk veel conservatiever zijn dan de praktijk. In ieder geval zijn geen ongevallen bij de auteur bekend t.g.v. het voortijdig instorten van kanaalplaatvloeren bij brand. Maar door het gebrek aan inzicht in de het bezwijken op afschuiving en verankering kan er geen ontwerp worden gemaakt dat optimaal recht doet aan zowel de veiligheid als de economie.

Het doel van het onderzoek is het verwerven van inzicht in het gedrag van kanaalplaatvloeren onder brandomstandigheden t.a.v. afschuiving en verankering, en het ontwikkelen van numerieke modellen om dit gedrag te voorspellen. Met deze modellen kunnen maatregelen worden beoordeeld om het ontwerp te verbeteren

Het toepassingsgebied blijft beperkt tot kanaalplaatvloeren zoals omschreven in de produktnorm prEN 1168 [1997], blootgesteld aan standaardbrandomstandigheden en statisch bepaald opgelegd op starre ondersteuning zoals wanden. De resultaten zijn conservatief voor vloeren met oplegcondities die de thermische uitzetting verhinderen.

In hoofdstuk 2 is een overzicht van de literatuur over kanaalplaatvloeren gegeven. De bezwijkvormen van kanaalplaten bij kamertemperatuur kunnen goed beschreven worden met bestaande rekenregels. Deze rekenregels zijn daarom gebruikt om de belastinggraad te bepalen in de brandproeven. Uit de brandproeven bleek dat geen goed onderscheid kan worden gemaakt tussen bezwijken op afschuiving en op verankering. Nieuwe proeven waren dus noodzakelijk. Het draagvermogen neemt in het begin van de brand snel af, hoewel de spreiding in de resultaten groot is. De afname wordt toegeschreven aan de thermische uitzetting waardoor schade ontstaat. De brandwerendheid wordt positief beïnvloed door een verandering bij de opleggingen van de thermische uitzetting in de overspannings-richting. Dikkere vloeren zijn gevoeliger voor deze bezwijkvormen dan dunnere.

Om deze schade te berekenen, moeten de numerieke modellen met het werkelijke constitutieve gedrag rekenen. In hoofdstuk 3 zijn daarom de bestaande constitutieve modellen op een rij gezet. Beton vertoont sterk niet-linear gedrag bij hoge temperaturen. De aanhechting van de strengen wordt sterk beïnvloed door eventuele slijtscheuren. Het aanhechtmodel moet daarom rekening houden met de opsluitende werking van het omhullende beton.

In hoofdstuk 4 worden 27 nieuwe brandproeven beschreven op kanaalplaten en op proefstukken bestaande uit dubbele ribben welke uit de kanaalplaten zijn gezaagd. De proefopstelling was de standaard dwarskrachtproef. In de dubbele rib proefstukken is de scheurvorming in elk lijf

geobserveerd. Daarnaast is het temperatuurprofiel en de slip van alle strengen gemeten in elke proef. In elke proef onstonden verticale scheuren in de lijven van het proefstuk na 14-16 minuten brand, zelfs als de thermische uitzetting in de overspanningsrichting gedeeltelijk werd verhinderd. Afhankelijk van de geometrie van het proefstuk en de positie van de strengen in de doorsnede, ontstonden na 20-22 minuten slijtscheuren en horizontale scheuren door het smalste deel van het lijf. In alle proeven nam de slip in het begin snel toe tot zo'n 15 mm net voor bezwijken. In de proeven kon onderscheid worden gemaakt tussen bezwijken op afschuiving en op verankering. Door de scheurvorming in de lijven kan de onderverdeling tussen afschuif-trekbreuk en afschuifbuigbreuk niet worden gemaakt. Door de slijtscheuren neemt de aanhechting van de strengen sterk af in het begin van de brand, waardoor in deze periode het scheurmoment bepalend is voor het bezwijken op verankering. De belastinggraad heeft een verwaarloosbaar effect op de scheurvorming en de slip, maar een groot effect op het tijdstip tot bezwijken. Het draagvermogen neemt in het eerste uur snel af, de verdere afname is gering. Om het gedrag van de kanaalplaat m.b.t. afschuiving en verankering te berekenen, zijn twee 2D EEM modellen gemaakt, welke zijn bescheven in hoofdstuk 5. Het eerste model is een model van de doorsnede van de plaat waarmee de horizontale scheuren, de slijtscheuren en de opsluitende werking van het beton rondom de strengen wordt berekend. De opsluitende werking is het gevolg van een radiale uitzetting van de streng. Het tweede model van de gehele vloer, maakt gebruik van een nieuw aanhechtmodel waarin de slip en de veandering van de axiale rek in de streng wordt gerelateerd aan deze radiale uitzetting. De berekende opsluitende werking (een druk) wordt in het tweede model als invoer omgewerkt tot een maximale aanhechtspanning m.b.v. een wrijvingscoëfficiënt. Met het tweede model kan de verticale scheurvorming, de slip en het bezwijken worden berekend. Beide modellen maken gebruik van een nieuw temperatuurafhankelijk betonmodel waarin thermische uitzetting, thermische kruip, scheurvorming en plasticiteit zijn meegenomen. De gedrag onder druk hangt bovendien af van de belastinghistorie. Het aanhechtmodel en het betonmodel zijn met succes gecalibreerd, zie hoofdstuk 6. Hiervoor zijn proeven op kleine schaal gedaan bij verhoogde temperatuur in een speciaal ontwikkelde testopstelling. De belangrijkste parameters zijn gecalibreerd in een smalle bandbreedte. Dit betreft de treksterkte en de scheurenergie van beton en de wrijvingscoëfficiënt om de strengen. De numerieke modellen zijn in hoofdstuk 7 met succes gevalideerd tegen de brandproeven uit hoofdstuk 4, o.b.v. de gecalibreerde parameters. De modellen kunnen alle scheuren, de slip en alle bezwijkvormen correct voorspellen. Het bezwijkgedrag bij kamertemperatuur en de inleiding van de voorspanning kan ook goed worden voorspeld.

Met een gevoeligheidsstudie is aangetoond dat een geringe thermische uitzetting en een grote scheurenergie van beton, een gunstige effect hebben op het draagvermogen van aan brand blootgestelde kanaalplaten m.b.t. het bezwijken op afschuiving en verankering. Ook een hoge wrijvingscoëfficiënt tussen de strengen het het beton draagt hieraan bij. Een verhindering van de thermische uitzetting bij de oplegging draagt hier ook aan bij, maar het wordt afgeraden hierop te rekenen zolang het onbekend is welke verhindering realiseerbaar is in de praktijk.

Indien de belastinggraad voldoende laag is m.b.t. het bewijken op afschuiving en de verankering van de strengen, treden deze bewijkvormen niet op bij brand. Omdat de numerieke modellen te complex zijn om te worden gebruikt in de dagelijkse ingenieurspraktijk, wordt het aanbevolen om voor elke op de markt beschikbare kanaalplaat deze belastinggraad te bepalen middels een parameterstudie. Deze belastinggraad moet dan als toelaatbare belasting in het ontwerp dienen.

# Table of Contents

<b>1</b>	<b>Introduction</b>	<b>1</b>
1.1	Background	1
1.1.1	Hollow core slabs	1
1.1.2	Fire resistance	2
1.2	Problem statement	3
1.3	Aim	6
1.4	Field of application	7
1.5	Outline	7
<b>2</b>	<b>Literature on structural behaviour</b>	<b>11</b>
2.1	Ambient conditions	11
2.1.1	Failure modes of HC slabs	11
2.1.1.1	Introduction	11
2.1.1.2	Flexure	12
2.1.1.3	Anchorage	13
2.1.1.4	Shear compression	16
2.1.1.5	Shear Tension	19
2.1.2	Capacity lines	24
2.1.3	Validation with tests	25
2.2	Fire conditions	31
2.2.1	Introduction	31
2.2.2	Theory of thermal stresses	31
2.2.3	Failure modes of HC slabs	36
2.2.3.1	Introduction	36
2.2.3.2	Flexure	36
2.2.3.3	Shear	38
2.2.3.4	Anchorage	39
2.2.4	Evaluation of fire tests	40
2.2.4.1	General	40
2.2.4.2	Strand temperature	41
2.2.4.3	Moisture	41
2.2.4.4	Thermal stresses	42
2.2.4.5	Load level	45
2.2.4.6	Practical measures	49
2.3	Non-rigid supports	50
2.3.1	Ambient conditions	50
2.3.2	Fire conditions	57
<b>3</b>	<b>Literature on constitutive behaviour</b>	<b>59</b>
3.1	Introduction	59
3.2	Concrete properties	60

3.2.1	Room temperature	60
3.2.1.1	Compression	60
3.2.1.2	Tension	60
3.2.1.3	Fracture energy	61
3.2.2	Elevated temperature	62
3.2.2.1	Compression	62
3.2.2.2	Tension	68
3.2.3	Considerations for testing	69
3.2.3.1	Mechanical actions	69
3.2.3.2	Chemical changes	70
3.2.3.3	Recommendations	72
3.3	Bond of strands	72
3.3.1	Room temperature	72
3.3.1.1	Overview	72
3.3.1.2	Concrete confinement	74
3.3.1.3	Bond slip models	77
3.3.2	Elevated temperatures	79
<b>4</b>	<b>Experiments on HC members</b>	<b>83</b>
4.1	Scope	83
4.2	Objective	83
4.3	Test description	88
4.3.1	Set up	88
4.3.2	Concrete mix	89
4.3.3	Instrumentation	89
4.4	Measurements	90
4.4.1	Overview	90
4.4.2	Crack patterns	91
4.4.3	Slip	96
4.4.4	Temperatures	100
4.5	Influence parameters	103
4.5.1	Load level	103
4.5.2	Axial restraint	104
4.5.3	Core filling	104
4.6	Conclusions & Recommendations	105
4.6.1	Failure modes	105
4.6.2	Practice	105
4.6.3	Modelling	107
<b>5</b>	<b>Numerical modelling</b>	<b>109</b>
5.1	Modelled phenomena	109
5.1.1	Shear and anchorage behaviour	109
5.1.2	Bond behaviour	109
5.2	Approach	110
5.3	Thermal response	113
5.3.1	FE formulation	113

5.3.1.1	General	113
5.3.1.2	Voids	114
5.3.2	Concrete and steel properties	116
5.3.3	Boundaries	118
5.4	Structural response	119
5.4.1	Global FE formulation	119
5.4.2	Bond model	121
5.4.2.1	FE formulation	121
5.4.2.2	Radial expansion - heating path	126
5.4.3	Concrete	127
5.4.3.1	Strain decomposition	127
5.4.3.2	Rankine-Drucker-Prager plasticity model	129
5.4.3.3	Tension	129
5.4.3.4	Compression	133
5.4.3.5	Transient creep	134
5.4.3.6	Thermal elongation	134
5.4.3.7	Loading history	135
5.4.3.8	Maturing assumptions	137
5.4.4	Steel	138
5.4.4.1	Thermal elongation	138
5.4.4.2	Strength and stiffness	138
<b>6</b>	<b>Calibration of the model</b>	<b>139</b>
6.1	Calibration tests	139
6.1.1	Objective	139
6.1.2	Approach	141
6.1.3	Test set up	143
6.1.3.1	Test frame	143
6.1.3.2	Loading	143
6.1.3.3	Stiffness of the restrained passive end	144
6.1.3.4	Heating rate	145
6.2	Calibration of model parameters	146
6.2.1	Concrete tensile strength	146
6.2.2	Fracture energy of concrete	148
6.2.3	Bond parameters	153
<b>7</b>	<b>Validation of the model</b>	<b>163</b>
7.1	Contents	163
7.2	Ambient conditions	163
7.2.1	Transfer length	163
7.2.2	Shear behaviour	165
7.2.3	Anchorage behaviour	166
7.3	Fire conditions	169
7.3.1	Thermal response	169
7.3.2	Vertical cracks	171
7.3.2.1	HVP260-40/40	171

	7.3.2.2	XB200 restrained vs unrestrained	173
7.3.3		Horizontal and splitting cracks	175
	7.3.3.1	VX265	175
	7.3.3.2	Splitting cracks in HVP260 and K400	176
	7.3.3.3	XB200 restrained	178
7.3.4		Slip development and failure behaviour	179
	7.3.4.1	HVP260-40/40	179
	7.3.4.2	XB200 restrained vs unrestrained	182
7.3.5		Conclusions	183
<b>8</b>		<b>Evaluation</b>	<b>185</b>
8.1		Introduction	185
8.2		Parametric study on the transfer length	185
8.3		Parametric study on fire exposed hc slabs	189
	8.3.1	External conditions	189
		8.3.1.1 Introduction	189
		8.3.1.2 Shear loading	189
		8.3.1.3 Restraining boundaries	192
	8.3.2	Material properties	193
		8.3.2.1 Aggregate type: thermal expansion and thermal properties	194
		8.3.2.2 Fracture energy of concrete	198
		8.3.2.3 Concrete tensile strength	200
		8.3.2.4 Friction coefficient	201
		8.3.2.5 Transient creep	202
	8.3.3	Geometrical properties	203
8.4		Fire safe design of HC slabs	204
<b>9</b>		<b>Conclusions and recommendations</b>	<b>209</b>
9.1		Conclusions	209
	9.1.1	Based on tests	209
		9.1.1.1 Ambient conditions	209
		9.1.1.2 Fire conditions	209
	9.1.2	Regarding the quality of the models	211
		9.1.2.1 Analytical models	211
		9.1.2.2 FE models	212
	9.1.3	Based on the models	214
9.2		Recommendations	215
	9.2.1	Testing	215
	9.2.2	Modelling	215
	9.2.3	Design	215
	9.2.4	Future research	216

<b>Notation</b>	<b>217</b>
<b>References</b>	<b>225</b>
<b>Appendix A: HC tests at ambient conditions</b>	<b>235</b>
<b>Appendix B: Transfer and development length</b>	<b>247</b>
<b>Appendix C: HC tests at fire conditions</b>	<b>253</b>
<b>Appendix D: Maturing assumptions for concrete</b>	<b>255</b>
<b>Curriculum vitae</b>	<b>261</b>



# 1 Introduction

## 1.1 BACKGROUND

### 1.1.1 Hollow core slabs

Hollow core (HC) slabs are precast prestressed concrete slabs made for floor structures in buildings. The slabs consist of elements that are typically 1.2 m wide. The depth depends on the desired span and ranges between 150-400 mm. The shape and the number of hollow cores is adjusted to the depth, see fig. 1.1.

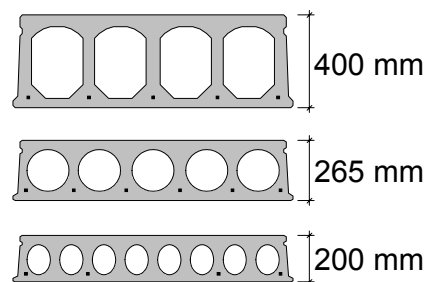


Figure 1.1: Cross sections of various HC elements

HC slabs have a market share of 30 % in the Netherlands in offices and housing. A minimum slab weight is obtained as a result of the hollow cores in combination with prestressed concrete of high quality (typically C45 - C65). Compared to massive concrete floors, HC slabs use 30 % less concrete and 50 % less steel. The minimum weight affects also the supporting structure underneath and the foundation. Apart from economy, this also results in a minimum use of natural resources. Moreover, the production of HC slabs causes hardly any waste since all lost material is collected and reused as granulate.

The slabs are competitive due to the almost complete automatization of the production process. The HC elements are manufactured on long benches (100 to 200 m). First, strands are prestressed along the bench. Subsequently, the concrete is cast automatically by a moulding and casting machine that is moved along the bench. Predominantly, two different processes are used. In the extrusion process, the concrete is pierced in one layer using a machine with pipes that cause the hollow cores. The machine pushes itself forward against the cast concrete. It is not possible to include mild reinforcement. In the slip form process, a casting machine with external traction casts the concrete in two or more layers. Mild reinforcement could be used, but is never applied for reasons of obstruction of the casting process.

After hardening, the external prestressing force is released and elements of required length are sawn out. Anchors for the prestressing steel are not used, because they would cause large splitting stresses. Therefore, the transmission of the prestressing force is only possible by direct bond stresses between the strands and the concrete.

### 1.1.2 Fire resistance

In order to ensure sufficient fire safety, national and international building regulations require a minimum fire resistance for structures. Eurocode 1 [PREN 1991-1-2: 2002] gives the following definition of fire resistance: *The ability of a structure, a part of a structure or a member to fulfil its function (load bearing function and/or separating function) for a specified load level, for a specified fire exposure and for a specified period of time.* HC slabs have a load bearing function and, in case the slab is part of the envelope of a fire compartment, also a separating function. Generally, the fire resistance is further precised to the standard fire resistance, defined as the time to loss of function under standard fire conditions [ISO 834-1: 1999], see fig. 1.2. The time-temperature relation of the standard fire curve is given by

$$\theta = 345 \cdot 10^{\log(8t + 1)} + 20 \quad \{1.1\}$$

in which  $\theta$  is the temperature in the fire compartment in °C and  $t$  is the time of fire exposure in minutes.

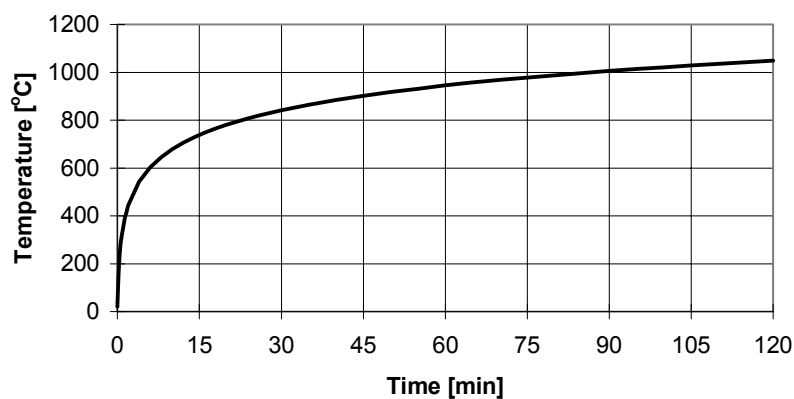


Figure 1.2: Time temperature relation of the standard fire curve.

With respect to the mechanical loading design codes, like for instance in Eurocode 1 [PREN 1991-1-2: 2002] consider fire as an accidental load case. In fire, other actions are assumed at their

characteristic value instead of their extreme value. Therefore the assumed mechanical loading in case of fire is typically 0.4 - 0.8 times the loading in the ultimate limit state at ambient conditions. Moreover, the partial safety factors are set to unity.

The standard fire resistance requirements are expressed in classes of 30 minutes time interval from 30 to 120 minutes and beyond, depending on the height and the occupancy of the building. A safety margin is implicitly taken into account by the use of the standard fire curve in combination with the fire resistance requirements.

The fire resistance is assessed either by testing or by calculation. Generally, an assessment of the entire structure under fire conditions is too complex. Therefore, the fire resistance is mostly assessed on the basis of a member analysis, i.e. a single slab, beam or column is considered, separated from the rest of the structure. The assumed support conditions can highly influence the conclusions, and the realistic support conditions should be followed as closely as possible.

## **1.2 PROBLEM STATEMENT**

From the analyses of fire tests conducted over the past thirty years, it appeared that shear and anchorage failure can dominate the fire behaviour of HC slabs further to bending failure. Moreover, failure can occur very suddenly as shear and anchorage failure are very brittle compared to bending failure.

Nevertheless, national and international building regulations do not give adequate rules that provide sufficient shear and anchorage resistance of fire exposed HC slabs. Moreover, the shear and anchorage behaviour of fire exposed HC slabs is not yet understood. Fire tests show large scatter in terms of the achieved fire resistance. Also, the type of failure was not always clearly reported.

On the other hand, shear or anchorage failure of HC slabs has never been reported in practice to have caused severe incidents in real fires, in spite of the large practical experience with HC slabs, as it has been one of the most popular flooring systems throughout Europe for the past thirty years.

As the behaviour of the slab is not sufficiently well understood, the current design rules can not ascertain adequate safety in all cases nor yield to an optimal economic design. In order to ensure sufficient fire safety, there is an urgent need for a basic understanding of the shear and anchorage behaviour of fire exposed HC slabs. In this way, the design of HC slabs can be optimised between safety and economy.

The shear and anchorage capacity of HC slabs rely completely on the tensile strength of plain concrete. After all, no mild reinforcement can be applied during the production process to bear the shear stresses or the splitting stresses around the strand. Shear loading causes shear stresses in the cross section, corresponding to tensile stresses in one of the principal directions. The principal direction does not align with the strand, and the maximum tensile stresses develop in the webs rather than in the vicinity of the strands, so the tensile stresses must be taken by the plain concrete. Anchorage of the strands causes splitting stresses in the plain concrete cover. Once a splitting crack develops, the anchorage capacity decreases dramatically.

The shear and anchorage behaviour are further affected by the way the HC slabs are supported. When the HC slabs are supported on non-rigid supports like beams, additional stresses are introduced into the direction perpendicular to the slab span. Pajari [1995a] developed a calculation model that accounts for these stresses in the evaluation of the shear and anchorage resistance at ambient conditions.

When assessing the fire resistance of HC slabs with respect to bending failure, design codes like Eurocode 2 [PREN 1992-1-2: 2002] recommend a plastic analysis of the cross section considering only the decrease of the strength at elevated temperatures of steel and concrete.

For the assessment of fire resistance with respect to shear and anchorage failure it is postulated here that other aspects need to be considered, that are explained below:

- Incompatible thermal strains
- Non-linear stress-strain relations
- Decomposition of strains in reversible and irreversible parts
- Influence of loading on the resistance reduction
- Support conditions
- Relation between fire safety and fire resistance classes

### **Incompatible thermal strains**

The shear and anchorage behaviour of HC slabs can only be described taking into account the effect of incompatible thermal strains on the load bearing capacity. The transient heat flow generates a large temperature gradient over the depth of the cross section which is distributed non-linearly. This non-linear temperature gradient is accompanied with non-linearly distributed thermal strains that do not comply with the compatibility requirements. In order to meet the compatibility requirements, mechanical strains have to develop to counteract the thermal strains, which result in thermal stresses. Compressive thermal stresses develop in the lower flange and upper flange of the HC slab and tensile thermal stresses develop in the web, see for a detailed explanation §2.2.2 on page 31. Also the strands are subjected to the imposed strains, which results in a combination of slip and change in steel stress, depending on the relative position of the strands in the cross section and the bond characteristics.

The mechanical strains that have to develop to counteract the incompatible thermal strains, can easily exceed the elastic limit in an early stage of the fire. This means that irreversible mechanical strains develop. This may result in cracking of the webs and slip of the strands, leading to a dramatic decrease of the shear capacity. Moreover, the incompatible thermal strains cause splitting cracks along the strands, which strongly reduce the confining action of the concrete around the embedded strands and consequently reduce the anchorage capacity of the HC slab. The loss of bond is accompanied with a large slippage of the strands.

Besides, there is an interaction between the shear and the anchorage behaviour. The strand must take over the tensile stress released in the web after crack formation.

In the past, the effect of thermal stresses on the shear and anchorage capacity of HC slabs was not taken into account in any model describing the shear and anchorage behaviour of concrete structures, up to the knowledge of the author.

### **Non-linear stress-strain relations**

In order to predict the thermal stresses adequately, the concrete model needs to take into account the non-linear behaviour of concrete and steel. Concrete shows significant transient creep under

load while heated. Furthermore, the stiffness and the compressive strength are significantly affected by the loading history during heating. Moreover, the stress-strain relations become more ductile at elevated temperatures than at room temperature. Steel becomes less stiff at elevated temperatures and shows more plastic deformation in the ascending branch of the stress-strain relation.

Due to the non-linear stress-strain relations, the thermal stresses are released. For instance, once the concrete webs crack, the imposed strains are concentrated in the cracks and the thermal stresses vanish. This explains why thermal stresses can be neglected in the calculation of bending failure on basis of the theory of plasticity. In the plastified cross section, no thermal stresses are present in the concrete cracked in tension nor in the strand that yields.

### **Decomposition of strains in reversible and irreversible part**

In order to avoid a strength recovery in the simulation once the thermal gradient decreases after some longer period of fire exposure, the constitutive models for concrete, steel and interface bond should allow for a permanent strength reduction after irreversible damage occurred like cracking of concrete, yielding of steel or slippage of the strand. Elastic stress-strain formulations are pointless, even if they are non-linear.

Furthermore, in order to avoid a decreasing slip due to the decreasing thermal gradients after some time of fire exposure, the slip must be decomposed into a reversible and an irreversible part. Modelling the bond behaviour with a unique bond-slip relation would result in a decreasing slip after some fire exposure time which seems physically meaningless.

### **Influence of loading on the resistance reduction**

In principle, the damage caused by the combined effect of thermal stresses and externally applied loading during fire exposure determines the load bearing capacity at the end of the exposure period. So, the decrease of the load bearing capacity depends on the applied loading, see fig. 1.3. In this figure, the load level is defined as the ratio between the applied load during fire exposure and the load bearing capacity at ambient conditions. Smaller (higher) applied stresses during fire exposure cause smaller (higher) damage and a higher (lower) load bearing capacity remains at the end of the fire exposure period. If the load is increased up to failure of the specimen at some stage of the fire exposure, the smallest resistance might be found at the time that the thermal stresses are at maximum. If the load is increased in a later stage of the fire exposure, once the thermal stresses vanish, the observed load bearing capacity can well be higher than allowable during the critical stage of fire exposure.

### **Support conditions**

The thermal stresses due to the incompatible thermal strains change significantly if the thermal strains are restrained at the supports. As a result, restraining conditions have a significant effect on the shear and anchorage behaviour of fire exposed HC slabs. However, it is hard, if not impossible to predict the actual restraining conditions of a HC slab in a practical application. Furthermore, there is an effect of non-rigid supports on the shear and anchorage behaviour, but it will be shown in the present research that this effect is small compared to the scatter in the fire test results.

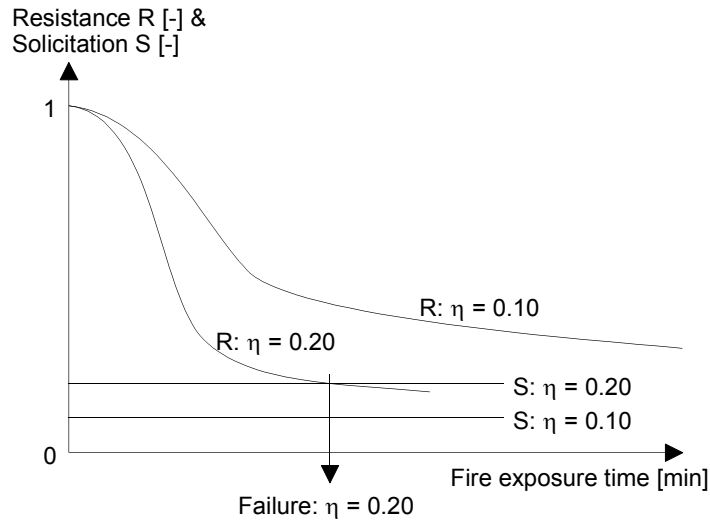


Figure 1.3: Schematic representation of the development of the load bearing capacity  $R$  during fire, depending on the applied load level  $\eta$  (solicitation / initial resistance).

### Relation between fire safety and fire resistance classes

Generally speaking, the thermal stresses reduce the shear and anchorage capacity in an early stage, whereas the deterioration of the mechanical properties leads to a further decrease of these capacities in a later stage of the fire. The thermal stresses decrease after some time of fire exposure once the temperature distribution starts to flatten out. As a result, the shear and anchorage capacity might barely decrease while the thermal stresses vanish until the decay of the mechanical properties governs the capacity.

A complication of the latter observation is that a design for 90 minutes fire resistance can be equal to a design for 60 minutes fire resistance. This conflicts with the implicit assumption in the design codes that a requirement of 90 minutes fire resistance results in a design with a higher safety level than a requirement of 60 minutes.

To overcome this complication, there is a need for a discussion on the desired level of fire safety depending on the type and the height of a building and the way design codes should provide this safety. After all, the current approach provides safety only in a very implicit way with the requirements defined in the time domain in combination with the standard fire exposure rather than in the reliability domain. Moreover, the fire resistance is normally assessed on the basis of a structural element rather than that of a complete structure. However, the discussion on the desired safety level is beyond the scope of this thesis. It was discussed in many documents, for instance [CIB W14: 1986]. The way the desired safety should be achieved for HC slabs is addressed in chapter 8.

## 1.3 AIM

The objective of the present research is to gain a basic understanding of the shear and anchorage behaviour of fire exposed HC slabs and to develop tools to predict this behaviour. Therefore FE models were developed that were validated by experiments. The FE models include the effect on

the shear and anchorage behaviour of both the deterioration of the mechanical properties at elevated temperatures and the thermal stresses due to thermal expansion.

New constitutive models were developed for the bond behaviour of strands and for concrete. The bond model is an elastic-plastic model, in which the yield strength depends on the confining action of the concrete around the strand. The concrete model includes the dependence of the stiffness and the compressive strength on the loading history during heating. Moreover, the plastic strain of concrete in tension at elevated temperatures is assumed to develop before the tensile strength is reached.

Small scale tests on the bond behaviour of strands at elevated temperatures were used to calibrate the FE models. Full scale tests on fire exposed HC slab elements were carried out to increase the understanding of the behaviour and to validate the FE models.

With the FE models the sensitivity of shear and anchorage failure to some model parameters was demonstrated. The sensitivity explains the large scatter found in previous fire test results and opens the way for improved design.

## **1.4 FIELD OF APPLICATION**

The present research is restricted to hollow core slabs of precast concrete with pretensioned strands which are in accordance with the European product standard prEN 1168 [1997].

The fire behaviour is only analysed under standard fire conditions according to ISO 834-1 [1999]. However, the FE models are formulated in a generic way, which opens the opportunity to simulate the fire behaviour of HC slabs under non-standard fire conditions as well. The constitutive relations in the structural FE models apply to the heating phase of the fire curve. For the cooling phase the accuracy of the constitutive models is weak, and therefore, extension of the application of the models to the cooling phase should be validated first.

The tests and the FE models concern HC slabs on rigid supports like walls only. The test results can not be extrapolated to HC slabs on non-rigid supports directly nor can the FE models be used for the analyses of HC slabs on non-rigid supports without further validation. Only limited attention was paid to restraining effects in the research, since it is hard to predict the actual restraining conditions of a HC slab in a practical application and this is outside the scope of the thesis. Moreover, conclusions drawn from the test results or from the FE models in which the restraining effects are disregarded, are on the safe side as far as the fire resistance of the HC slabs is concerned.

## **1.5 OUTLINE**

The structure of the research project and the thesis is outlined in fig. 1.4. The thesis starts with a literature overview. This overview is subdivided in two ways, i.e. ambient versus fire conditions and structural behaviour of HC slabs versus constitutive behaviour of concrete and the concrete-steel bond interface. The literature survey into the structural behaviour of HC slabs is presented in the chapter 2, the literature survey into constitutive behaviour is given in chapter 3.

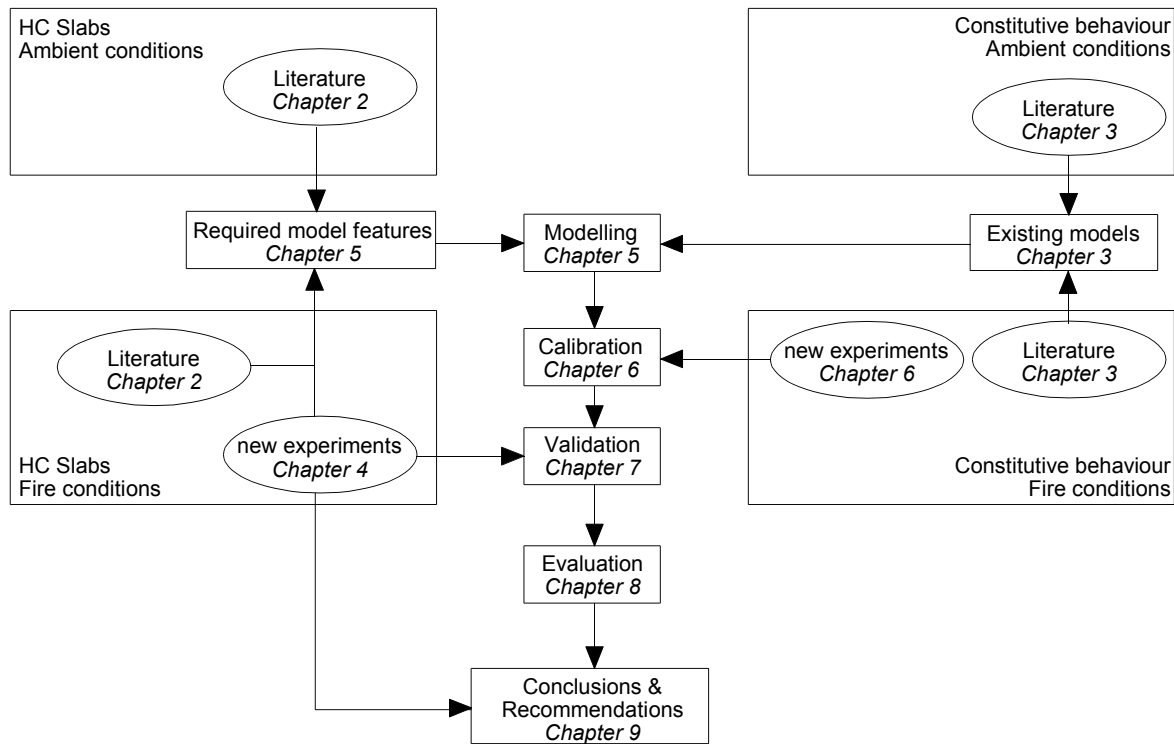


Figure 1.4: Approach of the research project.

Chapter 2 divides the structural behaviour of HC slabs further into four blocks, see fig. 1.5. Chapter 2 starts with a theoretical outline of the failure modes of HC slabs supported on rigid walls. In the first paragraph, the available theory covering HC slabs at ambient conditions is described and evaluated on basis of a comparison with 253 experiments.

In §2.2, the failure modes of HC slabs under fire conditions are treated. However, no conclusive descriptions are available for the failure modes of HC slabs under fire conditions. For shear and anchorage failure it was postulated in the problem statement that thermal stresses should be included in the analyses. In order to provide a better understanding of the fire behaviour of HC slabs, this paragraph starts with the theory of thermal stresses, providing the rationale for the necessity to include thermal stresses in the failure analyses of HC slabs with respect to shear and anchorage.

Next, the available fire tests on HC slabs are discussed and the necessity to include thermal stresses in the models is underlined. The available experimental data on HC slabs showed large scatter in terms of fire resistance and the reports were sometimes too limited to clearly extract the actual behaviour. Moreover, a large variation in applied test details was found, for instance, with respect to restraining conditions of the supports and additional mild reinforcement in end beams, joints, and concrete filled cores. In fact, most tests were designed in such a way that shear and anchorage failure was unlikely to occur. Therefore, the data did not provide a sound basis for the proper understanding of the shear and anchorage behaviour of the HC slabs and new tests were required.

	supports	
conditions	walls <i>ambient</i>	beams <i>ambient</i>
	walls <i>fire</i>	beams <i>fire</i>

Figure 1.5: Overview of four distinct research areas for HC slabs.

Chapter 2 ends in §2.3 with an overview of research into the structural behaviour of HC slabs, supported on beams. The effect of non-rigid supports on the load bearing capacity at ambient conditions is outlined. The effect of non-rigid supports on the fire behaviour of HC slabs was studied mainly in Switzerland [BORGOGNO & FONTANA: 1995, 1996, BORGOGNO: 1997]. From their limited test data, it seems that the reduction of the load bearing capacity by the non-rigid supports under fire conditions is relatively unimportant compared to the reduction due to the fire exposure itself, see §2.3.2. Therefore, it was decided to concentrate the research on the basic case of fire exposed HC slabs on rigid supports.

As stated in the problem statement, a model that can describe the shear and anchorage behaviour of fire exposed HC slabs, requires an appropriate description of the constitutive behaviour of the materials under transient conditions. In chapter 3 an overview is given of relevant models found in literature for the concrete behaviour at elevated temperatures. Models for the bond behaviour of the strands taking into account the confining action of the concrete cover are described, which form the basis for the numerical models developed in the present research project. It was concluded that the large scatter in the concrete properties as obtained from literature necessitated new small scale tests at elevated temperature to provide accurate input data for the numerical models. In addition, in order to calibrate the bond model that includes the confining action of concrete under fire conditions, new bond tests at elevated temperatures were required as well.

After consideration of the relevant literature, it was concluded that new tests into the shear and anchorage behaviour of fire exposed HC slabs were required. Chapter 4 presents these experiments. New structural fire tests were performed on double ribs sawn out of HC units. The main reason to saw ribs out of HC units is the opportunity to observe the crack propagation in each web of the specimen during the test. The specimens were simply supported on uninsulated steel plates without any structural connection with the support, to obtain the most simple structural system. In this way, the tests were used for the development and validation of the FE models that describe the fire behaviour of the HC slabs. However, as the test details with respect to supports and additional reinforcement differed significantly from practical applications, additional fire tests were carried out on complete HC units, on HC ribs with axial restraint and on HC ribs in which the hollow core was filled with reinforced concrete over the transfer length of the prestress. These tests which contributed to the practical recommendations, are described in chapter 4. To emphasise the importance of this relation, a separate link exists between the fire tests on HC slabs and the conclusions as shown in fig. 1.4.

From these tests, together with the experiments described in the literature survey, the required model features were established. Chapter 5 gives an overview of these features and describes the

FE model of fire exposed HC slabs, developed in the project. The FE models can predict crack patterns observed in these fire tests, which reduce the shear capacity, and they can simulate the anchorage capacity of fire exposed HC slabs.

The model contains new constitutive models for the bond interface and for concrete at elevated temperature, based on existing constitutive models listed in chapter 3. The bond model is based on an adhesion-friction analogy. Before the strand slips, the bond strength is based on adhesion. While slippage of the strand develops, the adhesion vanishes and frictional stresses increase. The friction depends on the confining action of the concrete cover around the strand.

The calibration of the model is presented in chapter 6. In order to calibrate the most important model parameters, tests were carried out on small scale concrete specimens at elevated temperature. These calibration tests are also presented in this chapter. The bond tests consisted of tests in which strands were pulled out from concrete cylinders with short embedment length. In addition so-called pull-through tests were carried out in order to determine the confining action of the concrete cylinder against radial expansion of the strands. Moreover splitting tensile strength tests on concrete cylinders were carried out to determine the actual decrease of the tensile strength at elevated temperatures of the concrete applied in the bond tests and in most of the HC slab specimens.

After calibration of the model parameters, the model was successfully validated against the observations of the anchorage and shear behaviour of HC slabs in the tests at ambient and fire conditions. In chapter 7, it is shown that the model is capable to predict the observed behaviour very well with respect to the crack pattern, slip and type of failure. However, the time to failure was not matched very well, which was attributed to the high sensitivity of the time to failure to some influencing parameters. A parameter study was carried out, presented in chapter 8, to evaluate the relevance of various influencing parameters on the time to failure, the slip development and the crack propagation. Small changes of some of the parameters have a large effect on the time to failure while their effect on the slip and the crack pattern is much smaller. The sensitivity of the time to failure to these parameters requires a reconsideration of the current approach to achieve fire safety by the requirements of the fire resistance expressed in a time to failure. Chapter 8 ends with this reconsideration.

Finally, the conclusions are presented together with recommendations for future research in chapter 9. The sensitivity analyses and direct interpretation of the tests on the HC elements both contribute to the practical guidelines given in this chapter.

## 2 Literature on structural behaviour

### 2.1 AMBIENT CONDITIONS

#### 2.1.1 Failure modes of HC slabs

##### 2.1.1.1 Introduction

Over the past thirty years failure theories for HC slabs on rigid supports were developed on an comprehensive experimental basis. This paragraph describes the relevant failure modes. HC slabs are designed as simply supported slabs. For this reason, the generalised cross sectional forces,  $M$ ,  $V$  and  $N$  can be calculated directly on the basis of equilibrium conditions only, irrespective of the constitutive relations.

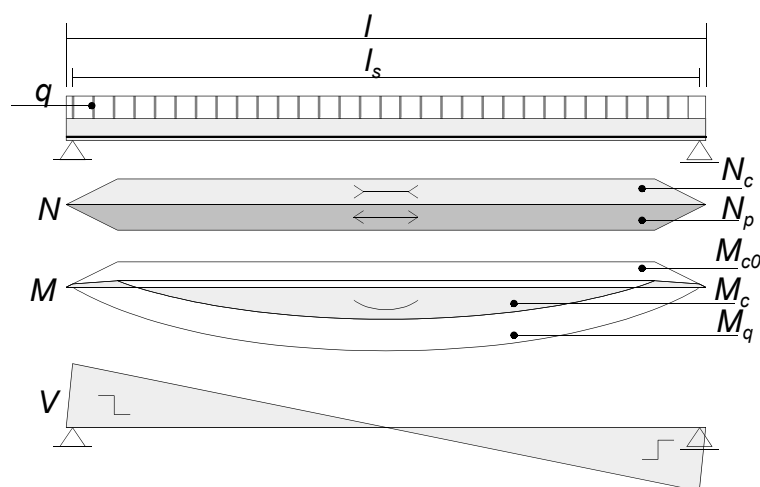


Figure 2.1: Generalised forces in simply supported HC slab.

The load causes a small increase of the steel stress, which is neglected in the drawing. Subscript  $c$  and  $p$  refer to the concrete respectively steel part of the cross section.

At ambient temperature, the stresses over the cross section can be calculated on the basis of linear elasticity. For this calculation, the prestress, the bending moment and the shear force have to be taken into account.

In 1983, the bearing capacity of HC slabs was analysed theoretically and experimentally [WALRAVEN & MERCX: 1983]. They determined four failure modes, e.g. flexure, anchorage, shear tension and shear compression. These failure modes will be discussed first. Subsequently the existing formulations will be compared with test results.

### 2.1.1.2 Flexure

In the unloaded stage, the strands are tensioned and the concrete is in compression, due to the prestress. The compressive stress increases towards the bottom of the slab because the elastic neutral axis of the strands is positioned eccentrically below the elastic neutral axis of the concrete cross section.

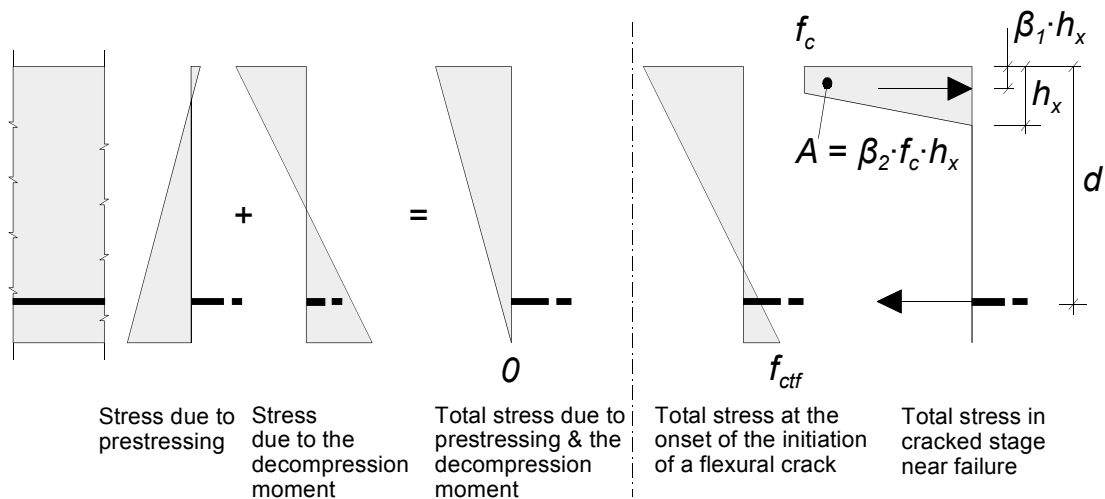


Figure 2.2: Linear elastic stress distribution over the height of the cross section due to prestressing and bending moments and non-linear stress distribution in the crack close to flexural failure.

Bending tensile stresses reduce the compressive stresses at the bottom and reach the tensile strength of concrete at some load level. Then vertical cracks develop perpendicular to the tensile stress due to bending. These so called flexural cracks grow from the lower side of the slab toward the upper side.

Flexural cracks do not immediate lead up to failure. The strands take over the stress released in the crack, leading to a local stress increase in the strands. The slabs have to be designed with sufficient strands such that the strands can undergo this stress increase without reaching the steel strength.

Further increase of the load increases the tensile stress in the strand and the compressive stress in the concrete compression zone. The slabs are designed in such a way that the strand reaches the yield strength before the concrete compression zone crushes. Rupture of the strands will occur after significant yielding and large deflection.

The bending moment capacity of a HC unit with  $n$  bottom strands is given on the basis of the

theory of plasticity by

$$M_F = \sum_j^n z^j A_p^j f_p^j = \sum_j^n (h - \beta_1 h_x - c^j) A_p^j f_p^j \quad \{2.1\}$$

The height of the compressive zone  $h_x$  can be calculated on the basis of horizontal equilibrium as

$$h_x = \frac{1}{\beta_2 b f_c} \sum_j^n A_p^j f_p^j$$

in which  $f_p$  is the steel strength,  $A_p$  the cross sectional area of each bottom strand  $j$ ,  $f_c$  the concrete compressive strength,  $b$  the width of the unit,  $h$  the slab depth,  $c$  the axis distance, i.e. the distance from the centroid of the strands to the bottom of the slab, and  $\beta_1$  and  $\beta_2$  shape factors for the concrete stress-strain relationship as explained in fig. 2.2. The ratio  $\beta_1/\beta_2$  ranges from  $1/2$  for a fully plastic rectangular stress block and  $2/3$  for a linear elastic triangular stress block. In the calculations a concrete stress block was adopted with 2.5 ‰ ultimate elastic strain and 3.5 ‰ ultimate plastic strain.

Generally, strands located near the top of the slab are conservatively neglected in the calculation of the plastic moment capacity, because the full plastic force can not always be reached in these strands without rupture of the bottom strands.

In §2.1.2, the accuracy of eq. 2.1 was evaluated. Because of the high accuracy of the model, eq. 2.1 is used in design calculations as well [PREN 1992-1-1: 2002, NEN 6720: 1995], without a partial safety factor for the model inaccuracy. For design calculations, just the design values of the material's properties are used rather than the mean value and  $\beta_1$  and  $\beta_2$  depend on the recommended shape of the concrete stress-strain relation.

### 2.1.1.3 Anchorage

If a flexural crack appears, the tensile stresses in the concrete drop. To reach a new state of equilibrium, the tensile force in the strand near the crack is locally increased, see also the schematic stress representation in fig. 2.5. The stress increment in the strand  $\Delta\sigma_p$  does not depend on the loading characteristics or the location of the crack but only on the concrete tensile strength and the ratio between the concrete area in tension that releases the stress and the cross section of the strands that takes over this stress. The tensile force can only be built up by bond stresses between the strand and the concrete. The maximum steel stress that can develop depends on the embedment length, i.e. the length over which the steel stress can be transmitted to the concrete cover. So the maximum steel stress decreases towards the end of the slab.

Anchorage failure can occur either in a brittle or in a ductile way. Which type occurs depends on the loading configuration. Brittle anchorage failure type occurs if the flexural crack is located close to the slab end. In that case, the steel stress increment due to crack initiation can not be developed in the strand. The strand is immediately pulled out. So, in this case the anchorage capacity equals the cracking moment resistance, which consists of the decompression moment  $M_0$  and a part causing tensile stresses in the bottom fibre as

$$M_{cr}(x) = W_0 f_{ctf} + M_0(x) \quad \{2.3\}$$

The decompression moment is the moment that counteracts the prestress to such an extent that no axial stress remains in the bottom fibre of the HC slab, see fig. 2.2. It depends on the distance from the slab end and the number of strands  $n$  and the prestress of each strand  $j$ . On the basis of the linear elastic beam theory the decompression moment reads

$$M_0(x) = \frac{W_0}{A_c} \sum_{j=1}^n A_p^j \sigma_{p\infty}^j(x) + \frac{W_0}{W_c} \sum_{j=1}^n e_c^j A_p^j \sigma_{p\infty}^j(x) \quad \{2.4\}$$

In which  $W_0$  is the section modulus of the lower half of the total cross section taking into account the contribution of the steel strands.  $W_c$  is the section modulus of the lower half of the concrete cross section only. The difference between the section modulus of the concrete cross section and of the total cross section is usually very small and therefore neglected. The eccentricity  $e_c$  is the distance from the centroid of the prestress to the elastic neutral axis of the concrete cross section. The  $f_{cf}$  is the flexural tensile strength of concrete. According to the Model Code [CEB-FIB: 1991],  $f_{cf}$  can be calculated from the mean splitting tensile strength  $f_{ctm}$  by

$$f_{cf} = f_{ctm} \frac{1 + 1.5 \left( \frac{h}{100} \right)^{0.7}}{1.5 \left( \frac{h}{100} \right)^{0.7}} \quad \{2.5\}$$

in which  $h$  is the depth of the cross section in mm.

Ductile anchorage failure occurs if the initial stress increment due to cracking can be sustained by the strand, but further increase of the load and consequently of the steel stress causes pull out of the strand before it yields.

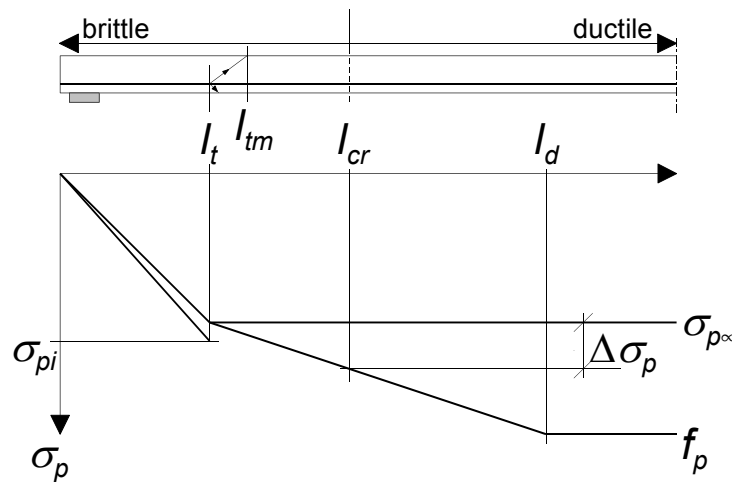


Figure 2.3: Stress envelope for the strands.

The transition between brittle and ductile anchorage failure is determined by the position of the flexural crack. If the flexural crack occurs within the so-called critical length  $l_{cr}$  from the slab end, the embedment length of the strand is insufficient to take over the stress released in the crack and cracking will cause brittle failure. If the flexural crack appears outside the critical

length but within the so-called development length  $l_d$ , ductile anchorage failure occurs. Outside the development length, the embedment length is long enough to allow for full yielding of the strand. In fig. 2.3, the maximum steel stress envelop is schematically presented.

The transfer length  $l_t$  is the length required to develop the full prestress. The transmission length  $l_m$  is defined by the cross section where the prestress is fully introduced over the total concrete cross section. As indicated in fig. 2.3, an increased slope of the steel stress envelope is used over the transfer length, because an increased bond strength is assumed over this length. Before the concrete is cast, the strands are pretensioned, causing a reduction of the strand diameter due to the Poisson contraction. When the prestressing force is released, the axial steel stress drops over the transfer length to zero at the end of the slab, which leads to an increase of the strand diameter in return. This radial expansion is restrained by the confining concrete and causes radial compressive stresses at the interface, which lead to an increased friction between steel and concrete. A more detailed description of the bond behaviour is given in §3.3.

In design codes [PREN 1992-1-1:2002, CEB-FIP: 1991, ACI 318:1995, NEN 6720: 1995] the stress envelope is simplified to a tri-linear diagram defined by the transfer length and the development length, see fig. 2.4. The large differences in the development length in the design codes can partly be attributed to the improvements in the production process that were made over the years. Zia et al. [1977] derived their results in 1977, while the relation of Mitchell et al. [1993] and the Model Code [CEB-FIP: 1991] were established in the nineties. The design code formulations are further discussed in Appendix B.

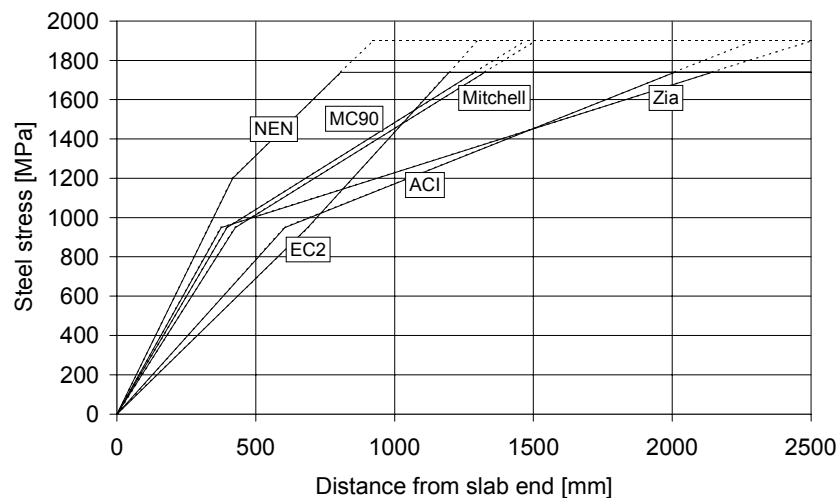


Figure 2.4: Steel stress envelope for 12.5 mm strand embedded in concrete with a compressive strength of 45 MPa at time of prestress release and a strength of 75 MPa after 28 days.

The calculation of the ductile anchorage capacity is similar to that of the flexural capacity, refer to eq. 2.1, i.e. the bending moment equals the tensile force in the strands multiplied with the internal lever arm. However, the maximum steel stress that can be taken in the considered cross section decreases toward the slab end.

The internal stress distribution, i.e. the distance of the compressive force to the strand, can not be solved on basis of equilibrium alone. It depends on constitutive and kinematic relations as well.

An upper bound value is found on the basis of theory of plasticity. Slip of the strands will cause the internal lever arm to increase. In the ultimate state, the lever arm grows until the compressive force is concentrated in the top of the slab. The internal lever arm  $z$  increases towards the slab end up to the effective slab depth  $d$  for  $\sigma_p(x) = 0$ . However, the variation of  $z$  over the length is negligible. The application of the theory of plasticity for anchorage failure is justified by the bond-slip behaviour, i.e. substantial slip can develop before the bond strength decreases, see §3.3. The anchorage capacity then reads as

$$M_A(x) = \sum_j^n z^j A_p^j \sigma_p^j(x) = \sum_j^n (h - \beta_1 h_x - c^j) A_p^j \sigma_p^j(x) \leq M_{cr}(x) \quad \{2.6\}$$

In order to calculate the anchorage capacity, the transfer length and the development length given by the Model Code [CEB-FIP: 1991] were used, see appendix B. As already shown in fig. 2.4, substantial variation exists between various design formulations for the steel stress envelope, which is the result of the variation in tests results. The Model Code accounts for the variation in test results with a model factor  $\alpha_o$  for the transfer length that ranges from 0.5-1.0, depending on the design check considered. The lower bound of 0.5 shall be used for the check on the occurrence of splitting cracks during the release of the prestress. The upper bound of 1.0 shall be used for the evaluation of anchorage failure. In the development length formulation, the model factor disappears, so it is implicitly taken equal to the upper bound value of 1.0. This is correct because the development length is only used for the ultimate limit state evaluation for anchorage failure.

The tensile strength of concrete is one of the parameters that determine the transfer length. Both the lower and upper bound of the transfer length are calculated on the basis of the lower bound characteristic value of the concrete tensile strength. So, also the mean value of the transfer length has to be calculated on the basis of this characteristic strength rather than the mean tensile strength. As a result, the safety margin between the mean transfer length and the design transfer length consists of the variation in the model factor  $\alpha_o$  only, i.e. the safety margin between the design tensile strength of concrete and the mean tensile strength is not incorporated in the transfer length formulation.

#### 2.1.1.4 Shear compression

Flexural cracks that are initiated in an area of both bending moment and shear force grow into inclined shear cracks. When a flexural crack is initiated, the tensile forces are carried by the strand. A new state of equilibrium can be found. The shear force is transmitted by aggregate interlock in the crack, the dowel action of the strand and by the uncracked compression zone. While the crack grows, the capacity of all contributions decreases up to failure. Since this failure mode starts with flexural cracks, it is sometimes also referred to as flexural shear failure.

The compression zone contributes more to the shear capacity with increasing concrete strength and with an increasing compressive stress. The latter can be reached by higher prestressing level or more reinforcement. Moreover, the cracks remain smaller with a higher reinforcement ratio, which favours the aggregate interlock.

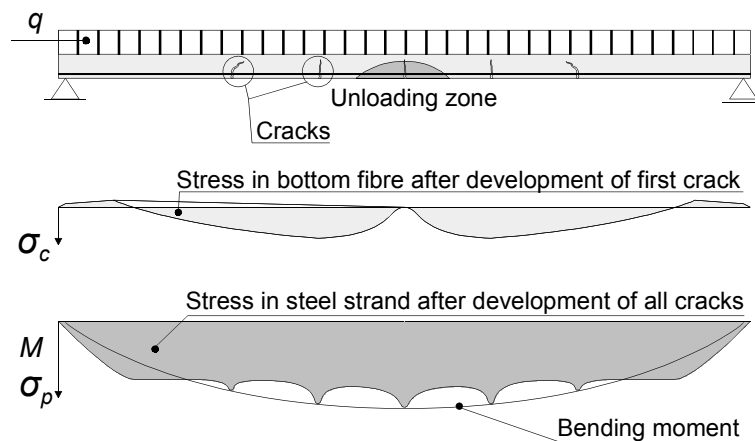


Figure 2.5: Development of flexural cracks and shear cracks and axial stress in bottom fibre of the concrete cross section and in the steel strands.

The shear capacity is affected by a size effect. While the crack grows, the uncracked concrete behind the crack is unloaded, see fig. 2.5. In this zone, energy is released during unloading which drives the crack growth. With increasing crack length, the zone of unloaded concrete increases too. As a consequence, larger cracks grow at lower loads than smaller cracks.

Over the past 40 years, various models were developed for shear compression failure [KANI: 1964, PRUISSERS: 1986, HEDMAN & LOSBERG: 1978]. The coefficient of variation (c.o.v.) of all these models compared to tests is relatively large. In order to take this variation into account, all shear formulations in design codes incorporate (implicitly) partial safety factors for the model uncertainty.

Kani [1964] developed an analytical model that describes the shear compression behaviour of reinforced beams without shear reinforcement. In this model a simply supported beam is considered, loaded by two equal point loads causing a constant bending moment without shear force between the point loads and a linearly increasing bending moment with a constant shear force from the supports to the point loads.

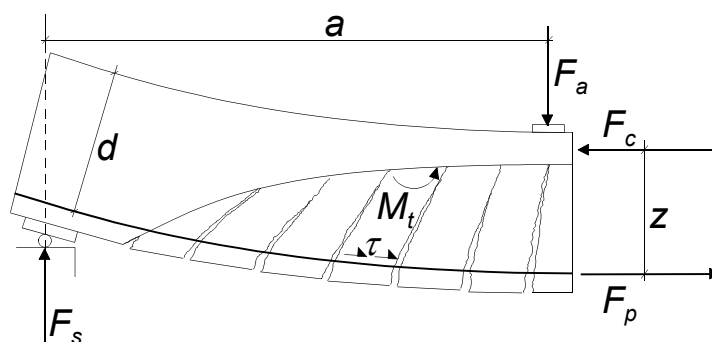


Figure 2.6: Kani's analytical comb-teeth model.

Due to the flexural cracks, the beam transforms into a comb-teeth like structure: The compressive zone of the beam is the backbone of the comb, while in the tensile zone the teeth are formed by the concrete separated from each other by flexural cracks, see 2.6. The teeth of the structure are loaded as cantilever beams by the bond stresses between the reinforcement and the confining concrete and inclined by the compressive zone. This loading causes the teeth to bend, leading to additional tensile stresses at the crack tip, which drives the crack propagation.

It appears that weaker bond of the strands increases the shear compression capacity. After all, lower bond stresses result in larger crack spacing, as the concrete tensile stress is built up from zero in the crack to the tensile strength over a longer length. And a larger crack distance enhances the bending capacity of the teeth and consequently enhances the shear compression capacity.

Hedman and Losberg [1978] derived after a statistical evaluation of shear tests on (prestressed) concrete beams a formula for shear compression that accounts for the size effect, the concrete strength, the reinforcement ratio and the prestress.

In the present research, for the evaluation of the shear capacity of HC slabs the formula of Hedman and Losberg was used, i.e.

$$V_{SC} = \gamma_{SC1} \Sigma b_w d k_s k_{ta} \left( 1 + 50 \frac{A_p}{\Sigma b_w d} \right) \sqrt{f_{cm}} + \gamma_{SC2} \frac{M_0}{a} \quad \{2.7\}$$

in which square root of  $f_{cm}$ , given in MPa, is a measure for the tensile strength, and therefore also is expressed in MPa. In this formula, the calibration factor  $\gamma_{SC1}$  is 0.104 and  $\gamma_{SC2}$  is 1.23 to predict the mean shear capacity and  $\gamma_{SC1}$  is 0.068 and  $\gamma_{SC2}$  is 1 to obtain a 95 % characteristic lower bound. In this way, these factors include the model accuracy.  $M_0$  is the decompression moment and  $a$  the distance between the point load and the support. Furthermore,  $k_s$  is the scale factor according to

$$k_s = 1.6 - d \leq 1 \quad \{2.8\}$$

with  $d$  in metres and  $k_{ta}$  is the factor taking into account the increased shear resistance near the support due to the load bearing mechanism of the tied arch, see also §2.1.1.5.

$$k_{ta} = \frac{3d}{a} \leq 1 \quad \{2.9\}$$

Walraven and Mercx [1983] and the FIP recommendations on HC slabs [FIP: 1988] safely take  $k_{ta}$  equal to 1 because the strands are not perfectly tied in HC slabs while eq. 2.7 was derived merely on basis of post-tensioned beams [LEONHARDT ET AL.: 1973, CAFLISCH ET AL.: 1970, 1971], pretensioned beams with large shear spans,  $a/d > 3$  [SOZEN ET AL.: 1959, OLESEN ET AL.: 1967], and pretensioned beams with very thin strands of 2 to 5 mm diameter [ARTHUR: 1965]. Equation 2.7 was further based on only a few tests on beams with pretensioned strands of 6 to 12 mm diameter with short shear spans [CEDERWALL ET AL.: 1974].

Nevertheless, the evaluation of the load bearing capacity of HC slabs in this thesis was based on  $k_{ta}$  according to eq. 2.9 because the tied arch action is limited by pull out of the strands and therefore a limited tied arch action should be covered by limitation of the anchorage capacity rather than a limitation of the shear compression capacity.

If the HC units are not simply supported, negative bending moments occur at the support. The

upper fibre is tensioned. Flexural cracks might start at the upper side of the HC element at some distance from the support, for instance if mild steel reinforcement was used in the longitudinal joints between the slabs. Since the HC units are barely prestressed at the upper side, there are no strands to take over the stress released in the crack and these cracks grow easily, causing an undesired brittle failure.

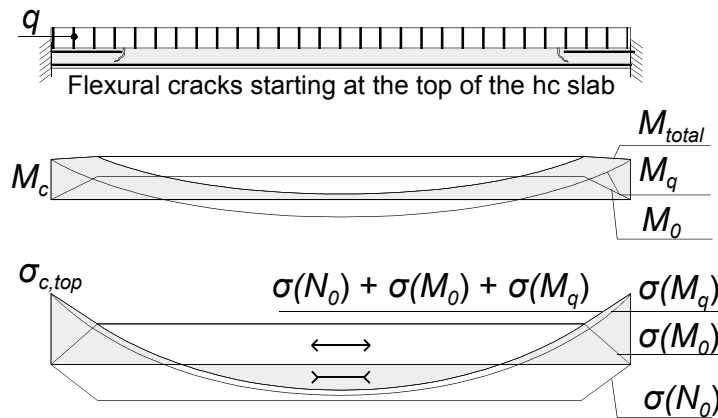


Figure 2.7: Crack development and axial stress of the upper fibre of the concrete cross section along the span due to negative bending moments at the support.

In design guides for HC slabs [FIP: 1988] special attention is paid to connection details in order to avoid such a failure.

### 2.1.1.5 Shear Tension

Shear tension failure starts with cracking of the HC slab near the support. On the contrary to the other failure modes, cracks are not caused by flexural tensile stresses in the lower fibre but by shear stresses in the web. When the web cracks, there is no reinforcement to take over the tensile forces and the shear tension capacity of the web drops directly to zero. The brittle behaviour does not allow for load redistribution over the webs after crack formation. So cracking immediately causes brittle failure.

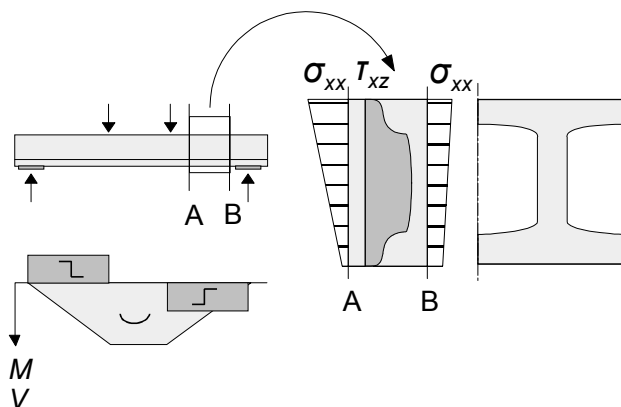


Figure 2.8: Schematic bending stress distribution (including prestress) and shear stress distribution over the depth of a HC slab.

On the basis of the theory of elasticity and using Bernoulli's assumption for beams that plane cross sections remain plane, the bending stresses are linearly distributed over the depth. The shear stress distribution over the depth depends on the cross sectional shape. In fig. 2.8 a schematic distribution is given for a HC slab.

The combination of shear stress and axial stress causes a principal tensile stress. The principal tensile stress has an inclination to the horizontal plane of approximately  $45^\circ$ . The maximum shear stress occurs at the support. Moreover, the prestress, that reduces the principal tensile stress, is not fully developed at the slab end. Therefore the principal tensile stress reaches its maximum in the thinnest part of the web near the support.

Nevertheless, the crack will not occur exactly at the support, because the stress distribution is disturbed near the support due to the vertical support pressure. The compression force in the upper flange is transformed into a vertical pressure near the support, see fig. 2.9. This compressive stress occurs only locally near the support and reduces the principal tensile stress. For very short shear spans, the slab can even act as a tied arch, which means that the support pressure is directly transferred to the point load through a concrete arch, tied by the strands. At the end of this paragraph, a lower limit for the load bearing capacity of the tied arch will be given.

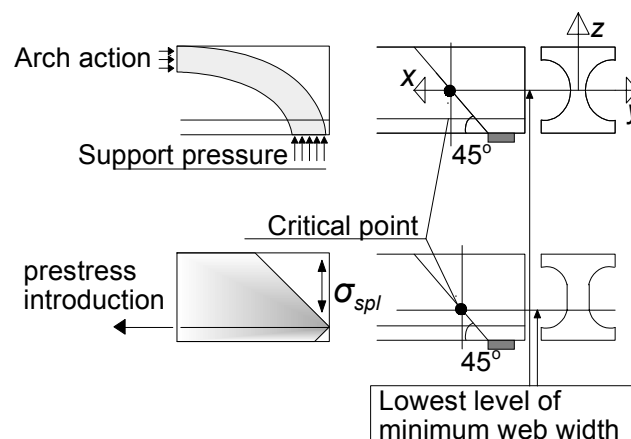


Figure 2.9: Critical point, assumed just outside the zone strengthened by the introduction of the support reaction and at the lowest level of the minimum web width.

So, the crack will be initiated in the web just outside the zone that is strengthened by the support pressure. In shear tension models, this starting point of cracking is called the critical point. The location of the critical point depends on the assumption for the introduction of the vertical support pressure and whether or not the shear stresses are considered that are caused by the introduction of the prestress over the cross section.

Walraven and Mercx [1983] assumed that the support pressure is introduced under an inclination of  $45^\circ$  from the inner support edge, see 2.9. Lin Yang [1994] investigated the location of the critical point for slabs with non-circular voids, i.e. units in which the minimum web width is not necessarily at mid-depth. He determined the critical point using 3D FE models. The FE model is validated with 59 test results of HC slab tests in which shear tension failure occurred. The

critical point appears at the intersection of the horizontal cross section of minimal web width with the line inclined under  $35^\circ$  from the centre of the support.

The stresses present in the critical point, are the axial stress caused by the prestress and the bending moment, and the shear stress, caused by the shear force and the prestress. In the critical point the prestressing force in the strand is not yet fully developed, since the critical point is located near the slab end. Moreover, Walraven en Merx [1983] assume that the prestressing force is introduced in the concrete cross section under an angle of  $45^\circ$ , see fig. 2.9. Therefore, the compressive stress at the critical point is calculated on the basis of the prestress in the strand at the inner edge of the support. The axial compressive stress is calculated by multiplying this prestress value with the ratio of the steel area relative to the total concrete area. This is a conservative calculation because the prestress is not introduced in the entire concrete area. Lin Yang and Pajari [1994] simply assume an angle of  $90^\circ$  for the introduction of the prestressing force and use the prestress in the strand at the critical point to calculate the compressive stress in the critical point.

The bending moments due to the imposed loads and the eccentricity of the prestress can be neglected without hardly any loss of accuracy, because the critical point is close to the slab end and near the centroidal axis. Moreover, the bending moments due to the prestress and the imposed loads level out each other. So the axial stress in the critical point reads as

$$\sigma_{xx} = \alpha_{cp} \frac{A_p}{A_c} \sigma_{p^\infty} \quad \{2.10\}$$

in which  $\alpha_{cp}$  is the reduction factor for the prestress in the critical point, ranging between 0.15-0.25 for practical cases.

The shear stress is caused by the vertical shear force.

$$\tau_{xy} = \frac{S_z}{\Sigma b_w I_z} V \quad \{2.11\}$$

In addition, Yang [1994] takes into account shear stresses due to the development of the prestress in the concrete, see fig. 2.10.

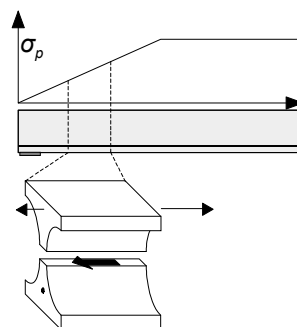


Figure 2.10: Development and distribution of the prestress giving rise to additional shear stresses in the webs.

The introduction of the prestress leads to an axial stress increment in the part of the cross section above the critical point which must be balanced by additional shear stresses, i.e.

$$\tau_{xy} = \frac{1}{\Sigma b_w} \int_{A_{cp}} \frac{d\sigma_{xx}}{dx} dA \quad \{2.12\}$$

In which  $A_{cp}$  is the area of the cross section above the critical point and  $\Sigma b_w$  is the minimum web width. Yang chose the critical point at the level of minimum web width. However, the inclusion of this term in the shear tension capacity equation has only limited influence. The additional shear stresses due to the introduction of the prestressing force were neglected in the design formulations.

Failure is assumed at the onset of the first crack in the critical point. The shear capacity is assumed to be reached if the principal stress equals the tensile strength as

$$\sigma_I = f_{ct} \quad \{2.13\}$$

The principal stress can be calculated on basis of basic tensor algebra by the stress invariants  $I_1$  to  $I_3$  as

$$\begin{aligned} I_1 &= \sigma_{xx} + \sigma_{yy} + \sigma_{zz} \\ I_2 &= \sigma_{xx}\sigma_{yy} + \sigma_{yy}\sigma_{zz} + \sigma_{zz}\sigma_{xx} - \tau_{xy}^2 - \tau_{yz}^2 - \tau_{zx}^2 \\ I_3 &= \sigma_{xx}\sigma_{yy}\sigma_{zz} + 2\tau_{xy}\tau_{yz}\tau_{zx} - \sigma_{xx}\tau_{yz}^2 - \sigma_{yy}\tau_{zx}^2 - \sigma_{zz}\tau_{xy}^2 \end{aligned} \quad \{2.14\}$$

The principal stress can be derived from

$$\sigma_I^3 - I_1\sigma_I^2 + I_2\sigma_I - I_3 = 0 \quad \{2.15\}$$

If  $x$  refers to the slab axis direction and  $z$  to the vertical direction, see fig. 2.9, we obtain in the critical point  $\sigma_{zz} = 0$ ,  $\sigma_{yy} = 0$ ,  $\sigma_{xy} = 0$  and  $\sigma_{yz} = 0$ . Substitution of these values in eq. 2.14 and together with eq. 2.13 in 2.15, lead to the following failure criterion:

$$f_{ct}^2 - \sigma_{xx}f_{ct} - \tau_{xy}^2 = 0 \quad \{2.16\}$$

which results in a shear tension capacity using eq. 2.11 and 2.10 equal to

$$V_{ST} = \frac{\Sigma b_w I_z}{S_z} \sqrt{\alpha_{cp} \frac{A_p}{A_c} \sigma_{p\infty} f_{ct} + f_{ct}^2} \quad \{2.17\}$$

The axial stresses due to bending are neglected in this formula. Yang [1994] showed on the basis of 59 tests that these simplifications only marginally affect the accuracy of the prediction (compare  $\mu = 1.02$  vs 0.92 and c.o.v. = 0.22 vs 0.21 for Yang's formulation including this stress components and eq. 2.17 respectively)

Some design codes use this formula [NEN 6720: 1991, PREN 1992-1: 2002] Safety is included by the use of the design tensile strength  $f_{ctd}$  rather than the mean tensile strength  $f_{ctm}$ . In addition, a lower bound value for the prestress is applied. The ratio  $f_{ctm}/f_{ctd}$  equals 2.14 [PREN 1992-1: 2002]. For the shear tension capacity, the ratio between the design and mean capacity ranges then approximately between 1.5 and 2.0. No additional model parameter is included.

ACI 318 [1995] uses

$$V_{ST} = \gamma_{ST} \left( 1.33 \sqrt{f_c} + 0.3 \alpha_{cp} \frac{A_p}{A_c} \sigma_{p\infty} \right) \Sigma b_w d \quad \{2.18\}$$

in which  $f_c$  is the cylinder compressive strength in [MPa] and  $\gamma_{ST}$  the safety factor for the model uncertainty of shear tension, equal to 0.85.

Up to this point, the principal tensile stresses were calculated on the basis of the theory of elasticity using Bernoulli's hypothesis of plane cross sections remaining plane.

However, the beam can also act like a tied arch. In order to explain the difference between the arch and the beam theory, the shape of the compressive thrust line is discussed for a beam without prestress. On the basis of the beam theory, the compressive thrust line is located at the top of the concrete cross section, see fig. 2.11. The principal tensile stresses that cause shear tension failure are the result of the curvature of the compressive thrust, see the expanded box in fig. 2.11.

In the arch analogy, the compressive thrust is completely tied at the support. The horizontal component of the compressive force is constant in the arch and completely transferred to the tie at the support. The internal lever arm follows the line of bending moment. In case of a point load, the thrust line is straight, see fig 2.11. As indicated in the expanded box, tensile stresses occur perpendicular to the curved thrust line. No shear stresses arise in the arch.

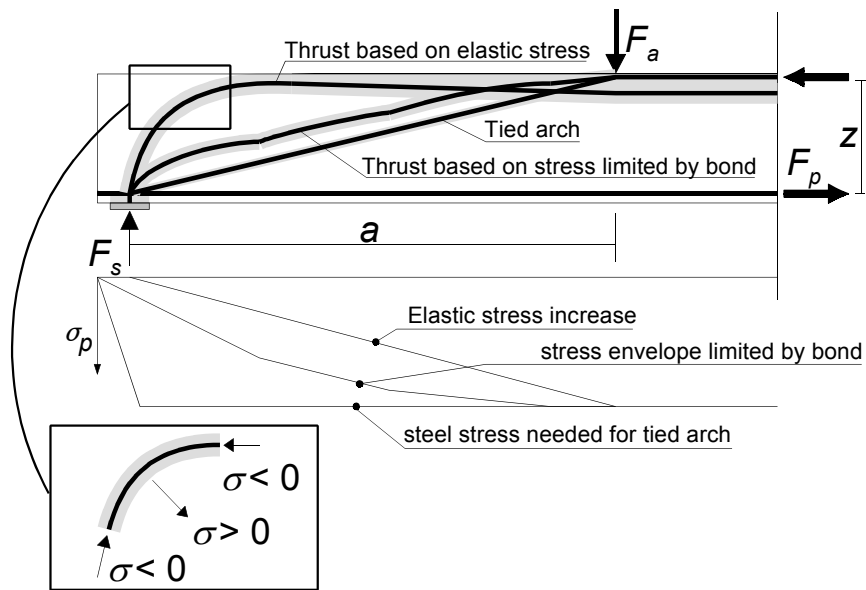


Figure 2.11: Location of the compressive thrust, depending on the assumed steel stress development.

Therefore, the shear tension capacity is at least equal to the load bearing capacity of the tied arch. Kani [1964] developed an expression for the load bearing capacity of the tied arch. He assumed that the arch is perfectly tied by the reinforcement. In that case the load bearing capacity of the arch is limited by the compressive force in the arch.

$$M_{ta} = \frac{d}{a} M_F = \frac{d}{a} z A_p f_p \quad \{2.19\}$$

However, the strands in the HC slab are not perfectly anchored. So, the load bearing capacity of the arch is limited by the anchorage capacity of the tie. Therefore, Kani's expression was modified, limiting the load bearing capacity to the tensile force that can develop in the strand for the slab end up to the nearest flexural crack. Kani assumed that this crack will occur at a distance  $h_x$  from the support, with  $h_x$  the depth of the compression zone. Although the prestress will force the first flexural crack to develop further away from the support, Kani's assumption was followed as a safe lower bound for the load bearing capacity of the tied arch. The tying force equals the steel stress at  $s+h_x$ , where  $s$  is the support width. The capacity of the tied arch now read

$$M_{ta} = \frac{d}{a} z A_p \sigma_{p\infty} (s+h_x) \quad \{2.20\}$$

with the internal lever arm  $z$  corresponding to the distance between the thrust line at the point load and the centroid of the strands. The internal lever arm nearly equals  $d$ , as the steel stress is limited that can develop in the first flexural crack and consequently, the compressive zone is small.

With the analogy of the tied arch, the interaction between shear tension failure and anchorage failure becomes clear. The actual location of the thrust line varies between the one corresponding to the elastic development of the steel stress over the length of the strands and the one corresponding to the ultimate steel stress increase limited by the bond of the strands see fig. 2.11. The minimum size of the tensile stresses for which equilibrium is still possible, decreases with increasing anchorage. The actual location of the thrust line and the actual size of the tensile stresses, however, depend on the constitutive and kinematic relations.

### 2.1.2 Capacity lines

In most tests a point load was applied at distance  $a$  from the support, which is the so-called shear span. In order to be able to compare moment failures with shear failures, the moment capacities related to flexural failure, anchorage failure, the cracking moment and the tied arch are rewritten to shear capacities according to

$$V = \frac{M}{a} \quad \{2.21\}$$

So, the shear capacity depends on the shear span  $a$  for all failure modes. In fig. 2.12 the shear capacity of the HC unit is plotted that was used most frequently in the fire tests given in chapter 4, i.e. the HVP260. The properties of this slab are given in appendix A.

The ultimate capacity is equal to the minimum of:

- The maximum of the flexural capacity and the flexural cracking capacity;
- The maximum of the shear compression capacity and the tied arch capacity;
- The maximum of the shear tension capacity and the tied arch capacity;
- The maximum of the anchorage capacity and the flexural cracking capacity.

The slab has to be designed in such a way that the flexural capacity exceeds the flexural cracking capacity by definition.

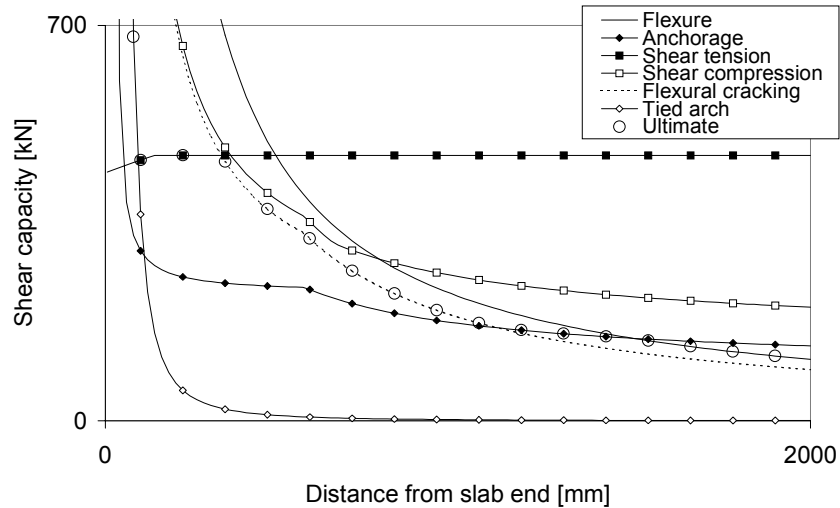


Figure 2.12: Mean load bearing capacity of HC unit HVP260 depending on the distance of the assumed point load from the slab end.

### 2.1.3 Validation with tests

In appendix A, 253 tests are collected that were conducted at ambient conditions on HC units on rigid supports. The experimental results are compared with the theoretical load bearing capacity of HC slabs according to par. 2.1.1 using the actual properties, if reported, and no safety factors. The accuracy of the calculation models was assessed by calculation of the ratios  $\chi$  between the experiments and the theoretical capacities with respect to flexural, anchorage, shear tension and shear compression failure. Also the theoretical cracking moment was compared with the observed value.

In case the loading history or crack patterns and photographs of the test were available, the failure mode was deduced from this data [KAMERLING & FIJNEMAN: 1980, SPANBETON: 1998, BORGOGNO & FONTANA: 1996, FELLINGER: 1999 & 2000]. Otherwise, the interpretation of the failure mode as given in the reference was followed [WALRAVEN & MERCX: 1983, BECKER & BUETTNER: 1985, PISANTY: 1992, PAJARI & KOUKARI: 1998]. In some cases, a difference of interpretation with respect to the actual failure mode exists between the reference and the author. Especially Borgogno and Fontana provided very detailed descriptions of the tests, which enabled a reassessment of the failure mode. In many cases, shear tension failures were defined as anchorage failures by these authors. In principle, they are correct, because the shear tension crack causes always pull out of the strand. However, it would be misleading to define such a test as anchorage failure, because the shear tension crack determines the failure rather than the pull out after the formation of this crack.

With respect to the geometry of the HC units, the nominal dimensions were used in the calculations except for the sum of the web widths, the height and the axis distances if measured. The mean concrete compressive strength  $f_{cm}$  was used in the calculations if measured. For 29 tests of the 253 tests, only the characteristic strength was provided in the reference. For these tests the mean strength was calculated using eq. 3.1. In the same way, the mean tensile strength  $f_{ctm}$  was

calculated from  $f_{ck}$  using eq. 3.3 whenever the tensile strength was not measured. This was the case in 202 of the 253 tests.

The prestress after losses due to shrinkage, creep and relaxation was estimated at 0.9 times the initial prestress. In 140 cases the initial prestress was not given. In these cases, it was estimated at 0.65 times the steel strength, which is a common value. The transfer length of the prestress was calculated according to eq. B.1 in appendix B using the mean splitting tensile strength at time of release  $f_{ctmi}$ , which was estimated at 0.6 times  $f_{ctm}$ . If the steel strength was not measured, it was estimated at 1.02 times the strength class, which corresponds to 1900 MPa for FeP 1860. The sensitivity of these assumptions was also evaluated.

The ratios  $\chi$  are presented in fig. 2.13 to 2.16 and the statistic characteristics are given in table 2.1. The ratio  $\chi$  with respect to the cracking moment was given in fig. 2.17. The figures show that the ratios can well be described with a normal distribution. The probability of each single data point was calculated according to the approach of Gumbel [NOWAK & COLLINS: 2000]. First all ratios are set in ascending order and each data point is indicated with increasing number  $i$  starting from 1 for the smallest ratio up to  $n$  for the highest ratio. The standard normal variate of each data point can now be calculated as

$$\beta = F^{-1}\left(\frac{i}{n+1}\right) \quad \{2.22\}$$

For normally distributed data, a graph of the ratio against  $\beta$  is a straight line. The slope of this straight line equals the standard deviation and the mean value is found at  $\beta = 0$ . Whether or not the data is normally distributed is indicated in the graphs by the correlation coefficient  $R^2$  between the data points and the approximated straight line, see also table 2.1.

**Table 2.1** Mean value and standard deviation of ratios  $\chi$  between the experimental and theoretical load bearing capacity with respect to flexural, anchorage, shear tension and shear compression failure and the cracking moment. Moreover, the correlation coefficient was provided with the normal distribution.

	Flexure		Anchorage		Shear Tension		Shear compression		Cracking moment
	I	II	I	II	I	III	I	II	
$n$	46	51	51	149	127	123	32	63	81
$\mu$ [-]	1.07	1.07	1.21	1.25	0.92	0.90	0.81	0.96	1.00
$\sigma$ [-]	0.11	0.10	0.27	0.22	0.21	0.16	0.16	0.20	0.22
$R^2$	0.91		0.98	0.99	0.92	1.00	0.99	0.97	0.98

I Based only on tests that showed the considered failure mode

II Based on tests that showed the considered failure mode + all tests for which the considered failure mode was expected, i.e.  $\chi > 1$ , but did not dominate.

III Based on all tests that showed shear tension except for the four cases marked in fig. 2.15, for which a suspiciously high ratio over 1.5 was found.

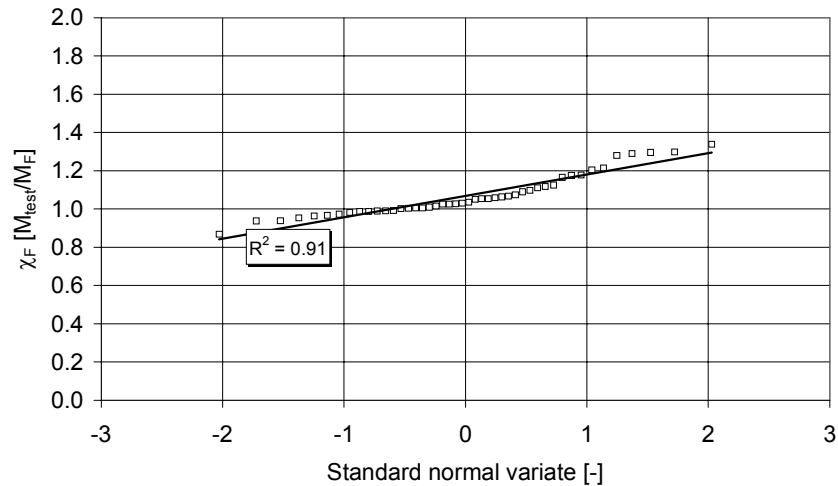


Figure 2.13: Distribution of the test to theory ratio with respect to flexural failure for all tests that showed flexural failure.

Even for the very predictable flexural failure some tests showed up to 10% lower values than predicted. As shown in appendix A, the shear span was short in all these tests. Probably, in these cases, either the failure mode was not determined correctly and anchorage failure actually had occurred or some strands slipped, causing others to take a larger tensile force which might have led to rupture of these well bonded strands.

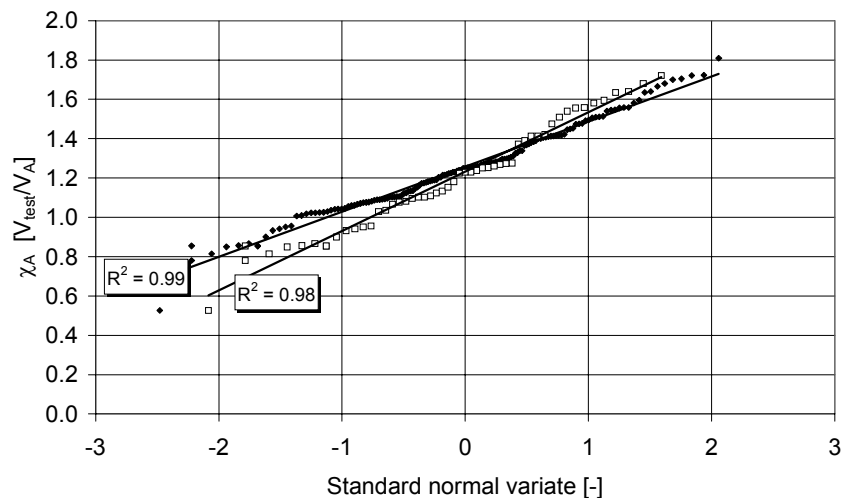


Figure 2.14: Distribution of the test to theory ratio with respect to the anchorage capacity for all tests that showed anchorage failure (open squares) and all tests that showed anchorage failure or for which anchorage failure was expected to occur, i.e.  $\chi_A > 1$  (solid diamonds).

In as many as 98 tests, anchorage failure did not occur although the theoretical anchorage capacity was exceeded in the test, which means that the theoretical value was too conservative for these tests (compared to only 51 tests that showed anchorage failure). In these tests, the actual anchorage capacity could not be measured but these tests show that the actual anchorage capacity was at least equal to the observed failure load. Taking into account this lower bound for the anchorage capacity in all these tests in the statistical assessment leads to a significantly higher

mean value and a different standard deviation. Therefore these statistical characteristics are given in table 2.1 as well and also presented in the figures. Also for shear compression failure these values are calculated since as many as 31 tests did not show shear compression failure although expected on the basis of the theoretical shear compression capacity. For flexural failure and shear tension failure, only a few tests did not fail in the failure mode expected and consequently, taking these tests into account hardly affected the mean value and standard deviation. They are not shown in the figure because it would mix up the image.

The direct consequence of the large number of tests that did not show anchorage failure while it was expected, is that the calculated mean value and standard deviation of the test to calculation ratio are just indicative and can not be used for recommendations to optimise the model parameter values. For the latter purpose, one should carry out tests on specimens that are designed in such a way that one failure mode must dominate the others even in the hypothetical situation of a test specimen for which the considered capacity occasionally would be very large and resistance against the other failure modes would be very small.

It is noted that in only 9 % of all tests corresponding to the solid diamonds in fig. 2.14 anchorage failure occurred at a lower load than expected. So, the theoretical formulation of anchorage failure seems rather conservative. In the calculation of the anchorage capacity, the mean value of the model factor  $\alpha_s$  that is used for the calculation of the transfer length had been chosen equal to 0.75, which is the average of the safe lower and upper bound that are provided in the state of the art report on bond by the FIB [FIB: 2000]. A best match would be obtained with  $\alpha_s$  equal to 0.6. This does not imply that the lower and upper bound must be modified as well. After all, the lower bound relates to splitting and bursting stresses, which can be observed directly after prestress release. So the consequences of splitting cracks can be limited by a simple rejection of the element and no high safety margin is required. The upper bound relates to anchorage failure which requires a higher safety level. The large margin of  $1.0/0.6 = 1.66$  is justified by the fact that the model factor  $\alpha_s$  is the only parameter that changes when the design anchorage capacity is calculated instead of the mean anchorage capacity (which was used in the current assessment). Contrary to the other failure mode formulations, the mean anchorage capacity is calculated with the design tensile strength of concrete rather than the mean tensile strength, see appendix B. As a result, the difference between the design capacity and the mean capacity is relatively small and a modification of the recommended design value of 1.0 for  $\alpha_s$  is not justified. On the basis of the findings with the current database, it is recommended to use a mean value for the model factor for HC slabs to  $0.75/1.25 = 0.6$ .

The ratio with respect to anchorage failure is also plotted against various input parameters but no significant trend could be found, which indicates that the input parameters are included in the calculation in a correct way. The ratio only decreases slightly for higher concrete tensile strengths, see Appendix A.

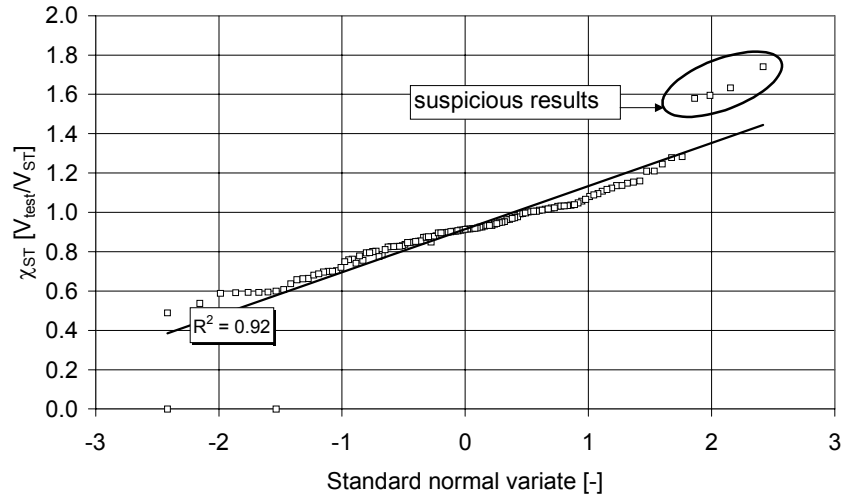


Figure 2.15: Distribution of the test to theory with respect to shear tension failure for all tests that showed shear tension failure.

Regarding shear tension failure, the mean value of  $\chi_{ST}$  corresponds well with the value obtained by Yang of 0.92 [1994]. In Appendix A, the ratio  $\chi_{ST}$  is also plotted against the tensile strength of concrete, which indicates a slightly decreasing ratio for higher strengths. The ratio is also plotted against other input parameters but no significant trends were found. So, it is concluded that the shear tension capacity formulation considers all relevant parameters in a correct manner. Four tests carried out by Becker and Buettner [1985] showed an extremely high test to theory ratio, for unknown reasons. Since these results are so far outside the rest of the results, maybe some error was included in the calculation of the theoretical value. Therefore, the mean value and coefficient of variation and correlation coefficient were also calculated for shear tension without these four tests, refer to column ST-III in table 2.1. The c.o.v. reduces to 16 % and the correlation between the distribution of the test results and the normal distribution increases to 100 %.

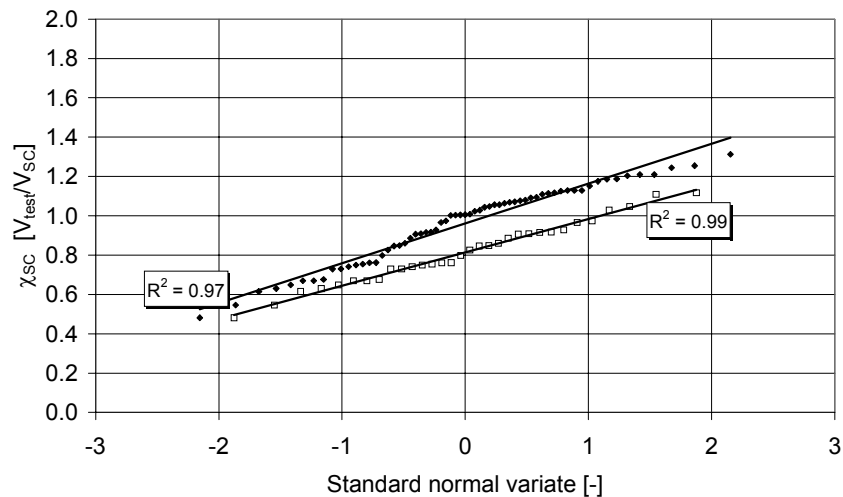


Figure 2.16: Distribution of the test to theory ratio with respect to the shear compression capacity for all tests that showed shear compression failure (open squares) and all tests that showed shear compression failure or for which shear compression failure was expected to occur, i.e.  $\chi_{SC} > 1$  (solid diamonds).

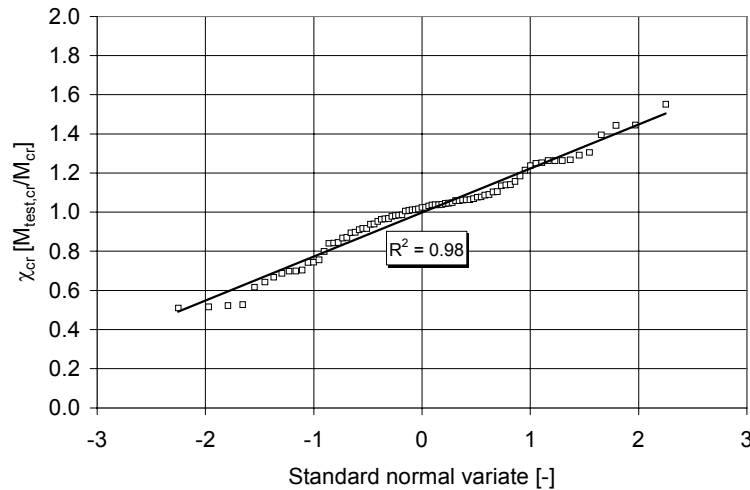


Figure 2.17: Distribution of the test to theory ratio with respect to the cracking moment for all tests in which the cracking moment occurred and was recorded.

Also the shear compression capacity can well be described by the model of Hedman and Losberg [1978]. On average the shear capacity is overestimated only 4 %. Using their partial safety factors to obtain a lower bound that is conservative in 95 % of all cases, results for the current data base of HC slab tests in 87.4% of all cases in a safe value. Given the fact that this result is partly based on tests that did not show a shear compression mode and the shear compression capacity consequently equals at least the failure load in these tests, the current assessment confirms the values of their model factors.

The assumption for the initial tensile strength at the time of the prestress release appeared to have a rather large effect on the calculated anchorage capacity but only little effect on the theoretical shear tension capacity. Modifying the assumption that the tensile strength at the time of the prestress release equals 60 % of the strength at time of the test to 50 % caused the mean value of the ratio  $\chi_{ST}$  to shift from 0.92 to 0.94 and the mean of ratio  $\chi_A$  from 1.21 to 1.31.

The assumption for the time dependent prestress losses of the prestress had a negligible effect on the calculated anchorage and shear tension capacities. However, the mean value of the ratio for the shear compression failure changed from 0.81 to 0.84 when  $\sigma_{pi}/\sigma_{p\infty}$  changes from 0.9 to 0.8 and the mean value of the ratio for the cracking moment from 1.00 to 1.03.

The observed scatter for anchorage, shear tension and shear compression failure is considerable. It must partly be attributed to the fact that the results were combined from various producers of various countries. The scatter within one plant is generally much smaller. The standard deviation of  $\chi_A$  of all slabs tested by Becker and Buettner [1985] is only 0.12 instead of 0.27 on the basis of all 253 tests and the standard deviation of  $\chi_{ST}$  of all slabs tested by Spanbeton [1998] is only 0.09 instead of 0.16.

From the statistical evaluation it is concluded that the load bearing capacity of HC units on rigid supports can adequately be described by the theoretical formulations given in this chapter. None of the ratios significantly depends on any input parameter which proves that all input parameters

are considered in an appropriate manner for all four failure modes. Therefore, the theoretical formulations can be used in order to evaluate the load level in the fire tests found in literature, as described in §2.2.4.5.

## **2.2 FIRE CONDITIONS**

### **2.2.1 Introduction**

As pointed out in the problem statement, the shear and anchorage behaviour of fire exposed HC slabs can be dominant in structural design. Furthermore, the shear and anchorage behaviour can only be assessed taking into account the effect of thermal stresses. Therefore, this paragraph starts with an outline of the background of thermal stresses. Hereafter the importance of thermal stresses on the behaviour will be underlined by means of fire tests on HC slabs found in literature. By assessing the data base of fire tests, other possible influencing parameters are investigated as well.

### **2.2.2 Theory of thermal stresses**

HC slabs expand under the effect of fire exposure as both concrete and reinforcement show thermal elongation at elevated temperature. This thermal expansion has great influence on the structural behaviour of both the fire exposed HC slabs and the unexposed structure connected to it.

The thermal elongation of the exposed side of the slab will cause thermal stresses over the entire cross section of the HC slab. Thermal stresses result from mechanical strains that have to develop to counteract incompatible thermal strains in order to meet the compatibility requirements. The actual distribution of these thermal stresses depends on the boundary conditions. Due to the thermal expansion, axial forces and bending moments can develop by restraining boundaries. At present working group 4.3.2 *Structural Applications* of the FIB task group *Fire Design of Concrete Structures* investigates the interaction between fire exposed structures and their unexposed boundaries.

Even though HC slabs are in principle simply supported and the thermal expansion is not restrained, thermal stresses will develop within the cross section if the temperature distribution over the cross section is non-linearly distributed.

The actual stress distribution has to satisfy the equilibrium conditions. Moreover, the actual constitutive behaviour of concrete and reinforcing steel shall be considered. The well known theory of elasticity is no longer applicable due to the thermal strains and the highly non-linear stress-strain relationships for concrete and prestressing steel at elevated temperature, see 5.4.3 on page 127 and 5.4.4 on page 138 respectively.

The calculation of the thermal stress distribution over the cross section is based on three principles, see fig. 2.18, i.e. kinematic conditions, constitutive laws and equilibrium.

Firstly, with respect to the kinematic requirements, the deformations should meet the boundary conditions. In case of simply supported HC slabs the boundary conditions allow for free expansion and rotation.

Moreover, the strain fields must satisfy the compatibility restrictions which follow from the fact that six strain components ( $\epsilon_{xx}$ ,  $\epsilon_{yy}$ ,  $\epsilon_{zz}$ ,  $\epsilon_{xy}$ ,  $\epsilon_{yz}$ ,  $\epsilon_{zx}$ ) were derived from only three displacement fields ( $u_x$ ,  $u_y$ ,  $u_z$ ). For the two-dimensional case, the compatibility requirement reads [KOK: 1991]:

$$\frac{d^2\epsilon_{xx}}{du_z^2} + \frac{d^2\epsilon_{zz}}{du_x^2} - 2\frac{d^2\epsilon_{xz}}{du_x du_z} = 0 \quad \{2.23\}$$

Thus, axial strains ( $\epsilon_{xx}$ ) that vary at a higher than linear degree with the depth ( $z$ ) must be accompanied with vertical or shear strains in order to satisfy the compatibility requirement.

For structural members with a high shear stiffness, this means that Bernoulli's hypothesis must be fulfilled, i.e. that plane cross sections should remain plane. Thus, the distribution of the total strains over the cross section can be described by the curvature and the axial strain at one point in the cross section as the fundamental unknown variables. The location of this point can be chosen freely. For the two-dimensional case, the total strain field reads as

$$\epsilon_{tot}(z) = \epsilon_0 + \kappa z \quad \{2.24\}$$

where the axial strain  $\epsilon_0$  in  $z = 0$  and the curvature  $\kappa$  are the fundamental unknowns.

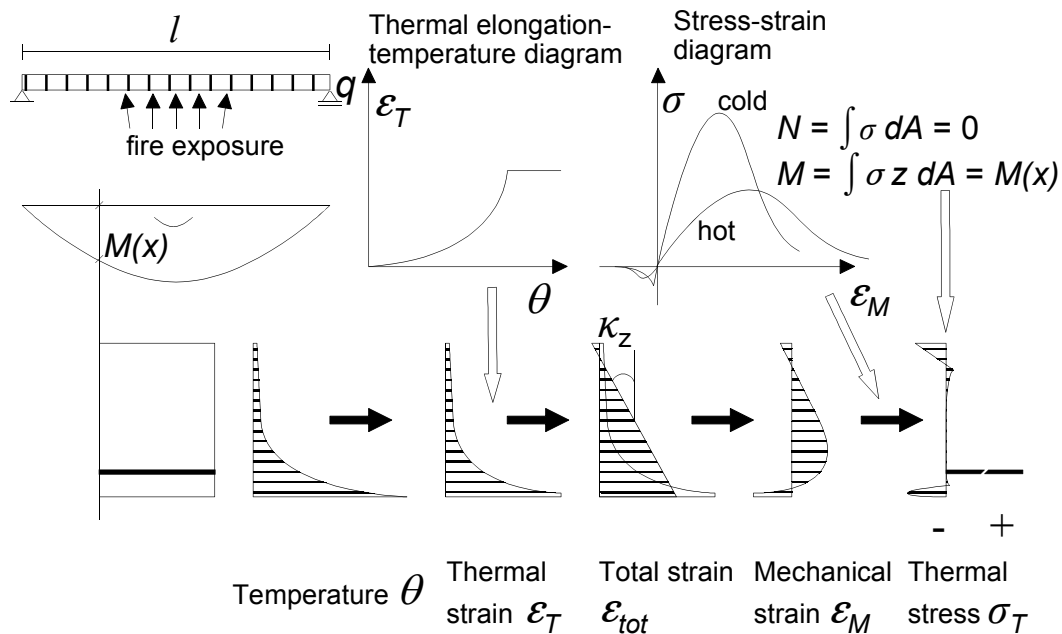


Figure 2.18: Graphical representation of the calculation of thermal stresses in a simply supported slab.

Secondly, with respect to the constitutive laws, it is assumed that the total strain at any position in a cross section can be decomposed into thermal strains and mechanical strains as

$$\epsilon_{tot} = \epsilon_T + \epsilon_M \quad \{2.25\}$$

The thermal strains solely depend on the temperature rise and the coefficient of thermal expansion, which is a material's property.

$$\varepsilon_T = \alpha_T(\theta - \theta_0) \quad \{2.26\}$$

The thermal strains do not depend on the stress level. So, once the temperature profile over the cross section is known, the thermal strain profile can be calculated directly.

In principle, the thermal strains are reversible. However, it must be noted that for concrete the thermal strains of the aggregates and the cement paste are not identical. As a result, irreversible mechanical strains have to develop in concrete, even when a uniform temperature was applied. The generalised thermal strains of concrete are therefore to some extent irreversible.

From these two requirements it follows that mechanical strains develop whenever the thermal strains do not comply with the kinematic requirements for the total strain field. The mechanical strains can exist of elastic, plastic and transient creep strains and deformations localised in cracks. It is noted that the term transient creep is somewhat misleading as these strains are mainly temperature dependent and barely time dependent [ANDERBERG & THELANDERSSON: 1976], [KHOURY ET AL.: 1985] and [SCHNEIDER: 1988].

Mechanical strains cause stresses. In the calculation of these stresses, the reduction of strength and stiffness at elevated temperatures should be taken into account as well as increasing ductility.

$$\sigma = f(\varepsilon_M, \theta) \quad \{2.27\}$$

The elastic strains are of a lower order than the transient creep strains and the thermal strains. Calculation of thermal stresses in fire exposed structures without taking into account the non-elastic strains therefore leads to completely unrealistic results and is pointless. As a consequence, the linear elastic model for the shear stress distribution presented in §2.1.1.5 on page 19 with regard to the shear tension capacity of HC slabs can not be used for fire exposed HC slabs directly.

Furthermore, it is important to note that thermal stresses result from imposed deformations. Stress relaxation occurs due to decreasing stiffness at elevated temperatures, the development of plastic strains and transient creep strains and crack propagation.

Finally, the stresses must satisfy the equilibrium requirements. In a simply supported slab, the generalised forces in each cross section, i.e. the normal force  $N$ , the shear force  $V$  and the bending moment  $M$  are exclusively determined by equilibrium. So, in this case, these forces do not depend on any constitutive model nor on any kinematic relation. Thermal stresses and strains therefore do not affect the distribution of the generalised forces in simply supported structures. In principle, the stresses should be calculated taking into account the imposed loading. So, the stress distribution over the cross section must balance the applied normal force  $N$  and the bending moment  $M$ .

$$\begin{aligned} \int_A \sigma dA &= N & (a) \\ \int_A \sigma z dA &= M(x) & (b) \end{aligned} \quad \{2.28\}$$

Thermal stresses can not simply be superimposed by stresses caused by imposed loading due to the highly non-linear constitutive behaviour of both concrete and reinforcement.

In the evaluation of the plastic bending capacity of a cross section, the thermal stresses are ignored since the critical cross section is generally cracked and the reinforcement yields. In the considered cross section, the thermal stresses have vanished due to relaxation by cracking and yielding, localised in this cross section.

Contrary to this cracked cross section, in cross sections outside the zone of localised deformations, the mechanical strains that are caused by the imposed loads are of a lower order than the mechanical strains that are required to counteract the incompatible thermal strains. For this reason, the thermal stresses can be calculated without consideration of imposed loads. So, the equilibrium equation to determine the thermal stresses can be simplified to

$$\int_A \sigma_T dA = 0 \Rightarrow \sum_{i=1}^n f(\varepsilon_0 + \kappa z_i - \varepsilon_{T,i}) = 0 \quad (a)$$

$$\int_A \sigma_T z dA = 0 \Rightarrow \sum_{i=1}^n f(\varepsilon_0 + \kappa z_i - \varepsilon_{T,i}) z_i A_i = 0 \quad (b)$$

{2.29}

From these two equations,  $\kappa$  and  $\varepsilon_0$  can be solved, which are the only unknown variables.

As indicated in fig. 2.18, compressive thermal stresses develop at the bottom and the top of the cross section and tensile thermal stresses in the web. The tensile stresses in the web can lead to vertical cracks, especially in HC slabs due to the reduced thickness of the web. The development of these cracks was already postulated by Borgogno [1997] and it is confirmed by the fire tests described in chapter 4. These cracks will be called thermal cracks further on. After the cracks initiated, the tensile stresses in the web are released and a new state of equilibrium must be found. Due to the crack propagation, the mechanical strains in the web increase, localised in the cracks and the compressive strains in the flanges decrease. So, the tensile stresses in the web are suddenly released after the crack formed. The decrease of the compressive stress in the flanges is not as sudden as in the webs. New equilibrium can therefore only be found if the strands take over the tensile stress released in the web. If no strand is present the crack will grow through the flanges as well. Also in the academic case that the strand is unbonded, the strand can not take over the tensile stress released in the crack and the crack would grow through the flanges.

In the transverse direction, no strands or mild reinforcement is present which explains the longitudinal cracks through the flanges below and above the hollow cores that developed in all tests described in chapter 4.

Outside the localisation zone of the cracks through the webs, thermal stresses built up again over some length until the tensile strength is again reached in an adjacent cross section, where a new crack will form. As a result, vertical cracks will develop at regular distances. This is also observed in the fire tests on HC slabs carried out described in chapter 4, see for instance fig. 4.5 on page 92.

The thermal cracks reduce the shear capacity. The strands must take over the tensile stress released in the crack. If the bond of the strand decreases due to the fire, the cracks will further grow and the shear capacity will also further decrease. So, the interaction between shear and

anchorage failure under fire conditions becomes evident.

At the end of a simply supported slab, no axial stresses can be present. This means that the thermal stresses have to build up over a certain development length. Over this length, the kinematic requirement of plane cross sections to remain plane is not fulfilled and the end surface will be warped to some extent, see fig. 2.19. Nevertheless, the compatibility requirement of eq. 2.23 is still satisfied, which means that the non-linear axial strain distribution is accompanied by shear strains. These shear strains lead to shear stresses that balance the built up of the axial thermal stresses. Moreover, additional bond stresses arise between the concrete and reinforcement to built up the thermal stress in the reinforcement as well. The magnitude of the shear stresses depends on the development length. The development length depends on the ratio between shear deformation and axial deformation. In the academic case that the shear deformation could develop without shear stresses, the development length would increase to infinity and no thermal stresses would built up at all. Bernoulli's hypothesis would not be valid. For concrete structures, the development length is approximated to be  $\frac{1}{2}$  the slab depth on the basis of some limited investigations with FE models.

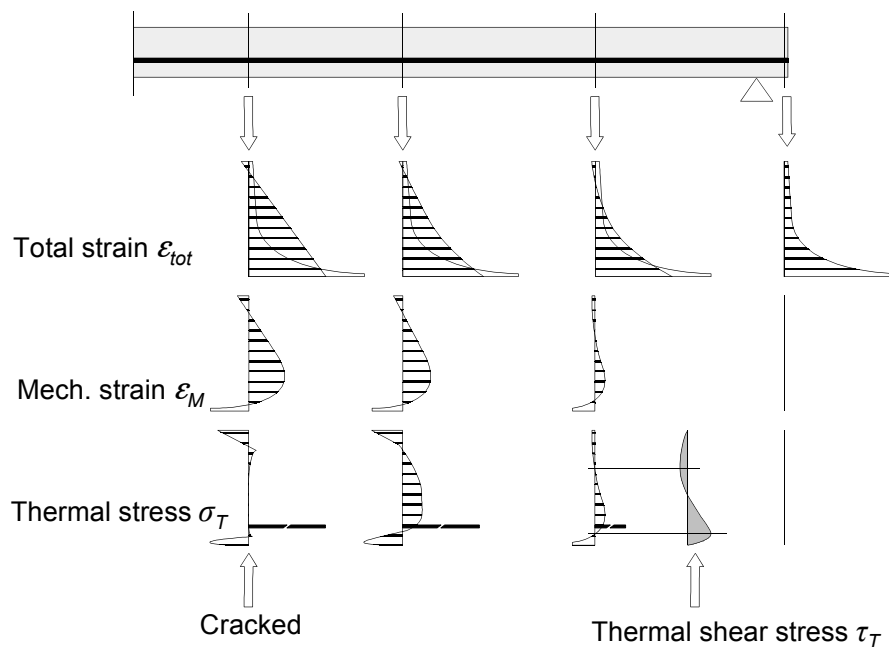


Figure 2.19: Development of thermal stresses near the end of a simply supported slab.

In practice, a perfect stress free simple support will never be constructed. The HC slab must always be connected with the support with reinforced concrete for reasons of overall structural integrity and to provide redundancy in the structural system. In hyper-static structures the distribution of the generalised forces ( $M$ ,  $V$ , and  $N$ ) in each cross section will change under the effect of thermal stresses. At the supports additional forces will develop that depend on the actual position and stiffness of the restraining boundary.

## 2.2.3 Failure modes of HC slabs

### 2.2.3.1 Introduction

The fire resistance of concrete structures is generally assessed by evaluation of bending failure (and buckling failure) since failure modes like shear are very uncommon for most concrete structures as noted in Eurocode 2 [PREN 1992-1-2: 2002] (not for HC slabs). Calculation rules are mainly developed to describe the bending moment resistance. Eurocode 2 states for other failure modes than bending: *Any potential failure mode not covered by the general calculation method shall be excluded by appropriate detailing (e.g. insufficient rotational capacity, spalling, local buckling of compressed reinforcement, shear and bond failure, damage to anchorage devices)*. What the *appropriate details* mean is not sufficiently defined.

As pointed out in §2.1.1 the shear tension and anchorage capacity of HC slabs depends strongly on the concrete tensile strength. Eurocode 2 requires to consider the actual fire behaviour, i.e. to carry out a fire test, whenever the load bearing capacity depends on the tensile strength. Alternatively, general (FE) models are allowed to calculate the fire resistance. In this case, the effect of temperature induced stresses and strains should be considered. The significance of these stresses and strains for the load bearing capacity, is explained in §2.2.2 on page 31. In that paragraph it was also pointed out that thermal stresses can be neglected in the calculation of the load bearing capacity of a cross section once the theory of plasticity can be applied like for the assessment of the flexural resistance.

### 2.2.3.2 Flexure

Only flexural failure is well defined in the codes as yielding and finally rupture of the strands. For flexural failure, design codes assume that the axis distance of the strands to the exposed side is the most important parameter. Eurocode 2 [PREN1992-1-2: 2002] gives axis distances for prestressing strands on the basis of an assumed critical steel temperature of 350 °C corresponding to a degree of utilization of 0.55, which is the ratio between the applied bending moment in fire conditions and the bending moment capacity at ambient conditions.

A small change in the axis distance has a large effect on temperature of the strand and the remaining yield strength. As a result, a relatively large variation in the degree of utilization corresponds to a relatively small variation in the required axis distance, in order to reach the same fire resistance. From the recommended reduction factor for the strength of prestressing steel at elevated temperature and the rule for a modified axis distance for critical strand temperatures other than 350 °C [PREN 1992-1-2:2002], it can be deduced that an increase of the axis distance with 10 mm corresponds to a 22.5 % higher allowable degree of utilization.

However, the strand temperature as measured in fire tests on HC slabs can vary considerably. From a survey of nine fire tests carried out at VTT in Finland in the eighties [LOIKKANEN & JUMPPANEN: 1984A,B,C,D,1985A,B; LOIKKANEN & KAJASTILA: 1990A,B,1991], it appears that temperature measurements vary in a range of more than 200 °C after 60 minutes, see fig. 2.20. This high scatter is uncommon for concrete structures. For instance Both [1998] obtained temperature measurements in cast-in-place steel-concrete composite slabs that could well be

reproduced. The scatter in HC slabs is attributed to the fact that no distinction between types of aggregate was made and to variations in axis distances that occur over the length of the slab due to the vibrations in the casting process of HC slabs, especially in extruded slabs. Moreover, the position of the thermocouple on the strand can not be guaranteed during production of HC slabs. Therefore, sometimes the thermocouples were drilled in the cast specimens from the soffit. However, thermocouples need to be aligned with the isotherms in the vicinity of the weld (which is the measurement point), in order to ensure an accurate temperature measurement, because the measured value is affected by the temperature of the wire over some length in the vicinity of the weld.

Finally, the thermocouple wires might have initiated splitting cracks that cause a local disturbance in the temperature field. As will be shown in chapter 4, splitting cracks can develop around the strands to the exposed soffit even without the weakening of the cover by the wire. Through the cracks vapour tends to flow, which can also have an effect on the measured temperature.

Furthermore, the strand temperature depends on the position of the thermocouple relative to the walls of the furnace. In all cases the soffit below the strand was directly exposed to the fire. Contrary to what one might expect, the strand temperature at 500 mm from the slabs's end tends to be slightly higher than at mid span, although this tendency is negligible compared to the scatter.

For the sake of comparison, the proposed profile of the mean temperature in Eurocode 2 [PREN 1992-1-2: 2002] is also drawn in figure 2.20.

In conclusion, the temperature of the strands in HC slabs can hardly be measured accurately by conventional thermocouples, especially in extruded HC slabs because the thermocouple wires might disturb the temperature field. Nevertheless, local disturbances in the temperature field due to cracks and moisture flow through these cracks might affect the local flexural capacity.

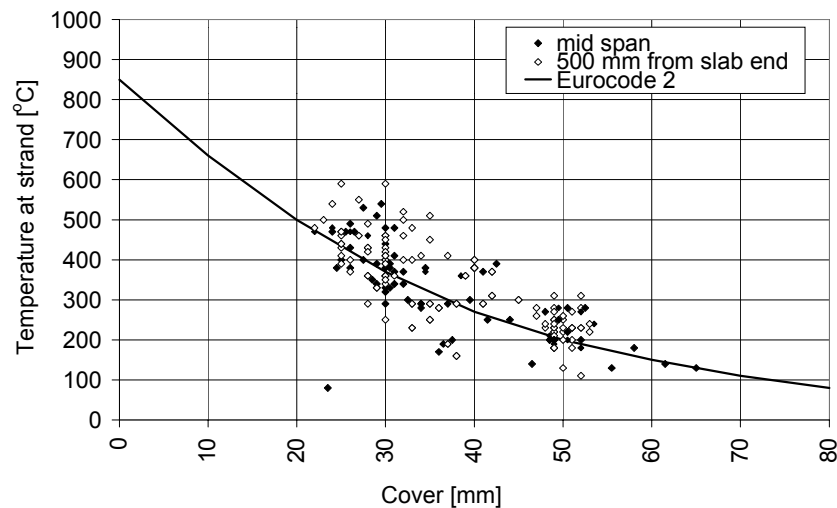


Figure 2.20: Scatter in measurements of the strand temperatures. Measurements were obtained at mid span and at 500 mm from the slab end after 60 minutes of fire exposure.

### 2.2.3.3 Shear

In the past no adequate descriptions of shear related failure modes were established. Borgogno [1997] tried to find a failure criterion for shear tension failure of fire exposed HC slabs. He suggested that failure occurs similar to the linear elastic beam theory for shear tension at ambient conditions once the tensile stress in webs reaches the tensile strength. He suggested to calculate the principal tensile stress by superposition of the tensile thermal stresses and the principal tensile stress that results from the shear stress. However, only the thermal stress were calculated on the basis of non-linear stress-strain relations. The shear stresses were calculated on the basis of linear elastic beam theory. As pointed out in §2.2.2, the calculation of stresses in fire exposed structures on the basis of the linear elastic theory is doubtful due to the influence increased non-linear stress-strain behaviour (creep, cracking, plasticity and non-uniformly distributed Young's modulus). So, linear elastic calculation of the maximum shear stress is not correct. Moreover, thermal stresses are released once the thermal strains are counteracted by cracks. For that reason, new equilibrium might be found after the formation of thermal cracks contrary to the failure mechanism that develops when a shear tension crack develops at ambient conditions. The evidence for the correctness of his approach that he gave [BORGOGNO: 1997] using a CTICM test [ZHAO: 1995a] must therefore be attributed to coincidence. Nevertheless, Borgogno's approach could be used to get a qualitative impression of the shear loading of fire exposed structures.

Due to the existence of thermal cracks, shear failure under fire conditions has more similarities with shear compression failure than with shear tension failure, since the calculation model for shear compression failure at ambient conditions is valid for the cracked part of the HC slab.

However, if the comb teeth analogy is followed, shear compression would not be likely to occur in fire exposed slabs. In §2.1.1.4 on page 16, it was explained that the shear compression capacity increases when the bond strength between the strands and the concrete cover decreases due to the larger crack spacing. Wider teeth have a higher resistance against shearing off of the comb. So, as the bond strength decreases during fire exposure the shear compression capacity increases. But the comb teeth analogy is not very accurate for HC slabs, since the crack propagation is also affected by the varying web width and splitting stresses along the strand. Very often, the cracks grow horizontally in the thinnest web width or along the strands, see for instance pictures taken during ambient tests, see fig. 2.21. Moreover, under fire conditions the cracks are initiated by temperature induced strains rather than flexural stresses, giving rise to additional tensile stresses in the webs. Also in fire tests [ZHAO: 1995a] horizontal cracks through the webs were observed.

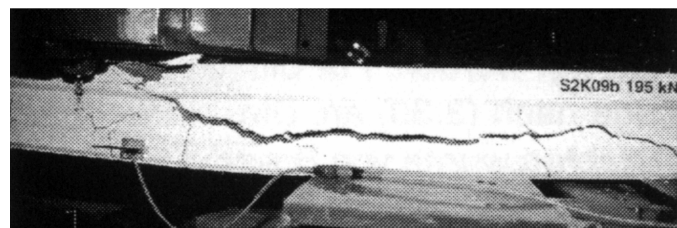


Figure 2.21: Horizontal crack in shear test on HC slab at ambient conditions by Borgogno [1997]

### 2.2.3.4 Anchorage

With respect to anchorage failure, only limited research data is available. Zhao [1993] attempted in vain to calculate the anchorage capacity of fire exposed HC slabs on the basis of literature data of a reduced bond strength at elevated temperatures.

As will be pointed out in §3.3, the bond strength of strands at elevated temperatures was only investigated neglecting the thermal stresses. Also bond-slip relations at elevated temperatures were established in the past without consideration of the thermal gradients. As shown in fig. 2.22, there is a huge scatter between the measured slip and the measured temperatures in HC slabs [LOIKKANEN & JUMPPANEN: 1984A,B,C,D,1985A,B; LOIKKANEN & KAJASTILA: 1990A,B,1991], showing that other factors than temperature of the strand alone must have an influence on the slip.

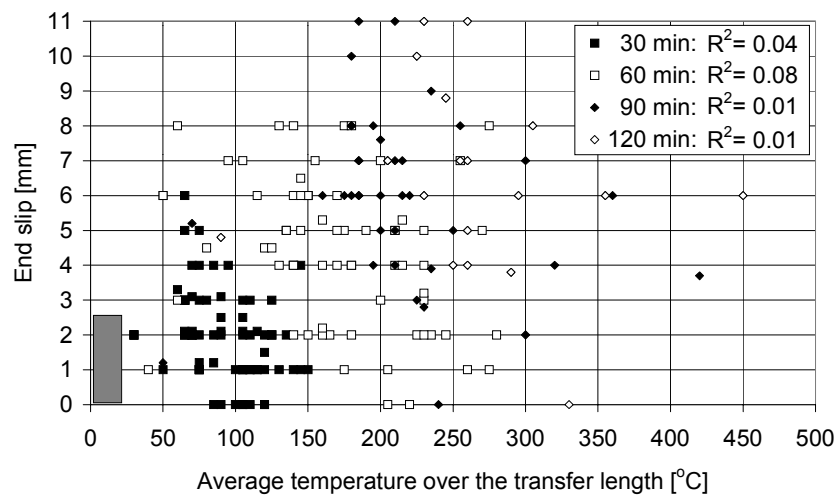


Figure 2.22: Slip of strands as function of the measured temperature over the transfer length obtained from eight Finnish fire tests on HC slabs, with the correlation coefficients  $R^2$ .

At ambient conditions, the slip of the strand after the release of the prestress is also a measure for the quality control after the production of the slab [PREN 1168: 1997]. Within the practical range of prestress levels and initial concrete strengths the acceptable slip is limited to approximately 2.5 mm for 12.5 mm strands. For the sake of comparison, the grey box, representing this tolerance, is added to the lower left corner of fig. 2.22. Individual strands are allowed to show a 30 % higher slip.

For ribbed rebars, Hertz [1982] distinguished between splitting and bond failure. He noticed that splitting failure might be affected by thermal stresses over the concrete cover that result from thermal gradients. However, he states that the time of anchorage failure during fire is the time when the bar is the warmest and that the effect of thermal gradients is negligible at this time. As will be shown in the next paragraph, this statement does not hold for prestressing strands. Anchorage failure can occur at such an early stage that thermal stresses will be present around the strand.

## 2.2.4 Evaluation of fire tests

### 2.2.4.1 General

Numerous HC slabs were tested under standard fire conditions over the past forty years. The main purpose of these tests was to demonstrate that HC slabs have sufficient fire resistance with respect to both the separating function and the load bearing function. As a consequence of this objective, most tests were stopped once the desired fire resistance was achieved and no information concerning the failure mode was obtained. Moreover, tests that showed failure due to lack of sufficient shear or anchorage capacity were mostly very briefly reported or not reported at all. So, not more than limited fundamental understanding of the load bearing behaviour was gained from these tests.

In order to assess the load bearing capacity of fire exposed HC slabs, 80 fire tests were collected that were carried out in Europe and the USA over the past forty years, see appendix C for references, most of which are confidential. In 51 tests the fire was stopped before failure had occurred. The time the test was stopped, ranged from 36 minutes for a specimen that reached a deflection criterion up to more than four hours. In four tests, flexural failure occurred. In two other tests, the test was stopped because the integrity criterion relevant for the separating function was violated, i.e. hot gasses and smoke could penetrate through the specimen due to large cracks. Explosive spalling was denoted as the cause of failure in three more tests.

A major problem arises in the definition of the failure type in the other 20 tests. In many cases, the failure mode was not undisputably defined in the test report. The distinction given in §2.1.1 for HC slabs at ambient conditions can not be given here.

All these 20 test specimens are considered to have failed due to a combination of shear and anchorage failure. The distinction between this failure combination and spalling or flexural failure is deduced by the author for each test on basis of the photographs and observations provided in the test report. A distinction between shear and anchorage failure was not made, even though some reporters of the fire tests indicated a specific failure mode. This is because there is an interaction between the shear failure and anchorage failure through the tied arch action, as pointed out in §2.1.1. It is unclear to which extent the relevance of this interaction changes under fire exposure due to the development of the thermal cracks near to the support. In the analyses, reference to these tests is given by a combination of shear and anchorage failure (S/A).

The fact that as many as one out of every four tests failed due to some kind of shear or anchorage mechanism, even though most tests were intentionally designed to successfully endure a certain fire exposure time, strongly underlines the need for design rules that cover this type of failure.

A survey into the relation between characteristics of the test and the fire resistance time and failure type was made, in order to find the most important influencing parameters that determine the type of failure and the fire resistance time. During the years of industrial research, several practical measures were applied to the test specimen in order to avoid shear or anchorage failure. The effect of these measures will be discussed as well as their practical relevance.

### 2.2.4.2 Strand temperature

In order to check the relevance of the strand temperature on shear and anchorage failure, the axis distance of the bottom strands to the exposed soffit was compared with the ultimate fire exposure time, because the axis distance is a measure for the strand temperature. Both the 20 tests that showed failure due to some kind of shear or anchorage (S/A) and the other 60 tests are presented, see fig. 2.23.

The figure remarkably shows that there is a slight tendency for S/A failure with increasing axis distance, which is completely opposite to the flexural behaviour. Furthermore, S/A failure occurs very often within 30 minutes of fire exposure even in HC slabs with strands at more than 80 mm from the exposed soffit. According to annex A of Eurocode 2 [PREN1992-1-2: 2002], the strand temperature is only 25 °C in that case. Apparently, the S/A failure does not depend on the temperature of the strand alone, if it is not completely independent of temperature.

As a consequence, attempts to predict the anchorage behaviour on the basis of the bond-slip relations at elevated temperatures alone are in vain. Other factors must be taken into consideration.

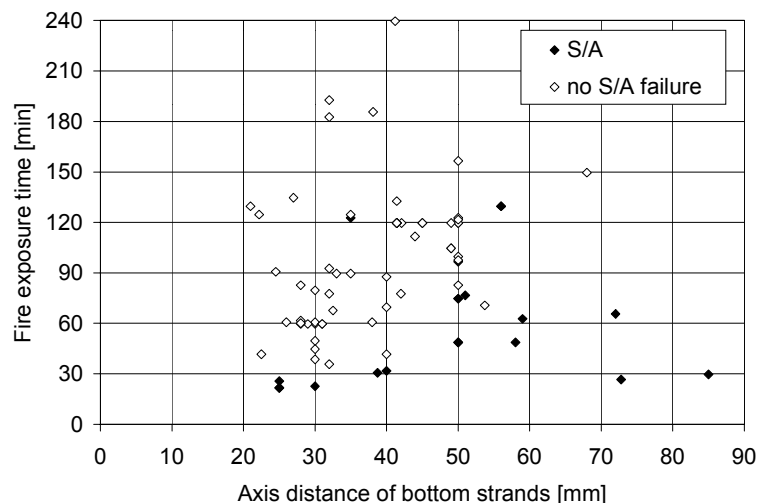


Figure 2.23: Relation between the weighted axis distance of the bottom strands to the exposed soffit and the fire exposure time for the tests that failed in shear or anchorage and the other tests.

### 2.2.4.3 Moisture

The hypothesis of Zhao [1993] that a the strand loses it's bond strength at a strand temperature of 100 °C due to the evaporation of moisture can not explain most of the S/A failures. The hypothesis was stated on the basis of the observation of moisture leaking out of the end of the slab around the strand just before failure. However, S/A failure at a strand temperature of only 25 °C can obviously not be explained by water vapour.

Nevertheless, the moisture content is one of the factors that might affect the result. It is generally accepted to assume that internal tensile stresses resulting from the evaporation of moisture in concrete is an important cause of explosive spalling. According to §4.5 of Eurocode 2 [PREN 1992-1-2: 2002] explosive spalling is not likely to occur if the moisture content is below 3%.

When HC slabs are stored indoor, the equilibrium moisture content can be assumed to be below this level. Even if no spalling occurred, the vapour pressures might have a detrimental effect on the load bearing capacity. Only for a few tests, the moisture content is known.

But for most tests, at least the age is known. During aging, the moisture content of HC slabs stored indoors will go down to the equilibrium moisture content. Therefore, HC slabs tested at young ages might be more sensitive to S/A failure than older slabs. Moreover, the concrete tensile strength increases during maturing, reducing the sensitivity to S/A failure. In fig. 2.24, the relation is presented between the fire exposure time and the age of the HC slab at the time of fire testing.

On the basis of fig. 2.24, it is concluded that the concrete age is not a dominant parameter on the occurrence of S/A failure. Only in one case, S/A failure could be influenced by the concrete age. In this test [Zhao: 1993], the HC slab was just 26 days old. In all other tests, the concrete age can not be attributed to the type of failure.

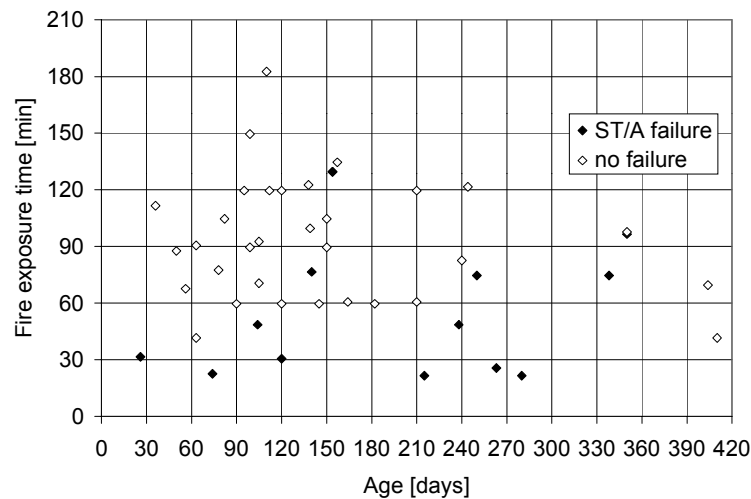


Figure 2.24: Relation between fire exposure time and age of the HC specimen at the time of testing.

#### 2.2.4.4 Thermal stresses

Probably the most important factor on the fire behaviour of HC slabs is the presence of thermal stresses, as postulated in the problem statement in chapter 1. As explained in §2.2.2, thermal stresses result from mechanical strains that have to develop to counteract the thermal strains in order to meet the compatibility conditions. Further, it was postulated that these mechanical strains can lead to:

- Splitting cracks along the strands reducing the anchorage capacity.
- Vertical cracks in the webs reducing the shear capacity.

Once cracks occur, the imposed mechanical strains are localised in the cracks and the thermal stresses are released.

#### Splitting cracks

At ambient conditions, splitting cracks sometimes occur over the transfer length due to the wedge

action of the strand at draw-in. Under fire conditions, splitting cracks along the strands can especially be expected to occur over this length due to a combination of differential thermal elongations over the concrete cover around the strand and the wedge action of the strand. Thermal insulation of the slab over the transfer length prevents the development of a thermal gradient and consequently the anchorage capacity might remain intact.

Early fire tests in Finland [HIETANEN: 1992] indeed showed that protecting the slab from heating over the transfer length of the prestress had a beneficial effect on the fire resistance. The HC slab either protruded the furnace wall over more than the transfer length or the slab was insulated by a protective layer. None of the 16 tests that were not heated near the support over more than 500 mm showed S/A failure, see the left picture of fig. 2.25. In case only 100 mm of the end of the slab was not heated, the effect was not significant.

One should keep in mind that the effectiveness of the cold support can not be attributed to the low strand temperature, as it was shown already that the strand temperature does not affect the failure type. Since temperature induced strains and stresses are present in the entire cross section, they can affect the bond between the strand and the confining concrete irrespective of the axis distance.

### **Vertical cracks**

As explained in §2.2.2, the size of the vertical cracks in the webs increases with the slab depth. Moreover, the distribution over the cross section of the mechanical strains that counteract the incompatible thermal strains, depends on the shape of the hollow cores and, last but not least, on the support conditions.

The relevance of the support conditions was already recognised in 1965 [CARLSON ET AL.: 1965]. It appeared that restraint of the thermal expansion might significantly increase the fire resistance. They stated after comparison of fire tests on HC slabs carried out in the USA with fire tests in Europe that *the effect of restraint often overshadows the effects of other factors such as steel cover, size and shape of the member, aggregate type, reinforcement type and load intensity.*

The effect of restraint was already recognised in ASTM E-119-00 [2000] decades ago. Structures are classified into those which are *restrained* to substantial thermal expansion and those which are *unrestrained*. HC slabs are classified as restrained if the slabs are supported and secured to a steel or concrete frame and either the frame resist the thermal expansion or the adjoining floor construction. Only HC slabs that form a single span or the end span of a multiple bay system must be considered as unrestrained.

If a structure is classified as restrained, the thermal expansion at the supports of a load bearing element should be resisted by external forces in the fire test. If the structure is classified as unrestrained, the element should be free to expand and rotate at the supports during the test.

Some of the 80 fire test specimens were (partially) restrained. In all American tests the specimens were confined in a cold restraining steel frame that provided both axial and transverse restraint. In several Finnish fire tests carried out in 1984 [HIETANEN: 1992], transverse restraining was established by applying a tight steel belt around the specimen near the support. The transverse restraint intentionally improves the bond behaviour by confining the strands locally and preventing splitting cracks. Later on, in 1985, the transverse restraint was established by a reinforced end beam cast at the end of the HC slab and tied to the HC slab units by means of rebars cast in the longitudinal joints or in concrete filled hollow cores. The reinforcement in the beam

takes over the tensile forces that are in equilibrium with the restraining compressive forces on the slab. In order to activate the rebars, they should be well anchored. Moreover, the slab must be well tied to the beam in order to transfer the restraining force from the reinforcement to the slab. Also in Belgium tests [TEIRLINCK: 1999], transverse restraining was achieved by casting a reinforced side beam along the longitudinal edge of the HC slab elements. Axial restraining was achieved by connecting the end beams to each other with rebars of 25-40 mm diameter located outside the furnace.

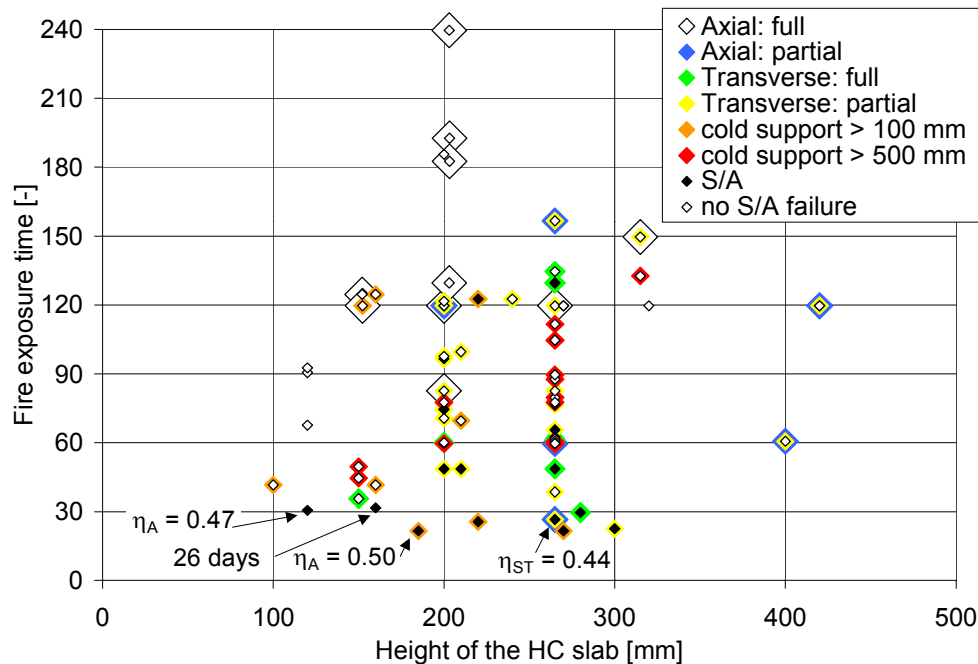


Figure 2.25: Fire exposure time versus the height of the HC slab. Measures to reduce the effect of temperature induced strains are marked with large markers around the marker that indicates S/A failure or no S/A failure.

The influence of the slab depth on the type of failure and the fire resistance time, is plotted in fig. 2.25. As the figure shows, shear and anchorage failure are more likely to occur in deeper slabs. Only three specimens with depths smaller than 200 mm showed such a failure, but this can be attributed to a high load level with respect to anchorage capacity in two cases and to the young age of the slab in the third case, as indicated in the figure.

Also the effect of restrained thermal expansion is presented in fig. 2.25. With an additional coloured marker, the type of restraint is indicated.

Clearly, axial restraint reduces the probability of S/A failure. None of the tests that were fully axially restrained failed prematurely due to an S/A mechanism (indicated with the large white marker around the dots). If the slab was only partially restrained by means of a reinforced side beam, S/A failure occurred in only one test out of six (blue markers). In this one test, S/A failure occurred within 30 minutes. However, this can be attributed to the relatively high load level with respect to the shear tension capacity, as will be discussed in more detail in §2.2.4.5.

The beneficial effect of transverse restraining is not as clear as axial restraining, whether it was

realised by means of a reinforced side beam or a confining steel belt. In 12 out of 43 tests in which some kind of transverse restraint was applied, S/A failure still dominated (green markers for tests with steel belts and yellow markers for tests with a reinforced end beam).

Thanks to the beneficial effect of (axial) restraining, premature S/A failure as observed relatively frequently in fire tests, did never occur in real practise, at least up to the knowledge of the author. In most practical applications, HC slabs will be built in a construction which can provide restraint to some extent, due to the general requirements of structural robustness. Nevertheless, it is uncertain to what extent restraint can be expected in practical floors and which degree of restraint is required to prevent S/A failure to occur. Recently, FIB established a working group to investigate the magnitude of restraining forces that can be expected in realistic structures.

Moreover, the position of the centroid of the restraining force in the cross section influences the contribution of the restraint to the fire resistance significantly, see also §2.2.2. In a real structure the vertical position of the restraining force depends on the detailing of the support. In Germany [HAKSEVER & WALTER:1980], three fire tests were carried out on identical concrete slabs with varying vertical positions of the restraint at the support. The restraining point was located at  $1/4$ ,  $2/4$  and  $3/4$  of the depth measured from the bottom. The fire resistance of the slabs varied from 69 minutes in the test with the restraining point at  $3/4$  of the depth from the soffit to more than 240 minutes in the test with the restraining point at  $1/4$  of the depth from the soffit. Also the measured restraining force varied significantly between the tests.

In conclusion, temperature induced stresses and strains play an important role on the occurrence of shear and anchorage failure of fire exposed HC slabs.

However, the postulate that the temperature induced strains cause vertical cracks through the web can not be proven nor rejected on the basis of the existing data set of fire tests. It was shown that axial restraining of the thermal expansion of fire exposed HC slabs contributes significantly to the fire resistance. Probably, the axial restraint reduces the temperature induced tensile strains and cracking in the web and consequently enhances the shear capacity. Nevertheless, it would be unsafe to count on it while no data is available on the required amount of restraint to avoid premature S/A failure and no practical design guides exist to ensure sufficient restraint.

In addition to the development of vertical thermal cracks, it was postulated that the temperature induced stresses and strains can cause splitting cracks along the strands, causing a reduction of the anchorage capacity. The splitting cracks result from the temperature gradient over the cross section. The possible existence of these cracks was evaluated comparing slabs that were insulated over (a part of ) the transfer length with unprotected slabs.

#### 2.2.4.5 *Load level*

Obviously, the fire resistance time might be affected by the load level, or the degree of utilization as it is called in the Eurocodes. In order to evaluate the effect of the load level, the fire exposure time was compared with the load level in all tests. Since the exact type of failure in the fire tests could not be determined uniquely, the load level was evaluated with respect to all three failure modes; shear tension, shear compression and anchorage failure.

As outlined in §2.1.1.3 , the anchorage capacity is limited by the cracking moment resistance within the critical length and the pull out resistance outside the critical length. It is assumed that vertical thermal cracks will grow into flexural cracks during fire over the entire length of the slab, (also within the critical length) and consequently that the pull out resistance limits the anchorage capacity. Therefore, load level with respect to anchorage failure was calculated relative to the pull out resistance rather than to the maximum of the pull out resistance and the cracking moment resistance. The load level with respect to anchorage failure was determined for each slab as the maximum at the transfer length  $l_t$ , the development length  $l_d$  and the shear span  $a$ , see fig. 2.26, because the pull out resistance and the applied bending moment vary along the length of the slab. Moreover, it is uncertain whether the transfer length and the development length will increase during fire with the same rate.

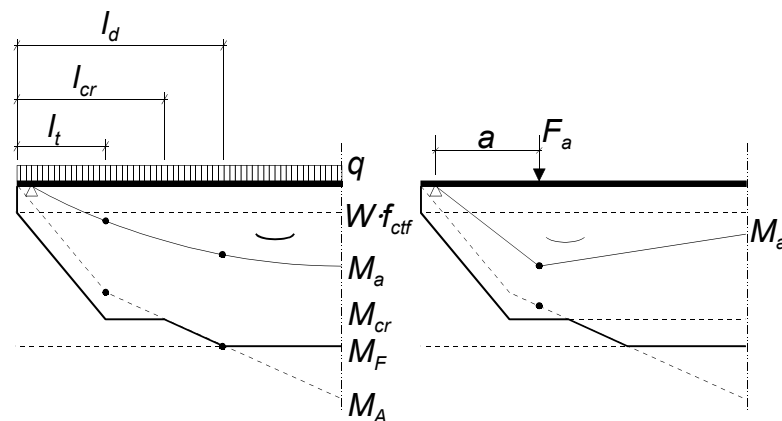


Figure 2.26: Ultimate bending moment capacity in HC slab with respect to flexure ( $M_F$ ) cracking ( $M_{cr}$ ) and anchorage ( $M_A$ ) and comparison with applied moment in case of a uniformly distributed load (left) and a point load (right)

In fig. 2.27, 2.28 and 2.29, the fire exposure time is plotted against the load level with respect to all three failure modes.

First conclusion is that S/A failure can occur between 20-130 minutes at load levels as low as 30-50 % with respect to the anchorage capacity or 10-25 % of the shear tension capacity or 15-40 % of the shear compression capacity. In practical applications, the load level that must be assumed at fire conditions is lower than at ambient conditions. The load level with respect to shear tension, shear compression and anchorage failure can be as low as 10 % in case the bending moment capacity limits the design at ambient conditions and the resistance against the other failure modes is far beyond the solicitation, but also be as high as 80 % in case one of these failure modes limits the design at ambient conditions and this resistance just meets the design criteria at ambient conditions. This means that the load levels applied in the fire tests can be considered as realistic and that S/A failure should be considered in the fire design of HC slabs.

Secondly, from fig. 2.28 it seems that a shear tension loading of more than 40 % causes failure within 30 minutes (the two tests represented by upper left dots), despite even some axial restraining by a side beam in one of these tests (blue marker). Off course it is uncertain whether

S/A failure would also have occurred in this test if the slab was better restrained. Also the transverse restraining by the end beam and the strengthening of the shear resistance by filling the cores could not prevent failure in case the shear tension loading was over 80 %. The high shear loading applied is explained by the fact that this test was conducted to check the fire resistance of a floor in a heavily loaded library. Design codes like the Dutch TGB 1990 [1991] assume for libraries that the frequent part of the variable load that is present during fire equals the extreme value. Apparently, the shear capacity dramatically decreases within the first 30 minutes. If the shear tension loading is below 40 % the effect of the strengthening measures becomes relevant, especially by virtue of the axial restraining.

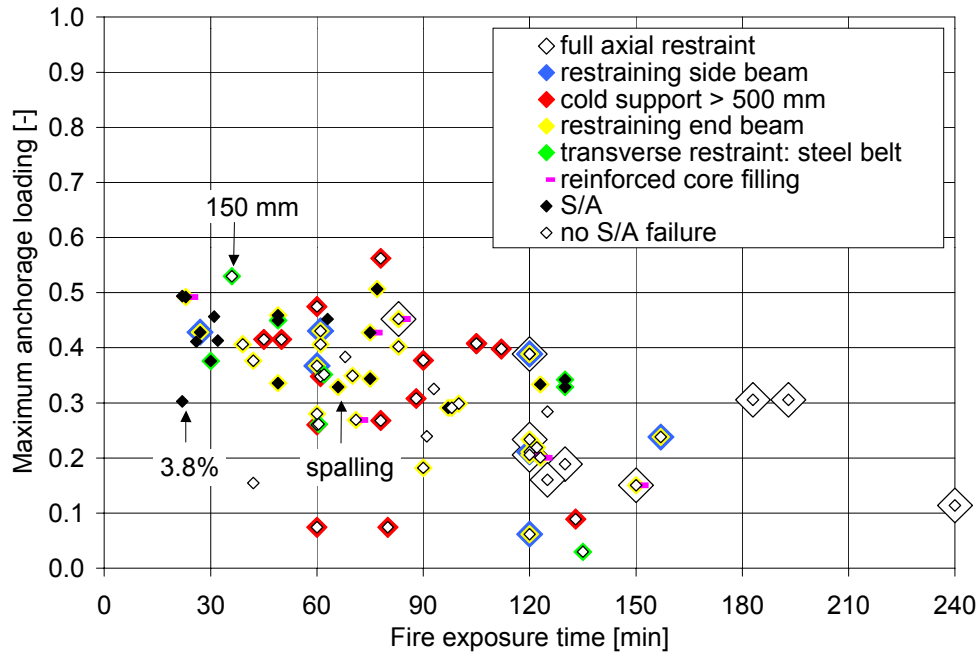


Figure 2.27: Fire exposure time versus the maximum anchorage loading applied in the fire test.

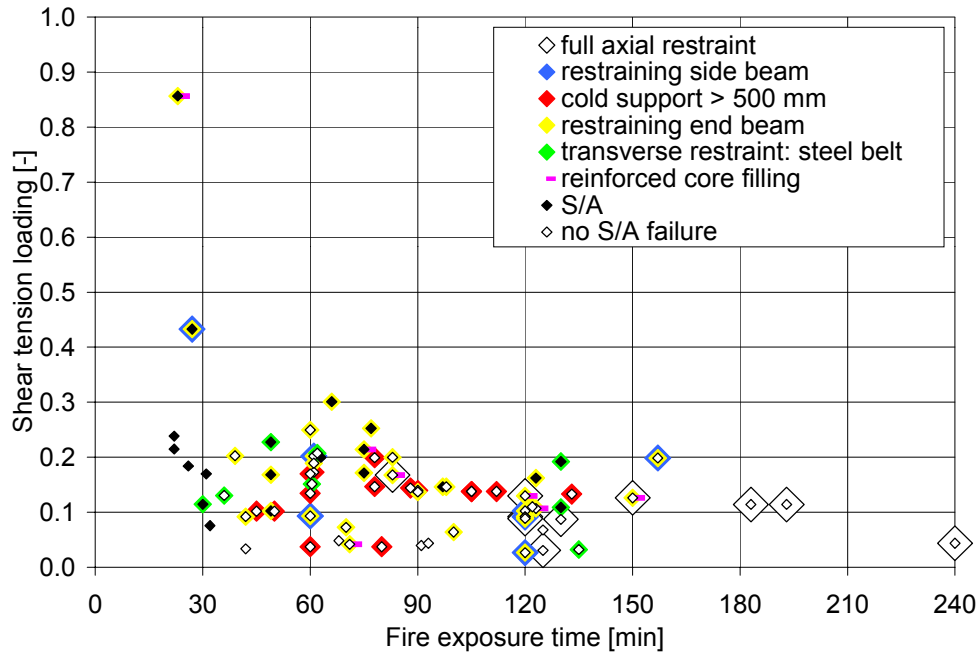


Figure 2.28: Fire exposure time versus the shear tension loading applied in the fire test.

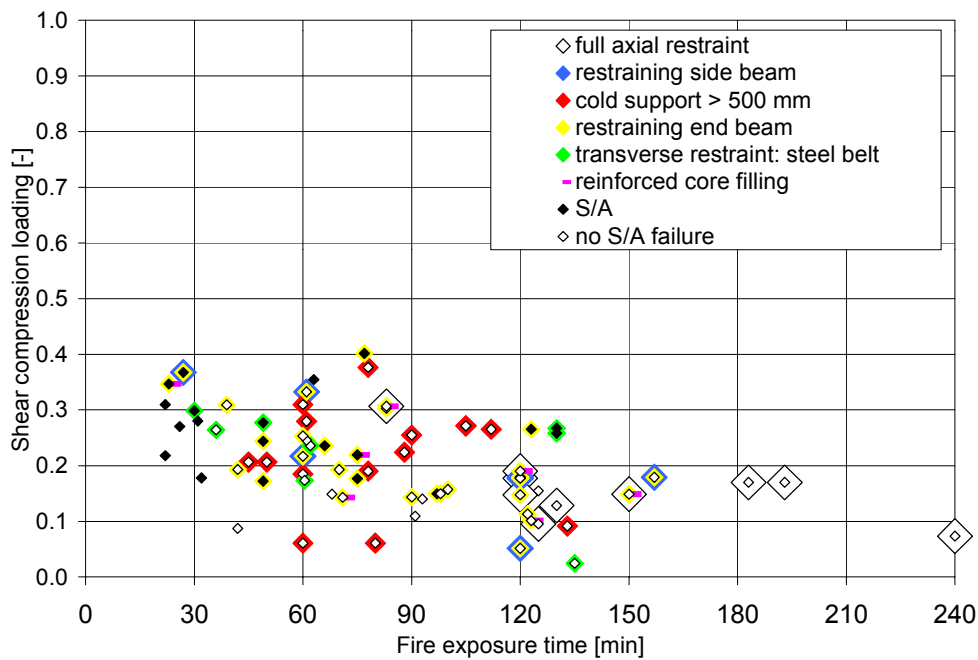


Figure 2.29: Fire exposure time versus the shear compression loading applied in the fire test.

Third conclusion is that there is a slight tendency that the fire resistance increases with decreasing load level, but the scatter is very high. If we consider the load level with respect to anchorage failure and we neglect the tests on specimens insulated over the transfer length (red markers) and the tests with axial restraint (blue markers and white boxes), we observe that most tests that showed failure due to an S/A mechanism have a higher anchorage loading than the tests that did not fail. Nevertheless, the scatter is high: Four tests in which S/A occurred had an

anchorage loading of less than 35 %, while many other tests had an anchorage loading between 35-45 % without S/A failure. But spalling was observed in one of these four tests while in another the moisture content was 3.8 %, which indicates that considerable tensile stresses might have developed due to evaporation of moisture. Another tests that did not show failure by an S/A mechanism while the anchorage loading was over 50 % were carried out on a relatively slim slab of only 150 mm height, see also fig. 2.27. In slabs with small cross sectional depths, smaller strains have to develop to counteract the thermal strains in order to satisfy the compatibility condition.

In four tests carried out in Gent, Belgium, the load was increased up to failure, after no failure had occurred within two hours of fire exposure. For instance, in test RG9158 the load level was increased from 14 % to 38 % with respect to shear tension failure or from 22 % to 60 % with respect to anchorage failure [TEIRLINCK & VANDEVELDE: 2000b], which is very high compared to the rest of the data base. Maybe, if the load level corresponding to failure would have been applied during the test, 120 minutes of fire resistance would not have been achieved. However, this is uncertain because the specimens gained the benefits of axial restraint which can also be the reason of the high ultimate resistance.

Nevertheless, it is possible that the damage caused by the temperature induced stresses and strains in combination with the applied loads was limited thanks to the relatively low load level during fire. And after thermal stresses had vanished considerably after two hours, the resulting resistance might have been much higher than during the test. This underlines the hypothesis that the assessment of the shear and anchorage capacity requires the recognition of irreversible damage due to the combination of thermal stresses and imposed stresses during fire exposure.

#### 2.2.4.6 *Practical measures*

Design recommendations [IPHA: 1998; BREKELMANS ET AL.: 2000] recognise the importance of the heating conditions of the HC slab near the support. When the HC slab is supported on an unprotected steel flange and the temperature of the flange exceeds 650 °C, the fire resistance of the floor system is assumed to be lower than otherwise. When the support flange is heated to more than 650 °C, the support flange might bend and the support reaction moves towards the flange of the supporting steel web, see fig. 2.30. So, the support reaction moves to the end of the HC slab, where the prestress is lower and consequently the shear tension and anchorage capacity of the slab are reduced.

However, the evaluation of the tests show that even a protected support zone of at least 100 mm does not effectively decrease the risk of S/A failure. Fig. 2.25 shows with orange markers the tests that had an insulated support zone between 100-500 mm. Four out of eight tests with a protected support zone of more than 100 and less than 500 mm, failed by an S/A mechanism, three of them within 30 minutes, one only after more than two hours.

In order to prevent the support reaction to move towards the end of the slab, the support force can alternatively be transferred to the beam by means of suspension reinforcement cast in two concrete filled cores, see fig. 2.30. The filling of the cores is known to enhance the shear resistance at ambient conditions. At fire conditions, in the strengthened zone, tensile thermal stresses are not concentrated in the web but spread out over the concrete filling as well, provided that the bond between the cast-in-place concrete and the slab is adequate. However, the

effectiveness of this measure could not be extracted from the current data

Fire tests were carried out on HC slabs strengthened near the support zone by filling the hollow cores with reinforced cast-in-place concrete over the transfer length of the prestress [TEIRLINCK: 1998, BORGOGNO & FONTANA: 1995, SCHEPPER ET AL.: 2000]. In all these tests, the slab was tied to an end beam that could provide some transverse restraint as well. In two out of six tests with concrete filled cores, S/A failure occurred, one of them within 30 minutes. However, the load level with respect to the shear tension capacity was extremely high in this test, i.e. the test corresponds to the dot in the upper left corner of fig. 2.28. In the other test, the load level and the failure time was within the same range as in the tests without concrete filled cores that resulted in S/A failure. The tests that did not show S/A failure, were either axially restrained or the combination of the load level and the failure time fitted well in the group of fire tests that did not fail due to S/A on specimens without concrete filled cores. So, the effectiveness of this strengthening measure remains unknown. At least, the application of the reinforced core filling with suspension rebars seems to counteract the detrimental effect of the shift of the support reaction by the transverse flexure of the steel flange of the supporting beam, as the support reaction can be taken by the concrete filling between the slab and the beam, see fig. 2.30. More definite conclusions regarding the effect of core filling can only be drawn once it is measured excluding other influencing parameters.

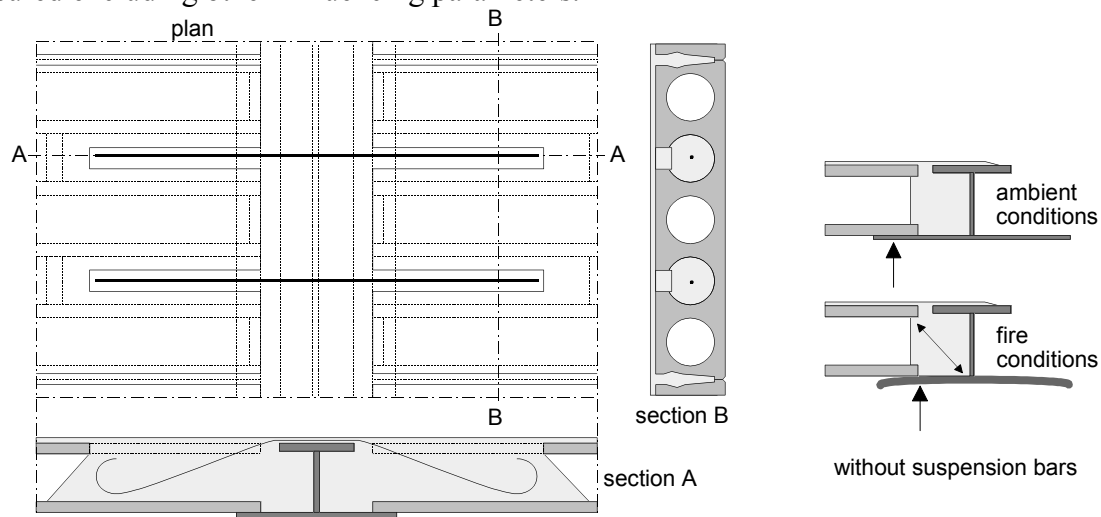


Figure 2.30: Detail (left) of HC slab supported on integrated steel beam using suspension reinforcement cast in two cores filled in cast-in-place concrete. Shift of the support reaction (right) due to bending of the supporting steel flange.

## 2.3 NON-RIGID SUPPORTS

### 2.3.1 Ambient conditions

Up to here, the failure modes of HC slabs were discussed assuming rigid support conditions. However, over the past decade, the application of HC slabs supported on beams, has raised significantly. As pointed out in the introduction of this chapter, the flexibility of the support reduces the shear capacity of the HC slabs. In this paragraph, the background is outlined and the

need is discussed for further research into fire exposed HC slabs supported on beams.

Due to the limited stiffness of the supporting beams, the HC slabs will deform not just in the spanning direction of the slab but in the spanning direction of the beam (transverse direction) as well, see fig. 2.31 which was taken from [PAJARI: 1995]. Depending on the stiffness of the supporting beam relative to the transverse stiffness of the HC slabs, the load is more or less directly transferred from the HC slab to the columns.

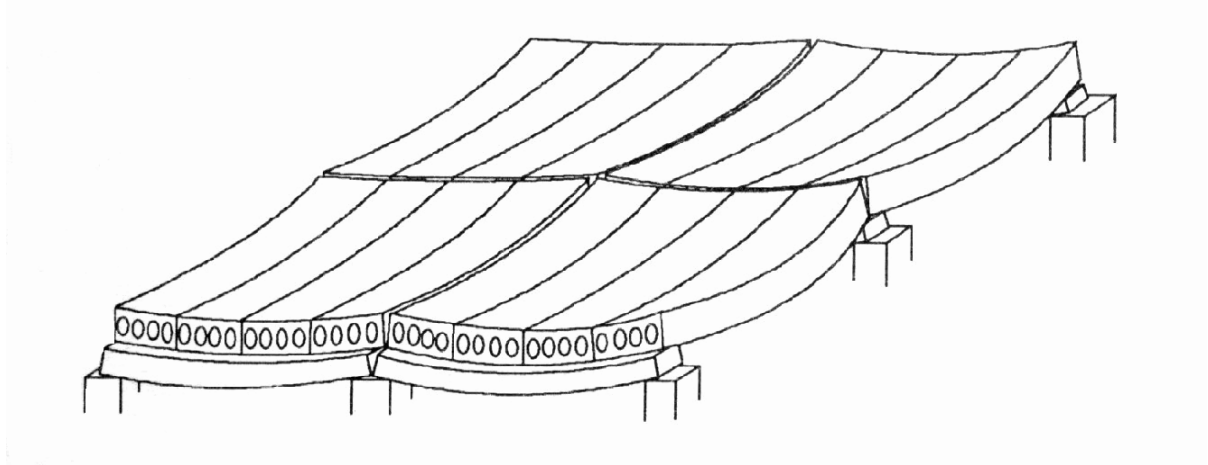


Figure 2.31: Principle of deformations of HC slabs on non-rigid supports according to Pajari [1995].

The beam and the slab will act together like in a composite beam, either intended in the design or not. This composite action causes additional transverse shear stresses in the webs of the HC slabs. Moreover, the vertical shear force will not be distributed uniformly over the webs. Peak shear stresses will arise near the columns. Due to the increased shear stresses, shear tension failure will occur at a lower applied load than in case the HC slabs are supported on rigid walls. Moreover, transverse bending stresses develop in the flanges of the HC slab. Depending on the position of the neutral axis of the composite beam, tensile stresses can occur in the bottom flange perpendicular to the strands. These tensile stresses increase the risk for splitting cracks along the strands which reduce the anchorage capacity.

The effect of the non-rigid supports on the load bearing capacity of the HC slabs was investigated extensively at VTT in Finland over the last decade. [PAJARI: 1995, LESKALÄ: 1990, 1991A&B, 1994, LESKALÄ & PAJARI: 1995, PAJARI & YANG: 1994, YANG: 1994 ]. In full scale tests [PAJARI & KOUKKARI: 1998] on HC slabs supported on beams, the shear tension capacity of HC slabs was found to be only 40-77 % of the shear tension capacity observed in reference tests on HC slabs supported on rigid walls. Therefore, the reduction in the shear tension capacity should be considered in the design of HC slabs supported on beams. The practical implication of this reduction is however limited for two reasons. The shear tension capacity generally does not govern the design of HC slabs and the load bearing capacity of the beam generally limits the allowable load on the floor system rather than the HC slab.

With regard to the shear tension capacity of the HC slab, the composite action between the HC slabs and the supporting beams is undesirable. However, some composite action can never be

avoided. Leskalä and Pajari [1995] postulated that *efforts at eliminating the composite behaviour may be regarded as acts of desperation*. Moreover, for reasons of structural integrity some connection between the HC slabs and the supporting beams should always be designed, which will cause shear interaction as well. Obviously, the amount of composite action depends on the type of connection between the HC slabs and the supporting beams.

Due to the hollow cores in the slab, the deformation of the HC slab in the transverse direction consists of bending and shear deformation. The contribution of shear deformation to the mid-span deflection of a HC slab supported along the edges ranges from 50 % for a 265 mm HC slab with five circular cores up to 90 % for a 400 mm slab with four cores [FELLINGER: 1998]. Therefore, the structural behaviour of the HC slab in transverse direction with the supporting beam can best be approximated with a bending member and a shear member, i.e. an element which deformation is predominantly caused by bending and shear deformation respectively.

Leskalä [1991b] developed a 2D FE model to describe the structural behaviour of the system, which allows for shear deformation of the HC slab in transverse direction and slip between the HC units and the supporting beam.

Borgogno [1997] developed a FE model to simulate Pajari's tests. He applied separate elements for the HC slabs in the spanning direction and the transverse direction. The elements in the spanning direction were provided with a bending stiffness and a torsional stiffness, the elements in the transverse direction were provided with a shear stiffness. The longitudinal joints between the HC units were modelled either as a hinge or as a full connection, depending on the occurrence of cracks through the joints in Pajari's tests. The model resulted in a shear force, a torsional moment and a transverse bending moment in the HC units. With a failure criterion that limits the combination of shear and torsion, Borgogno could predict failure in the tests of Pajari very well.

Pajari [1995b] developed design recommendations on the basis of a composite beam model that predicts the reduction of the shear tension and anchorage capacity. In this model, both the effective part of the HC slab and the supporting beam are considered as bending members, satisfying Bernoulli's hypothesis of plane cross sections remaining plane. The shear deformation of the HC slab and the longitudinal slip of the HC units along the beam are implicitly taken into account by an adjustment of the effective width  $b_{eff}$  of the HC slab contributing to the composite beam. By variation of  $b_{eff}$ , the calculated transverse shear flow in the webs varies accordingly. Torsional effects are not explicitly taken into account in Pajari's model. Excessive torsion is excluded by a limitation of the field of application to composite beams that remain linear elastic under the ultimate load with limited curvature.

Pajari assumes that shear tension failure occurs once the principal stress reaches the uni-axial tensile strength. This approach is similar to the shear tension failure criterion for rigidly supported HC slabs, but now the transverse shear stresses are added to eq. 2.13. He investigated the position of the peak tensile stress with the aid of a 3D FE model of a HC slab supported on a beam. He found that the peak stress can be assumed in the so-called critical point as defined for shear tension failure of HC slabs on rigid supports. With the use of eq. 2.14 and 2.15, the principal stresses in the web of the HC slab can be calculated from the stress components including  $\tau_{yz}$  resulting from the maximum shear force on the composite beam as [PAJARI: 1995a]

$$\sigma_I^3 - \sigma_{xx}\sigma_I^2 + (\tau_{yz}^2 + \tau_{xy}^2)\sigma_I - \sigma_{xx}\tau_{yz}^2 = 0 \quad \{2.30\}$$

The beam is considered to act as a composite beam once the joint concrete was grouted. Therefore, it is assumed that the self weight of the HC slab units does not contribute to  $\tau_{yz}$ . Pajari transformed this with the aid of eq. 2.13 to the following failure condition [1995b]

$$\frac{\sigma_{xx}}{2} + \sqrt{\frac{\sigma_{xx}^2}{4} + \tau_{xy}^2 + \beta_{cp}\tau_{yz}^2} \leq f_{ct} \quad \{2.31\}$$

with

$$\beta_{cp} = 1 - \frac{\sigma_{xx}}{f_{ct}} \quad \{2.32\}$$

On the basis of the aforementioned experiments, the effective width  $b_{eff}$  was calibrated for various types of beams in such a way that the failure condition eq. 2.31 is just met on the basis of the failure load in the tests. In the calibration process,  $\beta_{cp} = 1$  was simply used.

Alternatively, eq. 2.30 could be transformed after substitution of eq.2.13 into

$$1 = \frac{1}{\beta_{cp}} \left( \frac{\tau_{xy}}{f_{ct}} \right)^2 + \left( \frac{\tau_{yz}}{f_{ct}} \right)^2 \quad \{2.33\}$$

which is very similar to the design equation derived by Leskalä [1991a] who related the principal tensile stress to the tri-axial failure contour of Ottosen [1977]. On the basis of the approximation that  $\sigma_{xx} = -0.3f_{ct}$  in the critical point, he found  $1/\beta_{cp} = 0.84$ , whereas eq. 2.32 yields  $1/\beta_{cp} = 0.77$  in that case.

Further on in the calibration process, Pajari introduced in the design recommendations a reduction factor  $\beta$  for the transverse shear stress  $\tau_{yz}$  rather than  $\beta_{cp}$  for  $\tau_{xy}$  in order to account for alternative supporting details. In fig. 2.32, some basic cases are given for which  $\beta = 1$ . For alternative design solutions, like the application of a reinforced concrete topping or a concrete filling of the hollow cores over a depth equal to the slab depth, the reduction factor  $\beta$  was found to be between 0.5-1.

Filling of the hollow cores appeared to be an effective measure to increase the shear tension resistance. On one hand, the filling increases the transverse stiffness of the HC slab, causing more transverse shear to be transferred through the slab. On the other hand, filling of the void beyond the critical point, i.e. the point where the principal tensile stress reaches it's peak, enlarges the cross section that bears the shear flow and reduces the shear stress in the critical point.

In all full scale tests, the hollow cores were filled with concrete over a depth of at least 30 mm but mostly 50 mm, due to the application of hollow plastic plugs to close the voids, which is common practice in Finland. According to the author, this is the most critical configuration: the concrete filling increases the transverse stiffness of the slab, attracting more transverse shear flow, but the concrete cross section that is available in the critical point to take the transverse shear flow is not enlarged. Therefore it is postulated that Pajari's calculation model provides safe

solutions for HC slabs supported on beams without any concrete filling, which is common practice in countries like the Netherlands, where flat closures are often used to close the hollow cores.

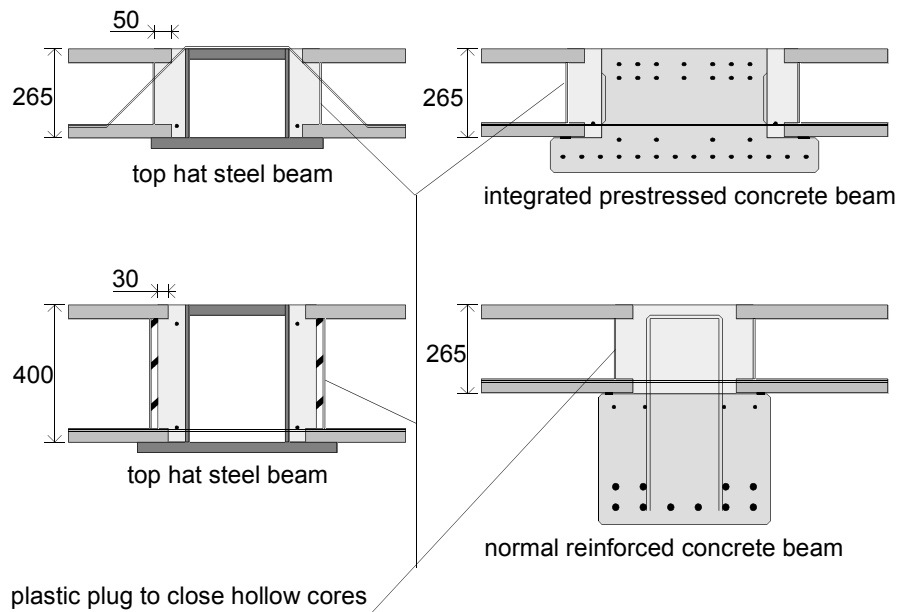


Figure 2.32: Examples of support details of HC slabs on beams in tests [PAJARI & KOUKKARI: 1998] for which the reduction factor for the transverse shear stresses equals unity.

Pajari calibrated his model not just for simply supported beams, but also for continuous beams. In the latter case, a large discrepancy exists between the shear distribution according to the composite beam analogy and the analogy of combined load bearing by a shear member (the HC slab in the transverse direction) and a bending member (the supporting beam), which is explained below. As mentioned before, the deformation of the HC slab in transverse direction is dominated by shear, so the actual behaviour is probably more similar to the latter analogy than to the composite beam analogy.

The differential equation for a load bearing structure composed of a shear member and a bending member reads [BOUMA: 1989]

$$q = EI \frac{d^4 w}{dx^4} - GA \frac{d^2 w}{dx^2} \quad \{2.34\}$$

So, the load is partly beared by the shear member with shear stiffness  $GA$  and partly by the bending member with bending stiffness  $EI$ . The boundary conditions at the supports are

$$\begin{aligned} w &= 0 & \text{(a)} \\ \frac{dw}{dx} &= 0 & \text{(b)} \end{aligned} \quad \text{for } x = 0; x = l \quad \{2.35\}$$

The shear force equals

$$\begin{aligned} \text{shear member} \quad V_{GA} &= GA \frac{dw}{dx} & (a) \\ \text{bending member} \quad V_{EI} &= -EI \frac{d^3w}{dx^3} & (b) \end{aligned} \quad \{2.36\}$$

Combination of the boundary condition 2.35b with 2.36a shows that the shear force in the shear member must be zero at the supports of the beam, whereas in the composite beam analogy of Pajari's model the maximum shear stress would appear at the supports. The maximum shear force in the shear member occurs in the point where the second derivative of the deflection equals zero, this is the point where the bending moment in the bending member is zero.

The actual transverse shear distribution in the HC slabs supported on beams is somewhere between the one derived with the composed beam analogy and the one derived with the analogy of a shear + bending member. Besides the fact that the HC slab does not purely deform by shear in the transverse direction, it is likely that in reality, the HC slab can rotate at the support of the beam by a crack in the longitudinal joint between adjacent HC units despite the beam being clamped at the support. Pajari made numerous FE analyses to find the transverse shear flow distribution in the webs of the HC slabs. He finally recommended to calculate the maximum transverse shear flow in the HC slab in the point of zero bending moment, which seems to be justified not just by his FE analyses but also by the simple analogy of the combined shear and bending member.

In order to evaluate the accuracy of Pajari's design recommendations, the ratio between the shear stresses calculated with the design recommendations on the basis of the failure load in the test and the shear stresses required to meet the failure condition eq. 2.31, was calculated for all ten full scale tests as

$$f_{ctm} = \frac{\sigma_{xx}}{2} + \sqrt{\left(\frac{\sigma_{xx}}{2}\right)^2 + (\lambda_{ST}\tau_{xy})^2 + (\lambda_{ST}\beta\tau_{yz})^2} \quad \{2.37\}$$

which suggests that the vertical and transverse shear are proportionally related to each other. This is not exact because the self weight of the HC slab units are not taken into account in the calculation of the transverse shear flow. With this definition of  $\lambda_{ST}$ , it is the reciprocal of the model accuracy factor  $\chi$ , i.e the ratio between the observed shear tension resistance  $V_{test}$  and the predicted shear tension resistance of HC slabs supported on beams  $V_{ST,flex}$ , i.e.

$$\chi_{ST,flex} = \frac{V_{test}}{V_{ST,flex}} = \frac{1}{\lambda_{ST}} = \sqrt{\frac{\tau_{xy}^2 + (\beta\tau_{yz})^2}{f_{ctm}^2 - f_{ctm}\sigma_{xx}}} \quad \{2.38\}$$

where  $\tau_{xy}$  and  $\tau_{yz}$  are the vertical respectively the horizontal shear stresses that develop in the test due to the failure load.

Ideally, the  $\chi$  should equal unity for all tests using the actual material properties. However, Pajari rounded off some parameters to the safe side. Moreover, he calibrated his parameters using the design value of the prestress rather than the mean value. As a result, the design recommendations predict slightly higher failure loads when using the mean value of the prestress, see table 2.2. Furthermore, in table 2.2 the ultimate shear force in the tests was compared with the common design shear tension capacity for rigid supported slabs. This was calculated using eq. 2.17 but now based on the design tensile strength  $f_{ctd}$  rather than  $f_{ctm}$  and the design value of the prestress according to Eurocode 2 [PREN1992-1: 2002] ( $\chi_{Rd,rigid}$ ). Only for test PC265 and RC265 the obtained values in the test did not reach the design shear capacity even though all tests were especially designed to investigate the reduced shear capacity.

**Table 2.2** *Ratio between observed shear tension resistance and prediction with composed beam model of Pajari [1995b] on the basis of the mean value of prestress  $\sigma_p$  and the design value  $\sigma_{pd}$ .*

Test	DE265	ST265	PC265	PC265E	PC265T	PC265N	RC265	PC265C	PC400	ST400	$\mu$	$\sigma$
$\chi_{ST,flex}(\sigma_p)$	0.91	0.96	0.92	0.97	0.97	1.17	1.04	1.17	0.96	0.92	1.00	0.10
$\chi_{ST,flex}(\sigma_{pd})$	0.94	1.00	0.96	1.01	1.00	1.21	1.08	1.21	1.00	0.96	1.04	0.10
$\chi_{ST,rigid}(\sigma_{pd})$	1.05	1.52	0.94	1.32	1.13	1.57	0.95	1.58	1.12	1.32	1.27	0.28
$\lambda_{flex}$	0.53	0.76	0.50	0.62	0.50	0.68	0.42	0.67	0.50	0.63	0.58	0.11

In conclusion, Pajari's model is appropriate to take into account the effect of non-rigid supports on the shear tension failure mechanism of HC slabs. Therefore, it will also be used to indicate the effect of non-rigid supports in fire tests on HC slabs supported on beams. For this reason, a final row is added in table 2.2. which provides the degree of flexibility in the tests. It is defined as

$$\lambda_{flex} = \frac{V_{ST,flex}}{V_{ST,rigid}} = \frac{\frac{V_{test}}{\chi_{ST,flex}}}{V_{ST,rigid}} \quad \{2.39\}$$

It is emphasized that the shear capacity of the flexible supported HC slab  $V_{ST,flex}$  is not a unique property of the HC unit and the flexibility of the beam, but is also dependent on the loading arrangement in the test. For instance an additional point load directly acting on the supporting beam increases the transverse shear stress and reduces the flexible shear tension capacity. Therefore, it can only be calculated once the loading arrangement is known using  $V_{test}$ .

For anchorage failure, Pajari recommends [1995b] to disregard some strands as they will be unbonded due to splitting cracks once the transverse bending stress in the bottom flange of the HC slab exceeds the tensile strength. No interaction between unbonded strands and the shear tension capacity needs to be considered since the bonding of the splitting cracks occur at mid span of the supporting beam and the shear tension failure occurs near the column.

### 2.3.2 Fire conditions

Ten of the tests presented in the previous paragraph were supported on beams rather than on a wall [BORGOGNO & FONTANA: 1995, 1996; ZHAO: 1993, 1995a, 1995b]. As pointed out in §2.3.1, the shear tension capacity of HC slabs decreases significantly due to the flexibility of the supporting beams.

In order to evaluate the effect of flexible supports on the fire behaviour of HC slabs, the reduction of the shear tension capacity by the flexible supports was calculated according to eq. 2.39, see table 2.3. The flexible shear tension capacity varied in these tests between 68-98 % of the shear tension capacity corresponding to rigid supported HC slabs.

**Table 2.3** Degree of flexibility in fire tests on HC slabs supported on beams.

Test ID	CTICM			ETH						
	INC93/204	95-E-467	95-E-533	PTT	B2-1	B2-2	B2-3	B2-4 PL	B3-1	B3-2 PL
$\lambda_{flex}$	0.68	0.98	0.98	0.69	0.86	0.70	0.84	0.70	0.97	0.97

The shear tension loading of these tests is plotted again in fig. 2.33. The shear tension loading is calculated relative to shear tension capacity of HC slabs on rigid supports and flexible supports. The flexible shear tension loading was calculated as  $V_{test}/V_{ST,flex}$  calculated with eq. 2.38. Figure 2.33 shows that taking into account the increase of the shear tension loading by the flexible supports barely improves the scatter found in the evaluation of fire test results. Premature S/A failure can not be attributed to the reduction in the shear tension capacity by flexible supports if there exists any negative effect of flexible supports on the fire resistance at all. Therefore, it was decided to concentrate the research project on the basic case of rigidly supported fire exposed HC slabs.

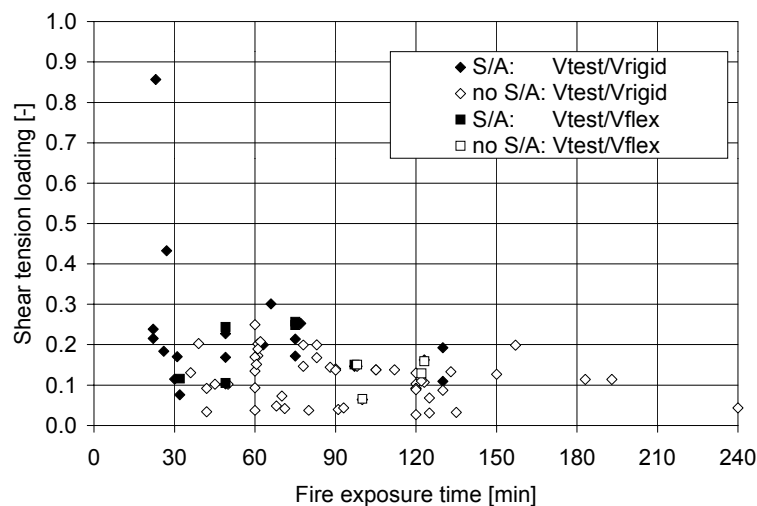


Figure 2.33: Effect of flexible supports on the S/A failure in the fire tests.



## 3 Literature on constitutive behaviour

### 3.1 INTRODUCTION

As pointed out in the problem statement, the shear and anchorage behaviour of fire exposed HC slabs is strongly influenced by the temperature induced stresses and strains. Furthermore, it was stated that an adequate prediction of the thermal stresses can only be achieved using non-linear constitutive models that consider irreversible deformations and damage. This chapter starts with the relevant descriptions of the concrete behaviour. First the behaviour at room temperature is presented, as it was used for the assessment of the analytical models presented in chapter 2. Then, the behaviour at elevated temperatures is discussed, providing a basis for modelling in chapter 5. The strength and stiffness of concrete decrease at elevated temperatures. As for instance stated in Eurocode 2 [PREN1992-1-2:2002], this decrease depends on the type of aggregate. As will be shown, there exists a huge scatter in available strength measurements at elevated temperatures. Moreover, results for the tensile strength tested at elevated temperatures are scarce. Therefore, there is a need for additional testing of strength. In order to limit the required number of tests at constant elevated temperatures, the tests must be performed at the points of inflection in the strength-temperature diagram to allow for interpolation between the test results. At the end of this paragraph, recommendations are given for the temperatures at which tests should be carried out. For that purpose, further understanding is required of the mechanical actions and chemical changes in heated concrete. These aspects are described and followed by some recommendations. After the description of the concrete properties, the bond behaviour of prestressing strands is outlined. Again, a distinction between room temperature and elevated temperatures is made. The investigations lead to recommendations for modelling.

## 3.2 CONCRETE PROPERTIES

### 3.2.1 Room temperature

#### 3.2.1.1 Compression

For the simulation of experiments, the strength properties have to be known. From experiments found in literature, the strength properties were sometimes not completely reported.

In case the compressive strength of concrete was not provided, the mean compressive strength  $f_{cm}$  was estimated from the characteristic strength  $f_{ck}$  according to the Model Code as [CEB-FIP: 1991]

$$f_{cm} = f_{ck} + 8 \quad [\text{MPa}] \quad \{3.1\}$$

For the calculation of the flexibility of the supporting beams in §2.3.1, the Young's modulus of concrete  $E_c$  was required. It was calculated according to Eurocode 2 [PREN 1992-1: 2002] as

$$E_c = 22000 \left( \frac{f_{cm}}{10} \right)^{0.3} \quad [\text{MPa}] \quad \{3.2\}$$

#### 3.2.1.2 Tension

According to the Eurocode [PREN1992-1: 2002] and the FIB Bulletin 1 [FIB: 1999], the mean splitting tensile strength can be calculated from the characteristic compressive strength  $f_{ck}$  in [MPa] as

$$\begin{aligned} f_{ctm} &= 0.30 f_{ck}^{2/3} & f_{ck} &\leq 50 \text{ [MPa]} \\ f_{ctm} &= 2.12 \ln \left[ 1 + \frac{f_{ck} + 8}{10} \right] & f_{ck} &> 50 \text{ [MPa]} \end{aligned} \quad \{3.3\}$$

The characteristic tensile strength relates to the mean tensile strength according to Eurocode 2 [PREN 1992-1: 2002] as

$$f_{ctk} = 0.7 f_{ctm} \quad \{3.4\}$$

The Model Code [CEB-FIB: 1991] uses a slightly different formulation. Furthermore, the design tensile strength according to Eurocode 2 reads as

$$f_{ctd} = \frac{f_{ctk}}{\gamma_c} \quad \{3.5\}$$

with  $\gamma_c$  equal to 1.5, the ratio between the mean and the design tensile strength equals 2.14.

### 3.2.1.3 Fracture energy

The fracture energy per unit area equals the area below the softening curve of concrete under tension after cracking. Throughout the thesis, the softening curve according to Hordijk [DE WITTE: 1999] was applied, see fig. 3.1, unless stated otherwise. A higher fracture energy means a higher residual strength in partly opened cracks.

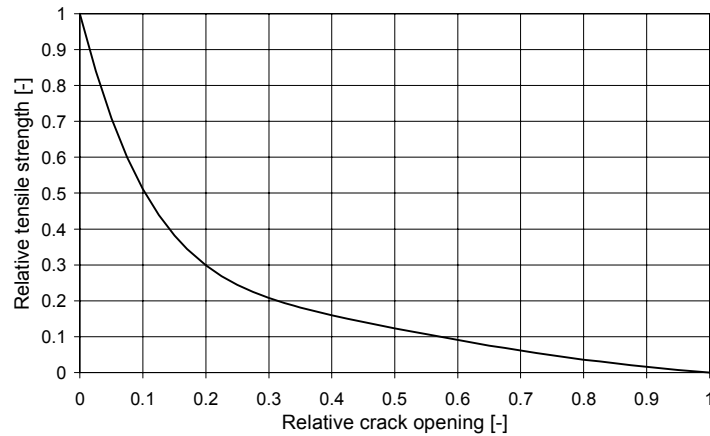


Figure 3.1: Softening diagram for concrete in tension after crack initiation relative to the ultimate crack opening  $w_u$  [HORDIJK: 1991].

The fracture energy relates to the ultimate crack opening  $w_u$  for which no tensile stress can be taken by the concrete as

$$G_F = 5.136 \frac{f_{ct}}{w_u} \quad \{3.6\}$$

As pointed out in §3.3.1.2, the anchorage capacity depends highly on the fracture energy of concrete through its effect on the confining action of the concrete around the strands mainly after the development of splitting cracks.

According to the Model Code [CEB-FIP: 1991] the fracture energy increases with the maximum aggregate size and concrete strength. HC slabs in the Netherlands have generally a maximum aggregate size of 14-16 mm and a mean compressive strength of 80 MPa, which corresponds to a fracture energy between 110-130 J/m<sup>2</sup> according to the Model Code.

However, Darwin et al. [2001] showed that the fracture energy depends mainly on the type of aggregate, see fig. 3.2. For concrete with basalt aggregate an average fracture energy of 140 J/m<sup>2</sup> was found versus only 50 J/m<sup>2</sup> for limestone aggregate. Moreover, they found that the fracture energy is largely independent of the water cement ratio, the concrete strength, the concrete age and the maximum aggregate size within the investigated range of 12 to 19 mm.

Because of the uncertainty of the actual fracture energy and the relevance for the anchorage behaviour, it is concluded that tests have to be carried in which the fracture energy can be established in the scope of this thesis.

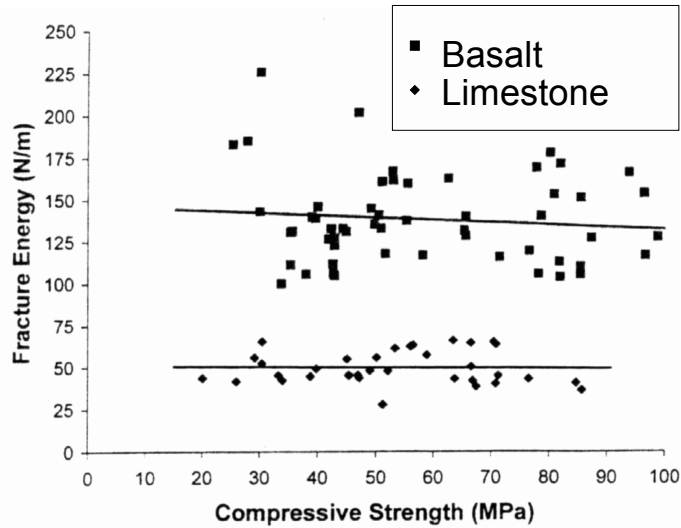


Figure 3.2: Measured fracture energy of concrete of various strengths with basalt and limestone aggregate [DARWIN ET AL.: 2001]

### 3.2.2 Elevated temperature

#### 3.2.2.1 Compression

The compressive strength was studied by various researchers, see fig. 3.3. Abrams [1971] determined the residual strength after heating and subsequent cooling. Bazant and Kaplan [1996] gave an upper and a lower bound on the basis of a collection of results.

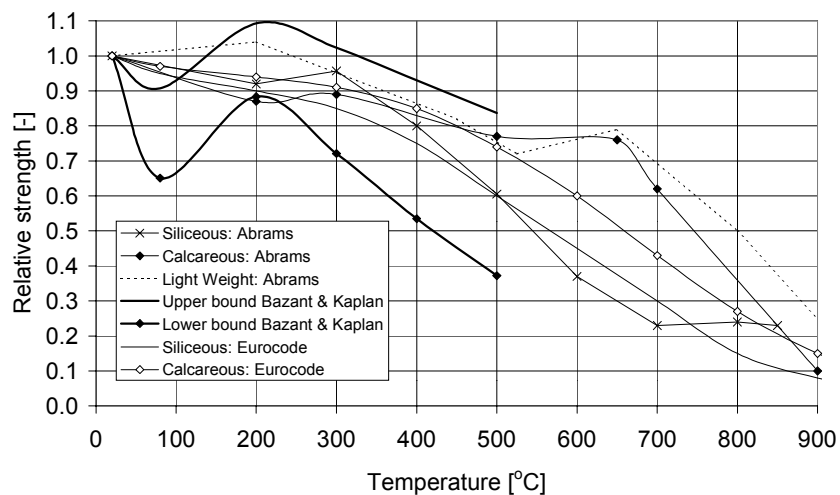


Figure 3.3: Decrease of the compressive strength according to various researchers and compared with the values of Eurocode 2 [PREN 1992-1-2: 2002].

At high temperature, the strength decreases due to the dehydration of the cement paste, the thermal instability of the aggregates and the incompatibility between the shrinkage of the cement paste and the thermal expansion of the aggregate particles.

The compressive strength of concrete loaded during heating, is higher than that of unloaded concrete. The effect of loading during heating found by several researchers is collected in fig. 3.4. The incompatibility between mortar and aggregate grains causes cracks in the mortar [BREUNESE: 2001]. Probably, a compressive load during heating can reduce this internal cracking.

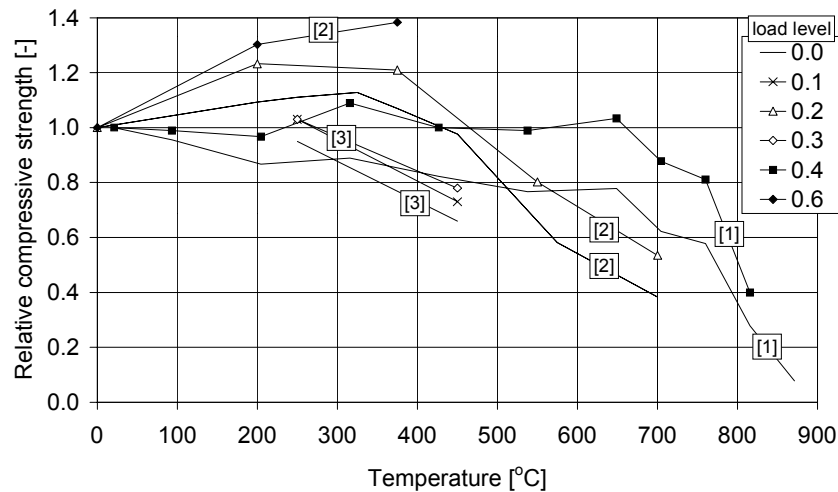


Figure 3.4: Effect of compressive loading during heating on the compressive strength at elevated temperatures. The references are [1] = Abrams: 1971, [2] = Purkiss & Bali: 1988, [3] = Schneider: 1988.

Also the plastic straining under loading depends on the load level during heating. Schneider [1988] derived fig. 3.5 for the sum of the elastic and plastic strain at peak stress. In the concrete model used in the research of this thesis the approximation was used as given in fig. 3.5. This concrete model is described in chapter 5.

At high temperature, the behaviour of concrete in compression is further affected by transient creep. Creep effects reduce the internal stresses caused by differential dimensional changes between cement paste and aggregate. Lea and Stradling [1920, 1922] showed already that the internal stresses in the cement paste around a spherical sand particle would directly cause cracking if the cement paste would behave elastically.

The transient creep of concrete under compression counteracts the thermal expansion considerably. In fig. 3.6, the strain components of concrete in a concrete column are presented as found by Anderberg and Thelandersson [1976]. Although in fig. 3.6 also a time dependent creep component was included, the time dependent creep can be neglected as far as fire exposed concrete is considered, in which generally a rapid heating over a limited time occurs [KHOURY: 1985, SCHNEIDER: 1988]. Khoury found that the compressive creep is purely dependent on the amount of cement paste. Schneider on the contrary found that the transient creep depends on the aggregate type.

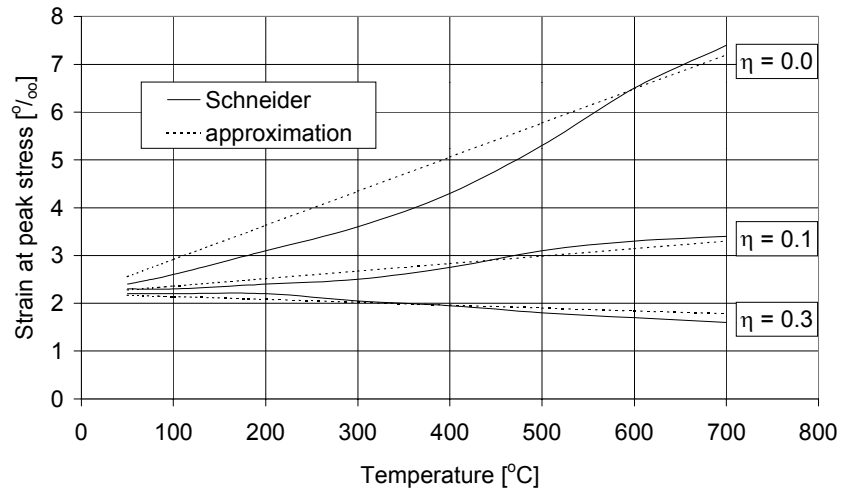


Figure 3.5: Sum of the elastic and plastic strain at peak stress according to Schneider [1988], depending on the relative external compressive load level  $\eta$  during heating.

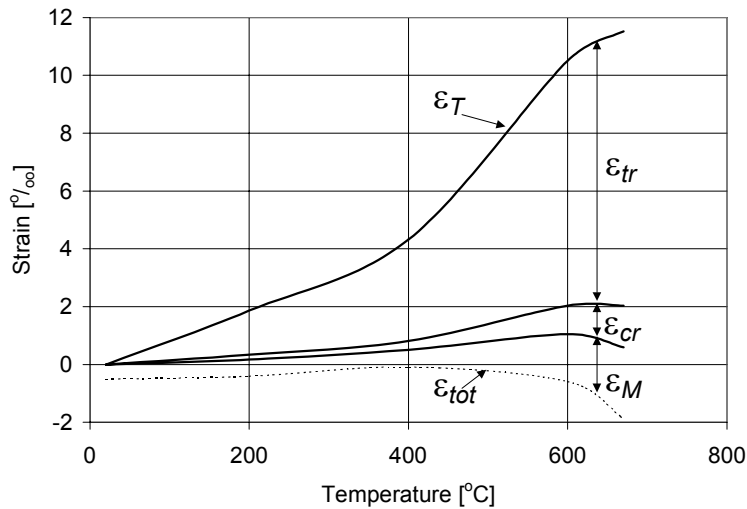


Figure 3.6: Strain components in concrete column under compressive loading of 35 % of the ultimate strength while heated [ANDERBERG & THELANDERSSON: 1976].

Schneider [1988] developed a model for concrete in compression: The strain is decomposed into a stress induced part and a temperature induced part, which is the result of dehydration shrinkage and thermal expansion

$$\epsilon_{tot} = \epsilon_M + \epsilon_T \quad \{3.7\}$$

The thermal strain  $\epsilon_T$  increases with temperature and depends on the type of aggregate, see fig. 3.7.

The thermal expansion is assumed to be independent of the loading conditions and the heating rate within the practical range of heating rates during fire. So, the thermal strain is known at each temperature.

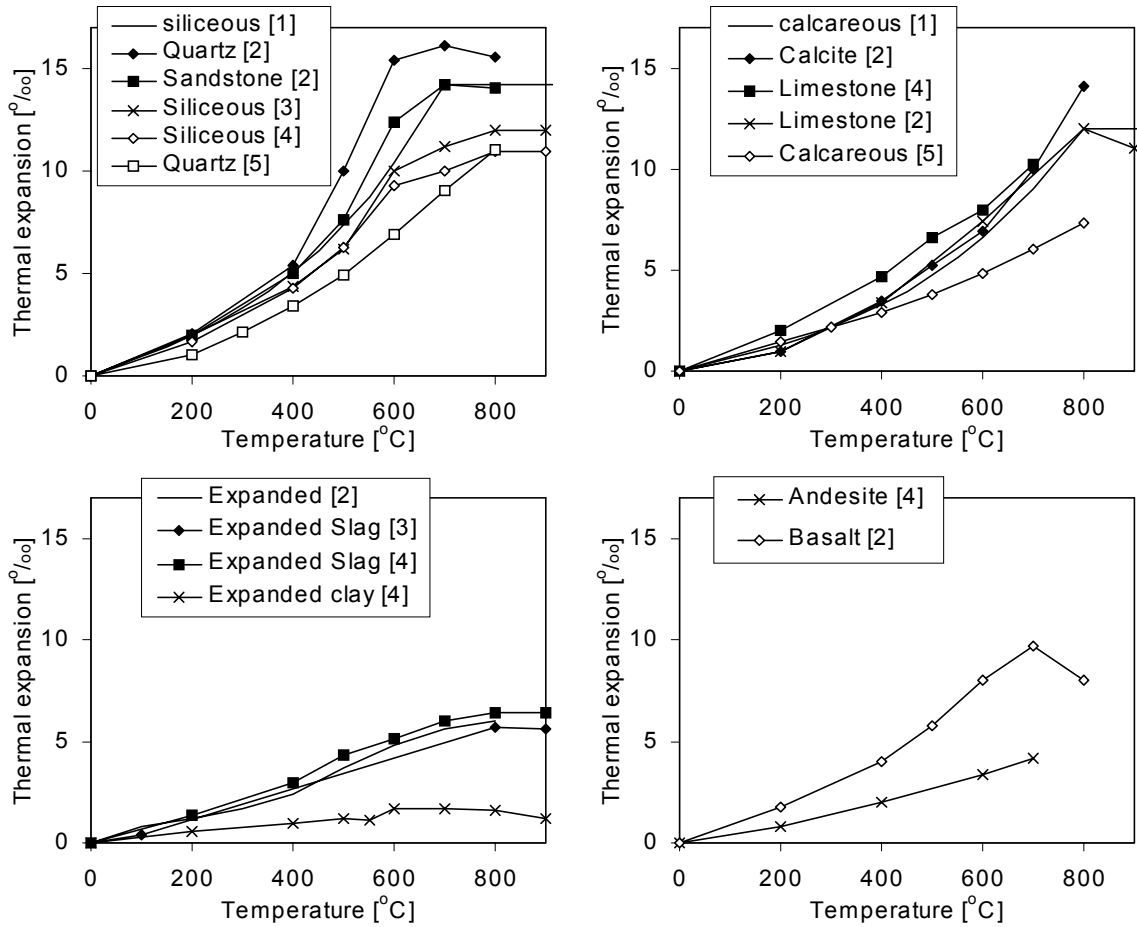


Figure 3.7: Thermal expansion coefficients for concrete with various aggregates according to: 1: [PREN 1992-1-2:2002], 2: [SCHNEIDER:1988], 3: [BAZANT & KAPLAN: 1996], 4: HARMATHY: 1970], 5: [REINHARDT: 1988].

From eq. 3.7 the stress inducing strain is simply given by

$$\epsilon_M = \epsilon_{tot} - \epsilon_T \quad \{3.8\}$$

Using a classical creep function  $J$  the stress inducing strain reads

$$\epsilon_M = \sigma \cdot J(\theta, t, t_0) \quad \{3.9\}$$

According to Schneider the classical compliance function  $J$  does not apply in fire since it does not take into account the dependence on the load level. Furthermore, the transient creep is assumed to be independent of the time within the practical range of heating rates in fire. Therefore eq. 3.9 can be simplified for the uniaxial case into

$$\epsilon_M = \sigma \cdot J(\theta, \sigma) = \frac{\sigma}{E_c} + \frac{\sigma}{E_c} (g_{pl} + g_{tc}) \quad \{3.10\}$$

where function  $g_{pl}$  represents the increase of the strain by plastic deformations, see fig. 3.5, function  $g_{tc}$  represents the increase due to transient creep as given in fig. 3.8 and  $E$  is the Young's modulus of concrete at high temperature.

The Young's modulus  $E_c$  depends on the temperature. Moreover, an external compressive load

positively influences the Young's modulus. Schneider derived for normal weight concrete

$$E_c = E_{c,20} k_E (1 + \alpha_E) \quad \{3.11\}$$

The non-dimensional parameter  $k_E$  depends on the temperature and the type of aggregate as given in fig. 3.9 and the non-dimensional  $\alpha_E$  depends on the load level during heating  $\eta$  as

$$\alpha_E = \eta \frac{\theta - 20}{100} \geq 0.3 \frac{\theta - 20}{100} \quad \theta \text{ in } [^\circ\text{C}] \quad \{3.12\}$$

where the temperature is expressed in  $^\circ\text{C}$  and the load level  $\eta$  is defined as the stress during heating divided by the compressive strength at ambient temperature. For normal weight concrete the increased stiffness due to external loading is also given in fig. 3.9.

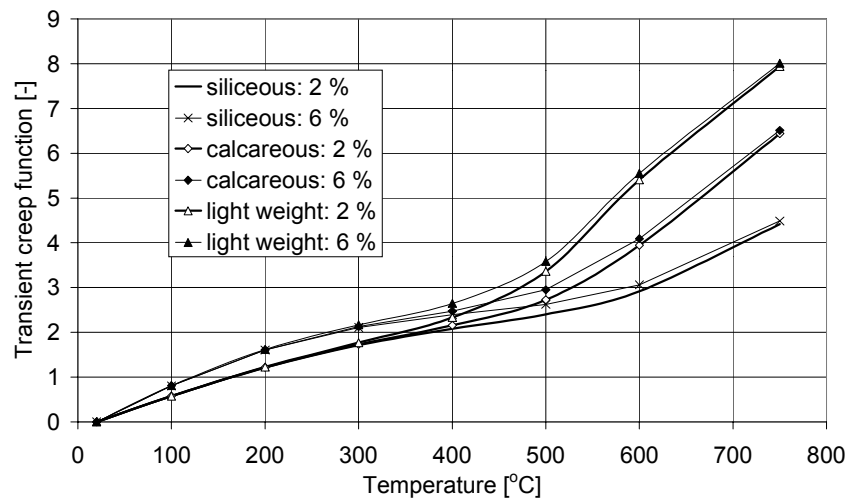


Figure 3.8: Transient creep function according to Schneider [1988]. The function depends on the type of aggregate and on the moisture content of concrete at the start of the fire.

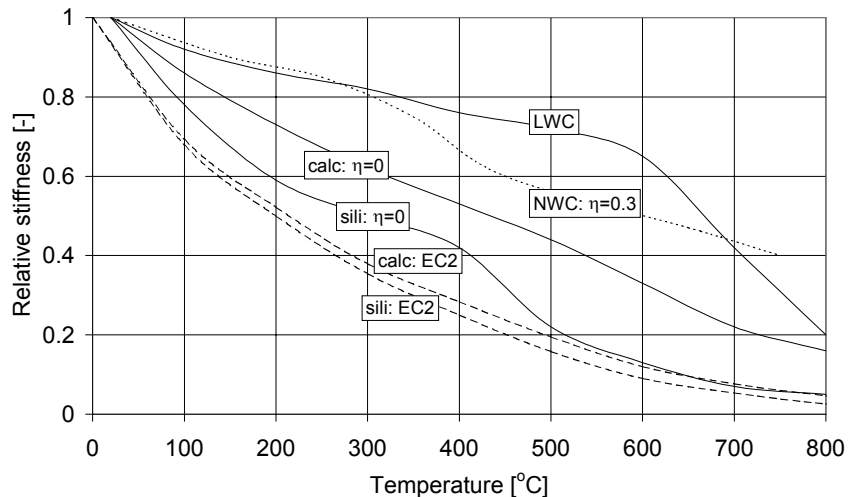


Figure 3.9: Decrease of the Young's modulus of concrete during heating according to Schneider [1988] depending on the load level  $\eta$  during heating and a comparison with the initial stiffness according to Eurocode 2 [PREN 1992-1-2:2002].

An alternative formulation is given in Eurocode 2 [PREN 1992-1-2: 2002]. Eurocode 2 does not explicitly define the stiffness of concrete. But, for the compression regime, Eurocode 2 provides uniaxial stress-strain relations at elevated temperatures that include transient creep. So, the transient creep is considered as a plastic strain.

Eurocode 2 [PREN 1992-1-2: 2002] describes the stress-strain relations with a function obtained from Popovics [1977] characterised by the peak stress  $f_c$  and the strain at peak stress  $\epsilon_{cl}$ .

$$\sigma_c = \frac{\left(\frac{\epsilon_c}{\epsilon_{cl}}\right)}{(n-1) + \left(\frac{\epsilon_c}{\epsilon_{cl}}\right)^n} f_c \quad \{3.13\}$$

with  $n = 3$  in the Eurocode. For the reduction of the peak stress at elevated temperatures, Eurocode 2 distinguishes between concrete made with siliceous and calcareous aggregate, see fig. 3.3. For the strain at peak stress, Eurocode 2 gives only one branch, valid for both aggregate types, see fig. 3.10.

The Young's modulus of concrete according to Eurocode 2 can be obtained from differentiation of the stress-strain relationship at  $\epsilon_c = 0$ . This results in the initial Young's modulus.

$$E_c = \left. \frac{d\sigma_c}{d\epsilon_c} \right|_{\epsilon_c=0} = \frac{n}{n-1} \frac{f_c}{\epsilon_{cl}} \quad \{3.14\}$$

With the aid of eq. 3.14, the reduction of the initial stiffness is presented in fig. 3.9. The Eurocode underestimates the Young's modulus compared to Schneider's results. This results from the fact that the stress-strain relation according to Eurocode includes transient creep.

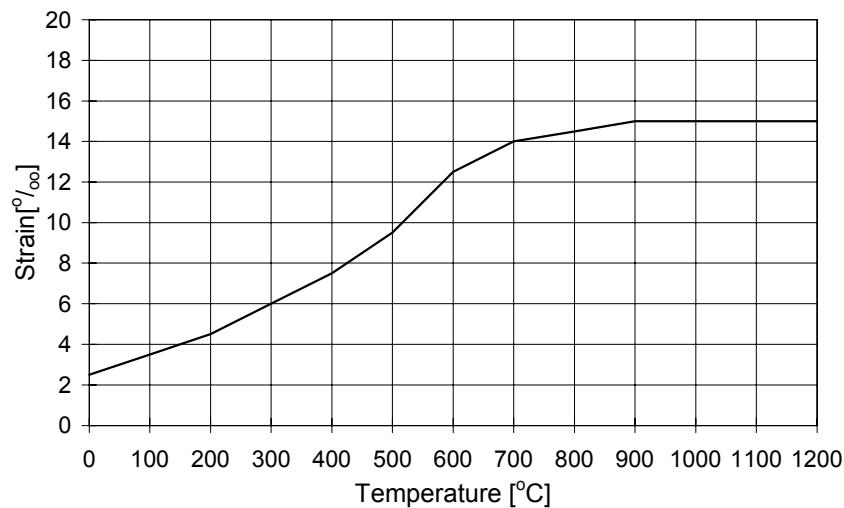


Figure 3.10: Increase of the compressive strain at peak stress for concrete according to Eurocode 2 [PREN 1992-1-2:2002].

The simplification of the Eurocode gives erroneous results when an instant loading is applied at constant temperature, since no creep occurs according to Schneider's formulation, while implicit creep strains would be assumed with the Eurocode formulation. Moreover, the increase in strength and stiffness due to a compressive loading during heating is not taken into account. The effect of these simplifications on the shear and anchorage behaviour of HC slabs will be evaluated in chapter 8.

### 3.2.2.2 *Tension*

A wide range of test results exists on the tensile strength at elevated temperatures, see fig. 3.11 [BLUNDELL ET AL.: 1976, BAŽANT & KAPLAN 1983]. The tensile strength of heated concrete is a generalised measure of the real strength of the cement paste, the aggregate and the bond strength of the interface, combined with the internal stresses due to the incompatibility between the thermal expansion of the aggregate and the shrinkage of the cement paste. Most of the results were obtained by loading after cooling. Measurements of the tensile properties of concrete at high temperatures are scarce. Furthermore, a large difference exists between the relative decrease of the tensile strength at elevated temperatures obtained in flexural tests and in direct tension tests [FELICETTI & GAMBAROVA: 1998].

A trough in the strength and stiffness curve between 80-200 °C was found in concrete by various researchers. Sager [1985] found a trough in the strength curve at 150 °C. Such a trough was also noticed for concrete in compression [DIEDERICH ET AL: 1987]. The drop in the strength is typical for short term heating and is not observed when the temperature is kept constant for long time (one day) at 150 °C, before loading [DIEDERICH ET AL: 1987]. A similar trough in the curve was observed by Blundell et al [1976], not at 150 °C but at 80 °C. And Harmathy and Berndt [1966] found that a drop in stiffness between 100-200 °C only occurred for short term heating of 1 hour and not for heating periods of 4 to 24 hours.

No conclusive explanation for the decrease can be given. Khoury [1992] attributed it to the evaporable water that gets warmer and less viscous, reducing the surface energy of the gel and the cohesive forces between the CSH layers. Such an influence of the forces related to the moisture was also observed by Budelmann [1987]. He found that the strength dropped linearly to 70 % when the moisture content of concrete was reduced from 6.5 to 2 % by dry weight.

At high temperatures, Eurocode 2 [PREN 1992-1-2:2002] gives a very rough estimate of the decrease of the tensile strength. It is assumed that the strength linearly decreases between 100-600 °C from 100 % of the strength at ambient temperature to zero, see fig. 3.11.

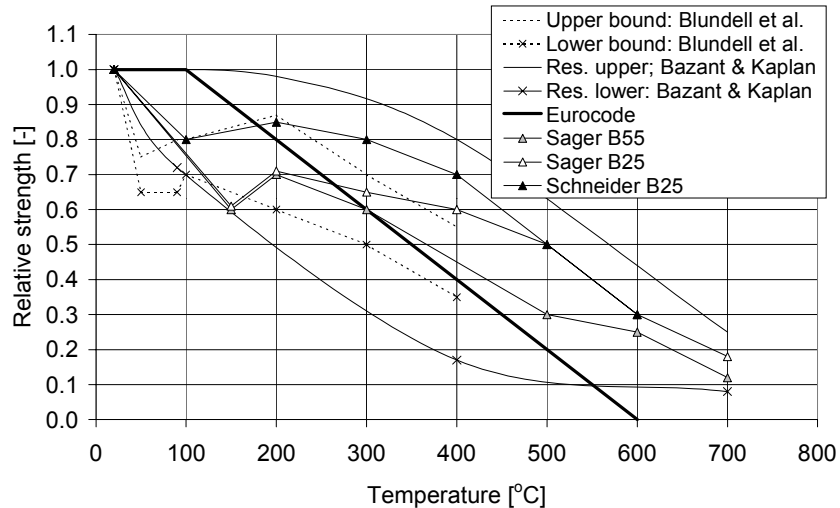


Figure 3.11: Various measurements of the splitting tensile strength of concrete at elevated temperatures.

### 3.2.3 Considerations for testing

#### 3.2.3.1 Mechanical actions

In rapidly heated specimens also pore pressures cause tensile stresses due to the evaporation of free moisture. In rapidly heated concrete also thermal gradients will occur that cause additional thermal stresses. In measuring the strength, one should apply a slow heating rate, to avoid these stresses.

Nevertheless, internal stresses can still occur even when the heating is so slow that no thermal gradients develop nor pore pressures. Due to elevated temperatures, the cement paste thermally expands. But due to the evaporation of free and physically bounded water, the cement paste contracts. Moreover, an autogenous contraction occurs due to sintering [LANKARD: 1970]. He showed that the thermal expansion and the combined contractions counteract each other up to 300 °C. Beyond this temperature, the contractions dominate, up to  $\alpha_T = 50 \cdot 10^{-6}$  for shrinkage compared to  $\alpha_T = 10 \cdot 10^{-6}$  for thermal expansion. Furthermore Lankard [1970] found that the shrinkage of the paste continued at constant temperature even when heating was as slow as 1 °C/min. As a consequence, the internal stresses that develop in concrete due to different deformations during heating of the cement paste and the aggregate, will depend on the heating rate even when the rate is as low as 1 °C/min. So, the measured strength depends on the heating rate even if the heating rate is sufficiently slow to obtain a uniform temperature in the test specimen.

The aggregate expands during fire. The amount of expansion varies considerably between different aggregate types. Although a large variety of aggregates exists, in design practise only three types are distinguished: siliceous, calcareous and light weight aggregates. Siliceous aggregate expands much more than calcareous aggregates or basalts. The light-weight expanded aggregates result in the smallest expansion (expanded clay or expanded slag). Furthermore in

siliceous aggregates  $\alpha$ -quartz transforms into  $\beta$ -quartz at 573 °C, which is accompanied by an instantaneous expansion of 4 ‰ [LEA & STRADLING: 1922]. As a result, siliceous concretes and concretes with sand as fine aggregates show a strong decrease in strength and stiffness around this temperature.

The incompatibility between the thermal expansion of aggregate and cement paste result in internal stresses. Breunese proved [2001] that this incompatibility easily causes cracking of the cement paste. He made a FE model for concrete with separate aggregate elements, mortar elements and interface elements. Internal cracking of the mortar caused increased deformations and a reduction in overall strength, but without losing all strength.

He further showed that internal cracking could explain the generalised decrease in strength and stiffness of concrete at elevated temperatures up to 400 °C, while he even assumed that the strength of the components remains unchanged at elevated temperatures. The latter assumption is in accordance with findings on the strength properties of cement paste, see next paragraph. For temperatures beyond 400 °C, the effect of dehydration of the cement paste on the strength should be taken into account.

As the decrease in strength and stiffness is the result of internal micro-cracking, it is likely, that the fracture energy of concrete decreases at elevated temperatures due to the internal cracking during heating, although chemical changes in the cement paste and bond between the aggregate and the cement paste might affect the fracture energy as well.

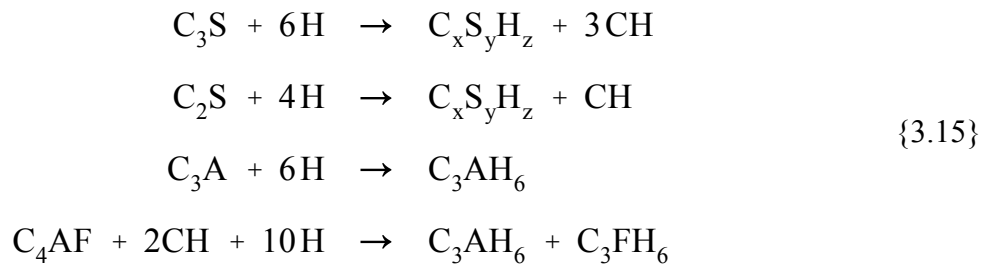
Breunese [2001] also pointed out that internal cracking is an important cause of the plastic straining under tension as found in tests by Felicetti and Gambarova [1999] and transient creep of concrete. Even without the assumption of creep strains in the mortar, he was able to predict realistic creep deformations. All creep deformations could be attributed to internal cracking.

As there exist huge differences between the thermal expansion of various aggregates, see fig. 3.7, the type of aggregate influences the strength decrease of concrete during heating. Therefore, when assessing the tensile properties of concrete at elevated temperatures, one should consider the type of aggregate used.

Moreover, an external compressive stress during heating results in a significantly higher compressive strength and stiffness at elevated temperatures [SCHNEIDER: 1988]. Compressive loading probably prevents the internal cracking resulting in higher strengths at elevated temperatures.

### 3.2.3.2 *Chemical changes*

Ordinary Portland cement (OPC) consists mainly out of [BAZANT & KAPLAN: 1996]: carbonate, CaO (60-67 %) simplified to C, silicate, SiO<sub>2</sub> (17-25 %) simplified to S, alumina, Al<sub>2</sub>O<sub>3</sub> (3-8 %), simplified to A and ferric oxide, Fe<sub>2</sub>O<sub>3</sub> (0.5-6 %) simplified to F. These basic elements are mainly present in the unhydrated cement as C<sub>3</sub>S, C<sub>2</sub>S, C<sub>3</sub>A and C<sub>4</sub>AF. These components react during hardening with water (H<sub>2</sub>O simplified to H) as



The main example of a  $C_xS_yH_z$  binding is  $C_3S_2H_3$ , known as tobermorite. On average the ratios between C, S and H are  $C_{1.62}SH_{1.5}$  [BRUNAUER, GREENBERG: 1962]. CH, or more precise  $Ca(OH)_2$  is called calcium hydroxide. Roughly, the  $C_xS_yH_z$  bindings amount up to 70 % of the total mass of the cement paste and calcium hydroxide 20 % [HARMATHY: 1993].

At increasing temperatures between 100-850 °C, the  $C_xS_yH_z$  bindings gradually dehydrates. Within research into the Chunnel fire [ULM ET AL: 1999] it was stated that the degree of hydration under fire conditions is solely dependent on the temperature, irrespective to the heating path and loading conditions. They showed this on the basis of a model that takes into account the thermodynamic equilibrium that includes the energy related to dehydration, elastic and plastic deformations and thermal expansion, besides the energy needed to increase the temperature of the concrete. Furthermore, they stated that the strength of the cement paste is more or less linearly dependent of the hydration degree. This implies a gradual strength loss between 100-850 °C that depends solely on the temperature corresponding to the dehydration of the  $C_xS_yH_z$  bindings, see fig. 3.12. The relative hydration degree was obtained from Bažant and Kaplan [1996].

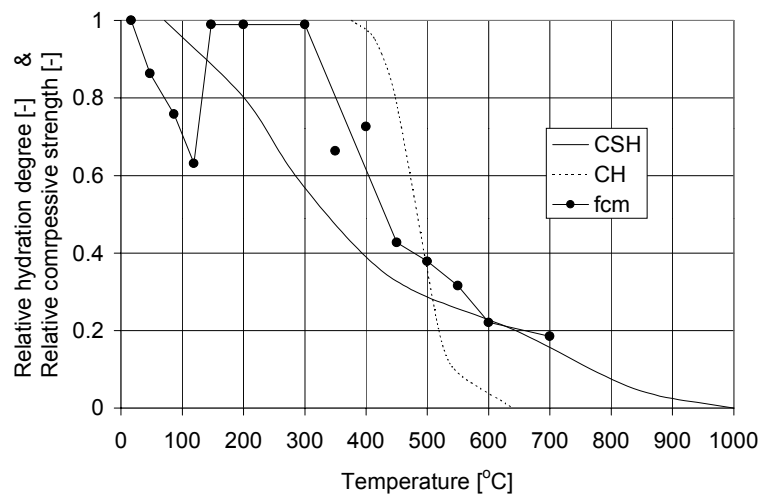


Figure 3.12: Conversion degree of CSH bindings and Calcium Hydroxide (CH), compared with the measured decrease of compressive strength of ordinary portland cement paste heated without load and tested at elevated temperature.

However, the real strength of the cement paste is affected by more factors than the relative hydration degree as shown in fig 3.12. The strength of the cement paste was obtained from Dias [1990]. The trough in the curve of cement paste at 120 °C can explain the trough that was

observed in the strength curve of concrete. It is unknown whether the trough in the curve for cement paste vanishes for long heating periods, like it does for concrete. Except for this trough, the strength is almost unaffected up to 300 °C, which underlines the approach of Breunese in the previous paragraph and the relevance of internal cracking on the strength and stiffness of concrete.

In addition to the dehydration of the  $C_xS_yH_z$  bindings, the calcium hydroxide dehydrates rapidly between 400-600 °C, forming C, see fig. 3.12. As the figure shows, this dehydration corresponds with a rapid strength loss of the cement paste. Graigner [GRAIGNER: 1980] found that puzzolanic cement has a significantly higher strength beyond 400 °C than ordinary Portland cement. This can be explained by the fact that during hydration the calcium hydroxide (CH) formed by the reaction of  $C_3S$  and  $C_2S$  is bounded by the puzzolana, and thus the amount of calcium hydroxide is reduced.

### 3.2.3.3 Recommendations

In conclusion, when testing concrete at elevated temperatures, it is recommended to carry out tests at 80 °C and 150 °C in order to cover the trough in the strength curve, at 400 °C, before the dehydration of CH, and at 600 °C after the dehydration of CH and the quartz transformation. Furthermore, the heating rate must be limited in order to avoid thermal gradients that cause thermal stresses. Thermal stresses due to temperature gradients should be taken into account in the calculation of the structural response of HC slabs and should not be included in the strength properties. Predictive calculations of the effect of thermal stresses on the measurement can determine the maximum heating rate.

The heating rate in tests does not have to be that slow that the trough in the strength curve around 80-150 °C vanishes, since this trough can be expected at the heating rates relevant in fire exposed concrete as well. Moreover, it is out of reach to adapt the concrete strength to the heating rate in calculations of the structural response of fire exposed HC slabs.

As no data on the fracture energy of concrete at elevated temperatures is available, tests need to be carried out tests at elevated temperatures to measure this property.

## 3.3 BOND OF STRANDS

### 3.3.1 Room temperature

#### 3.3.1.1 Overview

The bond behaviour of prestressing strands at ambient conditions was researched for many years by many researchers. In this respect, reference is made to a recently published state of the art report prepared by FIB Task Group Bond Models, working party 6 [FIB: 2000], which also gives a very extended list of references. The phenomena that are significant at ambient conditions are listed below.

- The bond stress over the transfer length is much greater than the bond stress over the development length, see also the steel stress envelope in §2.1.1.3. Design codes

recognised this difference, see appendix B. This phenomenon is explained by the Poisson contraction of the strand. Over the transfer length, the axial stress in the strand is reduced compared to the pretensioned state, which causes a radial expansion of the strand. The concrete cover restrains this radial expansion by the strand (perpendicular to the plane of the steel-concrete interface). This results in a radial compressive stress at the bond interface, fig. 3.13c. This radial compression enhanced the bond strength through a friction analogy.

- The bond strength of a plain wire drops with increasing slip after reaching some initial bond due to adhesion, see fig. 3.13a, The adhesion consists of chemical and physical bond between the cement stone particles and steel surface [FIB: 2000], which vanishes after some slip developed. On the contrary, the bond strength of 7-wire strands increases with increasing slip due to friction that develops after the adhesion vanished. The cross sectional shape of the 7-wire strand causes a lack of fit of the strand in the concrete embedment once it starts to slip. The inner wire of the strand has a slightly larger diameter than the outer wires which causes variations in the geometry of the embedment over subsequent cross sections. Due to this lack of fit, the strand pushes the confining concrete outwards, resulting again in radial compressive stresses at the interface, and, hence, frictional bond stresses.

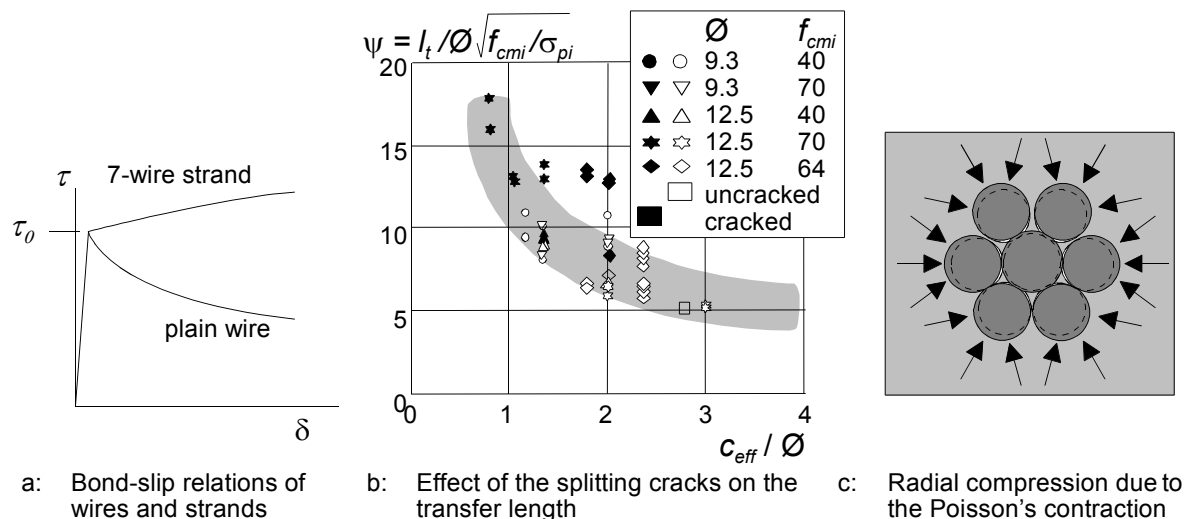


Figure 3.13: Overview of main phenomena of bond behaviour of strands at ambient conditions.

- The bond strength drops once the strand starts to yield. This is also explained by the transverse deformation of the strand. Once the strand starts to yield, the plastic volume change is zero, assuming a pressure independent flow rule like the *Tresca* or *von Mises* yield contour [DE BORST: 1991]. As the axial strain increases, the radial expansion drops and consequently the radial compression. Moreover, the stiffness of the strand in the radial direction drops once yielding starts, thus radial strains lead to smaller radial stresses.
- On top of the change of the bond stress due to the Poisson effect, the bond stress of 7-wire strands is further increased by a change in the steel stress, irrespective of the sign of the steel stress change. Stressing and stress releasing cause the pitch of the

strand to change, which is prevented by the helical shape of the concrete embedment forcing the strand to twist. There is still an ongoing debate whether the contribution to the bond strength is caused by frictional stresses that equilibrate the restrained torsion of the strand against the twist [RUSELL & BURNS: 1993] or some kind of lack of fit, similar to the effect of slipping, as the strand does not fit into the helical shape of the concrete embedment around the strand after straining [STOCKER & SOZEN: 1969].

Anyhow, Den Uijl [1992] derived from pull-out tests and push-in tests that the effect of the change in the steel strain on the bond strength is considerable even though the torsion of the strand was barely restrained outside the embedment length. Also the lack of fit caused by the slip that accompanies the change in steel strain over the embedment length could not explain the size of this contribution to the bond strength. He refers to it as the pitch effect, without pointing out the exact mechanism behind this contribution to the bond strength.

- If splitting cracks occur along the strand, the bond strength dramatically drops and the transfer length increases accordingly, see fig. 3.13b [DEN UIJL: 1995]. On the vertical axis the relative transfer length is plotted. The black dots represent specimens with splitting cracks, the white dots correspond to the specimens without splitting cracks. The splitting cracks reduce the confining action of the concrete cover around the strand and consequently the bond decreases, see §3.3.1.2. Furthermore the picture shows that splitting is more likely to occur for a small concrete cover than for a large cover.
- The prestress is transferred only 6 to 12 hours after casting the concrete. The concrete has just reached sufficient strength to anchor the strands. During further maturing, the strength and stiffness of the concrete increase. So, the confining capacity of the concrete cover will also increase. However, the slip that had developed at the time of the prestress transfer is irreversible.
- Significant variations in the bond strength were measured in past research due to various causes. For instance, the surface roughness of the steel strand affects the adhesion [DEATHERAGE ET AL :1994]. A few days of weathering reduced the transfer length up to 40 %. Also the compaction of the concrete around the strand affects the bond strength. Den Uijl [2001] found that the average transfer length of strands in self compacting concrete was more than 30 % smaller than on average for normal concrete.

Models to describe the bond characteristics are presented below. Design code formulations of the transfer length and development length are evaluated and summarized in appendix B. As pointed out in §2.1.1.3, the anchorage capacity of HC slabs can be calculated once the steel stress envelope is known.

### 3.3.1.2 *Concrete confinement*

As stated in the previous paragraph, the bond strength dramatically decreases after the formation of splitting cracks in the concrete cover. This is explained by the confining action of the concrete cover around the strand. Once the concrete cover splits, the generalised radial stiffness of the concrete cover drops and the radial stresses that develop at the steel-to-concrete interface

decrease accordingly.

Numerous research project into the response of the concrete cover to radial expansion of the strand were carried out over the last two decades. [TIMONSHENKO: 1956; TEPFERS: 1977; DANTUMA: 1987; VAN DER VEEN: 1990; KEUSER & MEHLHORN: 1990; ÅKESSON: 1993; DEN UIJL & BIGAJ: 1996; LUNDGREN: 1999]

Timoshenko [1956] derived the linear elastic response of a thick-walled cylinder against internal pressure. Tepfers [1979] added the effect of macro-cracks to it. He assumed that stress in the cracked zone drops to zero right away, which yields a lower bound for the compressive stresses. He also gave a plastic upper bound for the radial compressive stress of the thick-walled cylinder assuming full plastic behaviour, i.e. that the tensile strength of concrete could be reached over the entire depth of the cylinder.

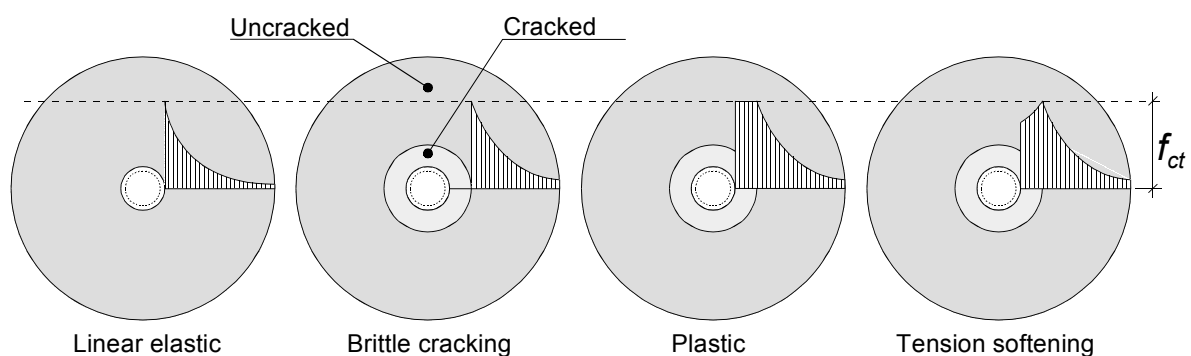


Figure 3.14: Four different models for the response of the thick-walled cylinder to radial expansion at the inner side.

Van der Veen [1990] improved Tepfer's model with the inclusion of tension softening. Den Uijl and Bigaj [1996] extended this model to the fully cracked stage and considered both radial and circumferential deformations. In fig. 3.15, a characteristic response curve to radial expansion is shown on the basis of the latter model. In the legend the independent input parameters are shown. Also the Poisson contraction of concrete plays a role, but it is so minor that it was not included. It can be found that the maximum radial compressive stress is found just before full cracking of the cylinder.

The confining action of the cylinder in the fully cracked stage strongly depends on the arbitrary number of cracks that is assumed to develop in the cylinder. Den Uijl and Bigaj [1996] found good agreement of their model with pull through tests assuming three cracks. For a description of these tests, refer to §6.2.2 on page 148, as similar tests were carried out within the present research.

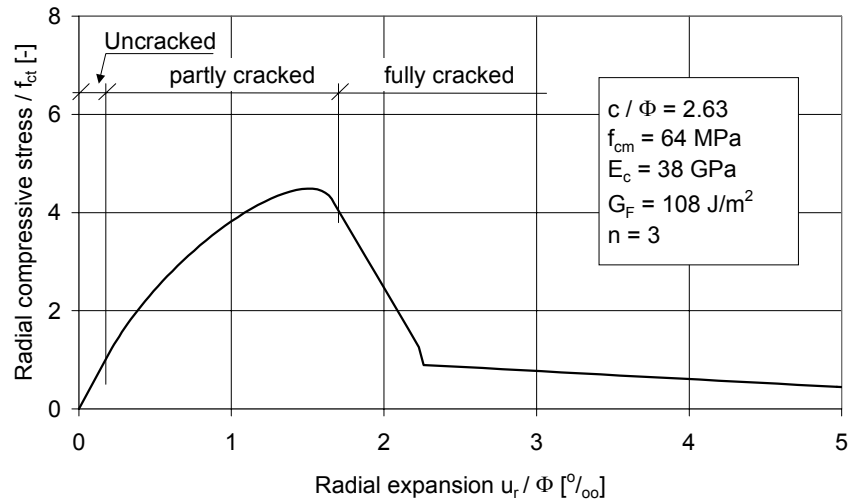


Figure 3.15: Characteristic compressive response of the thick-walled concrete cylinder to radial expansion.

A major advantage of the analytical models is their simplicity. With a general spreadsheet program, the effect of various geometries and concrete properties can rapidly be evaluated. A drawback of the analytical models is the limitation to axially symmetrical samples. As a consequence, for real structures like HC slabs always an equivalent concrete cover must be estimated.

Alternatively, the confining action can be calculated using FE models.

Vos [1983] made FE calculations with an axially symmetric model, in which he showed the importance of the tension softening relation. A linear softening relation in which zero strength is reached at an ultimate crack strain of 5 ‰ resulted in 2.5 times higher peak of the radial compressive stress than the lower bound of Tefpers. This 5 ‰ crack strain corresponds to approximately a crack opening of 0.1 mm at the steel-to-concrete interface, which is reasonable for normal concrete.

Dantuma [1987] made 2D FE calculations for a thick-walled cylinder using plane stress elements and a linear tension softening diagram, with a reduced ultimate crack strain in order to match the initial decrease in the softening diagram to the softening diagram derived by Moelands [DE WITTE: 1999]. For the compression regime of concrete, he used a linear elastic constitutive law. Furthermore he applied a spring between the concrete cover and the strand, that represented a weak interface layer, which he assumed to be of approximately 0.01 to 0.05 mm thickness. In his model, the splitting cracks did not localise automatically due to the axial symmetry. As a result, many cracks developed that barely opened and the calculated response approached the plastic upper bound. Therefore, he had to apply non-uniformity in the concrete strength over his model. In doing so, crack localisation was forced as the cracks started at the weakest elements. With the plane stress model, he was also able to calculate the confining action of beam cross sections. In these cross sections without axial symmetry, crack localisation developed automatically.

He concluded that the fracture energy of concrete has a major effect on the confining action. The shear retention factor that describes the shear resistance of a crack as a function of the crack

opening appeared to be relatively insignificant at least as far as the peak value of the radial compressive stress is considered.

Besides the major advantage that plane stress FE models can handle any arbitrary shape, also any constitutive model can be applied. With the aim of the simulation of the anchorage behaviour of fire exposed HC slabs, effects of decreasing strength and stiffness and increasing ductility at elevated temperature as well as the effects of thermal strains and asymmetrical heating demand a FE approach.

In conclusion, the confining action of concrete strongly affects the bond strength of strands. Especially in the fully cracked stage, the fracture energy plays an important role on the confining action and consequently on the bond strength.

Furthermore, the model of Den Uijl and Bigaj [1996] successfully matched test results. To simulate the anchorage behaviour of fire exposed HC slabs, FE models are recommended to calculate the confining action.

### 3.3.1.3 Bond slip models

In calculating the actual bond behaviour of strands, generally adhesion, friction and mechanical actions between the strand and the concrete cover are recognised [FIB: 2000]. As mentioned above, the friction and mechanical actions can be attributed to the lack of fit of the strand when slipping and the change in pitch of the strand and the Poisson effect when the strand is stressed or unstressed.

Den Uijl [1992] derived an empirical relation for the bond strength that accounts for all these effects on the basis of pull out tests and push in tests on strands with short embedment length.

$$\tau = 3 + 0.4\delta - 2.5 \cdot 10^{-3} \Delta\sigma_p + 1.5 \cdot 10^{-3} |\Delta\sigma_p| \quad \{3.16\}$$

in which the first term refers to the adhesion in MPa and the slip in the second term is expressed in mm. The adhesion is only reached after some initial slip  $\delta$  developed for which he recommends a value of 0.2 mm.

He based this formula on push-in tests and two types of pull-out tests, i.e. with restrained and unrestrained unloaded end of the strand. The strands had a diameter of 9.3 mm and the concrete cylinder of 55 MPa cube strength had 46 mm clear cover. The embedment length of 50 and 88 mm was so limited that barely any stress could develop in the pull out tests with unrestrained unloaded end. So, these tests could be used to find the dependency of the bond strength to the slip (the second term in eq. 3.16). The tests with restrained unloaded end together with the push in tests were used to separate the Poisson effect (third term) from the pitch effect (forth term). He found that the pitch effect always contributed to the bond strength in a positive way.

The validity of the empirical relation is limited to gravel concrete. The coefficients will be different for other types of concrete [DEN UIJL: 1997]. Moreover, the tests were carried out up to 5 mm slip and no yielding of the strands. In order to account for yielding of the strands to some extent, Den Uijl rewrote the third term representing the Poisson effect as function of the axial steel strain in order to cover yielding of the strands. This is just an approximation as the diameter contraction relative to the axial strain is significantly smaller in the elastic stage than in the plastic stage, since the steel volume during plastic flow remains constant [DE BORST:

1990] Nevertheless, with this approach he was able to predict pull out failure of strands in a prestressed beam in a realistic way [DEN UIJL: 1997].

The lack of fit effect, the Poisson effect and the pitch effect all depend on the confining action of the concrete cover. In the empirical bond relation of Den Uijl, the effect of the confining cover was not taken into account.

Alternatively, Bogaerts and Brosens [1995] calculated the bond stress of strands over the transfer length depending on the confining action of concrete. They carried out push-in tests on specimens with a short embedment length in which they measured the change of the steel stress and the slip. They calculated the radial compressive stress assuming that it is the response of the confining concrete to the change in the strand diameter due to the Poisson effect only. The Poisson effect could be derived from the measured steel stress.

Together with the bond stress measured as a function of the slip, a friction coefficient could be calculated as a function of the slip, defined as the ratio between the bond stress and the radial compressive stress.

Åkesson [1993] made a 3D FE model for the evaluation of the transfer length and the occurrence of splitting cracks at prestress release in HC slabs. He developed a plastic constitutive model for the interface elements between the strands and the concrete. In his model the plastic bond strength is a function of the radial compressive stress. Besides radial compressive stresses that are calculated in his model due to the Poisson contraction of the (3D modelled) strands, he introduced an expansion stress in the interface elements as a function of the slip.

The model of Bogaerts and Brosens and the one of Åkesson are both only valid to simulate the transfer of prestress, since the effect of the change of pitch on the bond strength was not taken into account. Pull out failure can not be calculated with these models.

Alternatively, Den Uijl developed a more advanced model that relates the lack of fit effect, the Poisson effect and the pitch effect to an artificial radial expansion  $\epsilon_{rr}$  of the strand. The lack of fit effect was directly related to the slip  $\delta$ . Both the Poisson effect and the pitch effect can directly be related to the axial steel stress in the strand, or better, to the axial steel strain  $\epsilon_p$ .

$$\epsilon_{rr} = \epsilon_{rr,lof} + \epsilon_{rr,v} + \epsilon_{rr,pit} = f_1(\delta) + f_2(\epsilon_p) + f_3(\epsilon_p) \quad \{3.17\}$$

In this approach, Den Uijl introduced several model parameters in the functions  $f_1$ ,  $f_2$  and  $f_3$ . Hereafter, the radial expansion was related with a thick-walled cylinder model to the confining stress. Finally, with a friction analogy, the confining stress was related to the bond strength and added to the initial bond strength caused by adhesion.

$$\tau = \tau_0 + \mu\sigma_{rr} = \tau_0 + \mu g(\epsilon_{rr}) \quad \{3.18\}$$

With this advanced approach, Den Uijl [1998] was able to calculate the bond behaviour including the confining action of the concrete cover. Due to the inclusion of both the pitch effect and the Poisson effect, the model can describe both the increased bond strength at the prestress transfer and the decreased bond strength at pull out.

For ribbed reinforcing bars, Hertz [1982] distinguished bond failure and splitting failure. Splitting failure is determined by confining action of the concrete cover. Bond failure can occur if the splitting resistance is high and it is limited by the compressive stress that can act in the

radial direction in the compressive struts behind the ribs of the rebar.

With a similar approach, Lindgren [1999] implemented an elastic-plastic bond model for reinforcing bars in the FE code DIANA. In this model only the Poisson effect determines the radial expansion. The plastic bond strength depends linearly through a friction coefficient on the radial compressive strength. But at higher radial compressive strengths, the bond is limited by a pull out yield contour, which is defined by a chosen limit for the compressive stress in the concrete struts behind the indentations of the rebar. This model seems irrelevant for strands since such high bond stresses can not develop around the strands.

In conclusion, in order to simulate the anchorage behaviour of HC slabs in a generic way by means of FE modelling, one should include both the lack of fit effect, the Poisson effect and the pitch effect in the constitutive behaviour of the bond interface. In doing so, it is expected that both splitting of the concrete cover and the interaction on pull out failure can be described acceptably well.

Therefore, the advanced model of Den Uijl was chosen as a basis for the constitutive bond model for prestressing strands in fire exposed HC slabs, see §5.4.2.

### **3.3.2 Elevated temperatures**

Within the large German research project *Sonderforschungsbereich 148* the properties of concrete, reinforcement and bond between them were studied extensively in the seventies and eighties of the previous century. The bond of prestressing strands was also investigated [ROSTÁSY ET AL.: 1980, DIEDERICHS & SCHNEIDER: 1981, SAGER: 1985]. Besides, investigations were made into the bond behaviour of mild reinforcement at elevated temperatures at other institutes [MORLEY & ROYLES: 1979; 1983, HERTZ: 1982].

The main objective of all these research projects was to derive bond strength characteristics of strands at elevated temperatures. Sager [1985] carried out tests on cylindrical concrete specimens with bars with short embedment length placed in the centre (40-80 mm) and pulled out at elevated temperature.

In fig. 3.16, the bond strength relative to the strength derived at room temperature are summarized for various types of steel. Apparently, the decrease of the bond strength for ribbed bars is similar to that of the compressive strength of concrete. The deterioration of the bond strength of plain bars is much higher. The surface roughness of plain bars has even a significant influence up to more than a factor 2 between 300-400 °C.

Moreover, it is found that the bond strength curve shows sometimes a trough between 80-200 °C. As was pointed out in §3.1, this trough was also observed in the strength and stiffness of concrete.

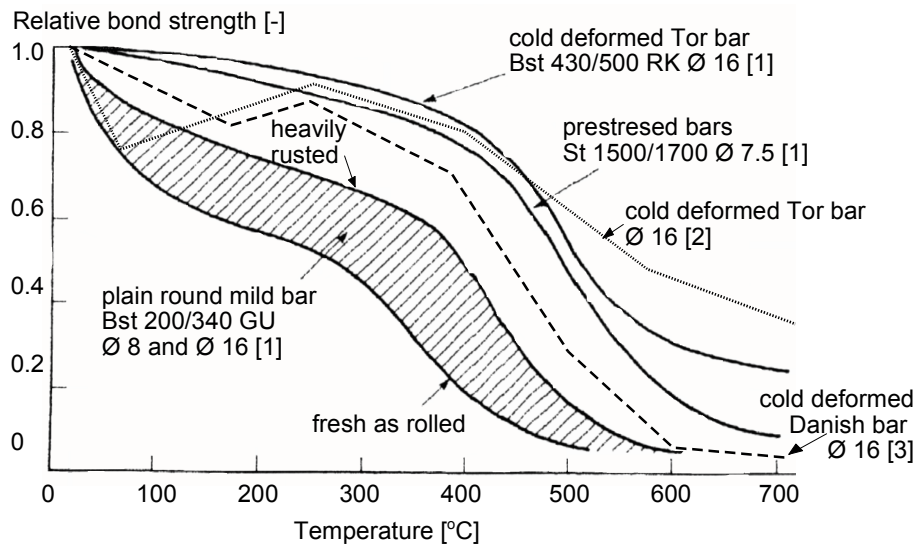


Figure 3.16: Reduction of bond strength of various types of steel bars at elevated temperatures. The references are: 1: [DIEDERICHS AND SCHNEIDER: 1981], 2: [MORLEY AND ROYLES: 1983], 3: [HERTZ: 1982].

Apart from the ultimate strength, also bond slip relations for prestressing strands at elevated temperature were established, see fig. 3.17.

Diederichs and Schneider [1981] and Sager [1985] recognised the effect of differential thermal elongations between reinforcing steel and concrete on the slip. As a result, slip was measured during heating even in unloaded specimens. Moreover, they found that the slip due to loading during heating was more or less proportional to the load.

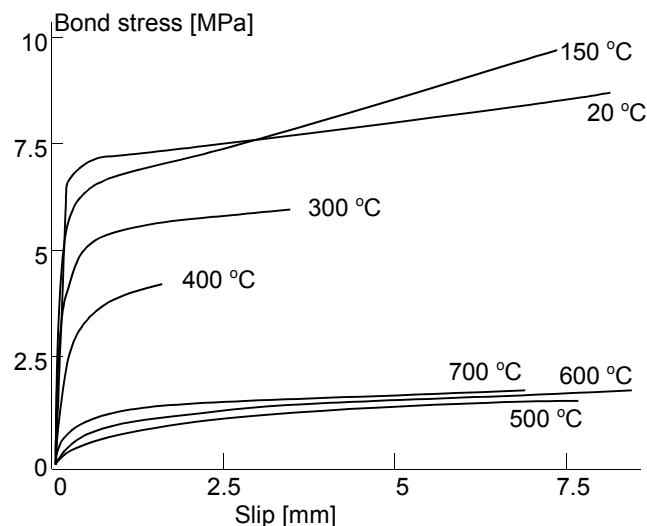


Figure 3.17: Bond slip relation of prestressing strands at elevated temperatures [ROSTÁSY & SAGER: 1985].

Nevertheless, all previous research to the knowledge of the author, concerned tests and analyses on bars embedded in concrete at a uniform elevated temperature. So, a slip induced by non-uniformly distributed thermal strains was not considered. Moreover, the effect of thermal stresses on the confining action of the concrete cover was not studied. Hertz [1982] stated that thermal stresses in the concrete cover can be neglected when considering anchorage failure of ribbed bars because thermal gradients will have vanished at the onset of anchorage failure. At least for prestressing strands, this assumption is not justified, since large slip was measured in early stages of fire, when the temperature of the bar barely increased, and large thermal gradients are present in the vicinity of the strands, see §2.2.4.

In conclusion, research into the bond of strands at uniformly distributed elevated temperatures showed that the bond strength decreases approximately in a similar way as the strength of concrete. As there exists a large scatter in the strength decay of concrete at elevated temperatures, it is likely, but unknown, that the scatter in the bond properties will be similar.

Differential elongation between steel and concrete causes slip, as shown by Sager [1985]. But the additional effect of thermal gradient on the slip development was not investigated up to the knowledge of the author.

However, the slip development is strongly affected by imposed thermal strains resulting from the thermal gradient, as pointed out in §2.2.3.4. In order to be able to simulate the loss of prestress during fire and the eventual pull out, there is a need to build a new constitutive bond model. The model should allow for slip development driven by the combination of applied forces and imposed thermal deformations.

Also the loss of the concrete confinement during fire due to the development of splitting cracks was not studied before. As the bond strength dramatically decreases at ambient temperature once splitting cracks develop, the loss of bond strength due to the loss of concrete confinement once splitting cracks develop under fire conditions should be included in the model as well.



## **4 Experiments on HC members**

### **4.1 SCOPE**

In chapter 2, it has been pointed out that the decrease in the shear and anchorage capacity of fire exposed HC slabs may limit the fire resistance and might govern the design. However, no comprehensive theory for these failure mechanisms under fire conditions is available as yet, neither qualitatively nor quantitatively. So, at present, no conclusive design guides can be provided for fire safe design of HC slabs against shear and anchorage failure.

Moreover, a theory into the shear and anchorage behaviour can not be derived from the fire tests on HC slabs as presented in the chapter 2. The fire tests on HC slabs as reported in chapter 2 were carried out mostly with a design-by-testing purpose rather than a scientific aim. As a result, the tests were often poorly reported, carried out with too complicated support conditions and not continued until failure of the specimens. So, new tests were needed to study the failure behaviour and to provide input for the FE models.

Two types of experiments were carried out, i.e. structural fire tests on HC elements and calibration tests. This chapter covers only the fire tests on HC elements. For the calibration tests, reference is made to chapter 6.

### **4.2 OBJECTIVE**

The objective of the experimental programme is the identification of the failure mechanisms for shear and anchorage failure of HC slabs during fire exposure. The experiments must also provide a basis for the development of numerical models.

Several hypotheses must be evaluated:

- Incompatible thermal strains can cause irreversible damage to the slab such as cracking of concrete and slippage and yielding of the strands.
- This damage reduces the remaining shear and anchorage capacity of the HC slab. Therefore, these strains can not be neglected in the assessment of the shear and anchorage capacity of fire exposed HC slabs.
- Cracking of the webs due to incompatible thermal strains does not have to cause direct failure provided that the cracked cross section can still bear the mechanical load, since the thermal stresses are assumed to vanish after crack formation.

A direct result from these three hypotheses is that the remaining shear and anchorage capacity after a specific fire exposure time depends on the loading and heating history, even if the thermal stresses have vanished already at this time.

In the underlying research project, 25 fire tests of HC slabs were carried out, see table 4.1. An extended documentation is given in test reports [FELLINGER: 1999b, 2000a,b, 2001,a,b,c]. The tests were designed in such a way that shear and anchorage failure could be expected. Moreover, failure should occur within a time of fire exposure that has practical relevance, say within 30-120 minutes. Flexural failure had to be avoided. For this reason, the standard shear test set up was chosen in which a single line load is imposed at a distance of 2.5 times the height of the specimen from the support [PREN 1168-1: 1997]. In doing so, the load level with respect to flexural failure can be low, while the load level with respect to shear and anchorage failure can be sufficiently high to expect such a failure.

From the objective it follows that the crack propagation and slip development have to be measured. Most tests were carried out on double ribs sawn out of HC slabs as to offer the possibility to view both webs and to capture the crack propagation on camera.

The thermal stress distribution depends on the concrete properties which show large scatter at elevated temperatures. For simply supported members, the calculation of thermal stresses is far more simple than for hyper-static members, because the generalised cross sectional forces  $N$ ,  $V$  and  $M$  follow directly from equilibrium. Kinematic and constitutive relations do not affect the distribution of these forces in this case. In order to simplify the interpretation of the fire tests, they were carried out on simply supported slabs.

On the other hand, chapter 2 showed that restraint to thermal elongation by an unexposed frame, dramatically influences the behaviour under fire, especially when axial restraint is applied. Therefore, three more tests were carried out on axially restrained specimens. These tests are mainly useful for the comparison of the crack propagation and the slip development between the restrained and unrestrained specimens.

As shown in chapter 2, the scatter in the achieved fire resistance is very high when the fire resistance is plotted against any parameter. In order to evaluate the reproducibility of fire tests on HC slabs, three identical fire tests were carried out on HC slab specimens, all taken from the same batch in the production process. These tests were carried out on complete HC slab units rather than double ribs sawn out of it. In addition, three more tests on complete HC slabs were conducted to check the effect of the use of the double ribs compared to the complete units.

The thermal stress distribution strongly depends on the geometry of the cross section. Therefore,

the first series of tests were carried out on slabs with five different cross sections, ranging from 200-400 mm slab depth, see fig. 4.1. In this figure, the dashed vertical lines indicate the sawing faces to obtain the double ribbed specimens. The X200 and XB200 had 8 bottom strands. The HVP260A had 1 bottom strand per rib, in two of them at 76 mm from the soffit, and at 40 mm in the other 4 ribs. The HVP260S had also 1 bottom strand per web, all at 40 mm from the soffit. Also the axis distance of the strands was varied, as the effect of thermal elongations on the slip development depends on the relative position of the strand in the cross section. For this reason, two identical slabs were tested that differed only in the axis distance of the strands, the X200 slab with the strand at 30 mm and XB200 with the strand at 45 mm, see fig. 4.1.

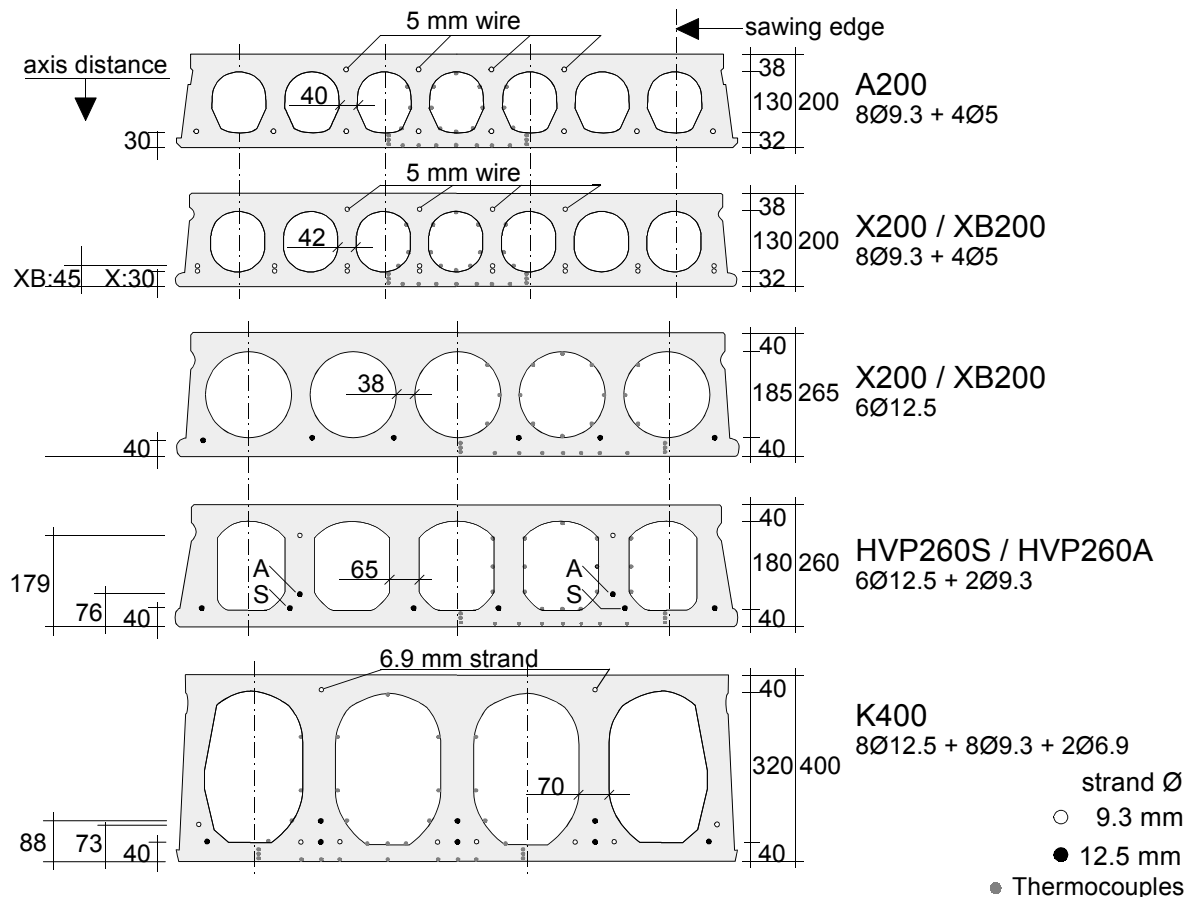


Figure 4.1: Cross sections of the specimens used in the fire tests.

In order to separate load induced damage from thermally induced damage, the loading had to be varied as well. During the first series of tests it was found that the time to failure seemed to be even more sensitive to the applied load level with respect to the shear or anchorage capacity within a range of 10-30 % than expected, although the importance of the load level was already recognised in design recommendations [ECCS/IPHA: 1998]. In the first three tests of the first series, the applied load in the fire test was based on a desired value relative to the design anchorage capacity at ambient conditions. In all later tests, the applied load was based on a desired value relative to the actual capacity at ambient conditions. As a result, the actual load level in the first three tests was lower than in the later tests, see table 4.1. Moreover, a test was carried out on a spare double rib K400 specimen. This specimen was strengthened with concrete, grouted in the cores over the transfer length in the production plant in a rough manner, without

proper compaction of the filling. Nevertheless, the shear tension capacity at ambient conditions was enhanced compared to the unstrengthened specimens. The load in the fire test was increased accordingly, resulting in an increased load level relative to the unstrengthened specimen from 23 % to 30 % compared to the K400 specimen without concrete filling. The time to failure decreased dramatically from 60 to 24 minutes.

In order to determine the effect of the load level, the load level was systematically varied in three additional tests using only HVP260 specimens. However, due to some complications in two tests, no conclusive determination of the load level effect could be given and therefore three new tests were carried out on the same type of slab, but with different strand positions. As a result, also the effect of the position of the strand could be determined in more detail.

In national and international guidelines [BREKELMANS ET AL.: 1999, ECCS/IPHA: 1998] for the application of HC slabs supported on integrated beams, it was recommended to enhance the fire resistance of HC slabs by means of a filling the cores with reinforced concrete over the transfer length. The idea behind it was that the reinforced filling enlarges the cross sectional area to bear the shear force in the relatively weak zone of reduced prestress. Moreover, it reduces the tensile thermal stresses in the web as these tensile stresses can be spread out over the web and the filling. The support reaction of the HC slab will shift away from the slab's end due to the suspension action of the embedded reinforcement in the filling. In chapter 2, it was shown that filling of the cores results in a high fire resistance in some cases. However, it was often combined with some restraint, either axial, transverse or both. Therefore, in the design guides the core filling was proposed in combination with provisions for some restraint by the overall structural integrity. In order to be able to separate the effect of the core filling from the effect of restraining, the effectivity of filling the cores with reinforced concrete over the transfer length was evaluated in three additional fire tests on a double rib HVP260 specimen. The central core of these specimens was provided with reinforced concrete, cast in one batch with a reinforced end beam. In order to evaluate the effectiveness of the filling in relation to the load level, the load level was varied up to the same levels as used in the tests on identical specimens without core filling.

**Table 4.1** Overview of the fire tests on HC slabs.

	Test ID	date	age [d]	moist-ure %	Fail. mode amb.	Load level % <sup>1)</sup>	Fail. mode fire	Fail. time [min]	Remarks	
double ribs	bare	R-A200	24-8-99	73	3.2	A	21	A	96	<i>no slip measured</i>
		R-X200	25-8-99	60	2.9	F/A	16	F	125	$V_u = 30 \%$
		R-XB200	27-8-99	61	2.9	F/A	18	A	125	$V_u = 34 \%$
		R-VX265	3-12-99	154	2.4	ST	23	S	35	
		R-HVP260A23	7-12-99	144	1.8	ST/A	23	S/A	55	
		R-HVP260A20	13-2-01	578	<1.8		20	S/A	56	<i>furnace failed</i>
		R-HVP260A17	31-1-01	565			17	S/A	114	
		R-HVP260A14	29-1-01	563			14	S/A	123	<i>loading failed</i>
		R-HVP260S23	3-10-01	97		0.7	A	23	A	48
		R-HVP260S17	4-10-01	98	17			A	45	<i>fluctuating load</i>
		R-HVP260S11	5-10-01	99	11			A	123	$V_u = 16 \%$
	R-K400	9-12-99	141	2.1	ST	23	S	60		
	restrained	R-XB200-R	16-12-99	169	<2.9	F/A	18	F	159	$V_u = 37 \%$
R-VX265-R		18-12-99	174	<2.4	ST	23	S	25		
R-K400-R		14-12-99	146	<2.1	ST	23	S	30	<i>restraining failed</i>	
filled cores	R-K400-F	28-3-00	247	2.6	ST	30	S	24	low quality filling	
	R-HVP260A23F	22-6-01	707	3.1	2)	23	S/A	49	reinforced end beam and reinforced central core	
	R-HVP260A20F	29-6-01	714			20	S/A	50		
	R-HVP260A17F	27-6-01	712			17	S/A	99		
HC units	bare	U-XB200	5-4-00	285	<2.9	F	19	F	117	
		U-VX265	7-4-00	280	<2.4	ST	23	S	33	
		U-HVP260A-1	11-4-00	270	<1.8	ST/A	23	S/A	40	
		U-HVP260A-2	13-4-00	272			23	S/A	42	
		U-HVP260A-3	14-4-00	273			23	S/A	39	
		U-K400	30-3-00	253	<2.1	ST	23	S	33	

<sup>1)</sup> Load level relative to mean strength determined in three reference tests at ambient conditions

<sup>2)</sup> No reference tests at ambient conditions were carried out for the HVP260 specimen with concrete filled cores as the HC units were identical to the unfilled specimens.

## 4.3 TEST DESCRIPTION

### 4.3.1 Set up

As explained in the previous paragraph, the fire tests were set up similar to the standard shear test at ambient conditions according to prEN 1168-1 [1997], see fig. 4.2. So, a line load was applied at one end only at a shear span of 2.5 times the slab height. At the loaded end, a roller support was applied. At the unloaded end, a free pin support was used to prevent torsional forces. In the fire tests on the HC ribs, the furnace was closed with a thin insulated steel plate. In the fire tests on HC units, the same test set up was used, however, the furnace closure by the insulated steel plate could be left out. The gap between the furnace wall and the specimen was then simply filled with mineral wool.

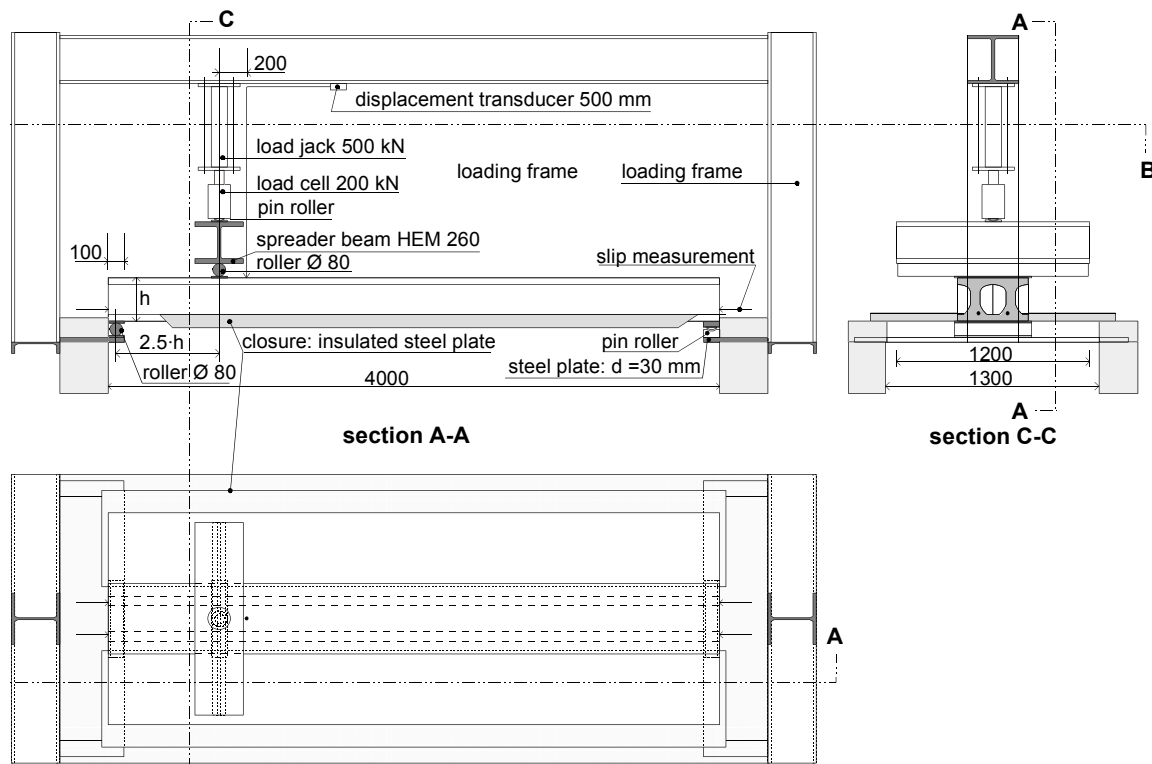


Figure 4.2: Test set up for the fire tests on double ribs sawn out of HC slabs.

In order to avoid splitting stresses at the introduction of the load and the support reaction, a gypsum layer was applied between the specimen and the 100 mm wide steel plates.

### 4.3.2 Concrete mix

In table 4.2, the main characteristics of the concrete mix for all HC slab types are given.

**Table 4.2** *Overview of the concrete composition of the fire test specimens.*

Slab type		A200	X200 XB200	VX265	HVP260A HVP260S	K400
Producer and location		Producer 1	Producer 2		Producer 3	Producer 4
Production process		slip form	extrusion		shear compaction	extrusion
Aggregate type	fine	siliceous	siliceous		siliceous	siliceous
	course (max diameter)	calcareous (14)	calcareous (14)		calcareous (10)	calcareous (14)
		concrete granulate (?)	calcareous concrete granulate (14)		siliceous (12)	
cement		Portland N and R	Portland N + Blast Furnace N		Portland R	Portland N +R
additives		slik	plasticizer		plasticizer	
w/c ratio		0.482	0.425		0.41	0.37

### 4.3.3 Instrumentation

In order to allow for a visual inspection of the crack propagation in the webs, a slim furnace closure of a 1 mm steel plate, insulated with mineral wool, was used, resting on the top of the lower flange of the specimen. (In fig. 4.2, the insulation is not drawn in section A-A near the support to be able to show the support detail, but in the test, the insulation was present along the entire length of the furnace). At both sides of the test set up, photo camera's captured the crack propagation every 2 minutes. At one side, also a video camera was installed.

In the first three tests, digital camera's with high resolution were used to picture the concrete surface of the sawn hollow core at regular time intervals. With special so-called SPICA software provided by KEMA, in Arnhem, the Netherlands, the concrete texture could be recognised from the pixels of the photo's. The movement of the texture could be followed from the differences between subsequent photo's, and the concrete strain at the surface could be derived, see fig. 4.3. In the first tests, it appeared that cracks could be observed with this technique. However, it also appeared that the moisture in the concrete escaped from the specimen through the cracks, marking the crack with a wet line, which could easily be viewed by human eye. Therefore, later on, the SPICA technique was not used any more.

The applied load was measured with a 200 kN load cell, the dead weight of the spreader beam was 2.44 kN. The deflection at 200 mm from the line load was measured with a linear variable displacement transducer (LVDT), see fig. 4.2.

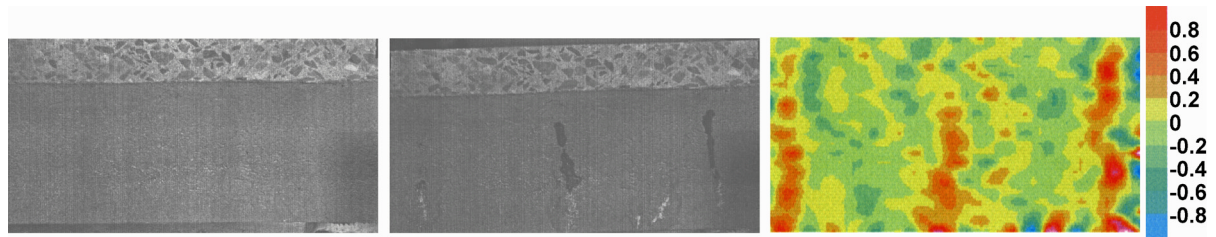


Figure 4.3: Principle of the SPICA measurement. Left, the concrete web surface before the fire starts, in the middle, the same concrete web surface after 30 minutes of fire exposure, and right the horizontal strains derived after the exclusion of the rigid body motions.

The slip of the strands was measured in two ways. In the fire tests, carried out in 1999, the slip was measured with LVDT's. In later tests, the slip was measured manually with a slip calliper, because the application of the LVDT's appeared to be too cumbersome and they sometimes yielded inaccurate readings [FELLINGER: 1999b].

The gas temperatures in the furnace were measured and controlled with four plate thermocouples in order to anticipate on European developments to harmonize the fire resistance tests between laboratories. In a European harmonisation project [VAN DE LEUR & TWILT: 1999] it was shown that differences in fire test results are significantly reduced between fire resistance furnaces of different fire test laboratories, once the furnace temperature is controlled with plate thermocouples rather than with conventional thermocouples.

The temperature in the specimens was measured with uninsulated type K (chromel-alumel) thermocouples, glued to the concrete surface at the inner side of the HC cores, where temperatures lower than 500 °C were expected. In fig. 4.1, the location of the thermocouples is shown. Nearer to the exposed surface glass-fibre insulated thermocouples type K were used, which can withstand more than 1000 °C. The high temperature did not allow for gluing and therefore, these thermocouples were embedded in a slit, sawn in the hardened specimen at 5, 8 16 and 24 mm from the exposed soffit [FELLINGER: 1999b].

No thermocouples were attached to the strands during production of the slab as these measurements appeared to show large scatter, see §2.2.4. No thermocouples were embedded in a slit in the vicinity of the transfer length of the strand as such a slit might initiate splitting cracks.

## 4.4 MEASUREMENTS

### 4.4.1 Overview

As pointed out in §4.2, the objective of the tests is to determine the crack propagation and slip development during fire. For the shear and anchorage behaviour, the deflections of the slabs are of minor importance. For the deflection readings, reference is made to the test reports.

Furthermore, the tests have to provide a basis for the validation of the numerical models, requiring the measurement of the temperature distribution over the cross section.

#### 4.4.2 Crack patterns

An overview of the typical crack patterns in the webs for all slab types, is sketched in fig. 4.4. In fig. 4.5 to 4.10 photo's taken during the tests are shown. On the photo's, the cracks can be recognised by the dark lines, as moisture appeared to escape from the specimens through the cracks, see also fig. 4.3.

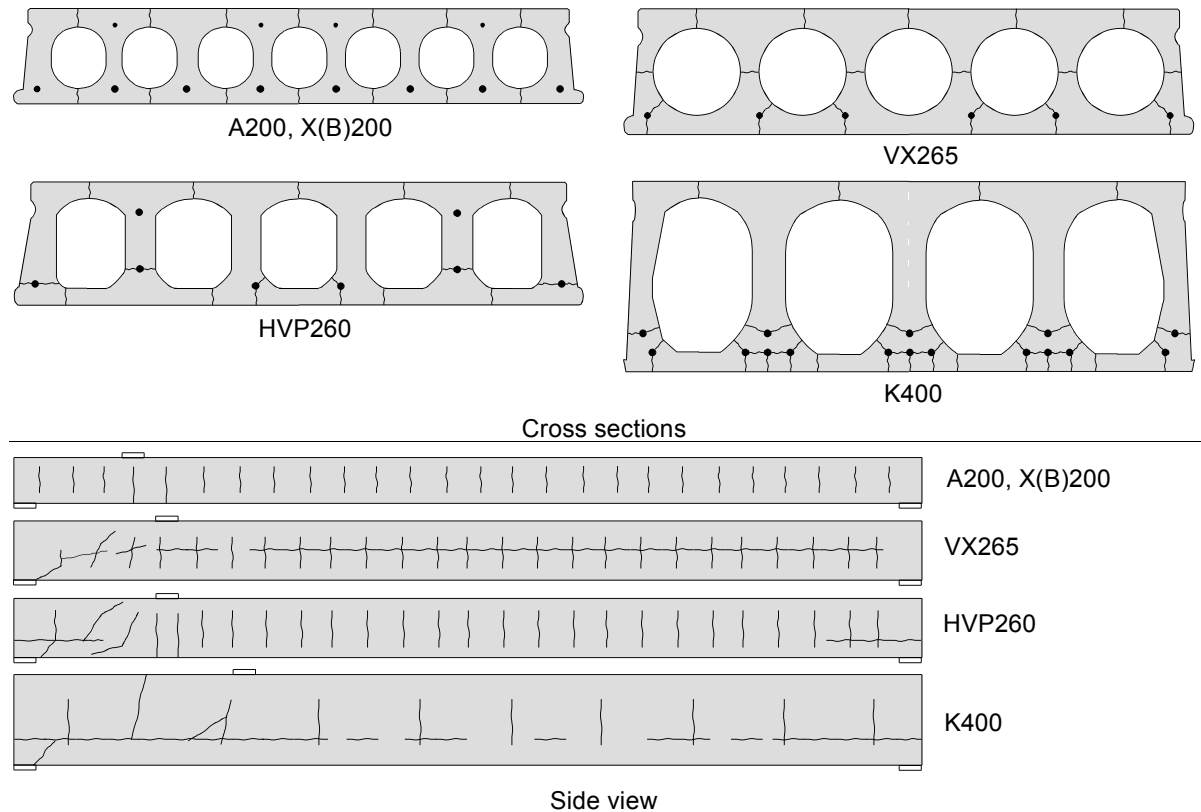


Figure 4.4: Sketch of the crack patterns for the 200 mm slabs, the VX265, HVP260 and K400 slab, shown from top to bottom.

As shown in the figure above, the crack propagation depended strongly on the geometry and the strand position. In all fire tests, vertical cracks were observed in the webs after 14-16 minutes even if the slabs were axially restrained. Notably, the vertical cracks through the webs did not directly lead to shear failure, whereas on the contrary, shear tension cracks in the webs cause directly brittle failure in tests at ambient conditions.

Near the point load, the vertical cracks were not perfectly vertical but slightly inclined up to approximately  $25^\circ$  to the vertical plane, indicating that the cracks in the webs were caused by a combination of (axial) thermal stresses and (diagonal) principal tensile stresses due to the shear loading.

Moreover, in all tests, vertical cracks developed above and below the hollow cores through the flanges, dividing the specimens into separate ribs, each spanning from support to support. So, these cracks had no direct effect on the structural behaviour except for the ability of stress redistribution. Near the supports and the line load, these cracks were restrained by the friction of the support and the loading plates respectively.

In the 200 mm deep slabs, shear failure did not occur at all despite the vertical cracks. In all these tests, the vertical crack in the web below the line load grew through the lower flange close to failure, resulting finally in either anchorage or flexural failure. The difference between the test on the HC unit (U-XB200) and the double rib specimen (R-XB200) was large. In both tests the vertical crack below the point load grew into a flexural crack. However, the U-XB200 test resulted in a flexural failure after 117 minutes while the R-XB200 test did not fail within 120 minutes with the same load during fire. The load on the R-XB200 specimen was increased after 120 minutes from 18 % to 34 % of the anchorage capacity before failure. The difference in the fire resistance between the unit and the double rib specimen is attributed to the weaker bond of the strand in the outer rib of the unit, leading to an increased slip of this strand and consequently to an increased opening of the flexural crack. Through the increased crack opening, the heat flow through this crack might have increased leading to an increased temperature of the strand.

In the tests on VX265 specimens, horizontal cracks propagated through the smallest part of the web at mid depth over the entire length after 20-22 minutes. The cracks initiated at various spots over the length, independent of the position of the loading point and grew together up to failure. After 35 minutes failure occurred by a rapid interconnection of the horizontal crack together with the vertical cracks in a few seconds. In the restrained VX265 test, the centroid of the restraining force was located in the lower half of the specimen at 65 mm from the exposed soffit. As a result, the lower part of the slab buckled suddenly after the horizontal cracks through the web had grown to one long crack over the entire length. The lower part of the specimen collapsed into the furnace.

In the tests on the VX265, HVP260 and K400 specimens, cracks were observed along the strands. In the VX265 tests, these cracks only occurred at the supports. In the HVP260 tests, these cracks especially occurred at both ends of the slab over the transfer length of the prestress, see fig. 4.4. In the K400 specimens, the cracks along the strands initiated at various spots along the length and developed over the entire length.

The orientation of the cracks along the strands depended on the concrete cover in all directions. The cracks along the strand positioned at 76 mm from the exposed side in the HVP260 specimens and the cracks along the strand positioned at 88 mm from the exposed side in the K400 specimens grew horizontally through the entire web. In all these tests, shear failure resulted from the opening of these cracks, which took a few seconds.

In the ribs with a strand at 40 mm in both the VX265 and HVP260 specimens, the cracks along the strand grew from one hollow core to the exposed side. No other vertical crack through the lower flange below these hollow core developed.

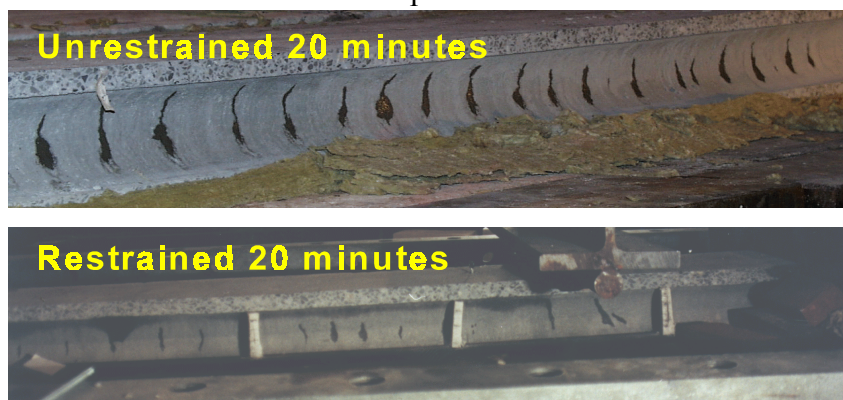


Figure 4.5: Typical crack pattern after 20 minutes in 200 mm deep slabs, either axially restrained or unrestrained.

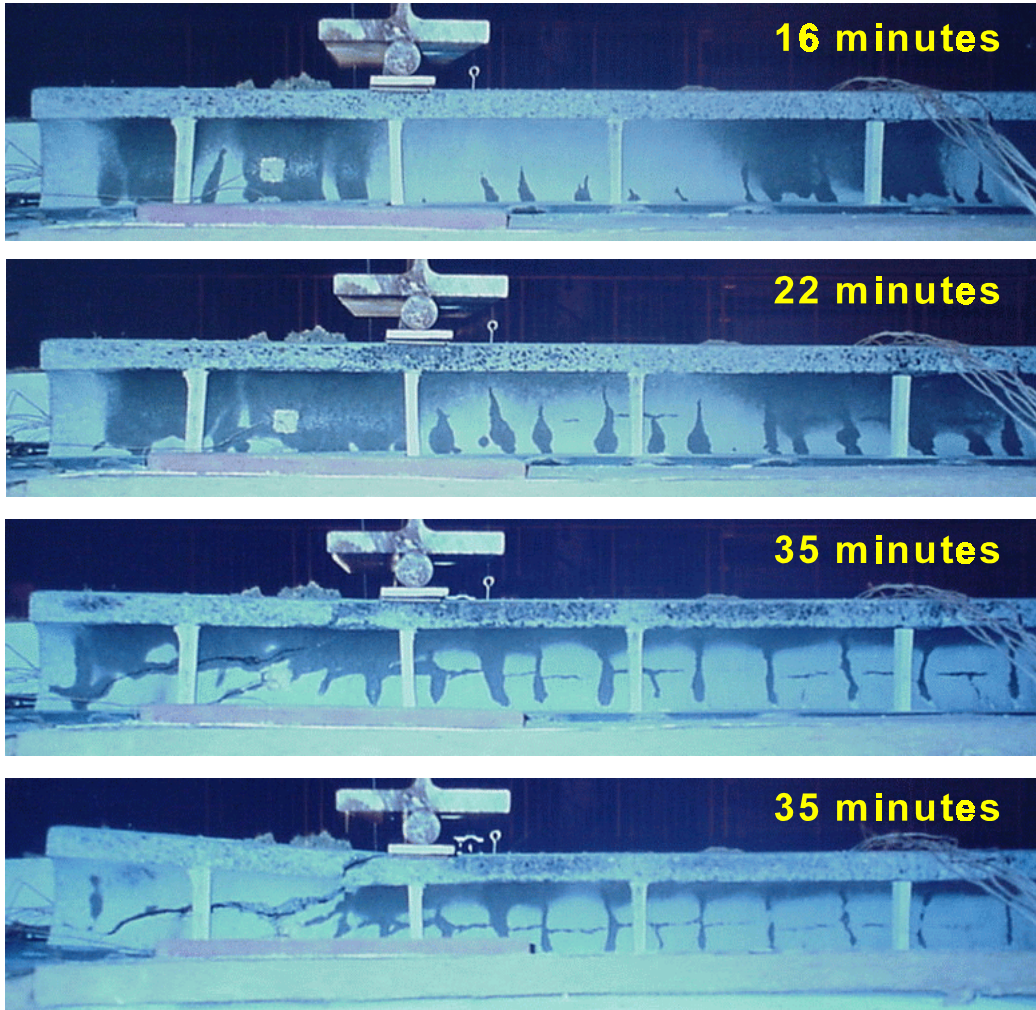


Figure 4.6: Typical crack pattern in unrestrained VX265 specimen.

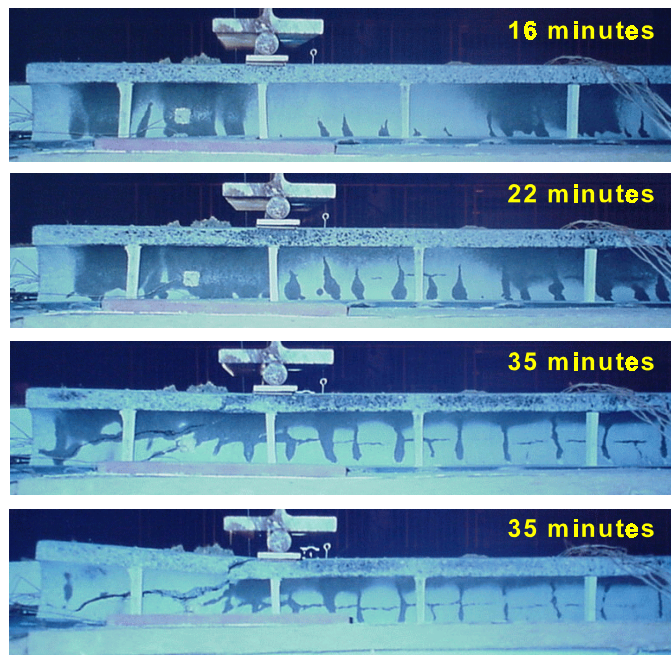


Figure 4.7: Crack pattern in restrained VX265 specimen.

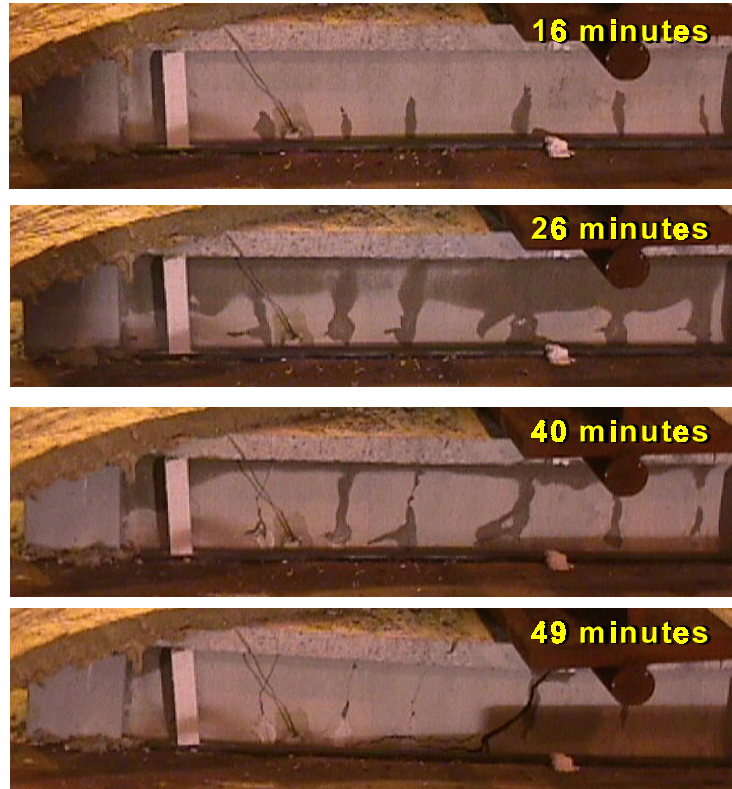


Figure 4.8: Typical crack pattern in the web of a HVP260 specimen with the strand in the web at 76 mm from the soffit.

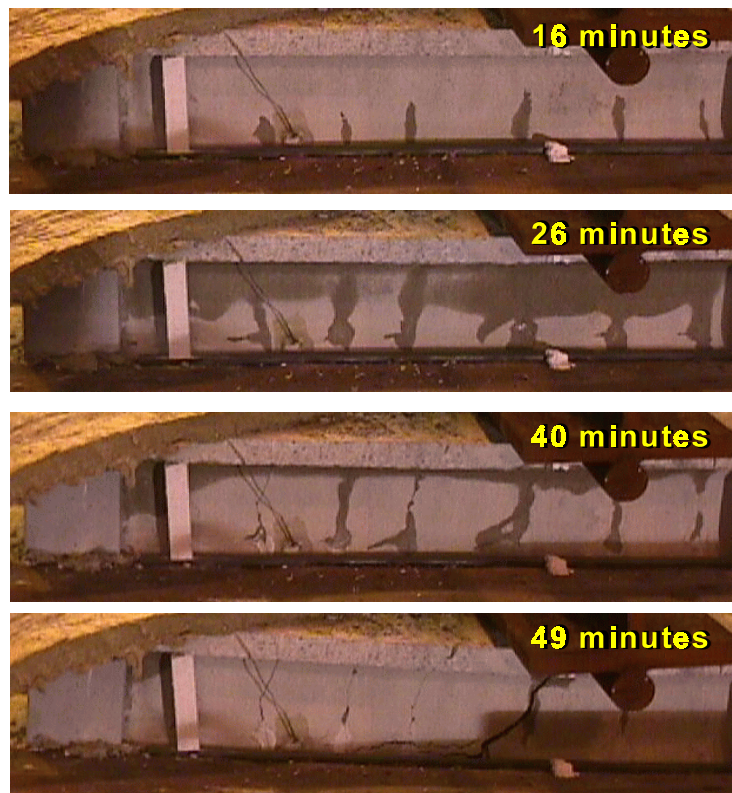


Figure 4.9: Typical crack pattern in the web of a HVP260 specimen with the strand at 40 mm from the soffit.

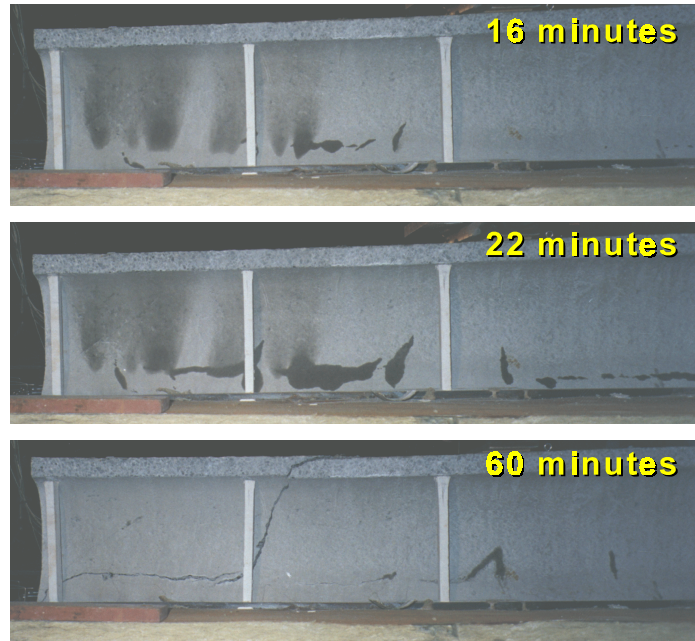


Figure 4.10: Typical crack pattern in K400 specimen.



Figure 4.11: Details of the splitting cracks in VX265 specimen (left) and K400 specimen (middle and right) as observed after cooling down. In the middle figure one of the ribs is given from the support (lower side of the photo) to the loading point (upper side of the photo), right a detail of the cracks in the cover around the strands at the support.

From the HVP260 tests with varying shear loading, it appeared that the shear load had a minor influence on the propagation of the cracks. Only the horizontal crack along the strand through the web in the ribs with a strand at 76 mm from the exposed side propagated slightly faster at higher loads, but the final failure pattern was almost independent of the load level. The difference between the crack patterns at failure of the test with a load level of 17 % and 23 % is shown in fig. 4.12.



Figure 4.12: Crack pattern after failure in two HVP260 tests, seen from the side with a strand in the rib at 76 mm from the exposed side.

Also filling the central hollow core with cast in-place reinforced concrete did barely change the crack pattern, compare fig. 4.12 with fig. 4.8 on page 94.

#### 4.4.3 Slip

All slabs showed significant slip of the bottom reinforcement. The upper strands and wires barely slipped. In the three identical tests on the HVP260 units, the scatter in the slip measurements was found to be limited, see fig. 4.13. The standard deviation was only 0.2-1.1 mm during the first 37 minutes of fire exposure for the strands at 40 mm from the exposed side (based on 9 slip measurements) and only 0.2-0.6 mm for the strands at 76 mm from the exposed side (based on 6 slip measurements). Note that all three specimens came from the same production bench, so the measurements were biased. For a random sampling, the scatter will probably be higher.

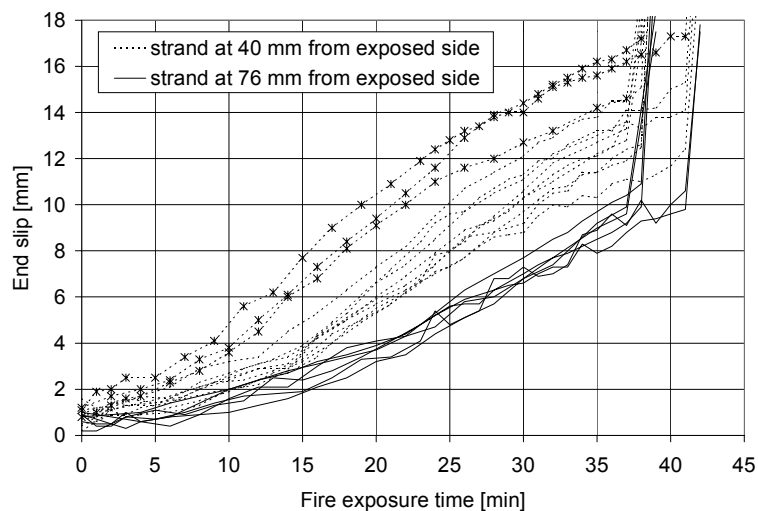


Figure 4.13: Scatter in the end slip measurements in three HVP260 units in identical fire tests, given for the strands at 40 mm and 76 mm from the exposed side.

In fig. 4.13, one strand at 40 mm from the exposed side positioned in same outer rib of each specimen, was presented with an additional marker because the slip of this strand was systematically higher in all three tests than of the strands positioned at 40 mm from the soffit in the other ribs. Probably the bond around this strand was coincidentally lower, which is in accordance with experience obtained in ambient tests that sometimes the bond of strands in the outer ribs is worse than the bond of the strands in the other ribs. It is attributed to a lower compaction pressure in the outer ribs during the production process. The slip measurements of this strand were excluded from the calculation of the standard deviation.

From these three identical tests, it was concluded that the slip measurements are reproducible, provided that the slab type, strand type and positions, concrete mix, and test set up are constant.

As fig. 4.13 shows, the strands positioned at 76 mm from the exposed side showed systematically lower slip values than the strands at 40 mm from the exposed side, over the main fire duration up to the onset of failure. Thus the position of the strand strongly affects the actual slip.

In the HVP260 specimens, a lower slip was measured in the strands with a higher distance from the exposed side. However, the opposite trend was observed in all K400 specimens, i.e. a larger slip was found for strands with a larger distance from the exposed side, refer to fig. 4.14. In this figure, the measurements were averaged over the strands in different ribs at the same nominal distance from the exposed side and with the same diameter.

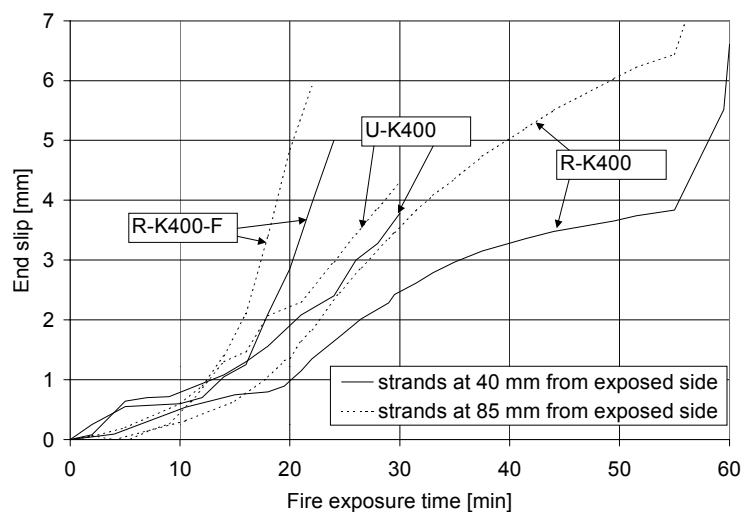


Figure 4.14: End slip measurements in K400 test specimens for 12.5 mm strands positioned at two different distances from the exposed side. Refer to table 4.1 for the test identification.

Comparison of fig. 4.14 and 4.13 shows that the slip of a strand at a distance of 40 mm from the exposed side in the HVP260 specimens is completely different than the slip of the same type of strands at the same distance in the K400 specimens. So, obviously, the slip development strongly depends on the geometry of the slab.

The observed trend in the K400 specimens might also result from the observed splitting cracks around the upper strand, that was initiated after some 15-20 minutes. Splitting cracks were also observed around the lower strand, however, only at inspection of the specimen after the test. So it is unknown whether these splitting cracks had developed in an earlier stage of the fire.

Further investigations into the slip development in the K400 specimens show that smaller strands show smaller slip than bigger strands at the same distance from the exposed side within the same specimen, see fig. 4.15. Smaller strands have a larger bond area relative to the cross sectional area, so smaller strands have a higher bond resistance. However, this trend is not very pronounced for the R-K400 test.

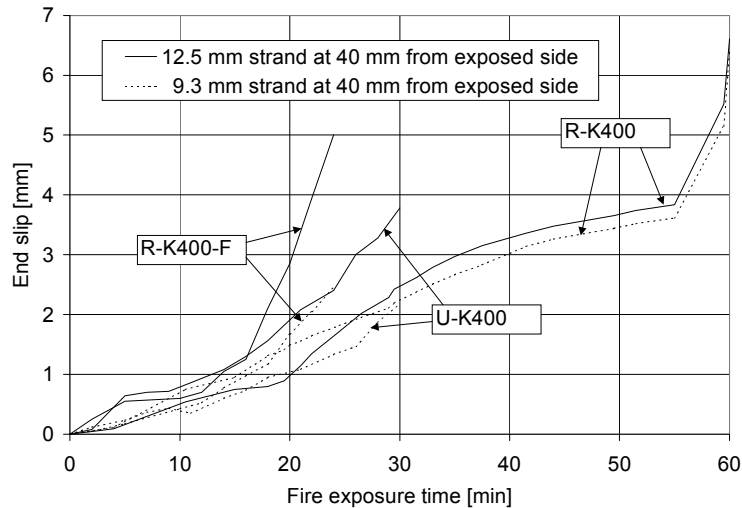


Figure 4.15: Comparison of the end slip of the  $\varnothing$  12.5 mm and the  $\varnothing$  9.3 mm strands in the K400 tests.

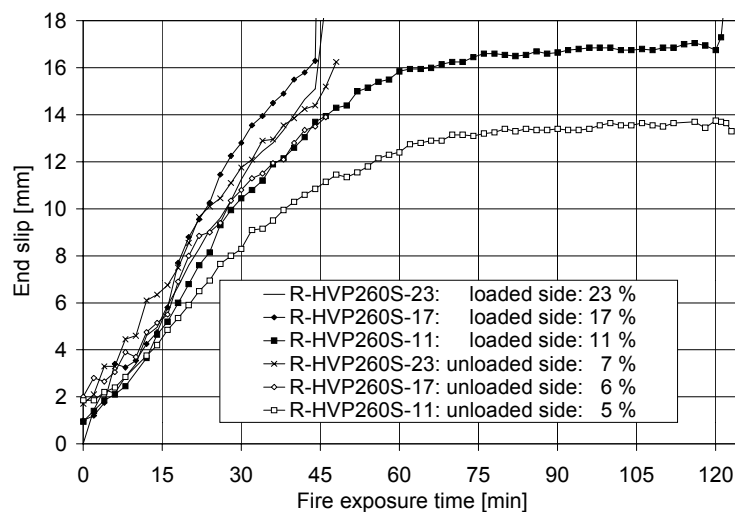


Figure 4.16: Average slip measurements in the symmetrical HVP260 rib specimens, depending on the anchorage load level.

Also, the effect of the load level with respect to the anchorage loading on the end slip was evaluated. For this purpose, the slip measurements of the rib tests on the symmetrical HVP260 specimens with variable anchorage loading were compared. In fig. 4.16, the measurements of the two strands in each specimen were averaged over each end of the slab separately. Due to the asymmetrical test set up, the load level in terms of the shear force at the loaded side was much higher than at the unloaded side.

The graph shows that there exists a small trend that a higher load level results in larger slip. However, the trend is so small within a load level variation of 5-23 % that it vanishes in the scatter of the slip measurements of 0.7-3.5 mm. From this comparison, it was concluded that the slip is mainly caused by imposed thermal elongations, rather than the anchorage loading.

Finally, the effect of axial restraint on the slip development was investigated on the basis of the R-XB200 and R-XB200-R tests, see fig. 4.17. Significantly less slip was observed in the restrained specimen compared to the unrestrained specimen. Note that in the R-XB200 test, the slip at the unloaded side was larger than at the loaded side during the fire up to a few minutes before failure, underlining the insignificance of the load level on the slip development.

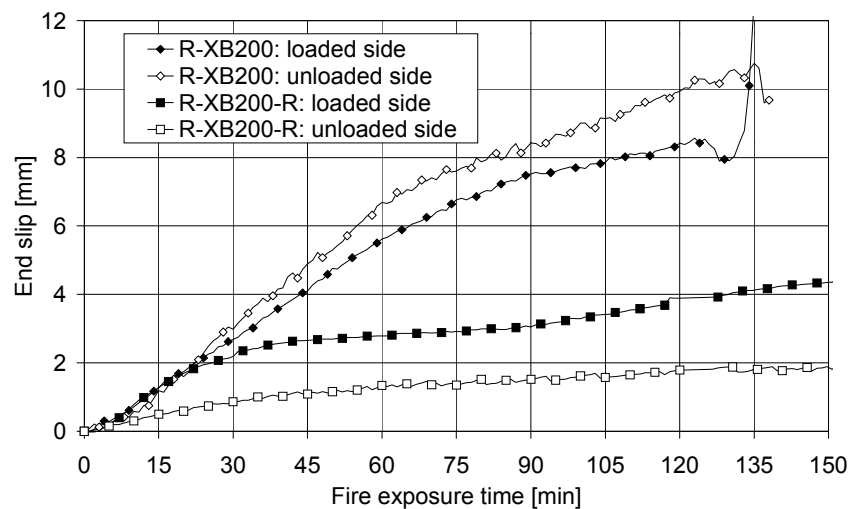


Figure 4.17: End slip in the XB200 rib specimens, comparison between the axially restrained tests and the unrestrained tests.

The difference in the end slip is caused by a restrained thermal expansion of the specimen at mid depth. In fig. 4.18, the measured axial displacement of the end surface at the level of the strand of the specimen was presented for both tests. As the end surface rotates, the axial displacement varies over the cross section. On the basis of three measurement points around the strand the axial displacement of the concrete part in the centre of the strand was calculated assuming that the end surface is plain. In order to exclude rigid body motions, the axial displacements at both ends of the specimen were summed.

The axial displacement of the strand was also measured. The difference between the axial displacement of the concrete surface and the strand equals the end slip. From fig. 4.18, it appears that the axial displacement of the strand is almost identical in the restrained and unrestrained tests. However, in the unrestrained test, the axial displacement of the concrete part is much larger than in the restrained test. So, also this comparison justifies the hypothesis that the end slip development is driven by the thermal elongations rather than by the loading at least up to a few minutes before failure.

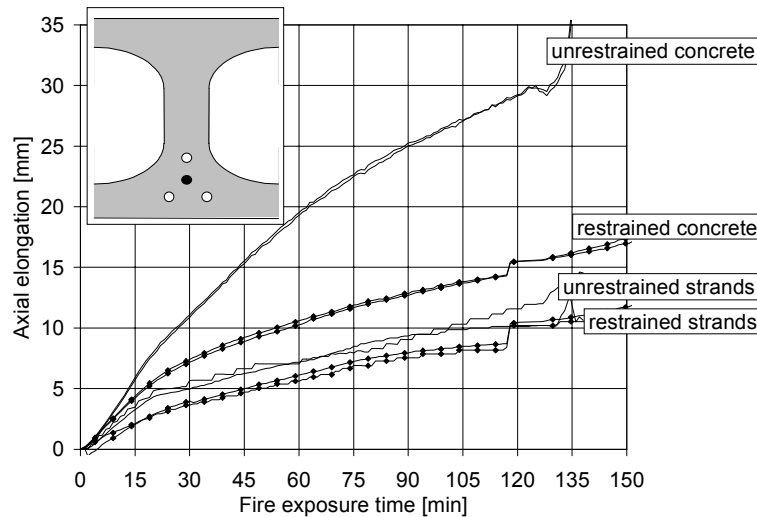


Figure 4.18: Total axial elongation (sum of both ends) of the strand and the concrete cross section at the location of the strand in the unrestrained R-XB200 and the restrained R-XB200-R test.

#### 4.4.4 Temperatures

In order to be able to predict the thermal elongations properly, the development of the temperature distribution over the cross section was measured. However, as concluded in §2.2.3.4, temperature measurements inside HC slabs show a large scatter, if the thermocouples are cast in the slab. Therefore, no thermocouples were cast in the slab. Thermocouples were only drilled in the hardened slab and attached to the inner surface of the hollow cores. In later tests, no thermocouples were even drilled in the specimens. Only inner core surface temperatures were measured. These later tests comprised tests on units and tests to investigate the effect of the load level and the core filling.

The objective of the concrete temperature reading is to serve the validation of the FE simulations of the thermal response. Therefore, the measurements must statistically be evaluated. The statistical evaluation comprises the calculation of the average temperature of readings at identical measurement positions and their variation.

All readings that showed a stable temperature increase with time are relevant for the first purpose. In order to retrieve statistical information, some test results were combined. Tests on specimens with an identical shape can be combined, since the furnace temperatures in all tests showed very little scatter, see appendix H of the test report [FELLINGER: 2000a]. So, the R-X200, R-XB200 and R-XB200-R temperature data were combined. Also the R-VX265 and the R-VX265-R temperature data were combined as well as the R-K400 and R-K400-R temperature data. Note that the restrained R-K400-R test failed in a structural sense. The HVP260 tests without a concrete core filling were grouped as well as HVP260 tests with a concrete core filling. Nevertheless, the temperature measurements were reliable. The R-A200 test was evaluated individually.

With the collection  $X$  of temperature readings at each position, the average temperature is

calculated as well as the corresponding standard deviation. On the basis of the average temperature and the standard deviation, the reliability of each individual reading was checked. The probability was calculated that an individual temperature reading  $x_i$  fits in the expected range corresponding to the calculated average and standard deviation and no systematic error had occurred. It was calculated assuming a normal distribution for the collection of temperature readings, according to [NOWAK & COLLINS: 2000]

$$P[x_i \in X] = 1 - \left( F \left[ \frac{|x_i - \mu|}{\sigma} \right] \right)^n \quad \{4.1\}$$

Where  $n$  is the number of readings,  $x_i$  the individual reading,  $\mu$  the average temperature and  $\sigma$  the standard deviation. For a probability  $P[x_i \in X]$  is smaller than 10 %, the reading is rejected. In the figure below, the relative distance of an individual reading to the mean value of the group is shown for which the reading is rejected. For a larger population of readings, it becomes more likely that an individual reading exists at a large relative distance from the mean value.

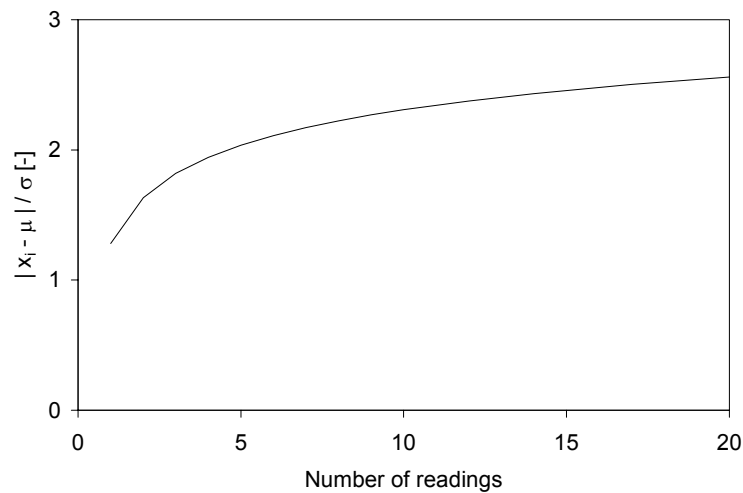


Figure 4.19: Relative distance of an individual reading to the mean value of the collection of readings, for which the reading is rejected, depending on the total number of readings.

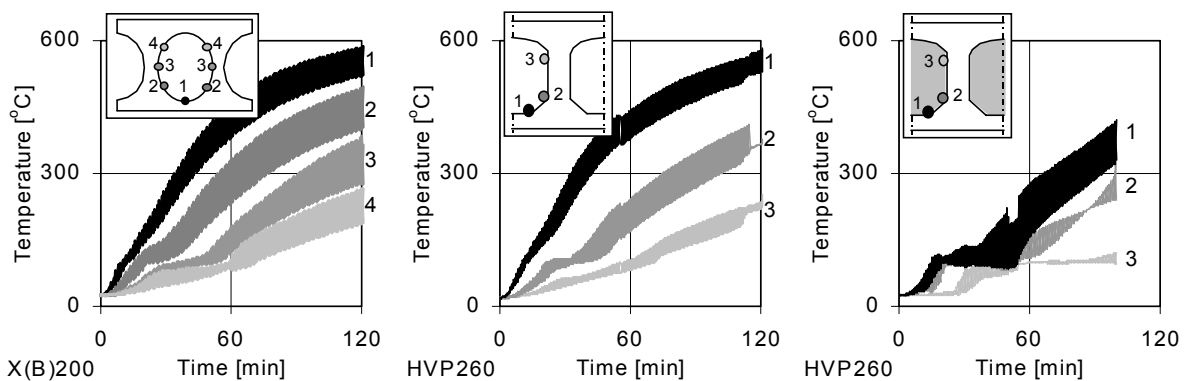


Figure 4.20: Temperature measurements at the intrados of the hollow cores in the rib specimens. Reliability interval of 16-84 % based on identical tests. Left: R-X200, R-XB200 and R-XB200-R. Middle: HVP260 rib specimens without core filling. Right: HVP260 rib specimens with core filling.

By means of example, the probability intervals of temperature developments at the intrados of the hollow core closest to the bottom strands are given for the extruded 200 mm slabs and the HVP260 specimens, see fig. 4.20.

The concrete core filling affects the intrados temperature, i.e. compare the middle picture with the right one. The temperatures at the intrados of the filled cores lack significantly behind the temperatures at the intrados of the unfilled cores. This is attributed to the heat accumulating capacity of the core filling. Moreover, apparently, significant heat flow takes place through the cores. Furthermore, a substantial plateau at 100 °C can be observed, especially at the specimens with filled cores. It is postulated that vapour escaping from the concrete condenses on the higher regions of the intrados and drops down to the upper side of the lower flange where it evaporates again. As a result, the moisture circulation in the core dominates the heat flow in the core.

The temperatures at the intrados of the sawn cores (at the outside of the double rib specimens) show a larger scatter, due to heat leakage through the specimen and the furnace closure. This scatter is therefore not representative for normal HC slabs and not presented in this thesis.

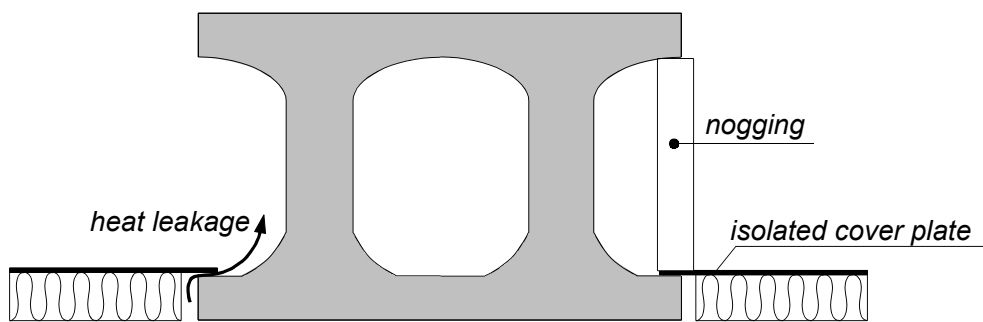


Figure 4.21: Left: Heat leakage through the gap between the specimen and the isolated cover plate, Right: Heat leakage limited by clamped nogging closing off the gap.

Also, the concrete temperatures in the R-A200 test were significantly higher than in the other tests on 200 mm deep specimens. This is probably caused by the fact that in the R-A200 test, the gap between the isolated cover plate and the specimen was not forced to remain closed during the test. In the other tests, the steel plate was pushed on the lower flange of the specimen by clamping wood blocks between the upper flange and the lower flange of the specimen. Other influencing factors for this difference were the slightly deviating shape of the R-A200 specimen from that of the X(B)200 specimens and the different concrete mix.

The standard deviation of the temperature readings remains below 60 °C for all thermocouple positions. The average temperatures were used later on as input values to calculate thermal gradients over the cross sections with the numerical models given in the next chapter and to calibrate the heat transfer parameters.

## 4.5 INFLUENCE PARAMETERS

### 4.5.1 Load level

The effect of the load level on the fire behaviour is a paradox. On the one side, the crack patterns and the slip development during fire exposure are barely influenced by the load level within the investigated range. On the other side, the time to failure is highly sensitive to the load level for both the HVP260 specimens and the K400 specimens, see fig. 4.22. Only tests that were undisputed are plotted. The R-HVP260S-11 test lasted 125 minutes with 11 % load and failed after a load increase up to 16 % (marked with a solid triangle). Also for the 200 mm deep slabs the dependency on the load level was observed, but the R-A200 and R-X200 specimen were not fully comparable, as the concrete mixes differed.

It appears that the load bearing capacity with respect to S/A failure decreases rapidly in the first 30-60 minutes of fire exposure, which is attributed to the damage caused by the incompatible thermal strains. During the later stages of fire exposure the load bearing capacity decreases only slightly.

If failure occurred within the 60 minutes, it seemed to be driven by the increasing damage by the incompatible thermal strains and the mechanical loading. If the load level was so low that failure did not occur within 60 minutes, failure was postponed to more than 90 minutes. On the basis of the observations that the end slip barely increases after some 60 minutes and the thermal cracks barely grew, it seemed that the thermal stresses, that remained after the thermal cracks had developed, further decreased between 60 to 90 minutes. It is attributed to a decreasing incompatibility of the thermal strains. If failure occurred beyond 90 minutes, it seems to be driven by the decreasing strength properties and the mechanical loading. Thermal stresses seemed to play a minor role. As a consequence, a small difference in the load level can result in a large difference in the time to failure.

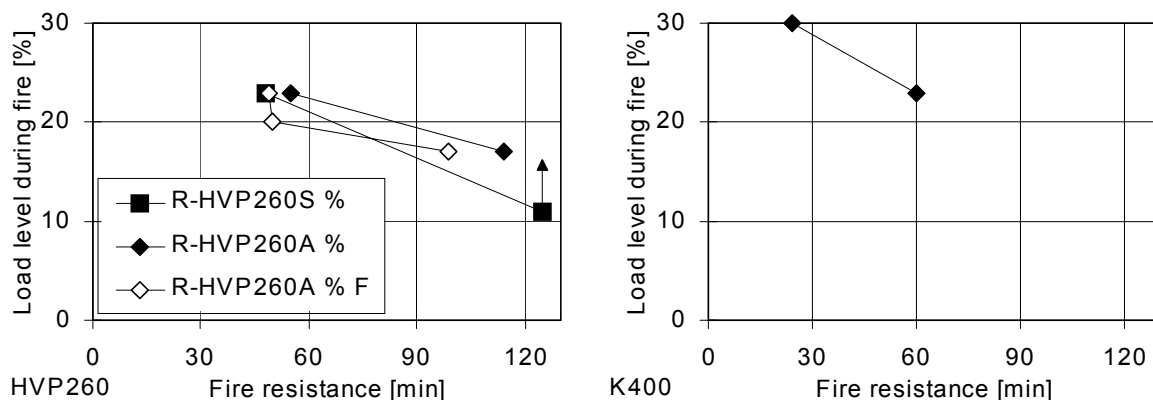


Figure 4.22: Fire resistance versus the load level with respect to the shear force during the test. Comparable tests are interconnected with a line.

#### 4.5.2 Axial restraint

Three tests were conducted in which the specimens were axially restrained. In the R-K400-R test, the load jack providing the axial restraint failed, and therefore this test is not further considered. In the test R-VX265-R, the axial restraint could not prevent the development of the horizontal crack through the smallest part of the web at mid depth, indicating that the horizontal crack is not driven by the axial thermal elongations. As a result, the axial restraint did not enhance the fire resistance.

Compared with test R-XB200, the axial restraint in test R-XB200-R, limited the growth of the vertical cracks to some extent, and in particular strongly reduced the slip development. In both tests, the shear load was increased after 159 minutes for the restrained specimen and after 123 minutes for the unrestrained specimen. Due to the restraint, the restrained specimen failed at a shear load of 37 % compared to 34 % in the unrestrained specimen, despite the 36 minutes longer fire exposure.

#### 4.5.3 Core filling

Three tests with mutually varying shear loading were carried out on HVP260 rib specimens in which the central hollow core was filled with cast-in-place concrete over 800 mm from the slab end. The concrete filling was reinforced with a hooked steel bar  $\varnothing$  10 that protruded into a 100 mm wide reinforced end beam which was cast at the end of the slab. The reinforced end beam provided some limited transverse restraint at the slab's end. For details reference is made to the test report [FELLINGER: 2001b].

In all three tests, the fire resistance was slightly lower than in the comparable tests without core filling. Opposite to the expectation, the filling did not prevent nor reduce the crack development in the webs of the HC slab, nor did it affect the slip development. This was explained by the fact that there was no bond between the HC slab and the filling, which was observed after the test. Vertical cracks in the precast part of the cross section did not continue in the filling. As a result, thermal stresses could not be spread over the composite cross section as they built up from the free supported end, but remained spread out over the cross section of the HC slab alone. So, the shear resistance was reduced in a similar manner as in the unfilled specimens.

The lack of bond between the filling and the HC slab might be attributed to differences in shrinkage which developed during maturing as the filling was cast more than two years after the production of the HC slab. Moreover, in order to speed up the drying of the filling, the specimens were stored 7 days after casting in a climate room at 20 °C and 40 % relative humidity for 2 months and at 40 °C and 20 % relative humidity for the rest of the storage period. These conditions may have increased the shrinkage differences. Maybe the filling was debonded from the HC slab already before the start of the test.

## 4.6 CONCLUSIONS & RECOMMENDATIONS

### 4.6.1 Failure modes

Anchorage failure, shear failure and combined shear and anchorage failure were observed in fire exposed HC elements. The actual failure mode depends on the slab geometry and the position of the strands, see also §4.4.2.

Anchorage failure of fire exposed HC slabs was observed in slabs in which no horizontal crack through the webs developed. It starts with a vertical crack in the web. As vertical cracks develop over the entire length of the specimen, they must be caused by incompatible thermal elongations. The vertical crack near the maximum bending moment grows through the lower flange. So this propagation is driven by the applied bending moment. Furthermore, the crack propagation through the lower flange indicates a decreasing prestress. The decreasing prestress is further documented by the slip, the splitting cracks along the strand and the decreasing stiffness of the strands and the concrete cross section at elevated temperatures. Finally at failure, the governing flexural crack opens and the strand is pulled out.

Shear failure occurs in slabs in which horizontal cracks through the webs had developed. The horizontal cracks developed in an early stage of fire exposure. During fire, the horizontal cracks grew into one crack with some of the vertical cracks. The horizontal crack either developed through the smallest web width at mid depth along the entire length of the specimen (VX265 specimens), or it developed as a splitting crack along a strand (HVP260 and K400). The latter crack developed only horizontally along the strands positioned at a sufficiently high level in the rib. Otherwise, the splitting cracks grew from to strand to the nearest hollow core and the exposed soffit. At failure, a combined horizontal and vertical crack opened, and the strands were pulled out.

A combined shear and anchorage failure was observed in specimens in which the strands were positioned at mutually different levels in different webs. So, in ribs with highly positioned strands, a horizontal splitting crack through the web could develop and shear failure occurred, whereas in the other ribs no horizontal crack through the web developed and anchorage failure occurred.

In all cases, at failure, the cracks opened that had developed in an early stage of the fire. The crack patterns, as summarized in fig. 4.4, are driven by incompatible thermal elongations. Moreover, the slip development of the strands is driven by these thermal elongations. No significant increase of the slip occurs at the initiation of the vertical cracks.

### 4.6.2 Practice

In accordance with the tests discussed in the reviewed literature, shear and anchorage failure can prevail over flexural failure in HC slabs exposed to fire in a standard shear test set up under practical load levels ranging from 11-23 % of the actual load bearing capacity at ambient conditions, which corresponds approximately to 20-40 % of the design capacity at ambient conditions.

There seems to exist a critical load level above which the applied load in combination with the

incompatible thermal elongations causes failure within 60 minutes and one below which the specimen survives fire exposure of more than 90 minutes until failure occurs due to decreased mechanical properties at elevated temperatures. This behaviour was observed in tests leading to a combined shear and anchorage failure as well as in tests showing pure anchorage failure.

For the HVP260 specimens that showed a combined shear and anchorage failure, the critical shear load was found to be between 17-20 % of the actual ultimate shear load at ambient conditions as observed in the reference tests, which corresponds to 30-35 % of the design anchorage capacity at ambient conditions. It is likely that the critical load level depends on the type of slab and the position of the strands.

The critical load level is low compared to load levels that can be expected in practical fire design, ranging from 15-70 %. In practise the load level for fire design ranges from 40-70 % with respect to the limiting failure mode, but the shear and anchorage capacity are often not limiting the design for ambient conditions, leading to a lower load level with respect to these failure modes. This means that in practical design situations, shear and anchorage failure might dominate the fire behaviour. Therefore it is recommended to search for ways to strengthen the shear and anchorage capacity at fire exposure. However, on the basis of the fire tests presented in this chapter together with the fire tests discussed in the literature review, it is important to note that the critical load level is also affected by the support conditions and the thermal insulation of the slab over the transfer length of the prestress. In this respect, the critical load level mentioned above, could be considered as a safe lower bound as it corresponds to unrestrained specimens, loaded in a standard shear test set up, with no thermal protection of the support zone of the specimen.

In order to enhance the fire resistance of the HC slabs, axial restraining and filling the hollow cores with reinforced concrete at the end of the slab was investigated.

Axial restraining reduced the slip development and the propagation of vertical cracks perpendicular to the restrained direction. But horizontal cracking at the smallest web width was not limited, so these horizontal cracks are driven by thermal stresses in a different direction. For specimens in which these horizontal cracks occur, it is recommended to investigate the effect of restraint in the transverse direction.

The fire resistance was not increased by filling the cores with reinforced concrete. This was explained by the lack of composite action between the precast concrete and the concrete filling. The lack of bond between the filling and the precast concrete can be explained by mutual shrinkage differences. For future investigations into this measure, the use of low shrinkage concrete is recommended for the filling.

One way to enhance the shear and anchorage capacity of HC slabs at fire conditions is by modification of the strand position.

Shear failure can be caused by splitting cracks propagating horizontally through the web when the strands are positioned too high in the rib. Therefore it is recommended to position the strand sufficiently low, avoiding such splitting cracks.

### 4.6.3 Modelling

In order to quantify the shear and anchorage behaviour by means of numerical models, the models must take into account the thermal elongations and must include the post-cracking behaviour of concrete.

In order to predict the incompatible thermal elongations, a proper thermal gradient must be calculated. The thermal gradient must be determined on the basis of the averaged temperature measurements because the individual measurements are subject to too large scatters.

With respect to the crack development, the numerical models should be able to explain the horizontal crack development through the smallest part of the web at mid depth in the VX265 specimens. Furthermore, the numerical models must be able to calculate the splitting cracks and the effect of the splitting cracks on the confining action and the resulting bond strength.

The models should be capable of calculating the slip and prestress development under the effect of incompatible thermal elongations. The slip formulation should include an irreversible part in order to allow for a non-decreasing slip development under a decreasing incompatibility of the thermal strains.

The opening of flexural cracks might have increased to temperature distribution locally, which may be the cause of premature failure. It is recommended to further investigate the mutual interaction between cracking and heat flow and take this interaction into account in the modelling approach. However, such an approach is not developed in the scope of this thesis, see chapter 5.



# 5 Numerical modelling

## 5.1 MODELLED PHENOMENA

### 5.1.1 Shear and anchorage behaviour

As shown in the previous chapter, fire exposed HC slabs can not only exhibit bending failure but also shear and anchorage failure. The effect of incompatible thermal strains has to be taken into account as these strains cause cracks in the concrete webs and slip of the strands. The cracks play a very important role in the shear and anchorage behaviour of the fire exposed HC slabs, as the final shear crack in all cases followed the combined vertical and horizontal cracks. More precisely, the model must be capable of predicting the vertical cracks as observed in all HC specimens, the horizontal cracks in the VX265 specimens through the smallest web width and the splitting cracks around the strands.

In order to simulate the thermal stresses correctly, the concrete constitutive behaviour has to be accurate both in the compressive and tensile regime, taking into account non-linear effects.

In order to simulate the crack propagation during fire, the development of the prestress must be calculated accurately. This requires a proper simulation of the bond behaviour of the prestressing strands, including the effect of the cracks along the strands that were observed in the tests.

### 5.1.2 Bond behaviour

The bond behaviour of prestressing strands was treated in detail in chapter 3. The phenomena that are significant at ambient conditions are taken into consideration in the bond model, developed in the current project. These phenomena are:

- Increasing bond stress at increasing slip.
- Bond stress depending on diameter change of the strand, both in the elastic and the

plastic stage.

- Inclusion of pitch effect to cover both push in and pull out.
- Inclusion of confinement action by concrete cover and the effect of splitting cracks.
- Allowance for irreversible slip, to avoid a calculated slip reversal once the confinement action increases during maturing or once the thermal gradients vanish during fire.

For the description of the bond behaviour under fire conditions, it was pointed out in chapter 4, that the effect of incompatible thermal elongations should be considered as well as the decrease of mechanical properties of steel and concrete.

## 5.2 APPROACH

The response of HC slabs to fire exposure was modelled in the FE package DIANA in three consecutive steps, i.e. the thermal response of the cross section, the structural response of the cross section and the structural response of the entire slab, see fig. 5.1. First the thermal response is calculated with a potential flow analysis. The time dependent temperature profile over the cross section as calculated in the thermal response model, was prescribed in both models of the structural response.

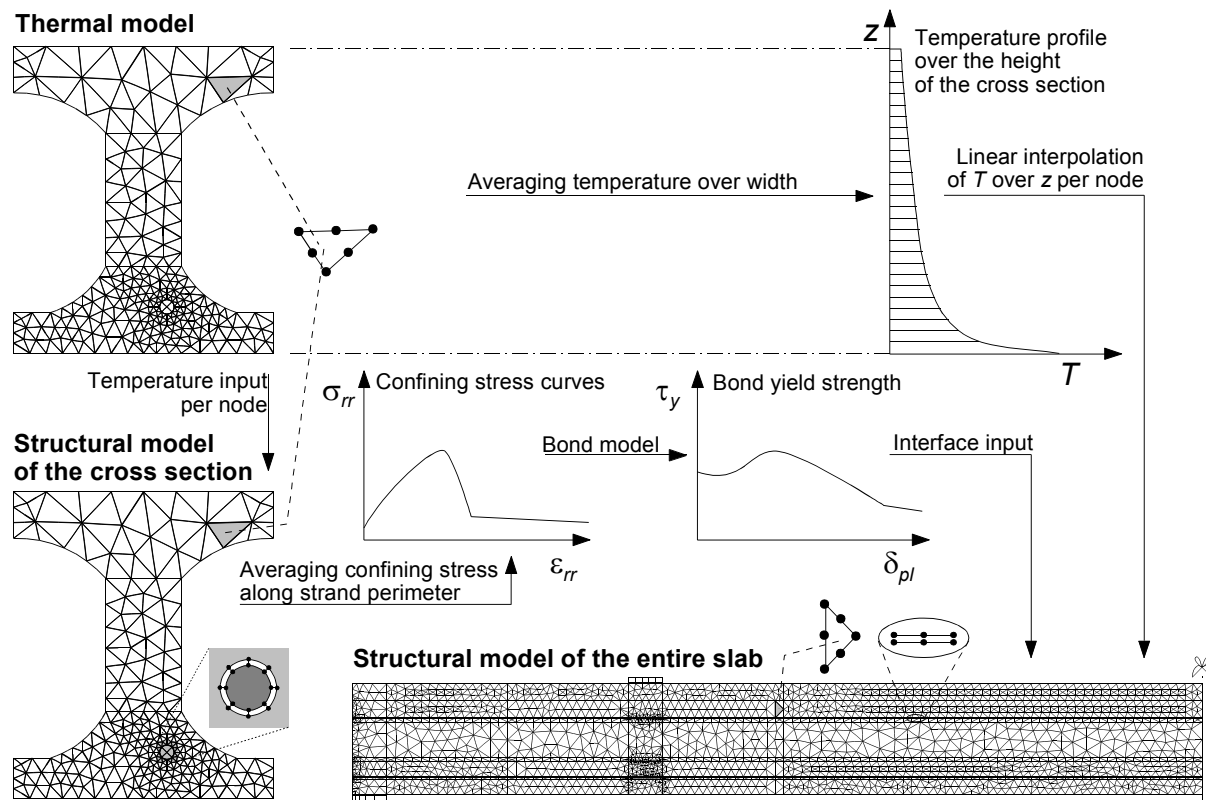


Figure 5.1: Overview of the modelling approach.

Within this approach, the deformations and damage calculated in the structural response models do not affect the thermal response model. In reality, moisture flows through the cracks affecting the heat flow through the slab and cracks might open so widely that substantial heat flow through the crack can occur, as discussed in the previous chapter. But these effects are neglected for sake of simplicity, which is in accordance with the guidelines for general calculation models in the structural Eurocodes.

Since the thermal gradient over the length of the slab is assumed to be small, the thermal response was calculated with 2D models of the cross sections. At first, the cross section was modelled with elements with four nodes and linear interpolation of the temperature field over the element between the nodes. With these models, a comparison was made between the temperature fields calculated on the basis of the measured temperatures along the edges of the cross sections and the fields based on the general boundary conditions of the ISO 834 curve at the exposed sides and of 20 °C at the unexposed sides, see chapter 7. Later on, the concrete of the cross section was meshed with triangular elements because these meshes could also be used for the calculation of the structural response of the cross sections, see fig. 5.1. Linearly interpolated boundary elements with two nodes were added to the mesh of the thermal response along the exposed and unexposed sides and at the inner side of the hollow cores. Linearly interpolated spring elements with two nodes were added to the mesh of the structural response between the strand and the concrete embedment. Both meshes used the same nodes. As a result, the temperature output of each node in the mesh of the thermal response could directly be transferred to the same node in the input file of the structural response calculation.

The triangular elements have six nodes, one in each angle and one in the middle of each side (the so-called mid-nodes). For the simulation of the thermal response, only the three nodes in the angles were used with a linear interpolation of the temperature field between the nodes. The temperatures of the mid-nodes were calculated afterwards by linear interpolation of the temperatures of the nodes in the angles. In doing so, the thermal strain field in the structural calculation varies also (almost) linearly over the element, since the thermal strain of concrete and steel is (approximately) proportional to the temperature. In the structural response calculation, the displacement field over the six nodes is quadratically interpolated, leading to a linearly distributed strain field, as the strain is the first derivative of the displacement field. In this way, the strain field is compatible with the imposed thermal strains.

For the transfer of the temperature field from the thermal response to the structural model of the entire slab, the calculated temperatures were averaged over the width of the cross section, leading to a (time dependent) temperature profile over the depth of the cross section. The temperature input for each node in the structural model of the entire slab was obtained through linear interpolation of this temperature profile on the basis of the vertical position of the nodes, see fig.5.1.

The first structural model is a 2D model of the cross section to simulate the development of the splitting cracks during fire exposure, the transverse cracks through the web at mid depth and the confining action of the concrete cover around the strand. In this model, the loading consists of a uniform expansion of the strand, leading to confining stresses and eventual splitting cracks. The sequence of load and time steps is discussed in §5.4.2.2.

The second model is a 2D model of the entire slab, with a varying thickness over the depth to

take into account the hollow cores with the reduced web thickness. In this model, the strands are modelled with quadratically interpolated truss elements that can only bear a normal force. The strands are connected to the concrete through quadratically interpolated interface elements with two rows of three nodes for which a new bond model was developed. The bond model accounts for the confining action of the concrete cover which was calculated in the model of the cross section, as is outlined in §5.4.2.

In the modelling approach a problem arises concerning the horizontal cracks that were observed in the tests. They might be caused by a combination of splitting and transverse shear stresses as calculated by the model of the cross section and horizontal shear stresses as calculated by the model of the entire slab resulting from the mechanical loading and the introduction over the slab depth of both the thermal stresses and the prestress.

In the two separate 2D models this combination of axial and transverse forces can not be calculated. For that purpose, a 3D model is needed, which was tried to develop. Moreover, with a 3D model, the effect of slip and change in steel stress on the confinement action of the concrete around the strand could be calculated directly. However, the development of the 3D model was not successful for two reasons. First of all, the number of elements needed is too large by far. As an indication, the 2D model of the cross section with acceptable accuracy contains already more than 500 elements. In the axial direction a mesh refinement is needed towards the end of the slab in order to properly calculate the introduction of the prestress. The maximum element length in the axial direction is limited to provide at least two integration points between each vertical thermal crack and by the maximum ratio between element length and width that the FE package permits.

Moreover, a short study with a 3D mesh of a slice of a slab between two vertical thermal cracks showed that convergence difficulties in a 3D mesh are even worse than in the 2D meshes. The plasticity model that proved to be relatively robust was only available for 2D elements. Therefore, it was decided to work with the two 2D models, despite of the drawbacks.

This chapter presents a detailed description of the modelling of the thermal response in §5.3 and of the structural response in §5.4.

For the thermal response, the basic potential flow features of the FE package DIANA were used allowing for a transient flow simulation on the basis of a temperature dependent heat capacity and conductivity, see §5.3.2. In addition to the basic features, a new software routine was developed to take into account the radiative and convective heat exchange in convex voids, in order to model the hollow cores, see §5.3.1.2. The thermal material's properties of the boundary elements were chosen in such a way that radiative heat exchange with the external temperature could be simulated with a time and temperature dependent convection coefficient, see §5.3.3.

In the simulations of the structural response, special attention was paid to the bond behaviour of the strands. For this purpose, a new bond model was developed that is presented in §5.4.2. It was originally based on the advanced model of Den Uijl, see §3.3.1.3. The bond model was applied to the interface elements between the strands and the concrete elements in the model of the entire slab. The bond behaviour depends on the confining action as calculated in the cross sectional model.

For both steel and concrete, thermal elongations and plasticity including hardening and softening were taken into account. For concrete, also cracking and transient creep were included. Moreover, the existing *Rankine-Drucker-Prager* plasticity model that covers cracking and

crushing within one plasticity model [DE WITTE: 1999], was extended with the effect of the loading history during fire exposure on the decrease of the mechanical properties, see §5.4.3.7. All properties were temperature dependent.

## 5.3 THERMAL RESPONSE

### 5.3.1 FE formulation

#### 5.3.1.1 General

The heat flow by conduction through a structure generally obeys Fourier's law of heat conduction. Combined with the conservation of heat within a body, the FE formulation used in DIANA [DE WITTE: 1999] reads

$$\mathbf{K}\theta + \mathbf{C}\frac{d\theta}{dt} = \mathbf{Q} \quad \{5.1\}$$

in which  $\mathbf{K}$  is called the conduction matrix,  $\mathbf{C}$  the capacity matrix and  $\mathbf{Q}$  the nodal discharge or external flux vector.

As the calculation of the thermal response of the construction exposed to fire is a transient phenomenon, eq. 5.1 is solved with an incremental iterative solution procedure. Starting with the known potential field  $\theta$  at time  $t$ , the time is incremented by  $\Delta t$ , and the new equilibrium is searched iteratively by direct time integration using a generalized trapezoidal rule. Eq. 5.1 is transformed using a modified conductivity matrix  $\mathbf{K}^*$  and a modified external flux vector  $\mathbf{Q}^*$  into

$$\mathbf{K}^*\theta = \mathbf{Q}^*$$

in which the modification of the conductivity matrix and the external flux vector depend on the time integration technique. In the underlying work a so-called implicit *Euler backwards* iteration scheme was adopted, which has first order accuracy without oscillations and numerical damping. For details of the solution procedure, reference is made to the DIANA manual [DE WITTE: 1999].

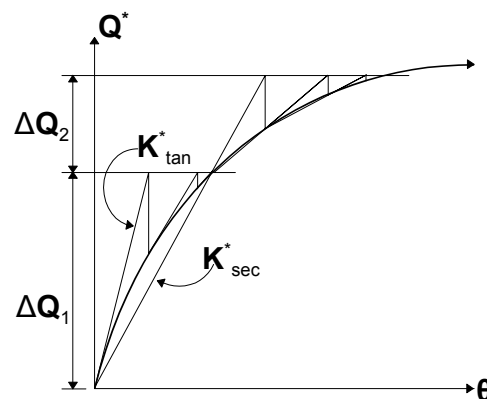


Figure 5.2: Incremental iterative procedure for deriving equilibrium in the FE heat flow analyses.

As the material's properties are temperature dependent, the potential field  $\theta$  at time  $t + \Delta t$  is found iteratively by updating the conductivity and the capacity matrix and the external flux vector every iteration as shown in fig. 5.2. As shown in this figure, the modified conductivity matrix can be considered as the predictor of the potential field. Either the tangential (*Newton* method) or secant (*Quasi Newton* method) conductivity can be used. The secant conductivity is simply obtained from the potential field of the previous iteration. The calculation of the tangential conductivity matrix consumes more time than the secant conductivity. However, a time step requires generally less iterations. In the underlying work, the *Newton* method was adopted as it appeared to be most time effective.

### 5.3.1.2 Voids

In structures containing voids, as for instance a core of a HC slab, heat will flow through the void through radiation and convection, see fig. 5.3. As shown in the previous paragraph, the flux can be prescribed at the boundaries in a FE model. However, in the case that the model contains a void, the flux at the inner side of the void is unknown.

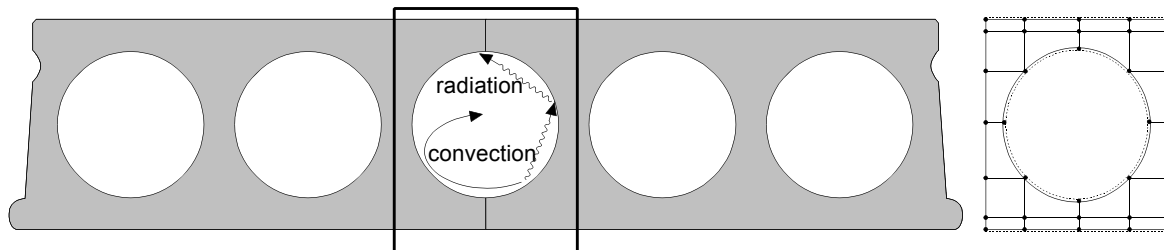


Figure 5.3: Example of a structure containing voids. Along the void surface, boundary elements are meshed (dashed lines in the mesh), to take radiative and convective heat transfer into account.

The flux can therefore not be prescribed but must be calculated by the programme. In order to allow for radiative and convective heat transfer through a void, the DIANA programme was extended with a module that calculates the fluxes inside the void on the basis of the surface temperatures.

The external flux vector of eq. 5.1 consists of three terms as

$$\mathbf{Q} = \int_V \mathbf{N}^T q_V dV + \int_S \mathbf{N}^T q_S dS + \int_S \mathbf{N}^T \alpha_{tot} \theta_E dS \quad \{5.3\}$$

Every iteration, the convective and radiative fluxes of each boundary element at the inner surface of the void are added to  $q_S$  of the external flux vector  $\mathbf{Q}$  as.

$$q_S = q_E + q_{con} + q_{rad} \quad \{5.4\}$$

in which  $q_E$  is the prescribed flux,  $q_{con}$  is the convective flux and  $q_{rad}$  is the radiative flux at the inner surface of the void. In this way, the heat transfer through the void effects only  $\mathbf{Q}$  in eq.5.1 and it does not contribute to the conductivity matrix  $\mathbf{K}$ . So, the prediction of the potential field within an iteration is not ideal as it neglects the effect of the void. As a consequence the convergence and stability of the calculation is not guaranteed, especially in cases where the void dominates the overall heat transfer. To minimize the disturbance of the void on the overall heat flow, the external flux vector  $\mathbf{Q}$  is updated every iteration. This formulation of the heat transfer

in voids proved to be satisfactory stable and accurate for structural applications, when combined with the implicit (*Euler backwards*) time integration and the use of the *Newton* method to derive the modified conductivity matrix.

In order to calculate the convective heat flux, one temperature of the medium inside the void was introduced as dummy degree of freedom. Thus, the temperature of the medium in the void is assumed to be uniform. The convective heat flux from an integration point of a boundary element at the inner side of the void to the medium of the void reads

$$q_{con,i} = \alpha_{con}(\theta_i - \theta_{void}) \quad \{5.5\}$$

For the sake of simplicity, it is further assumed that the heat capacity of the medium in the void can be neglected. This is justified as it is generally air. The heat capacity of air at room temperature is 1.2 kJ/m<sup>3</sup>K, which is approximately 1700 times smaller than the value of concrete. Furthermore it was assumed that the convective and radiative heat transfer inside the void are uncoupled. Thus the convective contributions of all finite surfaces inside the void equal zero.

$$\sum_i q_{con,i} A_i = 0 \quad \{5.6\}$$

This results for the temperature of the medium inside the void in

$$\theta_{void} = \frac{\sum_i A_i \alpha_{con,i} \theta_i}{\sum_i A_i \alpha_{con,i}} \quad \{5.7\}$$

Substitution of the latter equation in eq. 5.5 gives the desired convective heat flux per integration point.

The calculation of the radiative heat flux was based on Hottel's method [HOTTEL & SAROFIM: 1967]. The radiative flux from an integration point of a boundary element into the void is given by

$$q_{rad,i} = \frac{\epsilon_i}{1 - \epsilon_i} (\sigma \theta_i^4 - w_i) \quad \{5.8\}$$

in which  $\epsilon$  is the emission coefficient of the surface and  $\sigma$  is the Stefan-Boltzmann constant equal to  $5.677 \cdot 10^{-8}$ . The vector  $\mathbf{w}$  contains the gross ingoing fluxes obtained by

$$\mathbf{Rw} = \sigma \mathbf{Ap} \quad \{5.9\}$$

with the vector  $\mathbf{p}$  containing the temperatures to the fourth power of all integration points over the inner surface of the void:

$$p_i = \theta_i^4 \quad \{5.10\}$$

With the matrix  $\mathbf{A}$  reading

$$\begin{aligned} A_{ij} &= -A_i \frac{\epsilon_i}{1 - \epsilon_i} & i = j \\ A_{ij} &= 0 & i \neq j \end{aligned} \quad \{5.11\}$$

The matrix  $\mathbf{R}$  contains the radiative exchange factors, indicating the amount of radiative interaction between all finite surfaces at the inner surface of the void.

$$\begin{aligned} R_{ij} &= s_i s_j - \frac{A_i}{1 - \epsilon_i} & i = j \\ R_{ij} &= s_i s_j & i \neq j \end{aligned} \quad \{5.12\}$$

The mutual radiative exchange factors  $s_i s_j$  must be determined for every combination of two surfaces inside the void. These purely geometrical factors are given by the double integral

$$s_i s_j = \int_{A_i} \int_{A_j} \frac{\mathbf{n}_i \mathbf{r}_{ij} dA_i \mathbf{n}_j \mathbf{r}_{ij} dA_j}{\pi \|\mathbf{r}\|^4} \quad \{5.13\}$$

which is numerically solved for the 3D case. In this formula,  $\mathbf{n}_i$  is the normal vector pointing outwards the plane  $i$  with an area  $A_i$  and the vector  $\mathbf{r}_{ij}$  is the mutual distance between the planes  $i$  and  $j$ . For the 2D case it can be simplified to

$$s_i s_j = \frac{|AD| + |BC| - |AC| - |CD|}{2} \quad \{5.14\}$$

So it depends on the length of the lines  $|AD|$ ,  $|BC|$ ,  $|AC|$  and  $|CD|$  which are defined in fig. 5.4.

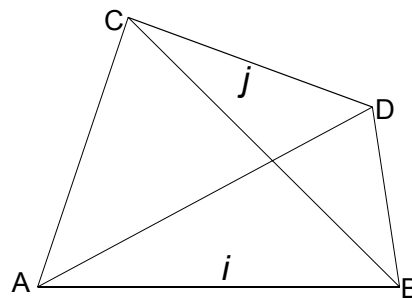


Figure 5.4: Definition of the lengths for the radiative exchange factor in the 2D case.

The radiative exchange factor  $s_i s_j$  equals the well known view factor  $\Phi$  of surface  $j$  to surface  $i$  multiplied by the surface area  $A_i$  and vice versa the view factor  $\Phi$  of surface  $i$  to surface  $j$  multiplied with  $A_j$ .

$$s_i s_j = \Phi_{ji} A_i = \Phi_{ij} A_j \quad \{5.15\}$$

### 5.3.2 Concrete and steel properties

The properties of concrete that have to be considered in the FE calculation of the thermal response are the thermal conductivity  $\lambda$  and the heat capacity per unit volume  $\rho c_p$ . The values used in the research were taken from Eurocode 2 [ENV 1992-1-2: 1995], see fig. 5.5 and 5.6. Throughout this thesis, the thermal properties of the old version of the Eurocode [ENV 1992-1-

2:1995] were used rather than the values of the current version [PREN 1992-1-2:2002], because, the adequacy of the old values were successfully demonstrated in an extensive research project concerning the fire behaviour of steel-concrete composite slabs in which a strong focus was put on the validation of the thermal models [BOTH: 1998].

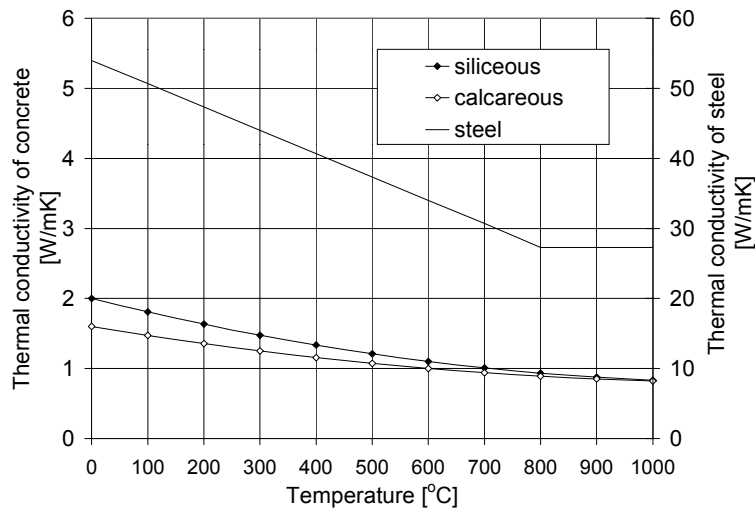


Figure 5.5: Thermal conductivity of steel and concrete of siliceous and calcareous aggregate.

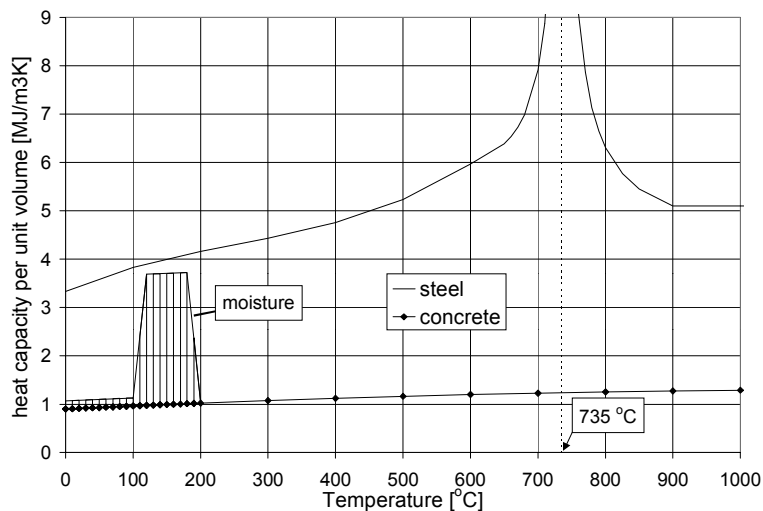


Figure 5.6: Heat capacity per unit volume of steel and concrete, including the effect of free moisture.

As pointed out in chapter 2, the properties of concrete strongly depend on the properties of the aggregate. Eurocode 2 makes a distinction between concrete with siliceous and calcareous aggregate, as far as the thermal conductivity is concerned. The Eurocode values were adopted throughout the research. The heat capacity of concrete is increased by free moisture. Up to 100 °C, the heat capacity of concrete is increased by the heat capacity of the free water. At 100 °C, the evaporation of the moisture has to be taken into account. In order to avoid numerical instability at 100 °C, the energy absorption by the evaporation of the free moisture was smeared out over a temperature range. This approach is justified by the increased boiling temperature of water at an increased pressure. An increased pore pressure can be expected when water thermally

expands and evaporates at elevated temperatures and the pressure can not be released through moisture flow quick enough through a dense concrete. In fig. 5.6 it was smeared out between 100-200 °C. The increase of the heat capacity by the moisture peak is calculated by

$$\int_{\theta_0}^{\theta_1} (c_p)_{moist} d\theta = \int_{\theta_0}^{\theta_1} (c_p)_{dry} d\theta + \omega U_e \quad \{5.16\}$$

In which  $\omega$  is the free moisture content in mass ratio [kg/kg] and  $U_e$  the energy needed to evaporate water,  $U_e = 2.26$  MJ/kg. Fig. 5.6 is based on a moisture content of 4 %.

### 5.3.3 Boundaries

At the boundaries of the mesh, boundary elements can be placed to define a mixed boundary condition, setting the relation between the flux into the structure and the external temperature.

For fire exposed structures, both convection and radiation contribute to the heat flux from the ambience to the structure as

$$\begin{aligned} q_S &= q_{con} + q_{rad} \\ &= \alpha_{con}(\theta_E - \theta_S) + \sigma \epsilon_{res}(\theta_R^4 - \theta_S^4) \end{aligned} \quad \{5.17\}$$

in which  $\alpha_{con}$  is the convection coefficient taking into account the convective heat transfer. According to Eurocode 1 [PREN 1991-1-2: 2002],  $\alpha_{con} = 25$  W/m<sup>2</sup>K at the fire exposed side. At the unexposed side  $\alpha_{con} = 8$  W/m<sup>2</sup>K was adopted. Furthermore,  $\sigma$  is the Stefan-Boltzman coefficient equal to  $5.677 \cdot 10^{-8}$  and  $\epsilon_{res}$  is the resulting emission coefficient. For concrete,  $\epsilon_{res}$  was taken equal to 0.7.

As the radiative heat flux is proportional to the temperature to the fourth power, this contribution dominates at high temperatures and has to be taken into account. However, the boundary elements in DIANA allow only for a convection coefficient. Therefore the combined convective and radiative heat flux through the boundary elements was taken into account by an artificial total convection coefficient as

$$q_S = \alpha_{tot}(\theta_E - \theta_S) \quad \{5.18\}$$

Substitution of eq. 5.18 into eq. 5.17 results in

$$\alpha_{tot} = \alpha_{con} + \sigma \epsilon_{res} \frac{\theta_R^4 - \theta_S^4}{\theta_E - \theta_S} \quad \{5.19\}$$

For the simulation of a standard fire test, the external radiation temperature  $\theta_R$  is taken equal to  $\theta_S$ . Thus  $\alpha_{tot}$  is a function of both the surface temperature  $\theta_S$  and the external temperature  $\theta_E$ . As the external temperature is a prescribed function of time, for instance the standard fire curve at the fire exposed side or a constant value at the unexposed side, an input table can be generated with  $\alpha_{tot}$  as a function of time and the surface temperature.

As an illustration, fig. 5.7 compares the artificial convection coefficient for radiative heat transfer

calculated on basis of an external temperature according to the standard fire curve with the convection coefficient that represents the real convection. In this graph it was assumed that the surface temperature either equals the external fire temperature (refer to ISO834 in the figure) or remains 20 °C during the entire fire exposure. These two assumptions are the extreme situations, as the real surface temperature will always be in between these two values. The figure shows clearly that the radiative heat transfer is significantly larger than the convective heat transfer within 5 minutes after the start of the fire, up to more than 10 times as large after 90 minutes in the case that the surface temperature equals the external fire temperature.

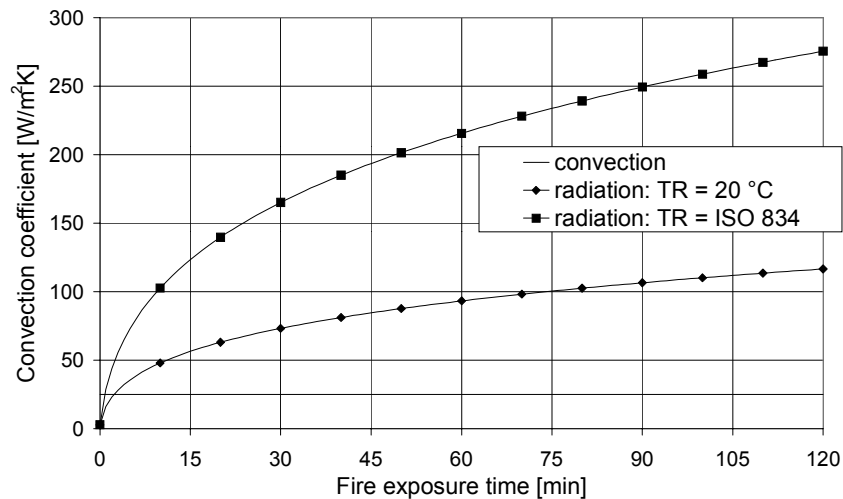


Figure 5.7: Comparison of the artificial convection coefficient for the radiative heat transfer with the convection coefficient on the basis of an external temperature according to the standard fire curve.

## 5.4 STRUCTURAL RESPONSE

### 5.4.1 Global FE formulation

In structural FE analyses, the unknown displacement field  $u$  must be calculated given the known volume forces  $\mathbf{g}$  and surface tractions  $\mathbf{t}$  on the boundary surface  $S_f$  and fulfilling the essential boundary condition that the displacement equals the specified value  $\bar{\mathbf{u}}$  at the boundary  $S_u$ .

In order to solve the problem, the structure is subdivided into separate elements. The elements provide the mutual relations between the displacements in the nodes, captured in the vector  $\mathbf{u}$ . DIANA applies the principle of virtual displacements to calculate the equilibrium between external loads and internal stresses [DE WITTE :1999]. Equilibrium is reached if the virtual work dissipated by the external forces equals the virtual strain energy for any admissible virtual displacement  $\delta\mathbf{u}$  from a compatible state of deformation. This results in the following system of equations:

$$\mathbf{K}\mathbf{u} = \mathbf{F} \quad \{5.20\}$$

In which  $\mathbf{K}$  is the stiffness matrix and  $\mathbf{F}$  is the external force vector. The system of equations of eq. 5.20 is solved using an incremental-iterative solution procedure. The principle is presented in fig. 5.8.

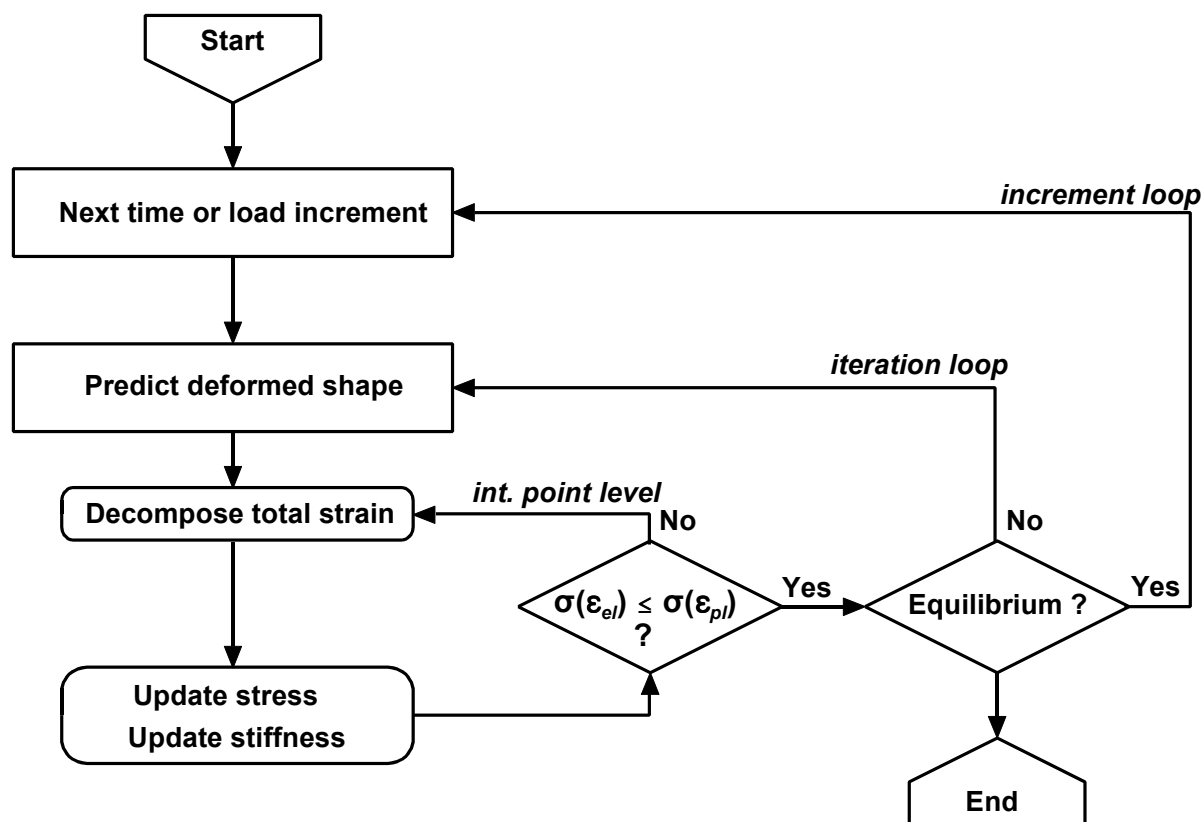


Figure 5.8: Principle of the incremental-iterative solution procedure.

Step 1 is to apply a load or time step to the structure. For a fire exposed structure a time step means a temperature increase, which has two effects. The thermal elongation is interpreted as an imposed deformation increment. Furthermore, the mechanical properties decrease at elevated temperatures.

Step 2 is to predict the deformed shape using some global stiffness. The global stiffness can be derived in several ways. As for potential flow analyses, a tangential stiffness or a secant stiffness can be used to derive a new displacement vector during the iteration process, see fig. 5.2. For the structural analyses, the tangential stiffness could successfully be used in analyses of structures at ambient conditions. For fire exposed structures, this iteration method easily failed. Therefore the secant stiffness was applied in this case, according to the so-called *BFGS* method, named after the developers Broyden, Fletcher, Goldfarb, and Shanno [DE WITTE: 1999].

Step 3 is to evaluate the stresses and strains on the basis of the predicted shape. In non-linear analyses, it means that the strains derived from the predicted shape are decomposed into an elastic and a plastic part and in case of fire analyses also thermal elongations and transient creep. The proper decomposition is carried out with an iterative process until one unique stress state is obtained that is in accordance with each strain component.

Step 4, finally, is the check of the global equilibrium. The stresses in each element are superimposed to the nodal forces and it is verified that these internal nodal forces balance the external forces. If no equilibrium is achieved, a next iteration is executed, in which step 2 to 4 are repeated, see fig. 5.8. Once equilibrium is reached, a next load or time increment is applied until the entire prescribed load or time path is followed.

## 5.4.2 Bond model

### 5.4.2.1 FE formulation

The bond model that was implemented in the FE package DIANA is based on the advanced model of Den Uijl that was discussed in §3.3.1.3. Similar to his model, the bond model implemented in DIANA is based on an adhesion-friction analogy. The bond strength is initially based on adhesion. While slip develops and the steel strain changes, the adhesion vanishes and bond stresses are transferred through frictional stresses. The ultimate frictional stresses are determined by the radial compressive stresses. These compressive stresses develop due to the lack of fit of the strand in the concrete embedment once the strand starts to slip and due to the Poisson contraction and the change of pitch of the strand once the steel strain changes. Both models relate the slip and the steel strain of the strand to a fictitious radial expansion of the strand. In both models the compressive stresses depend on the stiffness of the concrete cover and the eventual propagation of splitting cracks. However, Den Uijl used an axially symmetrical thick-walled cylinder model to determine the response of the concrete cover to the fictitious radial expansion. In the underlying bond model, the concrete confinement is calculated with the 2D model of the cross section, see fig. 5.9.

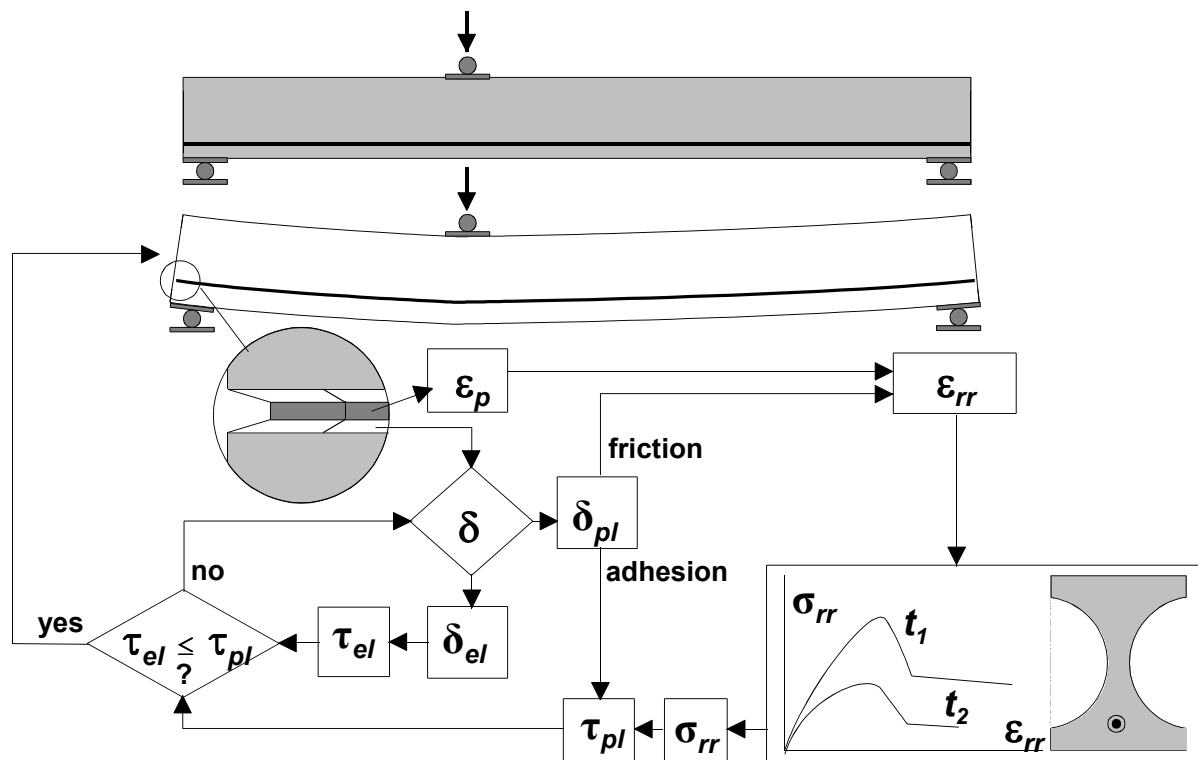


Figure 5.9: Overview of the bond model approach.

Contrary to the advanced model of Den Uijl, the bond behaviour in DIANA is described with an elastic-plastic slip formulation. So, the total slip is decomposed into an elastic and a plastic part. Moreover, compared to the model of Den Uijl, the FE model is extended with temperature dependent effects.

The bond model is applied to the interface elements between the strands and the concrete elements in the FE model of the entire slab, see fig. 5.9. In this model, the deformed shape is predicted on the basis of the load or time increment and some kind of model stiffness (for instance the stiffness of the previous step). From this deformed shape, the total slip in each interface element and the steel strain in the strand element adjacent to this interface element are obtained. Some basic model parameters relate the plastic slip and the steel strain to an fictitious radial expansion of the strand. In the model of Den Uijl, the total slip rather than the plastic slip was used in this respect.

In the cross sectional model, the confining compressive stress is separately calculated as a function of the fictitious radial expansion and the fire exposure time. This relation is used as input for the interface elements in the model of the entire slab. So, on the basis of the fictitious radial expansion of the strand, a compressive confinement stress is obtained. According to the friction analogy, this confining stress determines the frictional part of the bond strength. At the same time, the plastic slip determines the remaining contribution of the adhesion to the bond strength. The iteration process on integration point level is complete once the plastic bond strength equals the elastic bond stress during plastic flow. Below the mathematical formulations are given.

For the interface elements between the strand and the concrete, the total slip following from the predicted deformed shape must be decomposed into an elastic and a plastic slip.

$$\delta = \delta_{el} + \delta_{pl} \quad (a) \quad \{5.21\}$$

$$\Delta\delta = \Delta\delta_{el} + \Delta\delta_{pl} \quad (b)$$

The decomposition of the slip into an elastic and a plastic part can be calculated using a yield contour for the bond strength and introducing the hardening parameter  $\kappa_s$ . The hardening parameter  $\kappa_s$  is incrementally defined as

$$\kappa_s^{t+\Delta t} = \kappa_s^t + |\Delta\delta_{pl}| \quad \{5.22\}$$

This formulation leads to an always increasing value of the hardening parameter, irrespective whether the plastic slip is increasing or decreasing.

The yield function reads

$$f = |\tau| - \tau_y(\kappa_s) = 0 \quad \{5.23\}$$

The interpretation of this formulation for a loading cycle with increasing and afterwards decreasing slip is illustrated in fig. 5.10. Supposing a hardening diagram as given in the upper graph, a loading will result first in a linear elastic bond slip behaviour, until the equivalent stress corresponding to zero hardening is reached (1). Further loading will lead to plastic slip (2). If the loading is reversed after some plastic slip developed, elastic unloading will occur until the yield condition of eq. 5.23 is violated again (3). Further reversed loading will result in a decreasing plastic slip (4). Nevertheless, the hardening parameter  $\kappa_s$  still increases. Reloading will lead to an elastic increase of the slip until yield condition is violated again (5) and further loading leads to an increase of the plastic slip again (6).

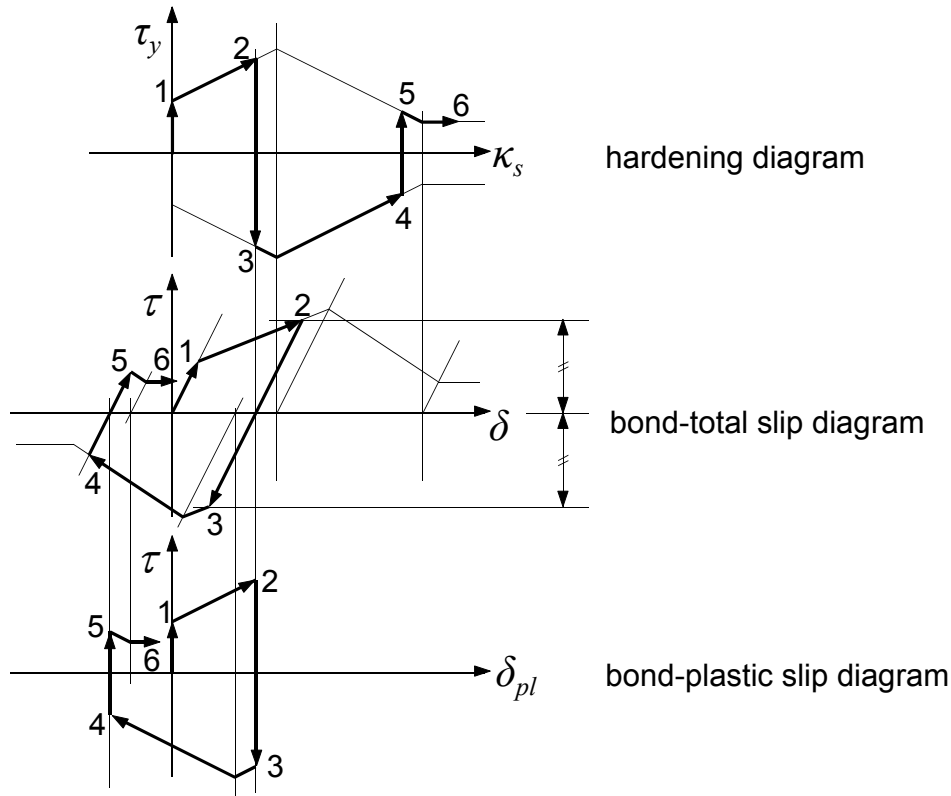


Figure 5.10: Principle of loading and unloading of elastic plastic bond model.

The yield contour of the bond strength is assumed to be a function of the confining action of the concrete around the strand. In fact a simple friction model is adopted introducing a dry friction coefficient  $\mu$ .

$$\tau_y(\kappa_s) = \tau_{ini}(\kappa_s) + \mu \sigma_{rr}(\kappa_s) \quad \{5.24\}$$

The initial bond strength  $\tau_{ini}$  decreases as a function of the hardening parameter

$$\tau_{ini} = \tau_0 \exp^{-c_{ini} \kappa_s} \quad \{5.25\}$$

In the advanced model of Den Uijl, this relation was used as well, to relate the adhesive part of the bond *stress* to the total slip rather than the adhesive part of the bond *strength* to the hardening parameter, which is the direct consequence of the introduction of the elastic-plastic bond formulation.

The radial stress perpendicular to the interface plane  $\sigma_{rr}$  is the response of the confining concrete to a radial expansion  $\epsilon_{rr}$ .

$$\sigma_{rr} = g(\epsilon_{rr}) \quad \{5.26\}$$

The concrete response to radial expansion is calculated using the FE model of the concrete cross section. A weak elastic interface layer is applied between the strand and the concrete, to avoid peak stresses around the strand that would disturb the calculation of the average compressive radial stress. Moreover, the compacting around the strand will never be perfect, leading to air inclusions and some spacing between the aggregate particles and the strand filled with relatively weak cement paste. The thickness and stiffness of this interface layer are two additional

parameters of the bond model that need calibration.

With the aid of the cross sectional model the bond strength can be calculated as a function of the radial expansion at any time during the maturing of concrete and during fire.

The next step comprises the relation between the slip and the steel stress or strain to the radial expansion strain. In order to take into account the lack of fit effect, the Poisson effect and the pitch effect, Den Uijl [DEN UIJL: 1998] suggested to calculate an fictitious radial expansion as

$$\epsilon_{rr} = \epsilon_{rr,lof} + \epsilon_{rr,v} + \epsilon_{rr,pit} \quad \{5.27\}$$

The radial expansion by the lack of fit effect is related to the plastic slip using the hardening parameter  $\kappa_s$ ,

$$\epsilon_{rr,lof} = c_{lof} \ln(c_{slip} \kappa_s + 1) \quad \{5.28\}$$

In the advanced model of Den Uijl, an exponential function was chosen. In the calibration process it appeared however, that the test results could better be predicted with the logarithmic function of eq. 5.28. Two calibration constants appear: the lack of fit coefficient  $c_{lof}$  and a slip coefficient  $c_{slip}$ .

The radial expansion by the Poisson contraction and the pitch effect are calculated on the basis of the strains in the strand element adjacent to the considered interface element.

If the axial steel stress changes, the Poisson effect results in a contraction of the strand in the radial direction. A positive steel stress change leads to a negative radial expansion and vice versa. The Poisson contraction of steel equals approximately 0.3 up to yielding. Once the strand yields, the straining in the radial direction dramatically increases up to the plastic straining in the axial direction but with opposite sign in the extreme case of ideal *von Mises* yielding without hardening. In that case, the radial expansion increases with more than a factor 3. However, hardening was actually included for steel.

DIANA calculates the transverse strain in the strand taking into account the effect of yielding and thermal expansion. The thermal expansion dominates the Poisson effect but it is already taken into account in the calculation of the response of the concrete cylinder. Therefore, the thermal strain must be subtracted from the total transverse steel strain to derive the radial strain that results into bond stresses. Furthermore, the change of the steel strain must be considered relative to the strain that is present at the moment the concrete was cast, so the initial contraction due to the prestressing must be subtracted from the total contraction resulting in

$$\epsilon_{rr,v} = c_v (\epsilon_{p,v} - \epsilon_{p,v,0} - \epsilon_{p,T}) \quad \{5.29\}$$

where  $c_v$  is a calibration constant. The contribution of the Poisson effect to the radial expansion can be positive or negative.

The second effect of a steel strain is the change in the pitch of the strand. According to Den Uijl, the change of pitch always leads to a positive radial expansion, irrespective to the sign of the steel strain change. During fire, the differential thermal elongation of the strand and the concrete will effect the change of pitch, but this effect is present in the slip already. Therefore, the thermal steel strain is excluded from the calculation of the pitch effect.

$$\epsilon_{rr,pit} = c_{pit} |\epsilon_p - \epsilon_{p,0} - \epsilon_{p,T}| \quad \{5.30\}$$

With  $c_{pit}$  a calibration constant and  $\varepsilon_p$  the total axial steel strain.

The overall derivation of the yield contour as function of the hardening parameter  $\kappa_s$  is shown in fig. 5.11. In (a) the relation is presented between  $\kappa$  and the radial expansion. The actual curve depends on the strains in the adjacent strand element. In (b), the response is schematically given of the confining concrete to a radial expansion as calculated on various times  $t$  with the cross sectional FE model. In (c), the results from (a) for steel strain  $\varepsilon_{pl}$  and (b) for time  $t_i$  are combined, leading to a relation between  $\kappa$  and the radial expansion. Finally in (d), the radial expansion stress is multiplied with the friction coefficient  $\mu$  and added to the initial bond strength  $\tau_{ini}$ , which decreases with increasing  $\kappa$ .

With the approach shown in fig. 5.11, the yield contour can be set up at every time during maturing and fire and for every steel strain. When the yield stress becomes negative (which can occur if the strand diameter decreases due to large plastic strains in the strand), the yield stress is set equal to zero.

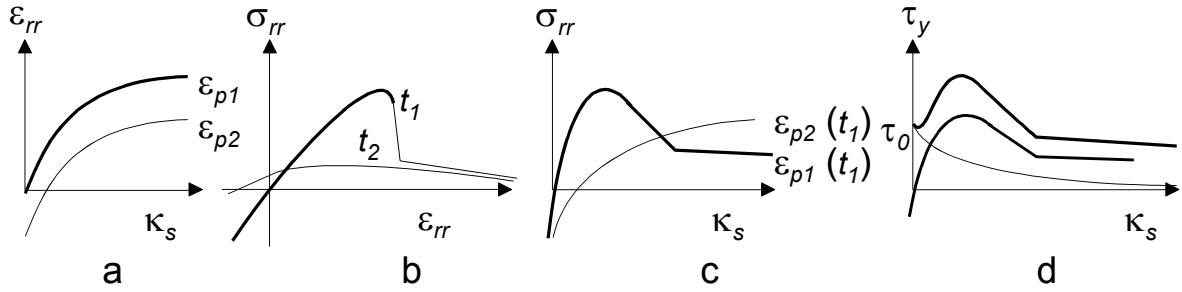


Figure 5.11: Overview of the derivation of the relation between the hardening parameter  $\kappa$  and the yield bond stress.

The bond stress at time  $t+\Delta t$  is calculated as

$$\tau^{t+\Delta t} = \tau^t + \Delta\tau \quad \{5.31\}$$

Introducing an elastic bond stiffness  $G_{el}$ , the bond stress increment relates to the elastic slip as

$$\Delta\tau = G_{el}\Delta\delta_{el} \quad \{5.32\}$$

Substitution of eq. 5.21, 5.31 and 5.32 into eq. 5.23, results in the following expression for  $\Delta\delta_{pl}$  which is solved with a default *Newton Raphson* iteration scheme.

$$\tau^t + G_{el}(\Delta\delta - \Delta\delta_{pl}) - \tau_y(t+\Delta t, \kappa_s^t + |\Delta\delta_{pl}|) = 0 \quad \{5.33\}$$

This iteration is conducted at an integration point level, within the global iteration loop.

The updated bond stress now reads

$$\tau^{t+\Delta t} = \tau^t + \Delta\tau = \tau^t + G_{el}(\Delta\delta - \Delta\delta_{pl}) \quad \{5.34\}$$

The updated tangential stiffness is calculated using 5.21 and 5.32 as

$$G_{tan}^{t+\Delta t} = \frac{\Delta\tau}{\Delta\delta} = G_{el} \left( 1 - \frac{\Delta\delta_{pl}}{\Delta\delta} \right) \quad \{5.35\}$$

An overview of the model parameters is given in table 5.1.

**Table 5.1** *Overview of the bond model parameters.*

Objective	Description	Symbol	unit
Radial expansion strain $\epsilon_{rr,tot}$	Lack of fit coefficient	$c_{lof}$	[-]
	Slip coefficient	$c_{slip}$	[mm <sup>-1</sup> ]
	Poisson effect coefficient	$c_v$	[-]
	Pitch effect coefficient	$c_{pit}$	[-]
	Interface spring stiffness in cross section	$K_i$	[N/mm]
	Concrete tensile strength	$f_{ct}$	[MPa]
	Fracture energy	$G_F$	[J/mm <sup>2</sup> ]
Bond strength $\tau_u$	Friction coefficient	$\mu$	[-]
	Initial adhesion	$\tau_0$	[MPa]
	Adhesion coefficient	$c_{ini}$	[-]
Elastic range	Linear shear stiffness	$G_{el}$	[MPa]

#### 5.4.2.2 *Radial expansion - heating path*

With the cross sectional FE model, the response of the confining concrete to radial expansion can be calculated at any stage during maturing and heating. The sequence of radial expansion, maturing and heating that a cross section of a HC slab undergoes in reality, consists of maturing - expansion by prestressing - further maturing - expansion by vertical loading - heating in fire. During prestressing and loading, some radial expansion occurs, due to slip and change of the steel stress. During heating and maturing a decrease respectively an increase of the mechanical properties occurs in addition to changes in slip and steel stress. Radial stresses develop during maturing and fire exposure due to shrinkage and thermal elongations respectively.

The amount of radial expansion by prestressing, vertical loading maturing and fire exposure depends on the location of the considered cross section along the strand. I.e. in the cross section at the end of the slab the change of the stress in the strand during prestressing varies from the initial prestress down to zero, accompanied with a large radial expansion. In a cross section at mid span, barely a stress change in the strand occurs during prestress release and consequently barely any radial expansion occurs.

As the sequence of the radial expansions due to prestressing, loading, maturing and heating is fundamentally unknown and varies mutually between the interface elements, an extensive series of calculations were calculated with the cross sectional model to provide input to the FE model of the entire slab for a wide range of possible sequences.

The series consisted of various steps. First a calculation of the concrete response during the beginning of the maturing phase (before prestressing) was made. Next the response to radial expansion of the slab at time of prestressing was calculated. The stress distribution over the cross section was saved for discrete values of radial expansion. For each of these saved states, the continuation of the maturing phase and the heating phase were calculated. Again the stress distribution over the cross section was stored for different durations of fire exposure. Finally, for each of these stored stress states the response to additional radial expansion was calculated, see fig. 5.12. In (a) the response of the confining concrete was calculated at various times during fire assuming that no expansion was applied during prestressing. In (b), the response was calculated at the same times during fire but now first some expansion during prestressing was assumed. Both sequences were calculated.

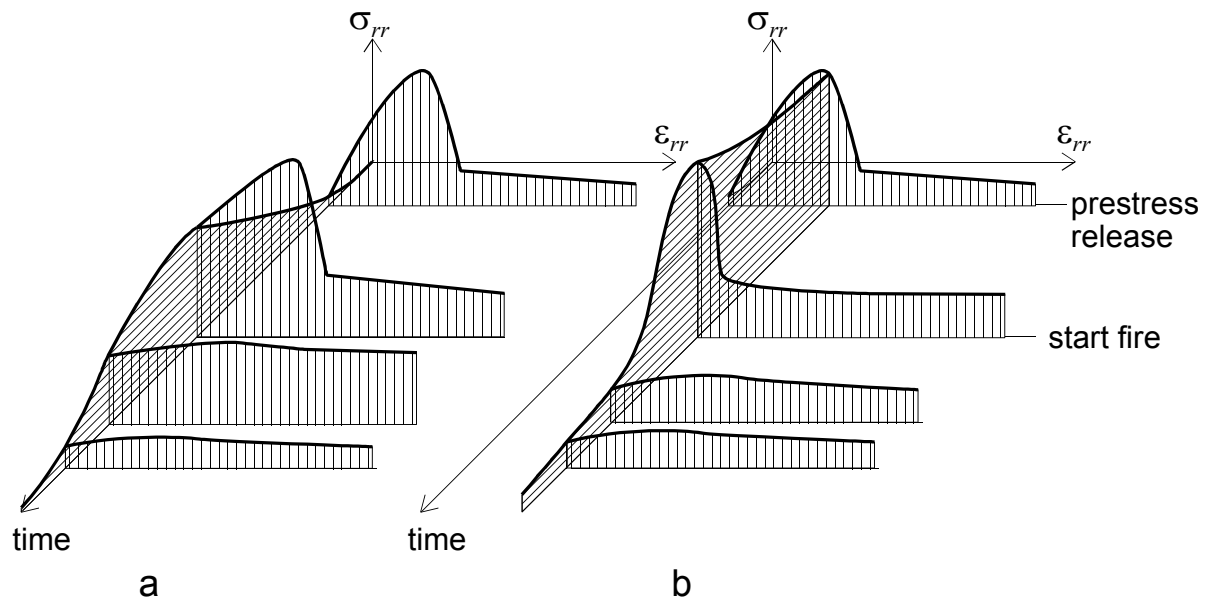


Figure 5.12: Sequence of the calculation of the radial expansion curves.

### 5.4.3 Concrete

#### 5.4.3.1 Strain decomposition

One of the major concerns in the modelling of the behaviour of fire exposed HC slabs is the proper choice of the constitutive model for concrete. During fire exposure, concrete shows a decrease in strength and stiffness accompanied with thermal elongation. Moreover, cracking and plastic straining in compression can occur, as well as transient creep during heating. Moreover, the concrete properties change during the time between the release of the prestress and the exposure to fire. I.e. during maturing, the strength and stiffness increases and shrinkage and creep strains develop. In general DIANA uses an incremental strain decomposition

$$\Delta \boldsymbol{\varepsilon} = \Delta \boldsymbol{\varepsilon}_T + \Delta \boldsymbol{\varepsilon}_s + \Delta \boldsymbol{\varepsilon}_{el} + \Delta \boldsymbol{\varepsilon}_{pl} + \Delta \boldsymbol{\varepsilon}_{cr} + \Delta \boldsymbol{\varepsilon}_{tr} + \Delta \boldsymbol{\varepsilon}_{crp} \quad \{5.36\}$$

The thermal strain  $\boldsymbol{\varepsilon}_T$  and the shrinkage strain  $\boldsymbol{\varepsilon}_s$  are independent of the stress state and can be considered as a kind of loading.

Cracks can be modelled by either discrete crack elements, smeared crack strains or equivalent plastic strains in DIANA.

With the discrete cracks, it appeared that only a *Newton Raphson* iteration scheme resulted in accurate stress patterns. In this iteration scheme, the actual tangential stiffness of the materials is used, which results in case of softening in negative stiffness terms. Combined with temperature influences divergency directly occurred. Secant iteration schemes use the positive secant stiffness and these are numerically stable but result in stress discontinuities between the solid elements and the discrete cracks. In the crack element the stress dropped after cracking to zero, but in the adjacent solid element the stress kept increasing. As a result far too high tensile stresses were calculated in the solids. Even at ambient conditions shear tension tests could not satisfactory be simulated with the discrete crack approach.

Using smeared cracks, one integration point could reach the stage of both cracking and plastic strains. The crack transforms the isotropic material into an orthotropic material, which disturbs the evaluation of plasticity that is based on isotropic material's behaviour. In the direction parallel to the crack unreliably high stresses were calculated. In general either divergency occurred or too extreme strains were calculated and only in rare cases the response of the cross section beyond 40 minutes fire exposure could be calculated. Moreover, the stability of the calculation could be destroyed with small changes in the mesh or the material's properties, which makes the model unsuitable for numerous simulations.

In the alternative formulation of plastic strains, cracking in tension was evaluated simultaneously with plasticity in compression, using the so-called *Rankine-Drucker-Prager* yield contour. This model is explained in the next paragraph. In principle, the plastic straining in tension rotates to the principal tensile stress, which makes it very similar to the rotating smeared crack concept. However, the solution procedures for the *Rankine-Drucker-Prager* model differs from the smeared crack approach. The *Rankine-Drucker-Prager* formulation, in combination with quadratically interpolated triangular elements appeared to be satisfactory in terms of numerical stability and was therefore used throughout this thesis.

The transient creep  $\epsilon_{tr}$  covers all creep effects during fire exposure as the creep during fire exposure is fairly independent of time.

The time dependent creep strains  $\epsilon_{crp}$  are only taken into account during maturing. It should preferably be taken into account using a visco-elastic creep model. However, visco-elastic models can not be combined with plasticity models in DIANA. Therefore, the time dependent creep during maturing was taken into account in an implicit way by modification of either the elastic strains  $\epsilon_{el}$  or the shrinkage strains  $\epsilon_s$ , depending on the application, see Appendix D.

So, the decomposition is reduced to an elastic, plastic and transient creep part, which is solved by requiring a unique stress state

$$\sigma(\epsilon_{el}) = \sigma(\epsilon_{pl}, \epsilon_{cr}) = \sigma(\epsilon_{tr}) \quad \{5.37\}$$

The relation between the elastic strain and the stress simply reads

$$\sigma = E_c \epsilon_{el}$$

The dependency of the stress to the plastic strains is explained in the next paragraphs. The relation between the transient creep and the stress is given in §5.4.3.5.

### 5.4.3.2 Rankine-Drucker-Prager plasticity model

In DIANA several *Rankine* plasticity models are available to simulate the simultaneous cracking and plastic behaviour of materials [DE WITTE :1999]. In these models cracking of concrete is simulated as yielding. Throughout this thesis, the *Rankine-Drucker-Prager* model in DIANA was used, which is limited to plane stress and plane strain analyses. In doing so, both yielding in compression and cracking in tension are treated with a yield surface. Once a yield surface is reached, a combined hardening/softening rule is followed.

The key difference between this model and a smeared cracking model is the fact that the material remains isotropic under all loading situations, which appeared to have a very positive effect on the numerical stability.

An associated flow rule was adopted for concrete, i.e. the dilatation angle equals the friction angle  $\varphi$ . Based on experiments on the bi-axial strength, a friction angle of  $10^\circ$  is recommended [DE WITTE: 1999]. In addition, the cohesion coefficient  $c_y$  has to be provided for the compression regime and the tensile yield strength  $f_{yt}$ . In order to transform the well known uni-axial stress-strain relations of concrete to these yield functions, the yield stresses have to be related to the strength properties of concrete and the hardening parameters to the concrete strain in the uniaxial case.

The peak value of the yield functions relate to the tensile and compressive strength as

$$\begin{aligned} f_{yt,\max} &= f_{ct} \\ c_{y,\max} &= -\frac{1 - \sin[\varphi]}{2\cos[\varphi]}f_c = -0.42f_c \Big|_{\varphi=10^\circ} \end{aligned} \quad \{5.39\}$$

The *Rankine-Drucker-Prager* model was used with a work hardening hypothesis. As a result, the hardening parameters relate to the principal plastic strains in the uniaxial case as [DE WITTE: 1999]

$$\begin{aligned} \kappa_t &= \epsilon_{pl,1} \\ \kappa_c &= -\frac{2\cos[\varphi]}{1 - \sin[\varphi]} \epsilon_{pl,2} \end{aligned} \quad \{5.40\}$$

In order to use this approach in the simulations of HC slabs under fire conditions, the hardening and softening rule had to be defined at elevated temperatures, see the next two paragraphs.

### 5.4.3.3 Tension

Two stress-strain curves for concrete in tension at elevated temperatures were used: with a linear and non-linear ascending branch. Concrete under tension is generally believed to behave linearly up to the peak stress just before cracking. Beyond the initiation of cracking a strong decrease in strength appears. However, at elevated temperatures, Felicetti and Gambarova [1999] showed that the stress-strain behaviour up to the peak stress is highly non-linear. Breunese [2001] showed that the differential thermal expansion between the cement paste and the aggregates causes this behaviour. Cement paste shrinks during heating while aggregate particles expand. A diffuse crack pattern develops through the cement paste during heating. If concrete is tensioned after heating,

all these small cracks start to open already at very low stresses and they grow towards each other. The tensile stresses increase until the cracks grew together into a fully propagated crack through the cross section. Hereafter, a localisation of deformation occurs in this large crack and the tensile stresses decrease again.

For his study, Breunese developed a FE model in DIANA that distinguishes between mortar and randomly distributed aggregate particles. He validated this model with the tests of Felicetti and Gambarova [1999] reasonably well. With his model he predicted the stress-strain curves at elevated temperatures of the concrete mix used in the calibration tests of next chapter, see fig. 5.13. In this prediction he took into account the aggregate-cement ratio and the type of aggregate. These curves were adopted in the concrete model in tension in the present study.

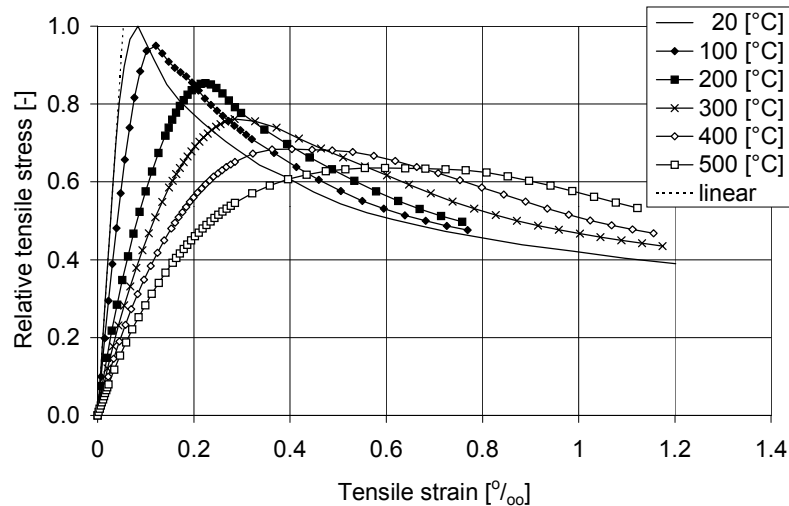


Figure 5.13: Stress-strain curves at elevated temperatures for the concrete mix used in the calibration tests described in the next chapter, derived with the FE model of Breunese [2001]

For the softening behaviour of concrete loaded in tension, a new approach was developed. Let us consider a concrete prism loaded in uniaxial tension. In the early stage, no localisation of deformation occurs, while the stress increases with increasing strain. The non-linear tensile strains increase over the entire length of the prism. Therefore, the axial strain can correctly be calculated as the total elongation divided by the length of the prism.

Up to the peak stress, the yield strength versus the hardening parameter was formulated as

$$f_{yt}(\kappa_t) = f_{ctp} + 2(f_{ct} - f_{ctp}) \frac{\kappa_t}{\kappa_{te}} - (f_{ct} - f_{ctp}) \left( \frac{\kappa_t}{\kappa_{te}} \right)^2 \quad \kappa_t \leq \kappa_{te} \quad \{5.41\}$$

Once the strength decreases with increasing strain, localisation of deformation will occur. The total elongation is now the sum of the rapidly increasing crack opening and the decreasing strain in the rest of the prism that unloads as the stress decreases. As a consequence, the strain can no longer be calculated by the total elongation divided by the length of the prism. Now, the total elongation must be subdivided into the crack opening in the localisation zone and the strain in the rest of the prism.

The crack opening that corresponds to zero stress is considered to be a material property, independent of the length of the prism. Thus, in a short prism the relative contribution of the crack opening to the total elongation is larger than in a long prism. In a long prism, the unloading

of the concrete outside the localisation zone can even give rise to snap back behaviour, i.e. the total elongation at crack initiation can be larger than after the crack fully opened.

In the plasticity model used in DIANA, the cracks are smeared out over the element, i.e. the crack opening is smeared out over the element length into crack strain. The crack strain is calculated as the crack opening divided by a representative element length. In order to obtain similar crack openings at zero stress independent of the element size, the stress-strain relationship has to be adapted to the element size.

In order to model the localisation of the deformation properly, the softening branch of the stress-strain diagram was modelled with a fracture energy based approach [HORDIJK: 1991]. It was assumed that the fracture energy does not change at elevated temperatures. Therefore, it was assumed that the softening branch at elevated temperature remains the same branch as used at ambient conditions.

The crack strain caused by heating will develop over the entire element without localisation and is therefore independent of the element size, see fig 5.14. After the peak stress is reached, a localisation zone will develop and the crack strain will grow further in the localisation zone only. In accordance to the results of Breunese [2001], it is now assumed that the decrease of the tensile strength at elevated temperatures is the result of internal cracking only. As a result, it is assumed that the crack opening in the localisation zone of heated concrete at peak stress corresponds to the crack opening in unheated concrete that is at an equal stress level in the cracked stage, see fig.5.14.

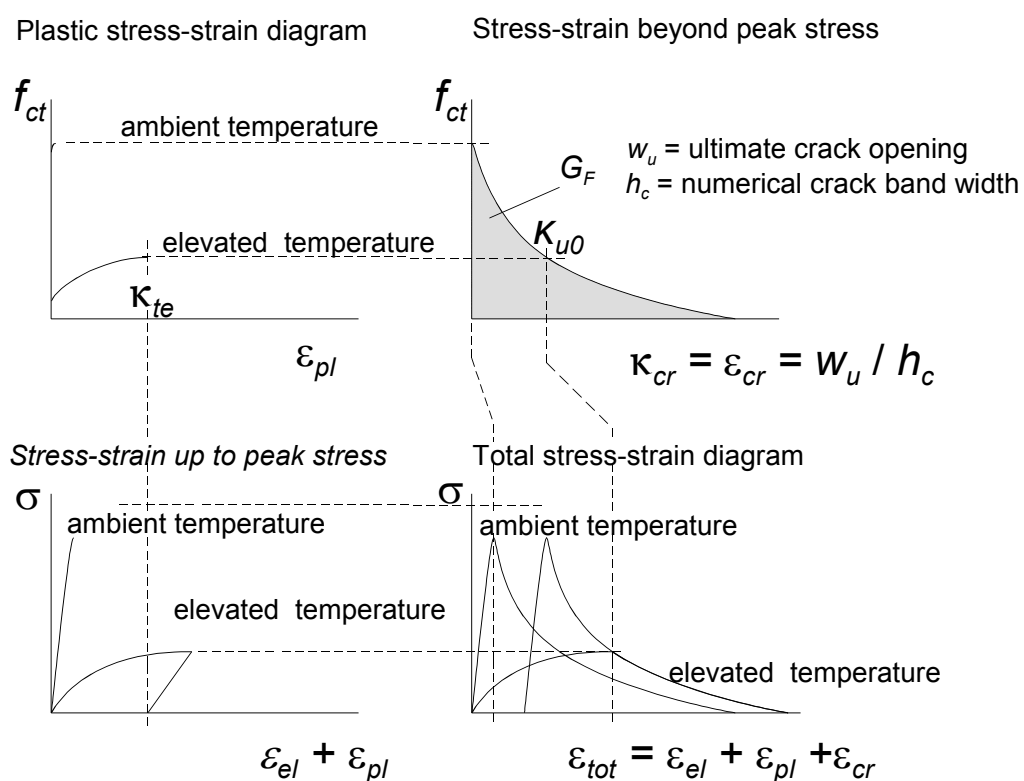


Figure 5.14: Approach for concrete in tension.

It is further assumed that the reduction of the tensile strength is the result of thermal damage, which also causes the non-linearity in the ascending branch of the stress-strain diagram. As a consequence, at elevated temperatures, the softening branch does not start at zero crack opening but at a crack opening  $\kappa_{u0}$  corresponding to the reduced tensile strength, see fig 5.14. The plastic stress-strain diagram and the softening diagram for cracked concrete are input properties. The total stress-strain diagram is deduced from these two diagrams. At ambient conditions  $\kappa_{u0}$  obviously equals zero, and the value increases up to unity if the tensile strength is reduced to zero. The values of  $\kappa_{u0}$  must be determined by inversion of stress-strain function of the descending branch, see eq. 5.43. Unfortunately the inversion has to be carried out iteratively, as the analytical solution of the inversion does not exist.

For the descending branch, a softening parameter was introduced as

$$\kappa_{cr} = \kappa_t - \kappa_{te} + \kappa_{u0} \quad \{5.42\}$$

Using this parameter, the softening rule according to Hordijk [1991] reads

$$f_{yt} = \left[ \left( 1 + \left( c_1 \frac{\kappa_{cr}}{\kappa_{tu}} \right)^3 \right) e^{-c_2 \frac{\kappa_{cr}}{\kappa_{tu}}} - \frac{\kappa_{cr}}{\kappa_{tu}} (1 + c_1^3) e^{-c_2} \right] f_{ct} \quad \kappa_{te} + d\kappa_{ro} \leq \kappa_t \leq \kappa_{tu} - \kappa_{u0} + \kappa_{te} \quad \{5.43\}$$

with the slope of the softening branch reading

$$\frac{df_{yt}}{d\kappa_t} = \left[ \left( \left( 3 - c_2 \frac{\kappa_{cr}}{\kappa_{tu}} \right) c_1^3 \frac{\kappa_{cr}^2}{\kappa_{tu}^2} - c_2 \frac{\kappa_{cr}}{\kappa_{tu}} \right) e^{-c_2 \frac{\kappa_{cr}}{\kappa_{tu}}} - (1 + c_1^3) e^{-c_2} \right] \frac{f_{ct}}{\kappa_{tu}} \quad \{5.44\}$$

The ultimate crack strain ( $\kappa_{tu}$ ) depends on the fracture energy  $G_F$  related to concrete in tension and the numerical crack band width  $h_c$ , which represents the representative length of the considered integration point of the element. In doing so, the cracking behaviour becomes mesh objective. Given the fixed values for  $c_1 = 3$  and  $c_2 = 6.93$ , it can be derived that

$$\kappa_{tu} = 5.136 \frac{G_F}{h_c f_{ct}} \quad \{5.45\}$$

In order to improve the numerical stability, the hardening diagram was smoothed at the peak stress. The descending branch according to eq. 5.43 starts with a very steep decrease in stress. A small parabolic curve was inserted between the ascending and the descending branch of height  $df_{ro}$  which reads

$$f_{yt}(\kappa_t) = f_{ct} - \frac{(\kappa_t - \kappa_{te})^2}{d\kappa_{ro}^2} df_{ro} \quad \kappa_{te} < \kappa_t < \kappa_{te} + d\kappa_{ro} \quad \{5.46\}$$

The slope of the round off curve at the intersection with the descending branch reads

$$\left. \frac{df_{yt}}{d\kappa_t} \right|_{\kappa_{te} + d\kappa_{ro}} = -2 \frac{\kappa_t - \kappa_{te}}{d\kappa_{ro}^2} df_{ro} \Big|_{\kappa_{te} + d\kappa_{ro}} = -2 \frac{df_{ro}}{d\kappa_{ro}} \quad \{5.47\}$$

The exponential softening curve according to Hordijk was scaled vertically by substitution of  $f_{ct}$  in eq 5.43 and 5.44 by  $(f_{ct} - df_{ro})$ .

The slope of the end of the parabolic curve was set equal to the initial slope of exponential softening branch, by adjusting the length of the round off curve  $d\kappa_{ro}$ . This was solved by further substitution of  $\kappa_{u0}$  for  $\kappa_{cr}$  in eq. 5.44, which resulted in

$$d\kappa_{ro} = - \frac{2}{\left( \left( 3 - c_2 \frac{\kappa_{u0}}{\kappa_{tu}} \right) c_1^3 \frac{\kappa_{u0}^2}{\kappa_{tu}^2} - c_2 \frac{\kappa_{u0}}{\kappa_{tu}} \right) e^{-c_2 \frac{\kappa_{u0}}{\kappa_{tu}}} - (1 + c_1^3) e^{-c_2}} \frac{df_{ro}}{f_{ct} - df_{ro}} \kappa_{tu} \quad \{5.48\}$$

In overview, the required input data to describe the entire stress-strain relation in the tensile regime are the temperature dependent tensile strength, the strain at peak stress and the Young's modulus, the fracture energy which is constant at elevated temperatures, and the arbitrary lower bound for the proportional limit.

#### 5.4.3.4 Compression

The shape of the uniaxial stress-strain diagram had to be chosen. No plasticity occurs under compression up to the proportional limit of the compressive strength  $f_{cp}$ . Hereafter, the hardening function according to Feenstra [1993] was taken:

$$c_y(\kappa_c) = - \frac{2\cos[\varphi]}{1 - \sin[\varphi]} \left( f_{cp} + 2(f_c - f_{cp}) \frac{\kappa_c}{\kappa_{ce}} - (f_c - f_{cp}) \left( \frac{\kappa_c}{\kappa_{ce}} \right)^2 \right) \quad \kappa_c < \kappa_{ce} \quad \{5.49\}$$

$$c_y(\kappa_c) = - \frac{2\cos[\varphi]}{1 - \sin[\varphi]} f_c \left( 1 - \left( \frac{\kappa_c - \kappa_{ce}}{\kappa_{cu} - \kappa_{ce}} \right)^2 \right) \quad \kappa_{ce} \leq \kappa_c < \kappa_{cu}$$

The principal is illustrated in fig. 5.15. The assumption for the strain at the peak stress depends on the way transient creep was taken into account, see next paragraph.

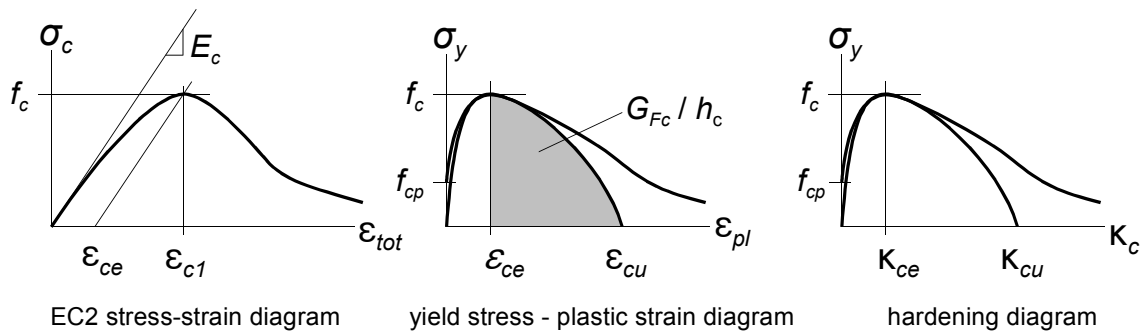


Figure 5.15: Transformation of the stress - strain relation according to Eurocode 2 [PREN 1992-1-2: 2002] into a yield stress- plastic strain relation.

Once the strains increase beyond the strain at peak stress, softening occurs with localisation of deformation. In order to be mesh objective, a fracture energy based approach was adopted. In doing so, the behaviour under compression after reaching the peak stress is mesh objective. The energy dissipates over the element from the strain at peak strength up to the ultimate strain at zero strength equals the fracture energy. The ultimate hardening value thus reads

$$\kappa_{cu} = \kappa_{ce} + \frac{2 \cos[\varphi]}{1 - \sin[\varphi]} \frac{3}{2} \frac{G_{Fc}}{f_{c,20} h_c} \quad \{5.50\}$$

The compressive fracture energy normally ranges between 10 and 25 kJ/m<sup>2</sup> [FEENSTRA:1993]. In the analyses, a constant value of 20 kJ/mm<sup>2</sup> was adopted. The sensitivity of the behaviour of the HC slabs to the compressive fracture energy is limited as will be shown in chapter 8.

#### 5.4.3.5 Transient creep

Two models were used for the transient creep throughout the thesis. The effect of the model on the shear and anchorage behaviour of HC slabs at fire conditions is demonstrated in chapter 8. The stress-strain curves of the Eurocode 2 [PREN 1992-1-2: 2002] were used, which include the transient creep strains implicitly. So, in this case, the transient creep was taken into account as an additional plastic strain.

Alternatively, a separate transient creep model was used in addition to the plasticity model. The transient creep can be considered as a function of the stress level and the temperature increase, and independent of time, see chapter 3. This transient creep model, which is also available in DIANA, was applied. This model uses an incremental formulation for the transient creep vector, reading as

$$\Delta \boldsymbol{\varepsilon}_{tr} = \frac{k_{tr} \alpha_T}{f_{c,20}} \Delta \theta \boldsymbol{\sigma} \quad \{5.51\}$$

So, the transient strain increment is aligned with the stress vector. As a measure for the total transient creep, DIANA calculates the equivalent transient creep on the basis of the principal shear stress  $\tau_p$ , which is invariant of the orientation, as

$$\boldsymbol{\varepsilon}_{tr,eq} = \frac{\int_{\theta_0}^{\theta_1} \alpha_T \tau_p d\theta}{1 + \nu} \frac{k_{tr}}{f_{c,20}} \quad \{5.52\}$$

#### 5.4.3.6 Thermal elongation

The thermal strain is proportional to the rise of the temperature

$$\Delta \boldsymbol{\varepsilon}_T = \alpha_T \Delta T \quad \{5.53\}$$

which is uniform in all directions.

As outlined in chapter 2, the coefficient of thermal elongation of concrete is mainly determined

by the type of aggregate. Eurocode 2 [PREN 1992-1-2:2002] distinguishes siliceous and calcareous aggregate. In fig. 5.16, the thermal strain is given as a function of the temperature. For the sake of comparison, the thermal elongation of prestressing steel was also included and the assumed thermal expansion for the concrete mix used in the calibration tests of chapter 6, that was derived by linear interpolation assuming  $2/3$  part siliceous and  $1/3$  part calcareous aggregate.

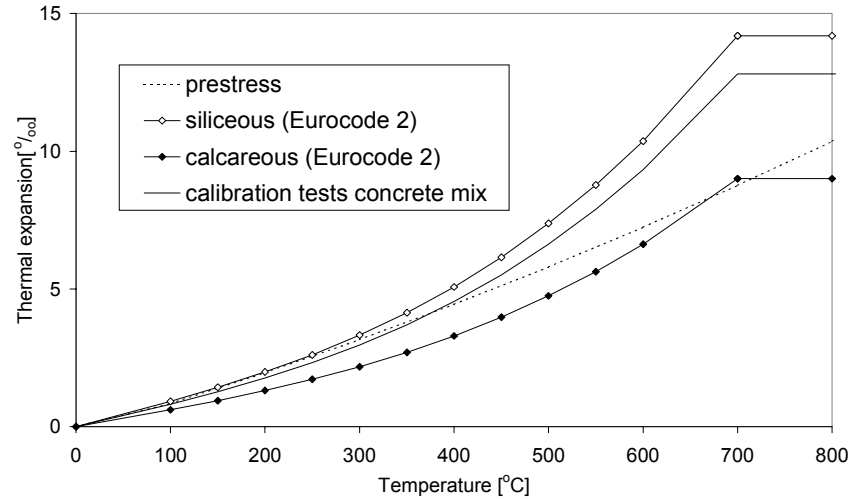


Figure 5.16: Thermal elongation at elevated temperatures of prestressing steel, concrete with siliceous or calcareous aggregate according to Eurocode 2 [PREN 1992-1-2: 2002] and the concrete mix used in the calibration tests.

#### 5.4.3.7 Loading history

In combination with the above approximation for the transient creep, the compressive strength and the strain at peak stress was made dependent of the compressive loading during heating. A problem arises in the extension of the observed strength increase under load in uni-axial tests to a 2D formulation. For this purpose, the load level was set equal to twice the ratio between principal shear stress and the compressive strength, because two times the principal shear stress equals the compressive stress in the uniaxially loaded case.

Furthermore, in the tests that demonstrated the increased strength of specimens loaded during heating [ABRAMS: 1971, PURKISS & BALI: 1988, SCHNEIDER: 1988], the load level was kept constant during heating, so no data could be found for the strength increase under variable compressive loading. As an approximation, the average stress over the temperature domain was applied. The load level was calculated using the equivalent transient strain. By integration of eq. 5.53 and combination with eq. 5.52, the load level during heating can be expressed as

$$\eta = \frac{\int_{\theta_0}^{\theta_1} 2\tau_I d\theta}{f_{c,20} \int_{\theta_0}^{\theta_1} d\theta} = 2 \frac{1+\nu}{k_{tr}} \frac{\epsilon_{tr,eq}}{\epsilon_T} \quad \{5.54\}$$

For the Young's modulus the value of compressed concrete during heating at a load level of 0.3

was taken, see fig. 3.9 on page 66. A decrease of the Young's modulus was taken into account using an increased strain at peak stress if the concrete remains unloaded during heating according to fig. 3.5 on page 63. For load levels higher than 0.3, the strain at peak stress corresponding to a load level of 0.3 was used.

The compressive strength was increased with the load level in accordance with fig. 3.4 on page 63. The compressive strengths found by various researchers was compared for different load levels, see fig. 5.17. On basis of this comparison the strength increase was defined as

$$\alpha_f = 1 + \eta \frac{\theta - 20}{780} \quad \{5.55\}$$

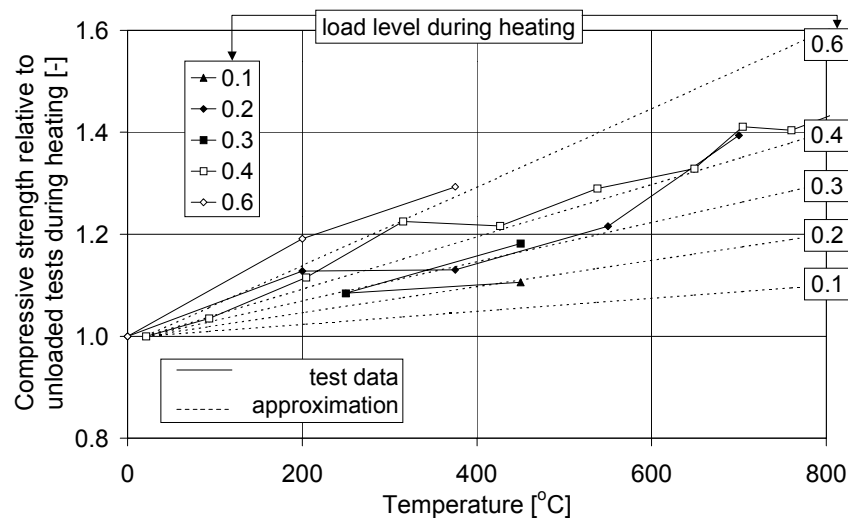


Figure 5.17: Approximation of the strength increase due to a compression during heating, based on test data presented in fig. 3.4.

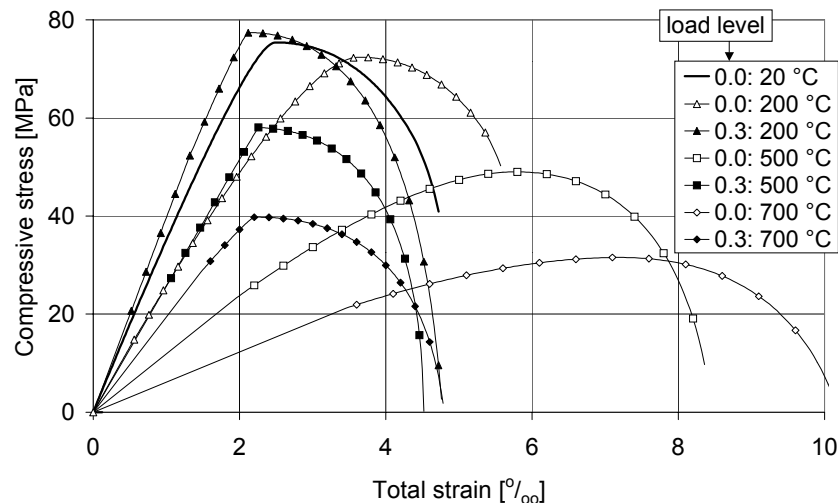


Figure 5.18: Simulated compressive stress-strain curves of concrete at elevated temperatures, depending on the load level during heating.

In fig. 5.18, the resulting curves are given for the stress-strain behaviour of concrete at elevated temperature. The figure distinguishes between zero load during heating and a compressive load of 0.3 relative to the ambient compressive strength during heating. In the figure, the total strain was shifted such that the stress-strain curve starts in the origin once loaded to failure, i.e. the thermal and transient strains at this point were subtracted from the total strain.

In summary, the strain at the peak stress and the increase in stress due to a compressive loading during heating are declared in the model. The decrease of the Young's modulus and the decrease of the compressive strength of unloaded concrete are free input values, which can be adapted to measurements or a given concrete composition.

#### 5.4.3.8 *Maturing assumptions*

During maturing, the strength and stiffness of concrete increase. Furthermore, shrinkage and creep strains develop. In order to distinguish between the concrete strength at the age of the release of the prestress and at the time of fire testing, the maturing of concrete was taken into account according to the Model Code [CEB-FIP: 1991] and the FIB Bulletin 1 [FIB: 1999]. As there are no test data available of the fire test specimen to validate the maturing assumptions, it is by no means intended to pretend accurate results for the effect of maturing. The Model Code notes that the coefficient of variation between the formulae and a test database is as high as 35 %. Nevertheless, it was realised that the response of the confining concrete to the radial expansion of the strand is significantly different at the time of the release of the prestress than at the time of fire testing. Therefore, the maturing effects were taken into account, including changes in the strength and stiffness as well as shrinkage and creep effects. A detailed description of the maturing assumptions is given in appendix D.

In DIANA, the strength and stiffness can not simultaneously be dependent on temperature and time. Therefore, the time that elapses during maturing was converted into a fictitious temperature rise of 100 °C from -80 to 20 °C. The strength and stiffness increase fictitiously from -80 to 20 °C simulating maturing effects, and continue with the appropriate decrease beyond 20 °C for the simulation of the fire exposure.

Shrinkage values were obtained from the FIB Bulletin 1 [FIB: 1999]. Creep strains in compression and tension were taken into account in an approximated way, because DIANA does not allow for the combination of a creep model and a plasticity model. Altoubat and Lange [2001a,b] showed that the shrinkage strains in restrained concrete are counteracted by tensile creep strains, which are of an order of 50-60 % of the shrinkage strains irrespective to the  $w/c$  ratio of the concrete and the relative humidity during maturing. Moreover, the ratio of the creep to shrinkage strains is approximately constant during the entire maturing phase. So, for concrete mainly loaded in tension during maturing, the creep could be considered by a reduction of the shrinkage strains. Creep under compression was approximated with a fictitious transient creep over the temperature domain from -80 to 20 °C, which represents the maturing period, see appendix D.

## 5.4.4 Steel

### 5.4.4.1 Thermal elongation

The thermal elongation according to Eurocode 2 [PREN 1992-1-2: 2002] was used. Figure 5.16 on page 135 shows the increase of the thermal elongation with elevated temperatures.

### 5.4.4.2 Strength and stiffness

For prestressing steel a commonly used *von Mises* yield contour was applied including hardening according to the elliptic stress-strain formulation of Eurocode 2 [PREN 1992-1-2: 2002]. The decrease of the strength and stiffness at elevated temperatures was shown in fig. 5.20. The Eurocode 2 simply assumes that the plastic straining starts from the 0.2 % proof stress on. Obviously, this is principally incorrect, as the 0.2 % proof stress is defined as the stress corresponding to 0.2 % plastic strain. However, the error is small and the Eurocode was followed throughout the thesis.

A Young's modulus at ambient conditions of 195 GPa was adopted. This results in the stress-strain relations at elevated temperatures of fig. 5.19.

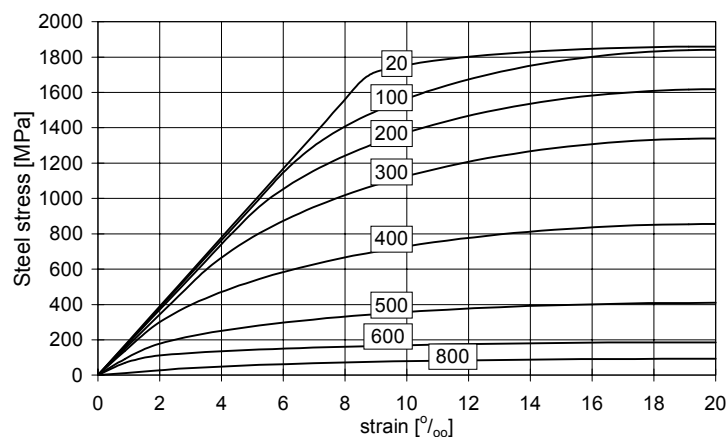


Figure 5.19: Stress-strain diagram for cold worked prestressing strands, assuming a strength of 1860 MPa at 20 °C.

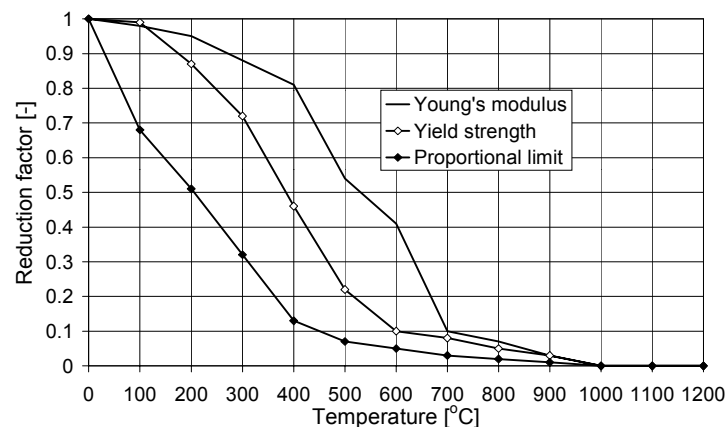


Figure 5.20: Reduction factors for strength and stiffness of cold worked prestressing steel.

# 6 Calibration of the model

## 6.1 CALIBRATION TESTS

### 6.1.1 Objective

The objective of the tests presented here is to calibrate the model parameters of the constitutive bond model that was implemented in the FE model. The model was described in §5.4.2 on page 121. An overview of the model parameters was given in table 5.1 on page 126.

The bond model is based on an adhesion-friction analogy. Although the initial adhesion might have an important effect on the bond behaviour at ambient conditions, it is of minor importance for fire exposed HC slabs. After all, it vanishes with increasing slip and large slip values were measured in the fire tests, as described in chapter 4. So, during fire the bond strength mainly consists of friction, which is determined by the friction coefficient and the confining stress curve. The confining stress curve depends on the development of the splitting cracks that arise during fire. The confining stress is determined by the fracture energy of concrete rather than any other concrete property, once these splitting cracks are formed. The sensitivity of the confining stress curves to the fracture energy and other mechanical properties of concrete is demonstrated in fig. 6.1. The curves in this figure were calculated using the thick-walled cylinder model [DEN UIJL & BIGAJ: 1996], assuming a concrete cover of 40 mm, a 12.5 mm strand, a bi-linear softening relation for cracked concrete and the development of three splitting cracks. In each picture, the reference case is given. This case was based on a tensile strength of 4.5 MPa, a fracture energy of 120 J/m<sup>2</sup> and a Young's modulus of 45 GPa. Other concrete properties such as the Poisson contraction of concrete and the ultimate crack opening have a smaller influence than the ones given in fig. 6.1. The number of splitting cracks influence the confining stress in

the cracked stage. The number of splitting cracks is hard to predict correctly in the axial symmetric case. However, the number of splitting cracks around the strands in the HC slabs depends on the geometry of the concrete cover and the position of the strand in the cross section and can therefore be predicted correctly in HC cross sections.

Moreover, the figure shows that the confining stress is relatively independent of the actual radial expansion once splitting cracks have formed. As a result, the parameters relating the steel stress and the slip to the radial expansion have a minor influence on the bond behaviour in this stage.

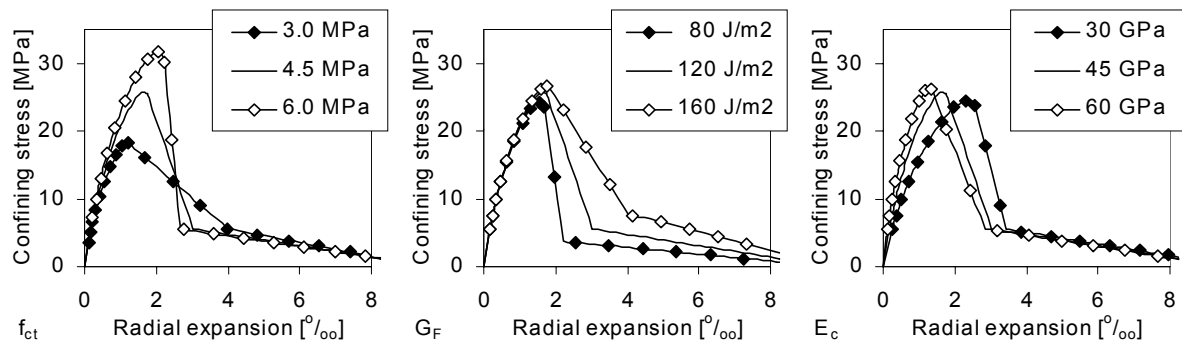


Figure 6.1: Confining stress curves depending on the tensile strength  $f_{ct}$ , fracture energy  $G_F$  and Young's modulus  $E_c$  of concrete.

Fig. 6.1 further shows that the tensile strength dominates the peak value of the confining stress curve. So, the tensile strength has an effect on the occurrence of splitting cracks. The tensile strength has also an effect on the development of the vertical thermal cracks and on the cracking moment capacity. In this respect, the tensile strength might have a substantial effect on the shear and anchorage behaviour. Moreover, the tensile strength of concrete needed to be determined in the calibration process anyway, as will be explained in the next paragraph.

On the basis of available research data, the dominant model parameters can be estimated at ambient conditions, see chapter 3. But the development of the friction coefficient and fracture energy at elevated temperatures is unknown and the decrease of the concrete tensile strength at elevated temperature is subjected to large variations according to literature data, see chapter 3. It depends for instance on the actual concrete mix.

Therefore, the calibration of the bond model concentrates on the fracture energy and tensile strength of concrete and the friction coefficient of the interface. The calibration tests were carried out at elevated temperatures. All bond model parameters were calibrated with these tests. However, in the calibration process, the variation of the above mentioned main model parameters was minimised.

The tests had to be carried out at uniform elevated temperatures in order to avoid errors due to thermal stresses. Furthermore, the specimens had to be heated at a sufficiently low rate in order to prevent damage due to thermal stresses during heating, see §6.1.3.3.

## 6.1.2 Approach

The test set up of the experiments and the corresponding simulation models are shown in fig. 6.2. Also, the calibration sequence is indicated in this figure. Each test was simulated with the corresponding FE model in order to calibrate the bond parameters. An overview of the number of calibration tests at each elevated temperature is given in table 6.1.

First, the splitting force was measured in the Brazilian splitting tensile test. The tensile strength of concrete was deduced not only using a standard relation [NEN 5969: 1997] between the splitting force and the tensile strength but also using the FE model of the splitting test, in order to determine the effect of the non-linear stress-strain behaviour on the predicted splitting force. Then, the confining stress as a function of the radial expansion was measured in the pull through test. With the confining stress curve and the tensile strength obtained in the splitting tests, the fracture energy of concrete could be deduced. Finally, the friction coefficient of the embedded strands was determined on the basis of the pull out tests using both the obtained tensile strength and the fracture energy.

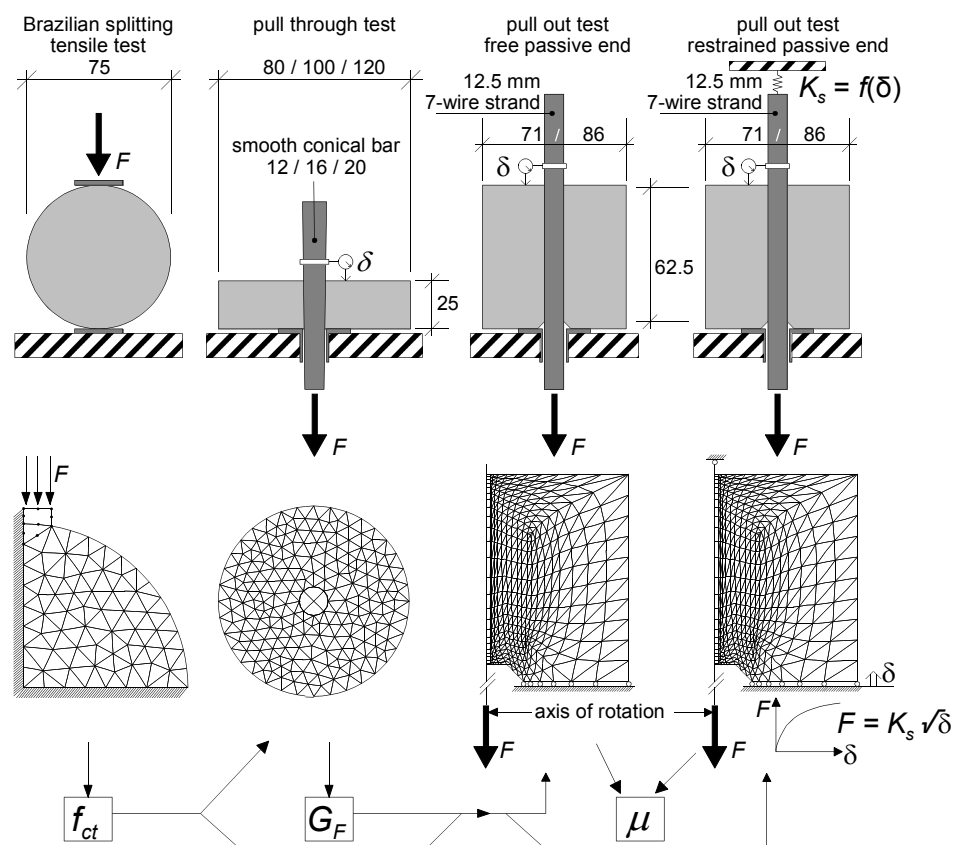


Figure 6.2: Overview of the types of specimens used in the calibration tests.

In the pull through test a smooth conical bar is pulled through a thin concrete cylinder in which a smooth conical hole was cast in the centre. When the bar is pulled through the cylinder, it directly imposes a radial expansion on the concrete cylinder. The measured pulling force directly relates to a bond stress assuming an uniform bond stress distribution over the interface surface. The bond stress can be related to the confining stress by the friction coefficient for the conical

bar. As this bar is very smooth due to polishing, it is assumed that the friction coefficient is constant over the pulling length. This friction coefficient can be determined by comparison of the peak value of the bond stress with the calculated peak value of the confining stress on the basis of the calibrated concrete tensile strength, since the peak value of the confining stress depends almost exclusively on the concrete tensile strength, see fig. 6.1. After fixing the friction coefficient of the smooth conical bar using the peak value of the confining stress curve, the fracture energy of concrete at elevated temperature can be established by matching the calculation with the measured curve in the fully cracked stage. As fig. 6.1 shows, the confining stress in the fully cracked stage mainly depends on the fracture energy. Finally, the friction coefficient of the strands and the other bond model parameters were determined with the pull out tests. With the calibrated values of the tensile strength and the fracture energy, the confining stress curve for the pull out tests can be calculated. Due to the short embedment length of five times the strand diameter, a uniformly distributed bond stress over this length can be assumed [DEN UJIL: 1995]. So, the bond stress follows directly from the measured pull out force, taking into account the bonded area. From the ratio between the measured bond stress in the pull out tests and the calculated confining stress, the temperature dependent friction coefficient of the embedded strands can be determined.

**Table 6.1** *Number of calibration tests with characteristic dimensions.*

Test type	diameter of strand or conical bar [mm]	embedment length [mm]	concrete cover / bar diameter	concrete diameter [mm]	concrete height [mm]	Temperature				
						20	80	150	400	600
Pull out free	12.5	62.5	2.3	71	67.5	2	2	2	2	2
		62.5	2.9	86	67.5	1	1	1	1	1
Pull out restraint	12.5	62.5	2.3	71	67.5	2	2	2	2	2
		62.5	2.9	86	67.5	1	1	1	1	1
Pull through	12	25	2.8	80	25	1	1	1	1	1
	16	25	2.6	100	25	1	1	1	1	1
	20	25	2.5	120	25	1	1	1	1	1
Splitting				75	75	3	3	3	3	3
Reference test at 20°C	Splitting tension			75	75	3	3	3	3	3
	Cube compression				150	3	3	3	3	3

The pull out tests provide also a basis for the calibration of the parameters setting the relation between the steel strain and slip to the fictitious radial expansion. If splitting cracks develop in the pull out tests, the slip and steel strain at that time correspond to the radial expansion at the steep drop in the confining stress curve. In order to measure the separate contributions of the steel stress and the slip to the radial expansion, two types of pull out tests were carried out, i.e. with free and restrained passive end of the strand. In the tests with a free passive end, only a very

small steel stress can develop during pull out due to the short embedment length. In the tests with the restrained passive end, a significant steel stress can develop, depending on the stiffness of the unloaded end. In these tests, the strand was loaded beyond yielding in order to measure the effect of yielding on the bond behaviour.

### 6.1.3 Test set up

#### 6.1.3.1 Test frame

For the calibration tests, a special test set up was developed in which an electrical furnace was built into a steel frame, see fig. 6.3. In the pull out tests with restrained passive end, the bond force equals the difference between the forces at both ends of the strand. It is of a lower magnitude than those forces. In order to obtain an accurate measurement of the bond force, the entire furnace was hung to load cells with a smaller measurement range than the load cells at both ends of the strands.

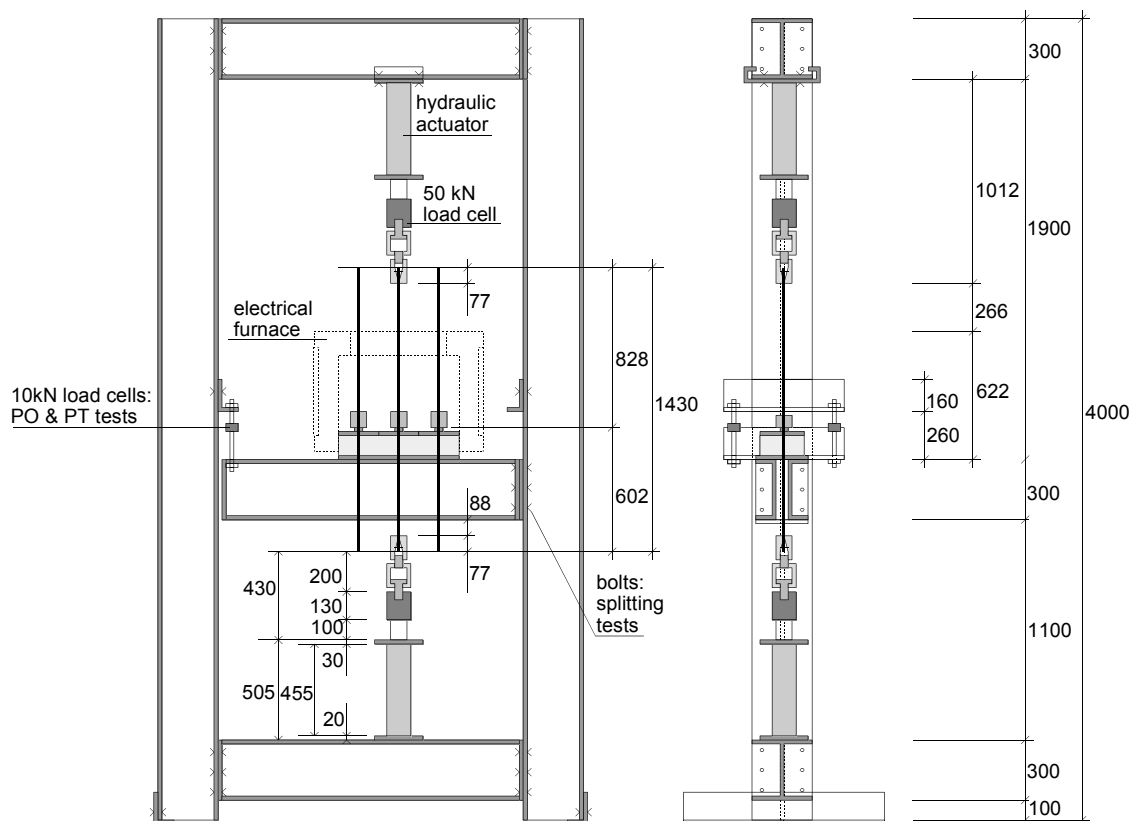


Figure 6.3: Overview of the test set up for the pull out tests with restrained unloaded end. The electrical furnace is shown with dashed lines.

#### 6.1.3.2 Loading

The load in the pull out tests and the pull through tests was applied by a displacement controlled hydraulic actuator at the lower end of the strand, respectively the conical bar.

The loading rate was established by trial and error. For the pull out tests with free unloaded end, the pull through test and the splitting tensile tests, a loading rate of 0.05 mm/s for the lower hydraulic actuator was found to be appropriate. At 80 and 150 °C the resulting force in the pull through test appeared to increase with rather unstable shocks, see next section. In order to minimize the shocks, the loading rate was reduced for the tests at 400 and 600 °C to 0.02 mm/s. For the pull out tests with restrained passive end, the loading rate was chosen at 0.01 mm/s. In these test, the steel stress rapidly increased with increasing displacement of the loaded end.

### 6.1.3.3 Stiffness of the restrained passive end

The stiffness at the restrained end was controlled with a hydraulic actuator at the unloaded end. Using a servo-engine controlled system, the restraining force at the unloaded end was adapted to the measured slip.

The stiffness of the restrained passive end was chosen on the basis of a simple investigation of the stiffness in a real slab, see fig 6.4. Consider a slice of the HC slab that is represented by the cylindrical test specimen with a force  $F_{pas}$  acting on the strand at the passive side. This force will cause a slip of the strand  $\delta$  at the interface between the slice and the fictitious part of the HC slab behind the slice. This force will be transferred into the concrete behind the slice over a distance that depends on the bond stress  $\tau$  at the bond interface in the fictitious part of the HC slab.

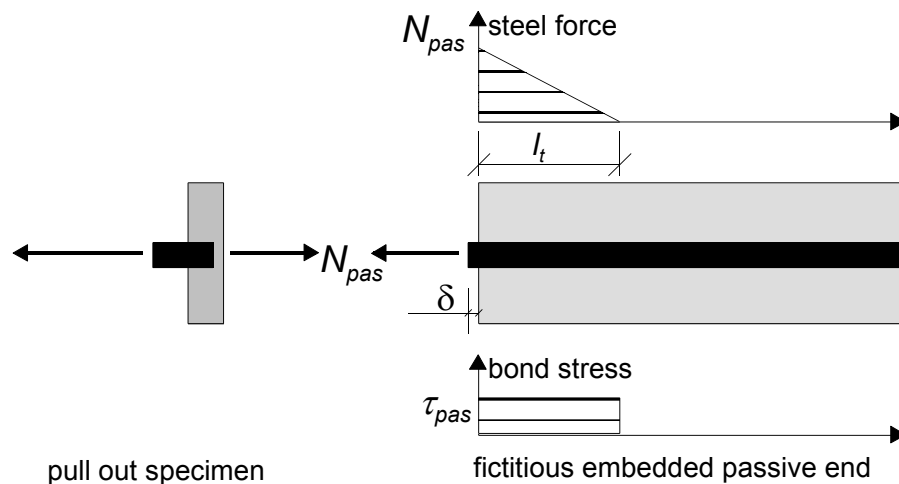


Figure 6.4: Analogy of the support at the restrained passive end with a real slab to determine the desired stiffness.

Assuming a constant bond stress  $\tau_{pas}$  as the most simple approach, the length  $l_t$  over which the force in strand is transferred into the fictitious part of the HC slab equals

$$l_t = \frac{N_{pas}}{\tau_{pas} O_p} \quad \{6.1\}$$

Using this result, and neglecting the axial deformation of the concrete, the relation between the force  $N_{pas}$  and the slip  $\delta$  reads

$$\delta = \int_0^{l_t} \epsilon dx = \frac{1}{2} \frac{N_{pas} l_t}{E_p A_p} = \frac{N_{pas}^2}{2 E_p A_p \tau_{pas} O_p} \quad \{6.2\}$$

Thus the slip is proportional to  $N_{pas}^2$ . Generally, a spring is characterized by a  $F-u$  relation, thus

$$N_{pas} = \sqrt{2 E_p A_p O_p \tau_{pas} \delta} = K_s \sqrt{\delta} \quad \{6.3\}$$

In this relation a constant bond stress  $\tau_{pas}$  was assumed for the fictitious part of the HC slab at the unloaded end. In all the pull out tests an arbitrary bond stress of 4 MPa was applied which corresponds with  $K_s = 76 \text{ kN/mm}^{1/2}$ . This bond strength was chosen on the basis of the bond stress found by Den Uijl in small scale bond tests [1992]

#### 6.1.3.4 Heating rate

The load-heating path that was applied corresponds to fig. 6.5a, i.e. first a temperature increase, and then a load increase at constant temperature until complete pull out. The load-heating path of fig. 6.5b was not applied, i.e. a constant load with increasing temperature. Such a test would be dominated by thermal gradients and the results found in a slow heating test would differ completely from a test with ISO 834 heating. In a such a test, a generalised structural property, which can not be applied in the models of the HC slabs, would be measured rather than a material property.

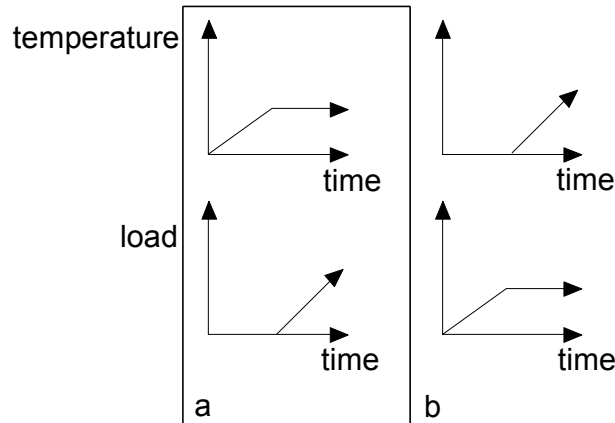


Figure 6.5: Load-heating paths. a: static with increasing load. b: transient with constant load.

Calculations were carried out with the FE model of the splitting tests of fig. 6.2, in order to determine the maximum heating rate for which the measured tensile strength is not disturbed by internal damage caused by thermal stresses due to thermal gradients at elevated temperatures and by internal stresses due to shrinkage at ambient conditions. In the calculations, it was conservatively assumed that the loading starts directly after the desired temperature in the hart of the specimen was reached. The splitting force  $F_{spl}$  was calculated, that could be transformed into a calculated tensile strength using [NEN 5969: 1997] as

$$f_{ct} = \frac{F_{spl}}{\pi r b} \quad \{6.4\}$$

in which  $r$  is the cylinder radius and  $b$  the cylinder width.

The calculated tensile strength as obtained from the maximum applied splitting load, decreases significantly for higher heating rates under the effect of thermal stresses, see fig. 6.6. In this figure, this calculated tensile strength was compared with the tensile strength that was put into the calculation. The tensile strength at elevated temperatures was taken from Eurocode 2 [PREN 1992-1-2: 2002].

The decrease of the observed strength due to a too high heating rate can partly explain the large scatter found in literature for the tensile strength at elevated temperatures.

On the basis of the calculations, it was decided that a heating rate of 0.2 °C/min was sufficiently slow for the splitting tests.

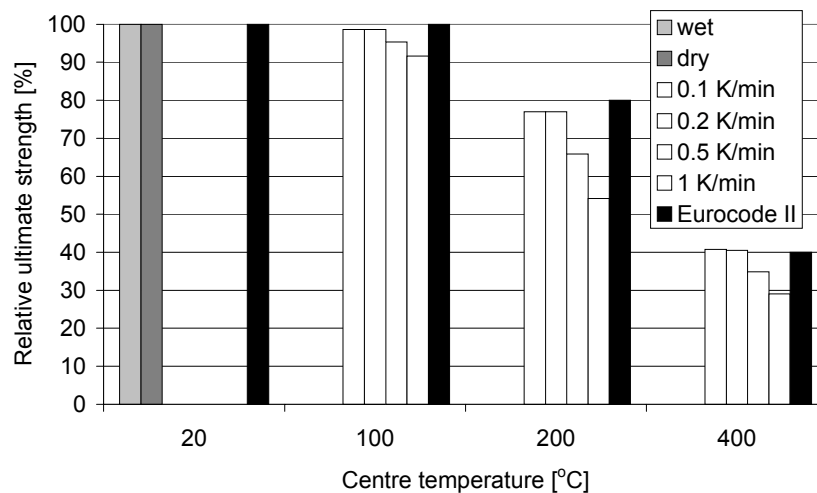


Figure 6.6: Relative tensile strength as calculated with a FE model of the splitting test specimen, depending on the heating rate.

In a similar way, the effect of the heating rate on the confining stress curve was determined using the FE models of the pull through specimens. It appeared that the heating rate had a smaller effect on the confining stress curve than on the splitting tensile strength. A rate of 0.5 °C/min for the pull out and pull through tests was found to be sufficiently low.

## 6.2 CALIBRATION OF MODEL PARAMETERS

### 6.2.1 Concrete tensile strength

As mentioned in the previous paragraph, the splitting strength is determined in the Brazilian splitting test in an indirect way using eq. 6.4. However, it is unknown whether this relation remains valid at elevated temperatures as the strength and stiffness do not decrease in a similar way and the shape of the stress-strain relation changes. In order to overcome uncertainties in this relation at elevated temperatures, the tensile strength was calibrated using the FE model of one quarter of the splitting tensile test specimens, see fig. 6.2. With this model, the input value for

the tensile strength was adapted iteratively until the calculated splitting load matched the observed splitting force in the tests, see fig. 6.7. For the collapse load reference is made to the vertical lines in fig. 6.7.

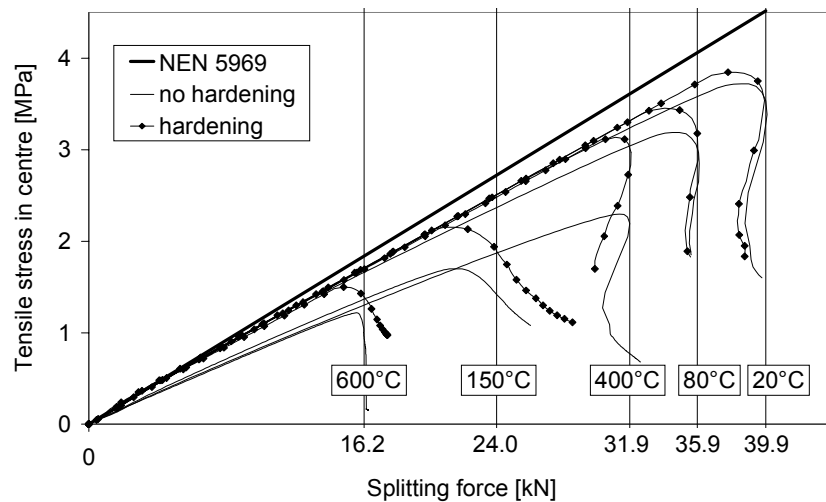


Figure 6.7: Comparison between the results obtained with the NEN 5969 method and the FE model for the calculation of the splitting tensile strength using an ascending stress-strain curve with and without hardening.

This iterative process was carried out for each temperature level given in table 6.1. In this way for each temperature level, a matching tensile strength was obtained.

The tests were simulated with two different stress-strain curves for concrete in tension up to the peak stress. Both the ductile stress-strain curves were used, as given in fig. 5.13 on page 130, including hardening up to the peak stress and the more commonly used simple linear relation. The Young's modulus for concrete at elevated temperatures was taken from fig. 3.9 on page 66.

The calculation at 150 °C drifted near collapse from the equilibrium path and no limit load was found. As the best possible indication, the point of inflection in the descending branch of the curve of fig. 6.7 was defined as the collapse load for this case. The relation between the compressive force and the tensile stress in the centre of the cylinder according to NEN 5969 [1997], i.e. eq. 6.4, is also given in the figure.

The tensile strengths obtained with both FE approximations is compared with the tensile strength according to NEN 5969 in fig. 6.8. The figure shows that a lower strength results from the FE simulations than from the NEN code. Inclusion of plastic hardening in the ascending branch of the stress-strain curve of concrete in tension results in a further decrease of the tensile strength, required to fit the test results. The tensile strength obtained with the FE model can be considered as the direct tensile strength of Eurocode 2 [PREN 1992-1-1:2002]. The ratio between the splitting tensile strength and the tensile strength obtained with the FE model is fairly consistent with the Eurocode 2 recommendation that the direct tensile strength is 90 % of the splitting tensile strength.

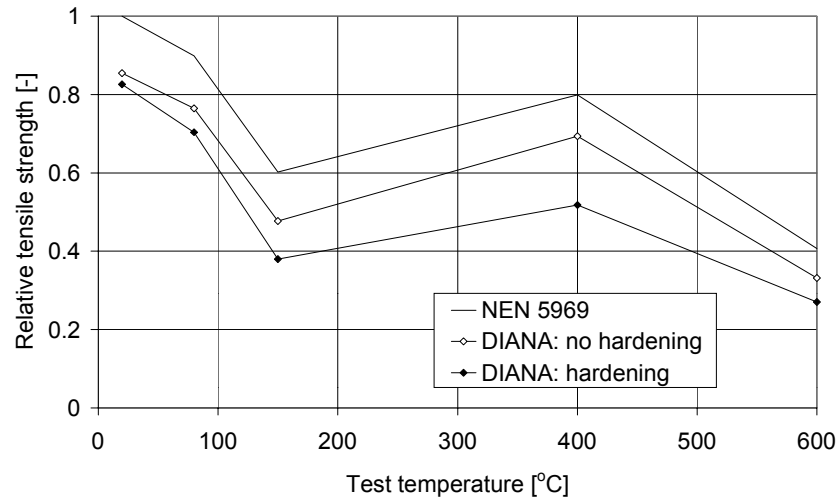


Figure 6.8: Comparison of the obtained tensile strength according to NEN 5969 and the FE model with and without hardening up to the peak stress.

Note that the difference between NEN and the FE simulations was not observed in fig. 6.6, which was obtained with the constitutive model for concrete according to Eurocode 2, without transient creep and a less brittle behaviour in compression, whereas the results of fig. 6.8 were obtained with the more advanced model for concrete in compression including transient creep.

## 6.2.2 Fracture energy of concrete

The fracture energy was calibrated on the basis of the pull through tests. The calibrated tensile strength at elevated temperatures was used to calibrate the fracture energy of concrete. As explained in §5.4.3.3, it is assumed that the internal damage that arises due to the incompatibility between the thermal expansion of the aggregates and the cement paste, causes a decrease of the fracture energy and the tensile strength at elevated temperatures. As a result, the decrease of the fracture energy is determined in the concrete model once the decrease of the tensile strength is known. So, only the fracture energy at room temperature had to be calibrated and the model assumption of the decrease had to be checked.

The FE model for the pull through test is shown in fig 6.2. A mesh was made for each of the three sizes of the pull through specimens. The specimens are further referred to by their inner diameter. Although the specimens are axially symmetric, the entire specimen was modelled, since the symmetry vanishes once crack localisation starts. I.e. if for instance one quarter of the cylinder would be modelled, this implies that the number of radial cracks in the full specimen can only be a multiple of four.

The node in the centre of the mesh was supported in all directions. The other nodes of the strand were supported in such a way that a rotation of the entire mesh around the centre was avoided. The load consists of an isotropic expansion of the strand elements.

Between the strand elements and the concrete elements, interface elements were applied to represent a soft layer. Such a layer must be expected near the sides of the concrete specimen, because the concrete compacting near the sides is worse than away from the sides, leading to an

increased porosity. Moreover, the relatively stiff aggregate particles will be covered with weaker cement paste near the sides.

Due to the increased porosity of concrete at elevated temperatures, compaction of the mortar at the interface can be expected, resulting in a decreased stiffness. The interface was modelled with solid elements that remain elastic. As will be discussed later, these solid elements were replaced by spring elements in a later stage of the calibration process.

The fracture energy was calibrated matching the horizontal branch of the calculated confining stress curves to the measured one, since the fracture energy has a significant effect on this branch. The interface stiffness and thickness was calibrated as well, matching the calculated radial expansion at the peak value of the confining stress to the measured one.

With the FE model of the pull through test, the confining stress curve is determined by averaging the stress in the steel-concrete interface along the perimeter. However, in the test, the pull through force was measured versus the slip of the conical bar, rather than the confining stress versus the radial expansion. In order to compare the test results with the simulation results, the slip was translated to a radial expansion using the change of the diameter of the conical bar per unit length. The pull through force was averaged over the contact area of the conical bar and the concrete cylinder, resulting in a bond stress. Then the bond stress was transferred to the confining stress by dividing the bond stress by a dummy friction coefficient of the contact plane between the conical bar and the concrete cylinder. This friction coefficient was calculated as the peak bond strength found in the test, divided by the peak confining stress in the FE simulation. In doing so, a separate friction coefficient was calculated for each simulation. The peak value of the confining stress curve depends almost exclusively on the tensile strength. The fracture energy and the thickness and stiffness of the interface have a very small effect on the peak value. So, using the calibrated tensile strength, the dummy friction coefficient could adequately be determined.

Notably, the dummy friction coefficient increased significantly with increasing temperature, due to corrosion at high temperatures of the conical bar. At 400 °C, the friction coefficient was even higher than unity. However, the relevance of this increase for embedded prestressing strands is small, as embedded strands are not in direct contact with the air and the conical bars were in direct contact with the hot air before being pulled through. As another effect of the corrosion, some initial radial expansion appeared before the confining stress increased. At higher temperatures, a larger stress-free initial radial expansion was observed. As this effect could not be modelled and was typical for the pull through tests only, the initial expansion was removed from the diagram before calibration. Furthermore, the measured confining stress curve showed increasing vibrations at elevated temperatures, which is also attributed to the increased roughness of the corroded conical bar at high temperature.

The radial expansion at which the confining stress drops is mainly dependent of the Young's modulus of concrete and the stiffness of the interface layer between the strand and the concrete cover. This strain was used to calibrate the stiffness of the interface. The Young's modulus of concrete at ambient temperature was fixed through the relation with the compressive strength as given in eq. 3.2 on page 60. The way the decrease of the Young's modulus was determined at elevated temperature, was outlined in §5.4.3.

A total of 900 simulations were carried out: three diameters of the specimens, five temperature levels of 20, 80 150, 400 and 600 °C, three levels of the fracture energy, i.e. 40, 60 and 80 J/m<sup>2</sup>, two interface thicknesses of 1 and 2 % of the bar diameter and five interface stiffnesses ranging from 1 to 50 ‰ of the concrete stiffness. Both the linear and the non-linear stress-strain curve for concrete in tension were tried in the calibration process.

The FE model is capable of calculating crack localisation even though the material properties are uniformly distributed, see fig. 6.9. In order to obtain a proper localisation, the mesh must be generated with randomly shaped triangles to obtain a non-symmetrical mesh. Also plastic deformations needed to be included for concrete in compression, otherwise the number of calculated cracks (>10) appeared to exceed the measured number (2-3) by far.

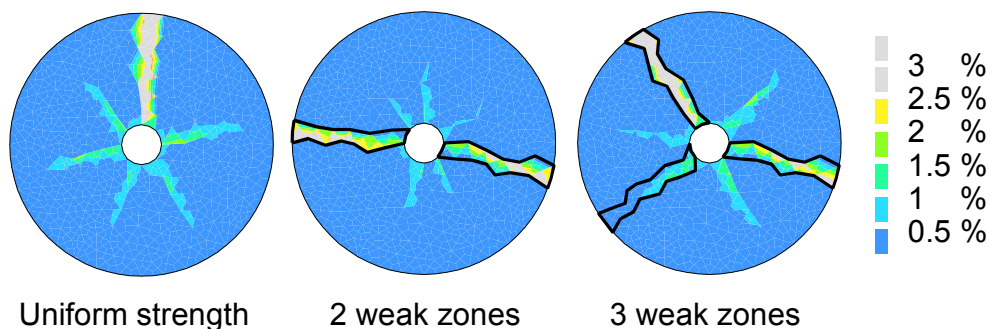


Figure 6.9: Principal plastic strains in the pull through specimen with a 12 mm inner radius, in the fully cracked stage at a radial expansion of 8 ‰.

The FE model calculates slightly too high confining stresses in the post-cracked stage of the expansion curve even when the fracture energy is as low as 40 J/m<sup>2</sup>, see fig. 6.10a. A further decrease of the fracture energy barely reduces the confining stresses in the fully cracked stage. The discrepancy between the simulations and the tests might be explained by the fact that a higher number of cracks was calculated than measured. In most specimens, two through cracks developed, whereas, in the calculations four to six localised zones with high crack strains developed. For instance, in the calculation of the specimen with a 12 mm inner diameter at 20 °C, one main crack developed and five smaller cracks, see left drawing in fig. 6.9. Therefore modified calculations were made in which elements along two radial lines were downgraded with a 10 % lower strength, in order to force only two splitting cracks to develop through these weaker elements. In fig.6.9, the zones with a 10 % reduced strength are drawn with the dark lines. However, the effect was small, see fig. 6.10b. Five more splitting cracks were calculated in addition to the cracks through the weak zones, which remained much smaller, see fig. 6.9. Also another calculation with three weak zones led to six calculated splitting cracks in total. It must also be noted that slightly different input values such as the Young's modulus of concrete or the interface stiffness, can have an effect on the calculated crack pattern as well.

In conclusion, the number of splitting cracks in the pull through specimens is very sensitive to a series of coincidences due to the axial symmetric characteristic of the problem. As a fracture energy lower than 40 J/m<sup>2</sup> seems to be unrealistic, compare for instance with fig. 3.2 on page 62, the fracture energy was fixed at 40 J/m<sup>2</sup>. The overestimation of the confining stress in the post-cracked branch is attributed to the elastic solid interface layer that contributes slightly to the

confining action. Later on, in simulations of the pull out tests, the solid interface elements were replaced by spring elements that can not provide circumferential stresses, which resulted in a improved match of the post-cracked branch.

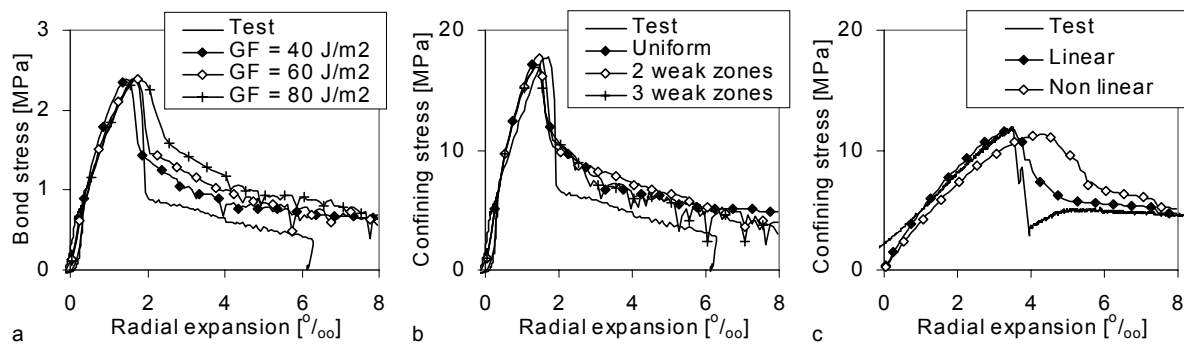


Figure 6.10: Main characteristics of the calibration of the pull through tests.

Fig. 6.10c shows that the shape of the calculated expansion curve matched the measured shape better using a linearly ascending branch in the stress-strain diagram of concrete in tension than a non-linear ascending branch, which includes some plasticity before cracking. The branch that includes plasticity was based on the work by Breunese [2001] who showed that the differential thermal elongation between aggregate grains and mortar leads to small cracks in the mortar during heating. In the latter case, the drop in stress after full crack propagation was not as sudden as in the tests and lead to a bigger overestimation of the confining stress after the stress drop, see fig. 6.10c. Therefore, further calculations were made with a linear (elastic) ascending branch for the stress-strain relation of concrete. No proper explanation could be found for the poor agreement obtained using the non-linear ascending branch for the stress-strain curve of concrete in tension.

In order to fit the radial expansion at peak stress in the calculations to the measurements, the interface stiffness was adapted. It appeared that the interface stiffness decreased with elevated temperatures, see table 6.2. Two tests differed so much from the other tests that they could not be simulated with the same interface stiffness as the other tests at that temperature. The 20 mm specimen at 600 °C and the 12 mm specimen at 80 °C were simulated with an interface stiffness of 1 % of the Young's modulus of concrete at room temperature rather than the value given in the table 6.2. The relevance of the interface stiffness is limited for the HC slabs, as it is only representative for the pull through tests.

The decrease of the interface stiffness can be attributed to an increased porosity of the cement paste at the inner edge of the concrete specimen and to the corrosion of the conical bar at elevated temperature. Corrosion of the bar could occur, as it was unprotected by the concrete specimen during heating. The strands in the pull out test specimens, on the contrary, were protected against corrosion as they were cast in the specimens and no air could penetrate to the strand during heating. As a result, the decrease of the interface stiffness obtained in the pull through tests can not directly be applied to the pull out tests, but it must be evaluated again.

The comparison of the tests with the calculations, using the calibrated values, are given in fig. 6.11.

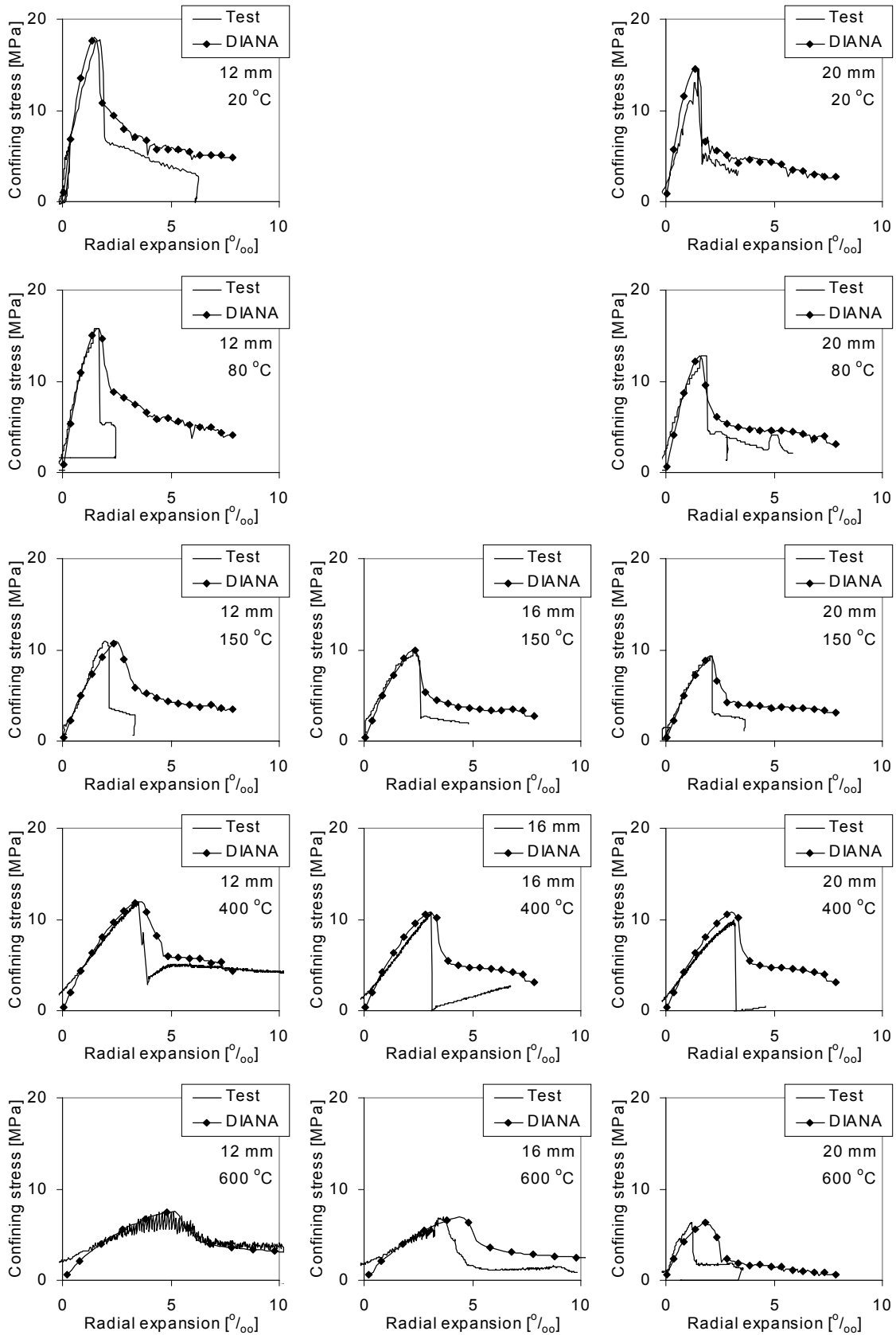


Figure 6.11: Comparison between the pull through tests and the FE model with the calibrated input values.

**Table 6.2** *Calibrated values of the concrete and interface properties on the basis of the pull through tests.*

Input parameter	Temperature [°C]				
	20	80	150	400	600
Tensile strength reduction [-]	1.0	0.90	0.56	0.81	0.39
$G_F$ [J/m <sup>2</sup> ]	40				
$d_i$ [% $r_p$ ]	1.0				
$E_i$ [% $E_{c,20}$ ]	1	0.5	0.2	0.1	0.1

The following conclusions were drawn from the pull through tests:

- The confining stress curves obtained with the pull through tests could reasonably well be simulated with the FE model, using the calibrated values as given in the table 6.2.
- The model assumption of a decreasing fracture energy at elevated temperature as outlined in §5.4.3.3 is acceptable.
- The crack localisation is calculated by the FE model, however, the FE model overestimated the number of splitting cracks in this axial symmetric case.
- A linearly ascending branch of the concrete stress-strain relation in the tensile regime leads to a better match with the pull through tests than the non-linear branch according to Breunese [2001] that includes plastic straining.

### 6.2.3 Bond parameters

The bond parameters were calibrated on the basis of a comparison of the results of the pull out tests with the results of the calculations.

The comparison was made on the basis of bond-slip-steel stress interaction curves for the pull out tests with the free passive end and the restrained passive end. The calculations consisted of two steps. First the confining action was the calculation with the same type of FE models that were used to simulate the pull through tests, but now adapted to the size of the pull out specimens. In this step, the calibrated values of the tensile strength and the fracture energy were used and the linearly ascending stress-strain diagram was used for concrete in tension. The stiffness of the interface between the strand and the concrete cylinder was calibrated in this step. The second step consisted of the calculation of the bond-slip-steel stress behaviour on the basis of the calculated confining stress curves. In the second step, the bond-slip-steel stress relations were made for each test with a general spreadsheet programme, assuming that the actual bond stress equals the bond strength over the entire range of measured slip. In doing so, the bond parameters could rapidly be calibrated. The second step was repeated afterwards with the calibrated bond parameters with the FE model of fig. 6.2, in order to demonstrate that the calibrated values are also correct when used in the FE model.

The bond stress of the strands was deduced from the measured bond force by averaging the bond

force over the interface area. The slip was measured at the unloaded side of the concrete cylinder. The steel stress was measured with a load cell placed in between the hydraulic actuator and the active end of the strand. In the pull out tests with restrained passive end, the steel stress was also measured with a load cell at the passive end. The steel stress varies over the bond length, however, the variation is small due to the short embedment length. The bond-steel stress relations were determined on the basis of the average steel stress. The bond-slip relations obtained in the tests, are shown in fig. 6.12. Each row presents measurements obtained at one temperature. The left column contains the bond-slip relations of the pull tests with the free passive end. The middle column contains the bond-slip relations obtained in the pull out tests with the restrained passive end. The right column contains the bond-steel stress relation obtained in the pull out tests with restrained passive end. In the tests with free end, barely any steel stress developed. Splitting cracks did never develop in the pull out tests with restrained passive ends. The occurrence of splitting cracks in the pull out tests with free passive end are summarised in table 6.3. Apparently, the probability of the occurrence of splitting cracks reduced with increasing temperature. This can be explained by the decreased stiffness of concrete and the bond interface at elevated temperature which led to reduced splitting stresses.

**Table 6.3** *Occurrence of splitting cracks in pull out tests: Number of cracked specimens/ total number of specimens.*

Passive end	Concrete cover / strand diameter	Temperature [°C]				
		20	80	150	400	600
Free	2.3	2/2	2/2	0/2	½	0/2
	2.9	0/1	0/1	1/1	0/1	0/1
Restrained	2.3	0/2	0/2	0/2	0/2	-
	2.9	0/1	0/1	0/1	0/1	-

Figure 6.12 shows that a fairly constant bond stress was found in both types of tests over a large range of slip development. Furthermore, a higher bond stress was systematically observed in the tests with a free passive end than in the tests with a restrained passive end, except for the tests at 150 °C. The tests with fixed passive end at 600 °C did not lead to useful results and are therefore omitted.

In the pull out tests with fixed passive end, a significant increase of the steel stress was realised. Especially at 150 °C, even yielding of the strand was successfully tested. Fig. 6.13 shows the stress-strain relation of the strands and the bond stress-steel strain relation. The steel strain was obtained by the difference between the slip of the strand and the displacement of the hydraulic actuator and dividing it by the strand length between these two measurement points. Clearly, the bond stress drops once the strand starts to yield, which is in line with the bond model that predicts a drop in the strand diameter once it starts to yield and, consequently, a drop in the frictional stresses.

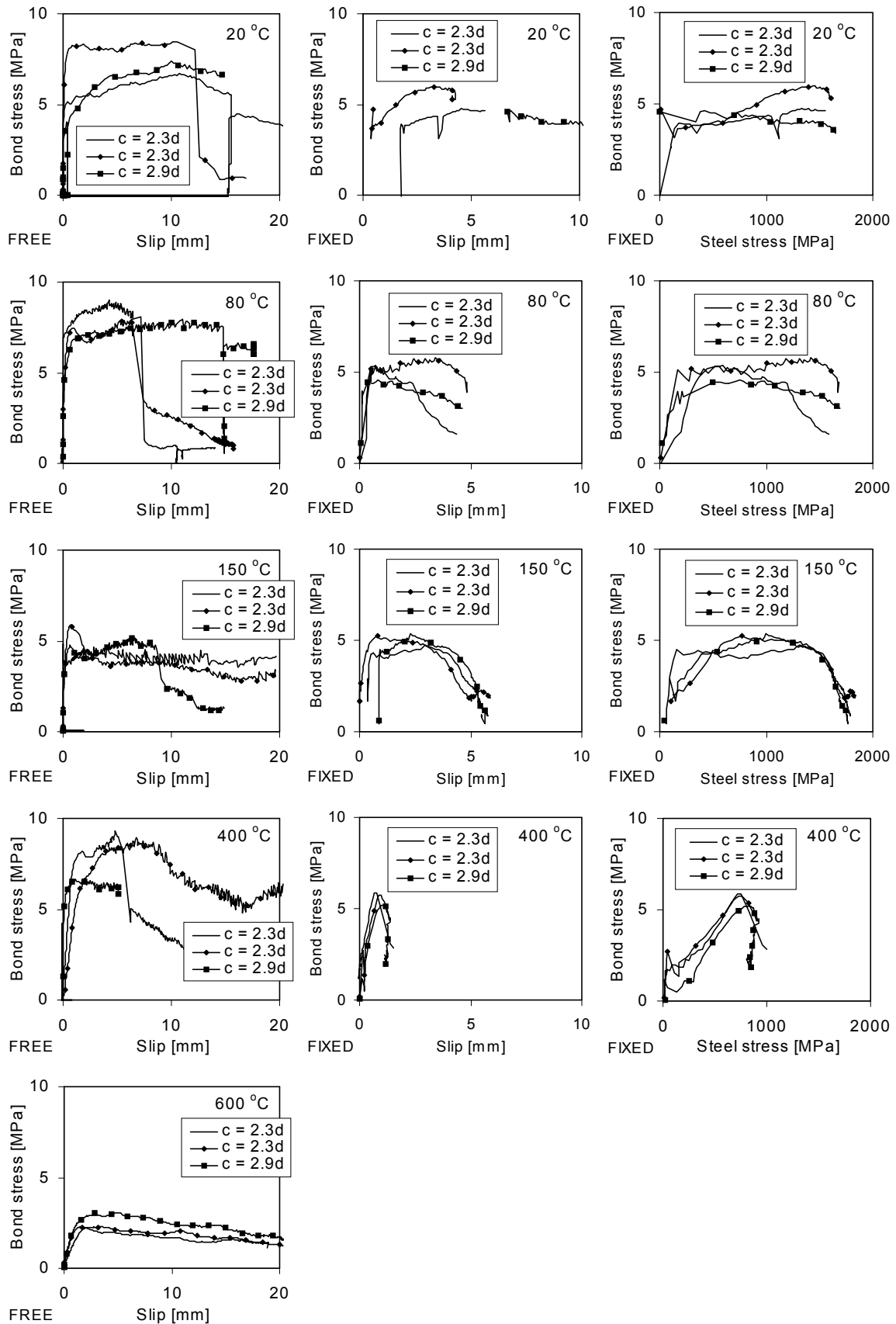


Figure 6.12: Results of the pull out tests.

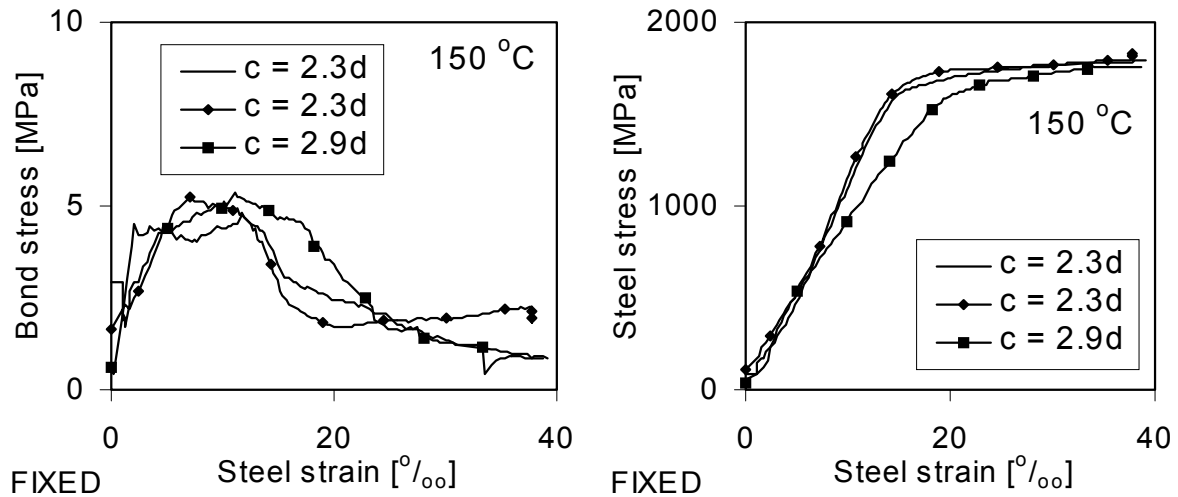


Figure 6.13: Bond stress-steel strain relation (left) and the stress-strain relation of the strand (right), both obtained in the pull out test with a restrained passive end at 150 °C.

The first step was the simulation of the confining action of the concrete specimen on the strands. The differential thermal expansion between concrete and steel led to a substantial initial confining stress at zero imposed radial expansion. This initial confining stress depends on the assumed thermal expansion of concrete and steel. Therefore, three simulations were made, one on the basis of the thermal expansion curve of calcareous concrete, one of siliceous concrete, both according to Eurocode 2 [PREN 1992-1-2: 2002] and one simulation with an intermediate thermal expansion curve for concrete based on an aggregate mix of  $\frac{2}{3}$  siliceous aggregate and  $\frac{1}{3}$  calcareous aggregate. The development of the confining stress during heating as a result of the incompatible thermal expansions of steel and concrete is given in fig. 6.14.

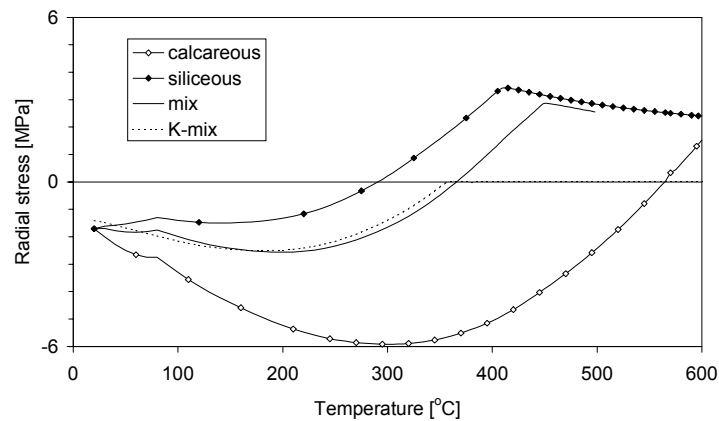


Figure 6.14: Development of the confining stress during heating due to incompatible thermal expansion between concrete and steel.

Clearly, beyond a certain temperature the concrete expansion exceeds the thermal expansion of steel and consequently, the interface is tensioned. As the solid interface elements behave in linear elastic way, the tensile stresses can increase up to the tensile strength of concrete. For both siliceous and mixed aggregate, the concrete elements next to the interface cracked in the

simulation at 410 and 450 °C respectively. Obviously, this is not in accordance with the real situation where the interface contact would be broken. Therefore a new calculation was made with the mixed aggregate properties, in which the solid interface elements were replaced by spring elements with multi-linear elastic behaviour. The stiffness in compression was equal to the solids. In tension, a negligibly small dummy stiffness was applied. In fig. 6.14, the resulting confining stress is labelled as K-mix. It can be seen that the behaviour is almost identical to the simulation with the solids as long as the interface remains under pressure. However, once the interface becomes tensioned, the interface stress remains approximately zero.

Also during maturing, a small initial confining stress develops due to shrinkage of the concrete. Therefore, all curves do not start at zero confining stress at room temperature.

Secondly, from the confining stress-curves, the bond-slip-steel stress interaction of the bond model was compared with the tests in a spread sheet programme, which allows for an easy and rapid calibration of the model parameters. The results of the simulation of the bond tests are shown in fig. 6.15 for the pull out tests on the cylinders with a diameter 71 mm and in fig. 6.16 for the cylinders with a diameter of 86 mm. All bond model parameters were modified separately for each test specimen. In the tests with the restrained passive end, the Poisson effect reduction coefficient and the pitch coefficient influence the result simultaneously and could not be calibrated independently. Therefore, the Poisson effect reduction coefficient was fixed to unity, which resulted in the given values for the pitch coefficient.

The variation in the used values are given in fig. 6.17. The friction coefficient varies only in a relatively small band. At ambient conditions, the coefficient of variation (c.o.v.) for the adhesion was 27 % and for the friction coefficient 14 %. The adhesion coefficient vanishes beyond 150 °C. Over the entire temperature domain from 20 to 600 °C, the c.o.v. of the friction coefficient remained below 24 %.

With the calibrated values, a FE simulation was carried out for the pull out tests on the cylinders with a diameter of 86 mm, to show the accurate performance of the bond model as it was implemented in DIANA. The simulations were made with the model shown in fig.6.2. The results of the FE simulations are added to fig. 6.16. For the calculations of the pull out tests with free passive end, the FE model and the spreadsheet give identical answers. Some discrepancy between the two packages was obtained for the calculations with the restrained passive end, due to the fact that in the spreadsheet the actual axial steel stress and the actual slip measurements were put in in order to calculate the bond stress, while in the FE model, the loading path was based on the intended steel stress - slip development as given in eq. 6.3. During the start up of each test, it was not easy to get the intended match between the actual steel stress and the slip, and small deviations occurred that explain the difference between the spreadsheet and the FE model.

In fig. 6.18 the total radial expansion is given as calculated by the FE model due to the lack of fit effect, the Poisson effect and the pitch effect. It shows that the radial expansion drops drastically once the strand starts to yield. This drop explains the drop in the bond strength.

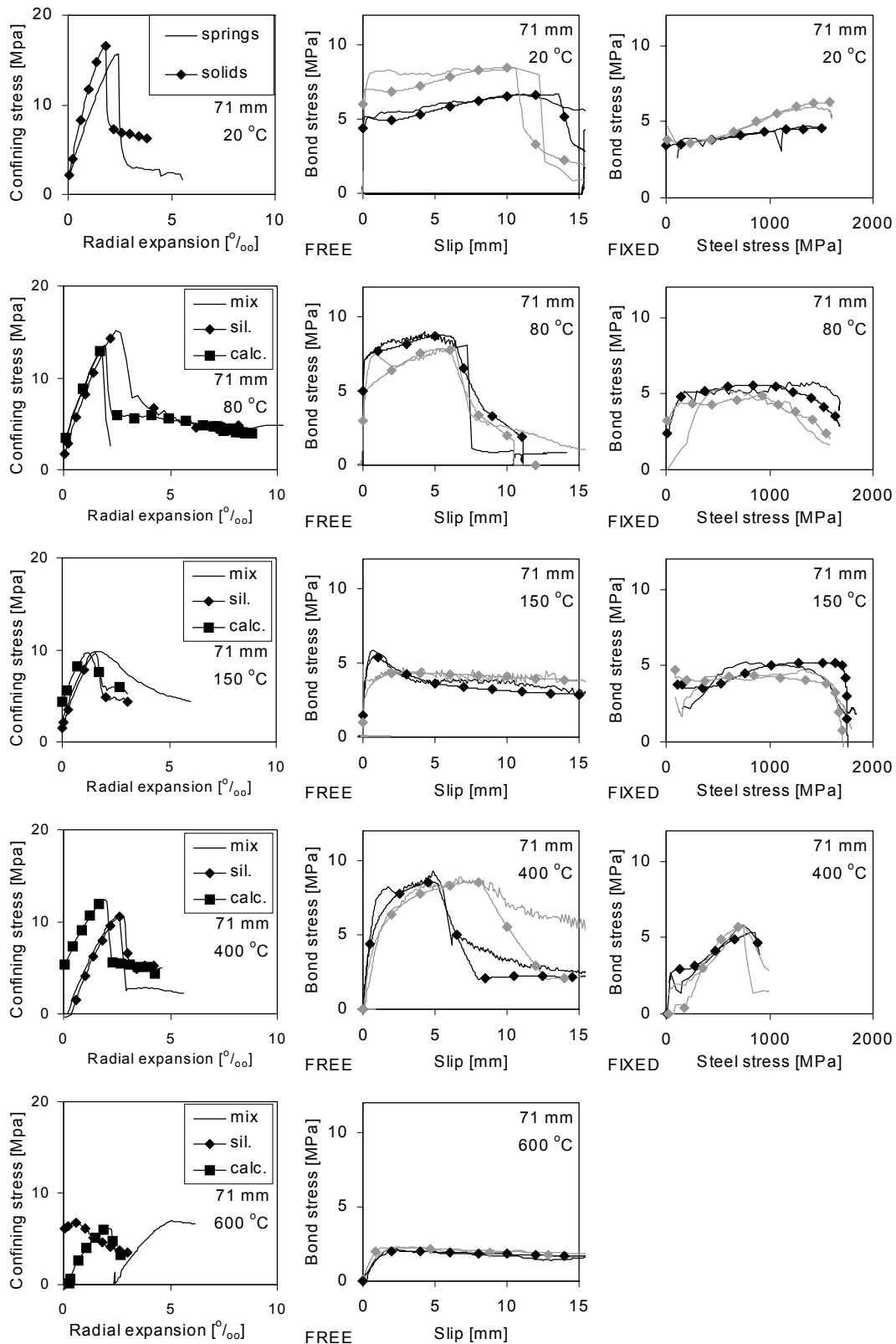


Figure 6.15: Calibration results for the pull out tests on the cylinder with a diameter of 71 mm. Calculated radial stress - expansion curves for three aggregate types (left) and comparison between the calculated and the measured bond - slip curve for the pull out tests with free passive end (middle) and the bond - steel stress curve for pull tests with restrained passive end (right).

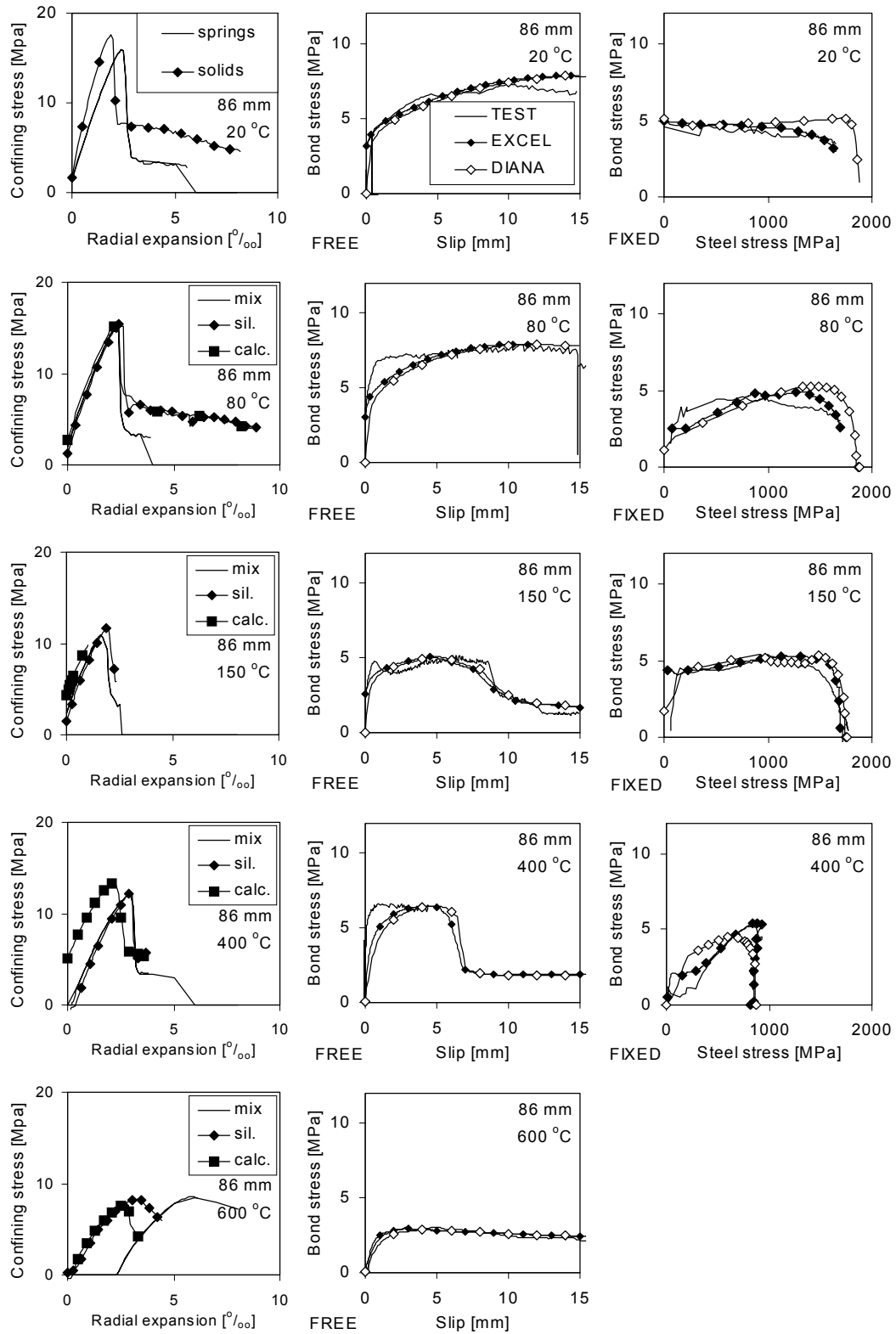


Figure 6.16: Calibration results for the pull out tests on the cylinder with a diameter of 86 mm. Calculated radial stress - expansion curves for three aggregate types (left) and comparison between the calculated and the measured bond - slip curve for the pull out tests with free passive end (middle) and the bond - steel stress curve for pull tests with restrained passive end (right) using the spreadsheet and using the FE model.

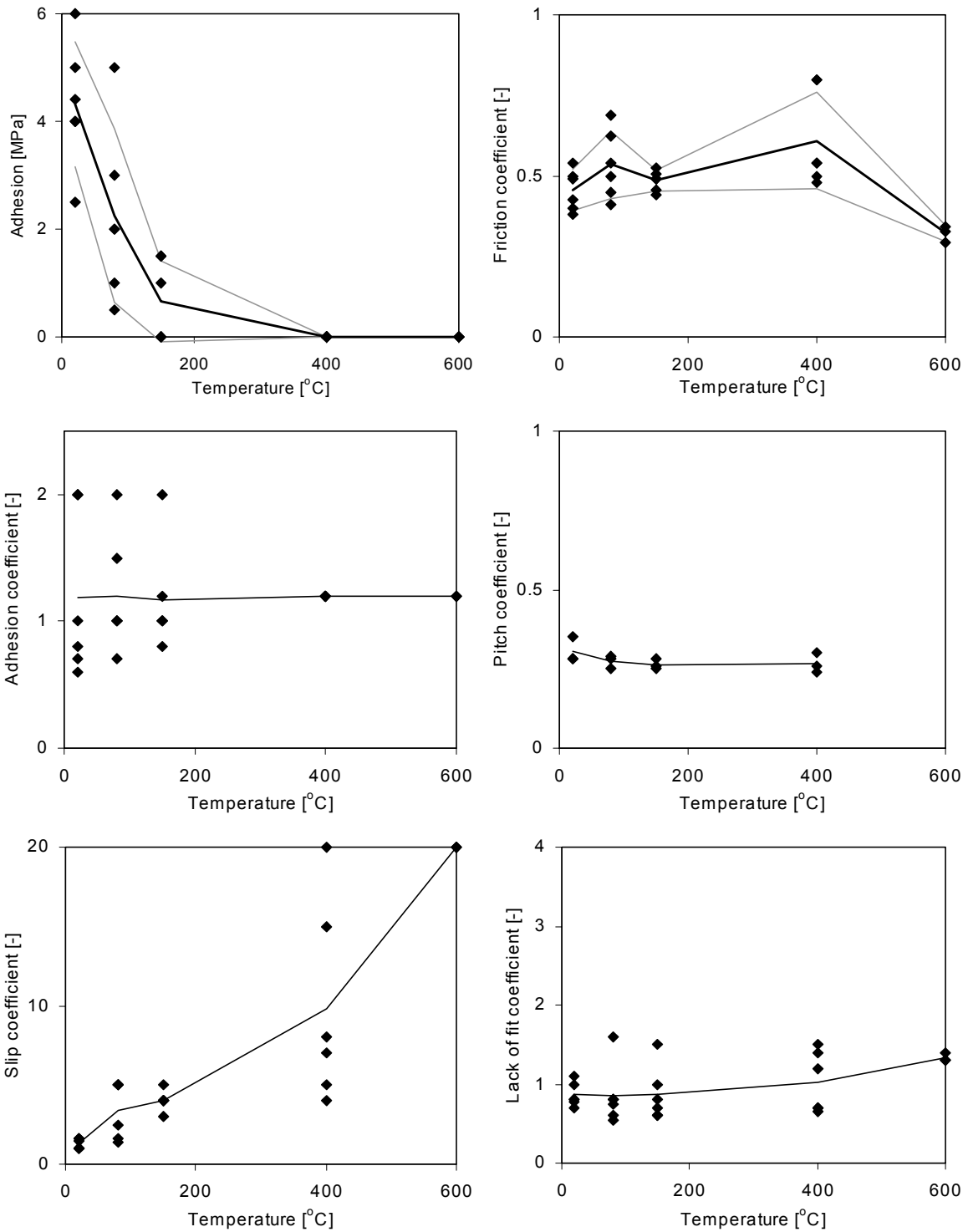


Figure 6.17: Calibrated values of the bond model parameters. Each dot represents the calibration of one pull out test. The line shows the temperature dependent average. For the adhesion and the friction coefficient also the 5-95 % reliability interval is shown with the grey lines.

**Table 6.4** Overview of the bond model parameters.

Objective	Description	unit	Temperature [°C]				
			20	80	150	400	600
Radial expansion strain $\epsilon_{rr,tot}$	Lack of fit coefficient	[‰]	0.9	0.9	0.9	1.0	1.3
	Slip coefficient	[mm <sup>-1</sup> ]	1.3	3.4	4.0	9.8	20
	Poisson effect coefficient	[-]	1.0				
	Pitch effect coefficient	[-]	0.30	0.27	0.26	0.27	
Confining stress curve	Interface spring stiffness	[% $E_{c,20}$ ]	0.25 (assuming a thickness of $0.01r_p$ )				
	Fracture energy	[J/m <sup>2</sup> ]	40				
Bond strength $\tau_y$	Friction coefficient	[-]	0.46	0.53	0.49	0.61	0.32
	Adhesion	[MPa]	4.3	2.3	0.7	0	0
	Adhesion coefficient	[-]	1.2	1.2	1.2	1.2	1.2
Elastic range	Linear shear stiffness	[MPa]	23				

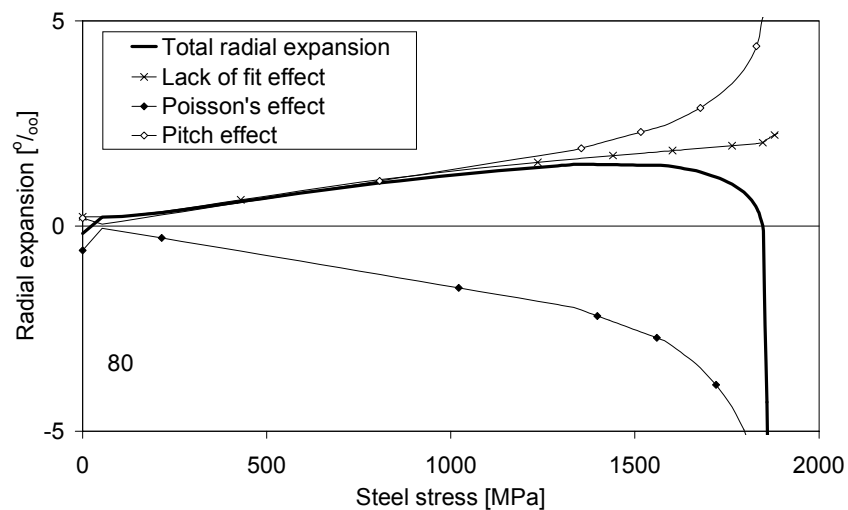


Figure 6.18: Contributions of the lack of fit effect, the Poisson effect and the pitch effect to the radial expansion, depending on the steel stress, based on the measurement in the pull out test on the 86 mm diameter specimen with fixed end, tested at 150 °C.

In conclusion, the bond model parameters were successfully calibrated. The friction coefficient which is the most important for the bond behaviour of prestressing strands in fire exposed HC slabs, was calibrated within a relatively small band. Moreover, it was successfully demonstrated that the bond model as implemented in the FE package was capable to simulate the pull out behaviour of the specimens, including the effects of splitting cracks and yielding of the strand.



# 7 Validation of the model

## 7.1 CONTENTS

In this chapter the FE models are validated. The capabilities and accuracy of the FE models are validated at ambient and fire conditions, using the calibrated properties of the bond model and the concrete model. The simulations of the HC slab at ambient conditions start with the calculation of the transfer length. Furthermore, the calculated crack propagation and load bearing capacity at ambient conditions are compared with the results from the reference tests, described in chapter 4. The quality and accuracy of the FE models of the fire exposed slab are assessed by comparisons of the crack propagation, the slip development, and the failure mode with some characteristic fire tests, described in chapter 4.

## 7.2 AMBIENT CONDITIONS

### 7.2.1 Transfer length

The prediction of the transfer length by the FE models is validated by means of the analyses of the HVP260 slab. The results of the FE models are compared with the predictions of the transfer length by the Model Code [CEB-FIB: 1991]. In both calculations, a tensile strength at the time of the release of the prestress of 3.86 MPa was assumed. The FE simulations started with the calculation of the response of the confining concrete cover to a radial expansion. For this purpose a cross sectional model of a rib of the HVP260 was made with the strand at the actual location of 40 mm from the bottom side, see fig. 7.1. Also the typical crack pattern is shown. The lines are perpendicular to the crack plane and the length indicates the crack opening. The model calculates that the main crack localises from the strand to the closest hollow core.

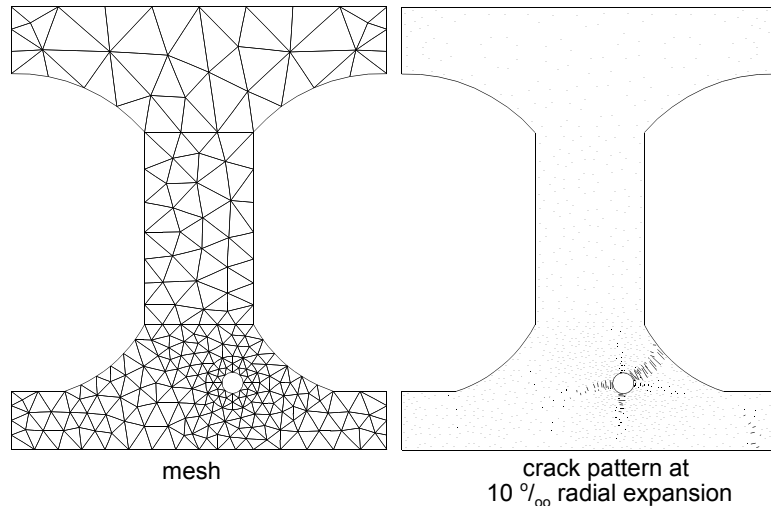


Figure 7.1: Cross sectional mesh used to determine the confinement stress curves for the HVP260 specimens with strands at 40 mm from the exposed side.

Subsequently, the calculated confining action was used as input for the FE model of the entire slab. Using the calibrated bond model of table 6.4 on page 160, a transfer length of 453 mm was calculated. For this purpose, the transfer length was defined as the length over which 95 % of the maximum prestress (at mid span) was introduced. The calculated transfer length is in acceptable agreement with the transfer length of 421 mm predicted by the Model Code formulation [CEB-FIB: 1991] as given in Appendix B. In the Model Code calculation the model factor  $\alpha_9$  was set equal to 0.6 on the basis of the evaluation of the analytical model for the anchorage capacity at ambient conditions, given in chapter 2.

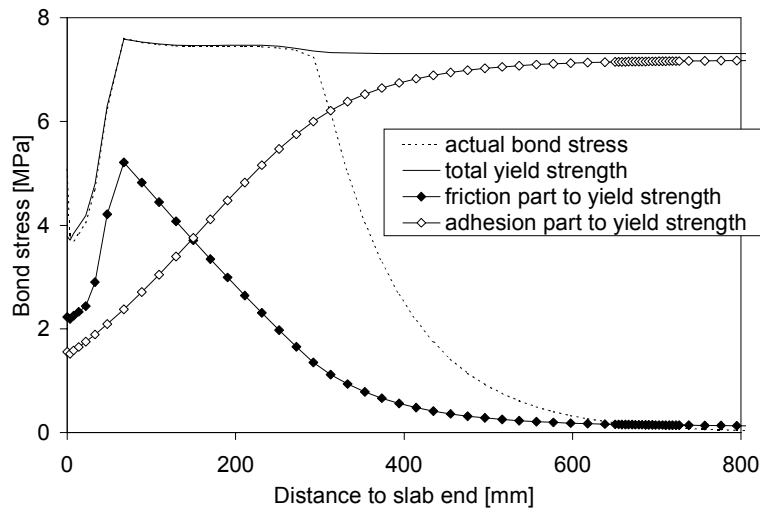


Figure 7.2: Development of the actual bond stress and bond strength along the strand as calculated with the calibrated values of the bond model parameters. Also the separate contributions of the friction and the adhesion to the bond strength are given.

In fig. 7.2, the development of the bond stress due to the release of the prestress and the corresponding bond yield strength along the strand near the end of the slab are presented as calculated with the FE model of the entire slab. Also the contributions of the friction and the

adhesion to the total bond yield strength are given. Near the end of the slab, splitting cracks develop over a limited length, see also the development of the radial strain in the right picture of fig. 8.4 on page 188. As a result, the contribution of the friction to the bond yield strength drops over this length. It is shown that the actual bond stress is limited by the bond yield strength over some 300 mm. Hereafter, lower bond stresses are required to reach internal equilibrium. Further away from the slab end, the slip decreases and consequently, the adhesion part increases. Apparently, the decrease of the friction part and the increase of the adhesion part almost level each other out leading to an almost constant bond strength along the transfer length except for the zone of splitting cracks.

### 7.2.2 Shear behaviour

In order to prove the ability of the model to simulate shear tension failure at ambient conditions, a double rib specimen of the VX265 slab was modelled, since this slab type showed an undisputed shear tension failure in reference tests at ambient conditions [FELLINGER: 1999b]. The slab has five circular cores, leading to a relatively small web width of only 38 mm at mid depth. In advance of the fire tests, four double rib specimens were loaded in a standard shear test until failure, to obtain the reference shear tension capacity at ambient conditions. In all four tests, shear tension failure occurred.

In the FE model of the double rib specimens, the mean value of the measured geometrical and material's properties were applied. The specimen contains two 12.5 mm strands at an actual axis distance of 37 mm with an initial prestress of 1150 MPa. The tensile strength was measured in Brazilian splitting tensile tests on three concrete cores of 50 mm diameter, which were drilled out of the webs of the HC slab. On the basis of the standard relationship between the splitting force and the splitting tensile strength of NEN 5969 [1997], a mean tensile strength of 5.7 MPa and a coefficient of variation of 2.3 % was obtained. A compressive strength of 82.3 MPa with a c.o.v. of 4.3 % was found in standard compressive tests.

The confining action was calculated first using a cross sectional model of a rib of the VX265 slab. The calibrated value for the fracture energy of 40 J/m<sup>2</sup> was applied, although the concrete mix of the VX265 slab differs from the mix of the HVP260 slab that was used to calibrate the fracture energy, see also table 4.2 on page 89. The calibrated values of the bond model were used for the FE model of the entire slab.

With the FE model of the entire slab an ultimate shear force of 110.1 kN was calculated. The average ultimate shear force found in the reference tests was 92 kN with a coefficient of variation of 3.7 %. The difference is explained by the use of the splitting tensile strength obtained through the NEN 5969 relation between the splitting force and the tensile strength rather than the actual tensile strength. The ratio between the measured and calculated failure load of 0.84 is consistent with the ratio of 0.85 between the splitting strength according to the NEN 5969 [1997] and the calibrated tensile strength, which was obtained for the concrete of the HVP260 specimens with the FE models at 20 °C, as discussed in §6.2.1. The failure crack pattern is shown in fig. 7.3. In the dark gray area, the crack strain exceeds 0.1 ‰, which approximately corresponds in this case

with a crack opening of 0.0012 mm. Failure is initiated by cracking of the web at the smallest web width. Clearly shear tension failure is calculated, although the crack propagates in the simulation through the section of the smallest web width while in the reference test a crack inclined at approximately 45° with the horizontal plane was observed. Note however that the crack opening is still very small at the onset of numerical collapse, so the actual direction of crack propagation could not be simulated. At failure, barely any increase of the slip was calculated nor any change of the steel stress anywhere along the strands.

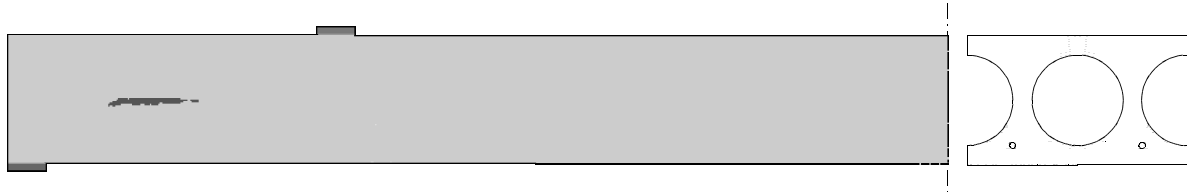


Figure 7.3: Calculated principal crack strain at the failure load in VX265 double rib specimen.

It is concluded, that the FE model predicts the actual failure mode within acceptable accuracy. Further investigations into the shear tension behaviour at ambient conditions are outside the scope of this thesis.

### 7.2.3 Anchorage behaviour

In order to demonstrate the ability of the model to simulate anchorage failure at ambient conditions, a double rib specimen of a HVP260 slab was modelled with 2 strands at 40 mm axis distance, refer to R-HVP260S in table 4.1 on page 87 and fig. 4.1 on page 85. In all three reference tests carried out on these specimens, anchorage failure was observed. The ultimate shear load was 99.0 kN on average with a standard deviation of 7.2 kN.

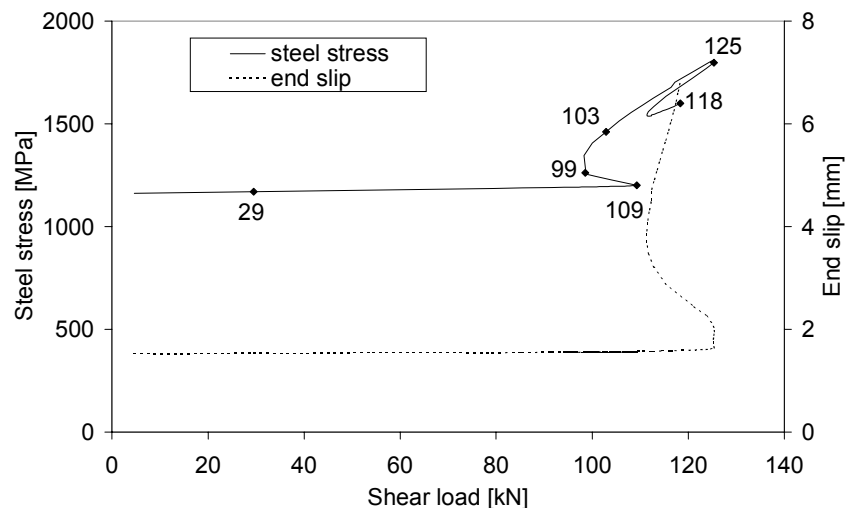


Figure 7.4: Simulation of anchorage failure of double rib of HVP260 slab with two strands an axis distance of 40 mm at ambient conditions. The steel stress in the flexural crack below the point load and the slip of the strand are shown.

The specimen was simulated with the FE model, using the calibrated values of the bond parameters of table 6.4 on page 160, combined with a concrete tensile strength of 6.0 MPa, which was obtained in splitting tests on cores drilled out of the HC slab specimen.

Anchorage failure was calculated, using a displacement controlled loading. Although the hydraulic actuator was controlled manually in the reference tests, it was comparable to a displacement controlled test. The applied load dropped as soon as the flexural cracks developed and the deflection rapidly increased. In the simulation, first, a flexural crack below the point load was calculated at a shear load of 109 kN. Then, the shear load dropped to 99 kN with the same deflection of the loading platen. The strand took over the released stress in the crack, resulting in an increase of the steel stress. A further increase of the deflection led to a further increase of the shear force until failure occurred at a shear force of 125 kN. In fig. 7.4, the development of the steel stress in the flexural crack is shown together with the slip development at the end of the strand. In the calculation, a yield strength of 2000 MPa was used for the strand. The figure shows that this ultimate stress was not reached, so no flexural failure was calculated. Moreover, the slip increases dramatically at the onset of failure, so pull out failure was calculated undisputably. The development of the steel stress, the bond stress and the slip along the strand are shown in fig. 7.5, 7.6 and 7.7. Each line corresponds to a loading stage that is marked in fig. 7.4. The figures clearly show how the strands are pulled out.

In conclusion, the model is very well capable to simulate anchorage failure. The difference between the failure load in the reference tests and the simulation can be attributed to the variation in the bond parameters. It is outside the scope of the present research to further investigate the discrepancy.

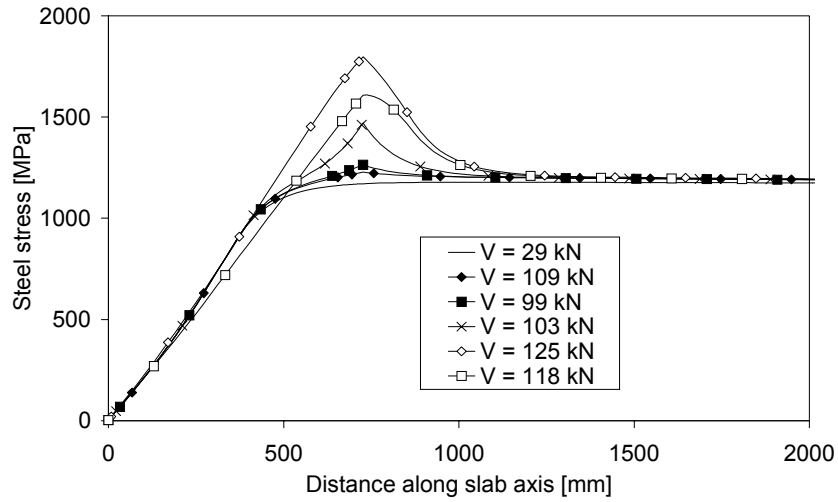


Figure 7.5: Development of the steel stress along the strand at various stages of loading.

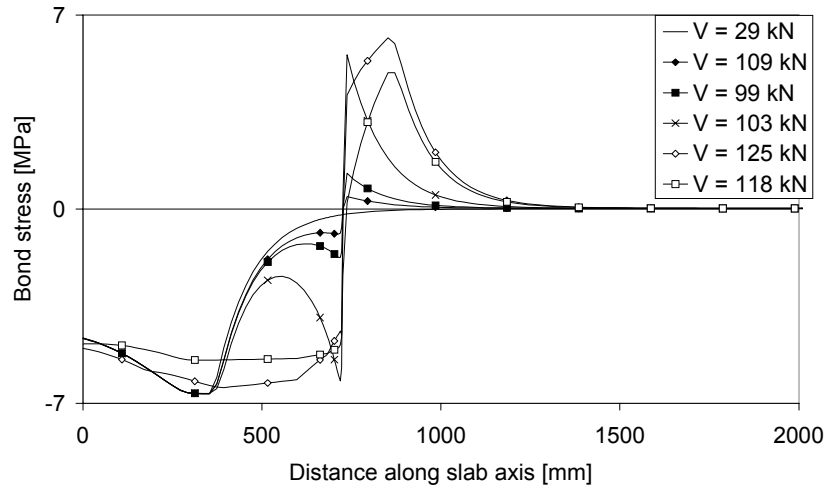


Figure 7.6: Development of the bond stress along the strand at various stages of loading.

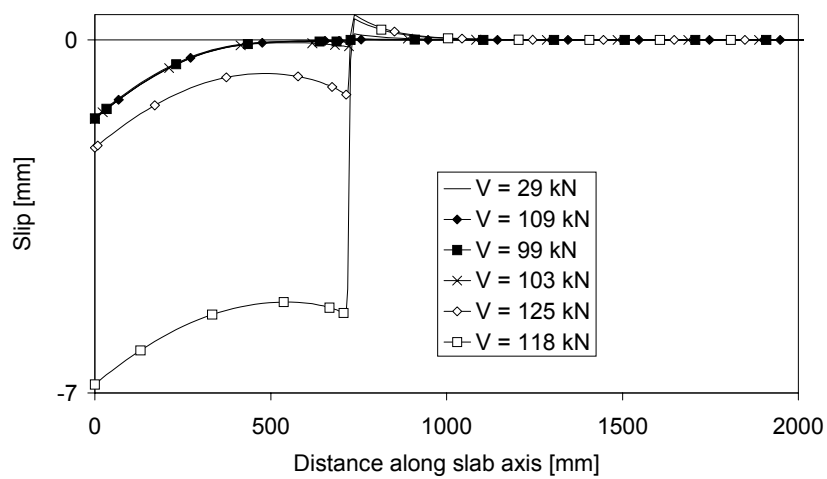


Figure 7.7: Development of the slip along the strand at various stages of loading.

## 7.3 FIRE CONDITIONS

### 7.3.1 Thermal response

In chapter 4, the temperature readings were presented as measured in the tests on the double rib specimens, see §4.4.4.

The temperatures at the surface of the hollow core were affected by the heat flow in the hollow core, that were dominated by moisture transport. As a result, the temperatures at the surface of the hollow core can not be considered to be representative for the temperatures inside the concrete at a same distance from the exposed side.

On the other hand, it was concluded that the scatter was limited to a standard deviation of 60 °C over the measurements at the surface of the hollow cores. So, the average measurements can be used as input values in the simulations of the thermal response to calculate the temperature profile.

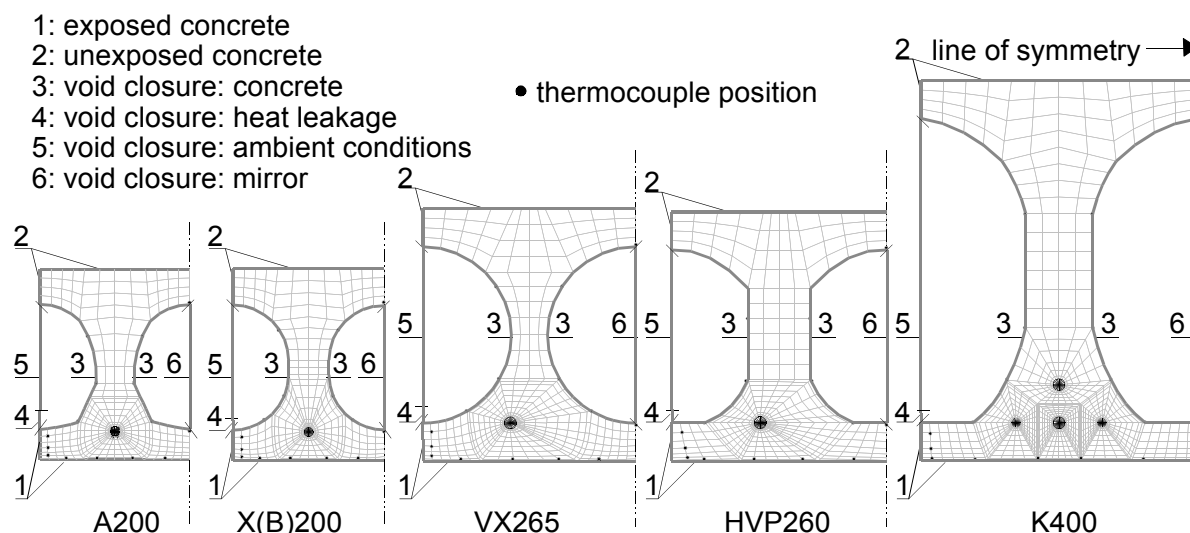


Figure 7.8: Cross sectional meshes of the five types of HC slabs for the calibration of the thermal response.

The thermal model was validated by the comparison of two calculations of the temperature distribution, with the meshes of fig. 7.8:

- on the basis of the measured temperatures, see thermocouple positions in fig. 7.8, combined with adiabatic boundary conditions at the edges, i.e. no heat flow through the boundaries was assumed.
- on the basis of general boundary conditions, i.e. assuming the ISO 834 fire time-temperature curve as the boundary condition at the lower side of the lower flange, ambient conditions around the upper flange, and using the radiative and convective heat exchange model of §5.3.1.2 in the hollow cores. Over the symmetry plane a heat reflecting mirror was applied to close the void. In the other hollow core, two planes were used to close the void. Preliminary calculations showed that the surface temperature at the surface of the hollow core would substantially be underestimated if no heat leakage was assumed through the joint between lower flange and the

insulating plate that covered off the furnace.

Therefore, new calculations were made, assuming the left hand side of the lower flange being directly fire exposed, and using two special planes closing the void in the left hollow core. The larger top face remains at room temperature during fire, the smaller bottom face follows the ISO 834 fire time-temperature curve, representing the heat leakage from the furnace to this core through the joint of the lower flange and the insulation that closes the furnace. Furthermore, the dominant effect of vapour in the cores on the heat transfer, as mentioned in §4.4.4, was considered. Since moisture transport can not be directly taken into account in the heat flow simulations in DIANA, the effect was taken into account using a strongly increased convection coefficient of 200 rather than 8 W/m<sup>2</sup>K between 80-120 °C along the perimeter of the voids. Obviously, this approach is just an approximation of the actual combined heat and moisture transport in the hollow cores. More detailed calculations into the combined heat and moisture flow are outside the scope of this thesis.

As an example, the temperature distributions as calculated with the second approach after 60 minutes of fire exposure are given in the fig. 7.9.

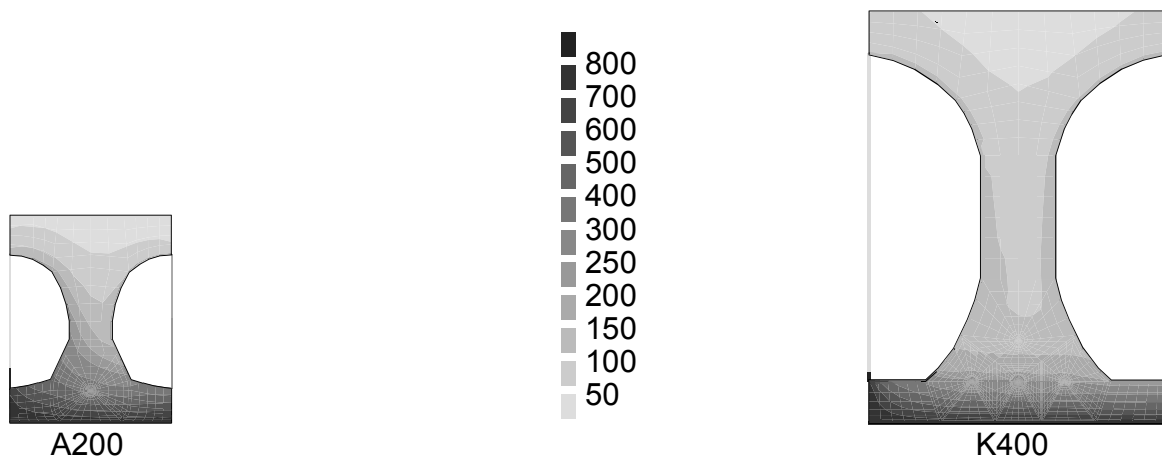


Figure 7.9: Temperatures in double rib specimens R-A200 and R-K400 after 60 minutes based on ISO834 boundary conditions.

These temperature distributions were averaged over the width of the rib in order to be used in the models of the entire model. In these models no temperature variation over the width of the specimens can be taken into account. The comparison between the two calculations was made in terms of these temperature profiles over the depth, see fig. 7.10. The correspondence of the simulations based on the general boundary conditions with the simulations based on the measured temperatures are satisfactory: The differences remain below 50 °C over the entire depth and for all five cross sections over the entire time domain, which is of the same order of magnitude as the standard deviation in the temperature measurements. Therefore, it is concluded that the thermal models are appropriate to further simulate the thermal response.

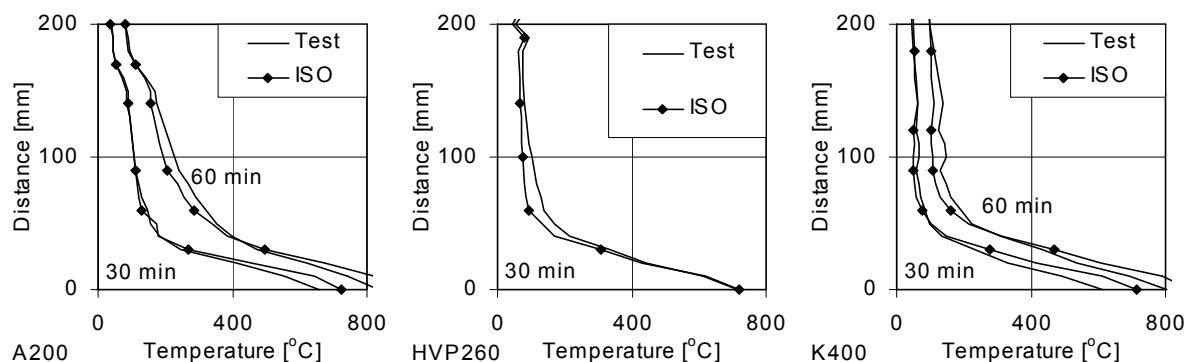


Figure 7.10: Comparison of the calculated thermal response based on measured temperatures with ISO 834 boundary conditions. Left: the A200 specimen. Middle: HVP260 specimens without core filling, Right: K400 specimen.

## 7.3.2 Vertical cracks

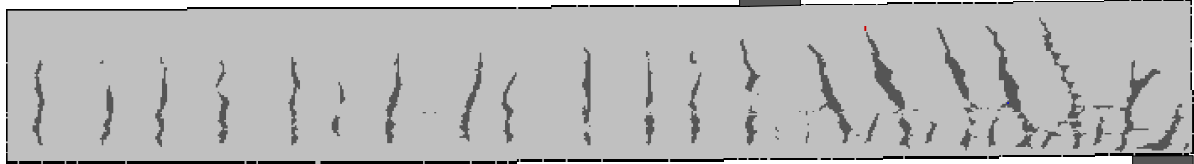
### 7.3.2.1 HVP260-40/40

The vertical cracks as observed in the R-HVP260S-11 specimen were simulated with the FE model of the entire slab. First, the entire slab was modelled, because of the asymmetrical loading. However, the calculation time was too long and the time increments were too large to keep the solution on the equilibrium path. Moreover, the difference between the calculated crack pattern and slip and at the loaded side and the unloaded side was minor, like in the tests. Therefore, only the half of the slab was modelled hereafter, allowing for smaller time increments of only 0.01 minute, within an acceptable simulation time. With the model of half the slab, various simulations were carried out.

The crack development was simulated using the calibrated concrete properties given in table 6.2 on page 153 and the calibrated bond model properties of table 6.4 on page 160. For the estimation of the thermal properties and the thermal expansion, a concrete composition was taken of  $\frac{2}{3}$  siliceous and  $\frac{1}{3}$  calcareous aggregate. The confining action of the concrete cover under the influence of the development of splitting cracks was simulated with the cross sectional model, see §7.3.3.

As shown in fig. 7.11, the vertical cracks develop already within 20 minutes, similar to the measured crack pattern. In that figure, the cracks are visualised above 5 ‰ plastic strain, which corresponds with a crack opening of 0.01 mm, which is based on a typical element size of 4 mm. The cracks are localised in the FE model, even though uniform material properties were used. During the final stage of fire exposure, some vertical cracks near the load grow through the lower flange and the strands are pulled out, i.e. anchorage failure is simulated.

R-HVP260S-11  
20 minutes



R-HVP260S-11  
failure



Figure 7.11: Comparison between calculated and measured crack pattern in R-HVP260S-11 specimen.

The bottom flange is in compression during the first 40 minutes. However, after 60 minutes, the bottom flange turns to be tensioned in the axial direction, see fig. 7.12. The figure shows that the plastic strain in the axial direction changes from negative (compressive stress) to positive (tensile stress) after 40 minutes. This is explained by the fact that the thermal expansion of concrete does not increase beyond 700-800 °C, see fig. 3.7 on page 64, so after 40 minutes, the thermal expansion of the lower flange remains constant. Nevertheless, beyond 40 minutes, the curvature keeps increasing, because of the increasing thermal gradient in the colder parts deeper inside the concrete. The lower flange has almost no strength and no stiffness left, so the contribution of the lower flange to the horizontal equilibrium is negligible, i.e. the thermal gradient in colder parts deeper inside the section determine the thermal curvature. This shift from compression to tension at the exposed side can also explain why explosive spalling of concrete is normally only observed in the early stages of fire exposure, since explosive spalling is commonly at least partly attributed to buckling of the exposed side due to compressive thermal stresses.

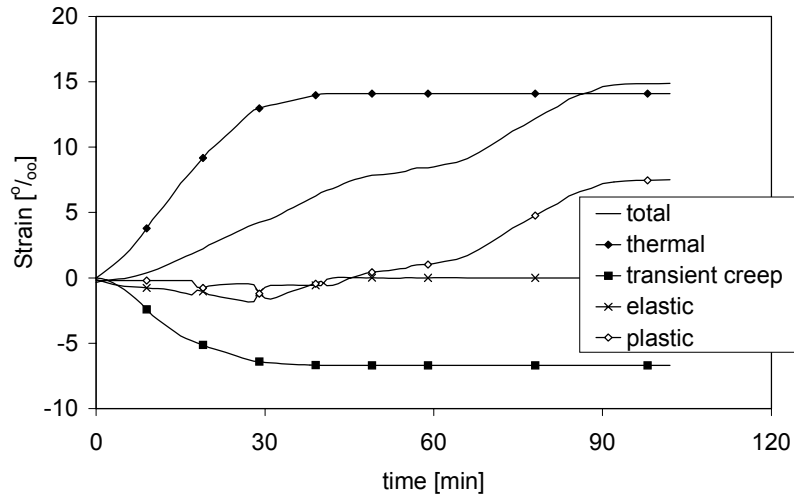


Figure 7.12: Development of the strain components in an element in the bottom flange below the load.

In fig. 7.13, the strain distribution over the depth of the cross section is shown between two vertical cracks below the loading point. It appears that plain cross sections do not remain plain. Over the length of the vertical cracks, the axial strain between the cracks lacks behind the straight line and the deformations are localised in the vertical cracks.

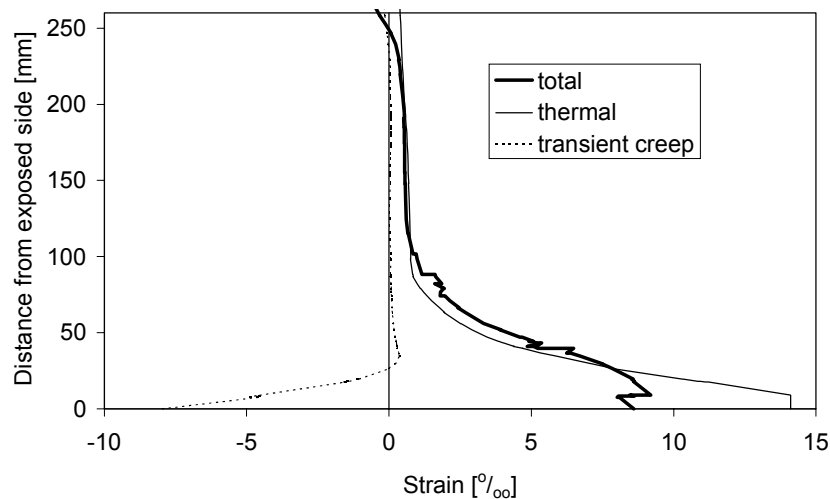


Figure 7.13: Strain distribution over the depth of the cross section of the HVP260 after 60 minutes of fire exposure, below the load, between two vertical cracks.

### 7.3.2.2 XB200 restrained vs unrestrained

As was found in the fire tests on the ribs out of XB200 units, the development of vertical thermal cracks depends on the amount of axial restraint. The axial restraint of 50 kN/mm in the R-XB200-R test, did not prevent the development of vertical thermal cracks, but the length of the cracks remained smaller than in the unrestrained R-XB200 test. In the tests, the time of crack initiation and the mutual crack distance was barely influenced by the restraint.

The capabilities of the FE model to simulate the influence of axial restraint on the vertical thermal crack development was validated by a simulation of the R-XB200 and R-XB200-R test. For this purpose, first the response of the concrete cover to a radial expansion of the strands was calculated using a cross sectional model of the XB200 slab. In this model, the tensile strength and the compressive strength at room temperature were taken from measurements on cores drilled out the XB200 specimens. The decrease of the tensile strength was taken in accordance with the decrease found with the calibration tests, although these tests were carried out on a different concrete mix, i.e. the concrete mix of the HVP260 slabs. Also the fracture energy was taken from the calibration tests at 40 J/m<sup>2</sup>. The XB200 slabs were made with calcareous coarse aggregate with sand as fine aggregate. In the simulations, the thermal expansion was taken from Eurocode 2 [PREN 1992-1-2:2002] assuming <sup>2</sup>/<sub>3</sub> calcareous and <sup>1</sup>/<sub>3</sub> siliceous aggregate.

The calculated and measured crack development after 20 minutes are compared in fig. 7.14. As the figure shows, thermal cracks develop similar to the observations in the tests. Like in the fire tests, the crack spacing nor the time of crack initiation is affected by the axial restraint. Also, the reduced length of the cracks in the restraint specimen is in accordance with the experimental findings.

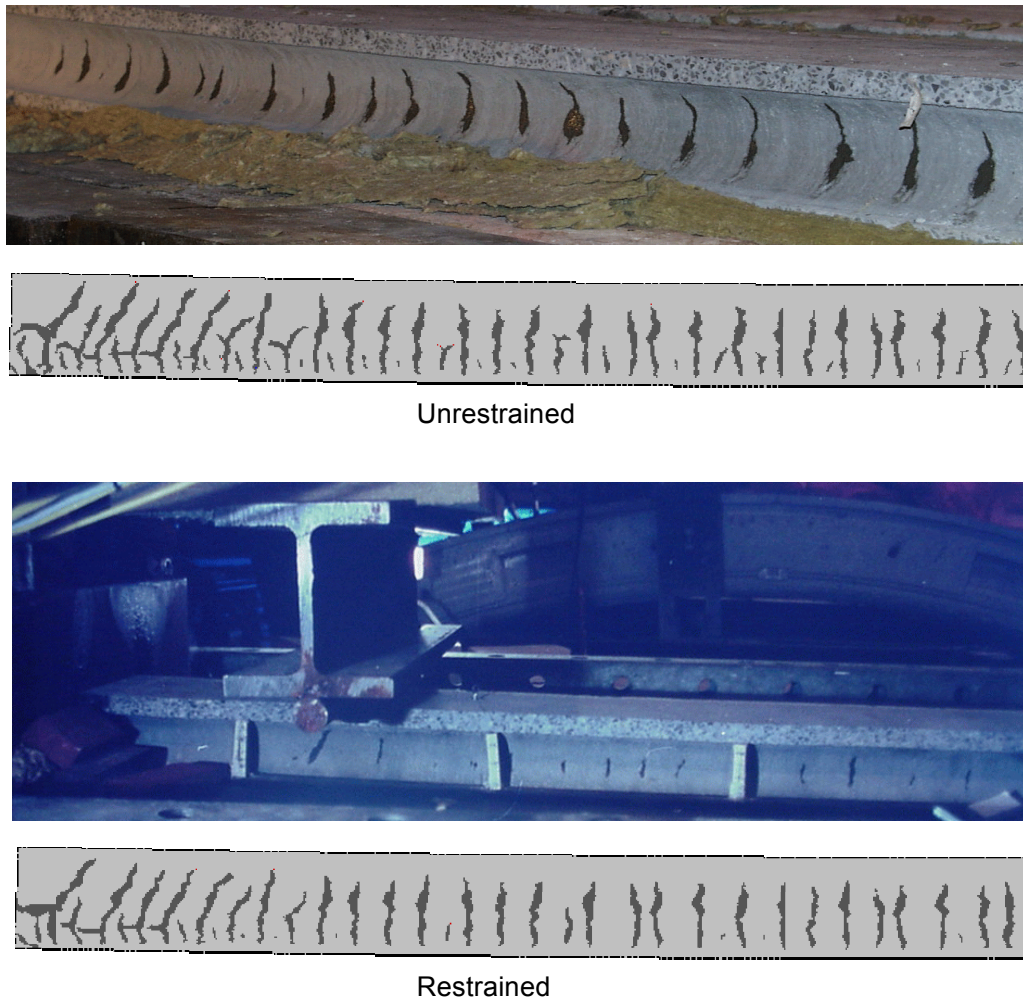


Figure 7.14: Crack development in XB200 rib specimens after 20 minutes of fire exposure.

In conclusion, the FE model is capable to account for the effect of axial restraint on the development of vertical thermal cracks.

### 7.3.3 Horizontal and splitting cracks

As observed in the fire tests, described in chapter 4, horizontal and splitting cracks develop in the specimens. All these cracks were simulated successfully as outlined below.

#### 7.3.3.1 VX265

In the fire tests on the VX265 specimens, horizontal cracks developed through the web at the smallest web width, as described in chapter 4. Also splitting cracks along the strands were observed near the slab end.

The horizontal crack that developed in the VX265 rib specimens (R-VX265 and R-VX265-R) can well be simulated with a FE model of the cross section, see fig. 7.15. The principal plastic strains after 45 minutes are given and the principal tensile stresses after 15 minutes. The deformations are scaled by a factor 10 in this figure. The cracks can be explained by the thermal expansion in the cross sectional plane only. Due to the thermal gradient in the lower flange, the bottom flange tends to bend in transverse direction. As a result, a bending moment develops in both the web and the upper flange. The transverse bending moment causes a crack in the weakest cross section.

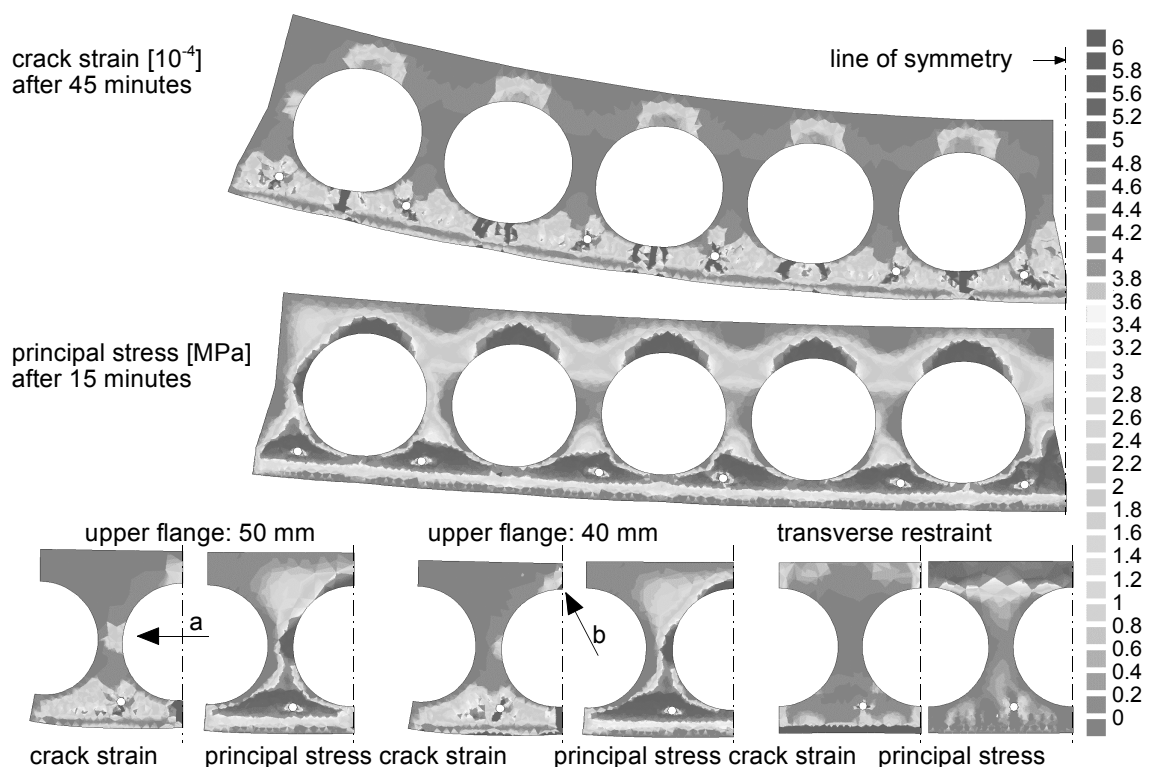


Figure 7.15: Crack strain and principal tensile stress in the cross section of the VX265 specimen.

Fig. 7.15 shows, that in case the nominal thickness of the upper flange was modelled (40 mm), the crack due to the transverse bending develops mainly through the weakest part of the upper flange (arrow b). While in case the actual upper flange thickness of 50 mm was modelled, the web is the weakest cross section and a horizontal crack develops (arrow a). Once the crack initiates, the transverse bending moment vanishes. However, the crack can grow and lead to failure due to the additional load induced shear stresses in the web that do not vanish after crack initiation.

In the fire test on the VX265 unit, the horizontal cracks through the webs were less pronounced than in the tests on the double rib specimen, which is in accordance with the simulations. In the cross sectional model of the entire HC unit, smaller transverse bending stresses develop in the webs, except for the outer web. As a consequence only the outer web cracks. Still horizontal cracks could develop in the test due to the additional shear stresses, required to balance the external load and to introduce the prestress and the thermal stresses in the axial direction.

Finally, a simulation of the rib specimen was carried out in which the transverse deformation was fully restraint. As a result, no bending transverse moment develops nor a horizontal crack in the web. Furthermore, it is shown that the principal tensile stress around the strand vanishes. As will be shown later, the transverse restraint has a beneficial effect on the confining action of the concrete cover on the strand.

### 7.3.3.2 *Splitting cracks in HVP260 and K400*

In the HVP260 and K400 specimens, splitting cracks were observed along the strands. In the ribs in which the strand was positioned near the web, the splitting crack developed horizontally from hollow core to hollow core reducing the shear capacity of this web. In the ribs, in which the strand was positioned lower in the lower flange, the crack grew from the nearest hollow core to the exposed side.

With the cross sectional models, these cracks were simulated, see fig. 7.16. The length of the lines indicate the crack opening. The scale of these lines varies between the cross section in order to control the clarity of the picture. Clearly, the splitting cracks were calculated in the observed direction, although more cracks were calculated in the lower flange than just the splitting cracks.

The splitting cracks can be explained by the thermal expansion. The gray part shows that the thermal expansion of steel and concrete is almost identical. However, the strand has a more or less uniform temperature leading to an axially symmetrical thermal expansion, while the concrete cover at the bottom side of the strand expands more than the concrete at the top side. As a result, the shape of the concrete void around the strand changes from a cylindrical one to an ellipsoidal one, leading to contact points where compressive forces develop, that lead to splitting cracks. With the inclusion of the splitting stresses due to the radial expansion of the strand during slippage, larger splitting cracks are calculated, see the third picture in fig. 7.16.

The propagation of splitting cracks results in a decreasing confining action. The mean radial compressive stresses caused by radial expansion of the strand were calculated after various periods of fire exposure. A distinction is made to cross sections that undergo a large radial expansion of the strand during the release of the prestress, nearly up to the development of

splitting cracks and cross sections that do not undergo any radial expansion during the release of the prestress. In fig. 7.17, the resulting confining stress curves are shown for the R-HVP260S specimens using the calibrated values for the fracture energy, the concrete tensile strength and the interface stiffness, as given in table 6.2 on page 153. The thermal expansion was based on the assumption of  $\frac{2}{3}$  siliceous and  $\frac{1}{3}$  calcareous aggregate.

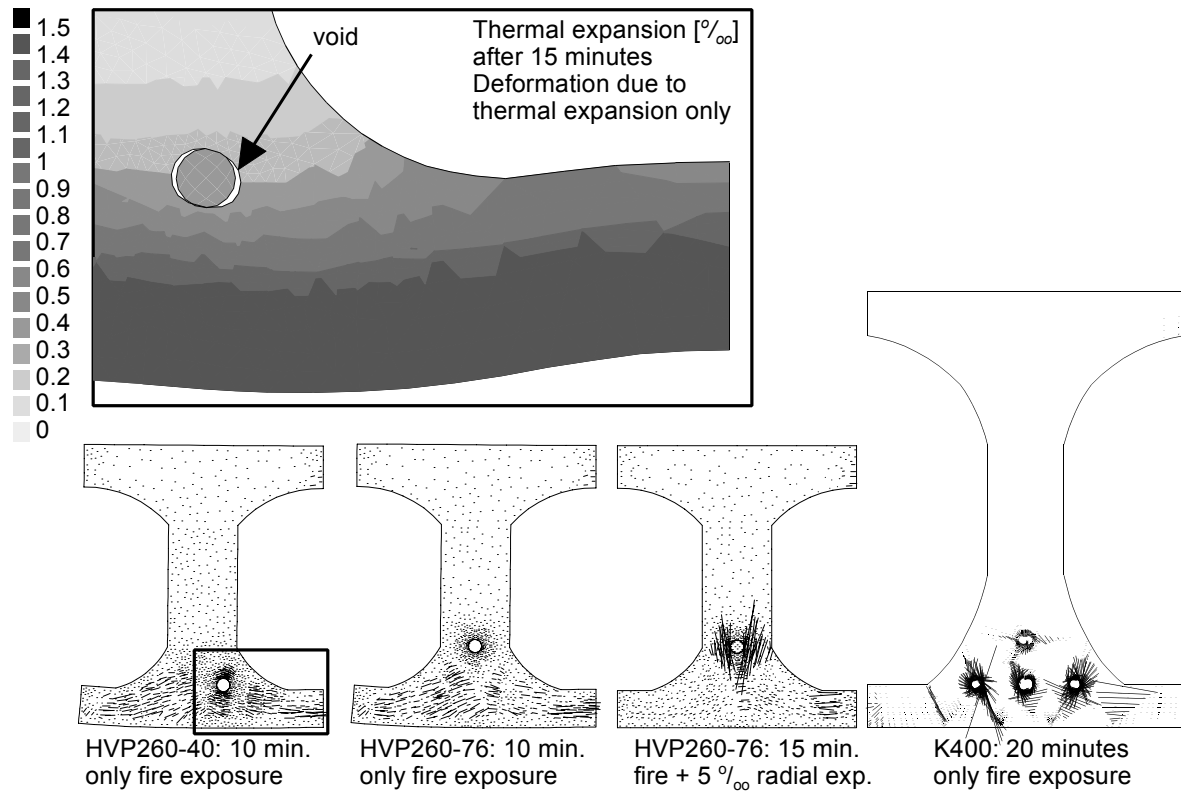


Figure 7.16: Calculated splitting cracks during fire exposure.

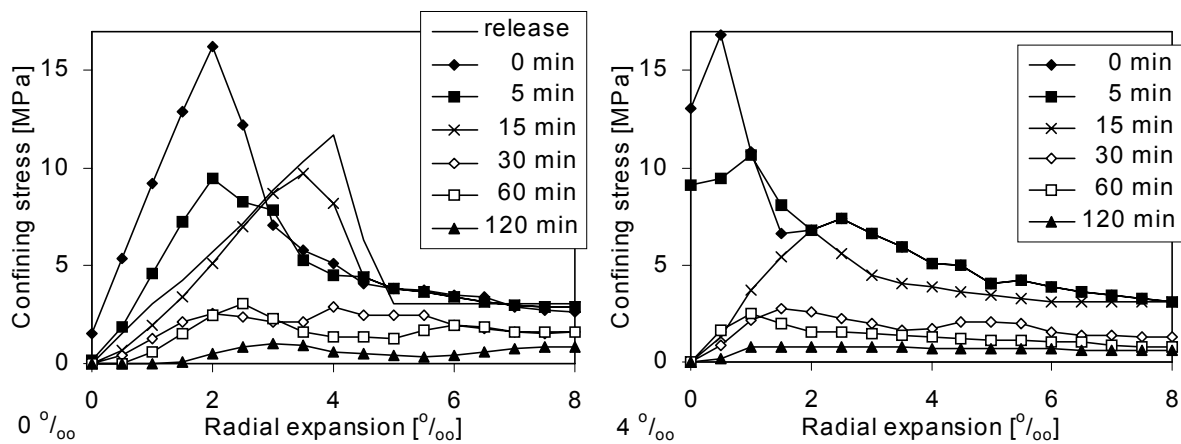


Figure 7.17: Confining stress curve for R-HVP260S specimens, based on the calibrated properties for concrete and the interface. Left: Simulation of fire and radial expansion without initial radial expansion due to the release of prestress. Right: with  $4\text{‰}$  initial radial expansion due to the release of the prestress.

Also the shear stresses cause horizontal cracks in the web. However, due to the use of a separate 2D model of the cross section and a separate 2D model of the entire slab, the effect of the shear stresses caused by the applied loading and the introduction of the prestress and the thermal stresses in the axial direction could not be combined with the splitting stresses and thermal stresses in the cross sectional model. Nevertheless, with the model of the entire slab of the symmetrical HVP260 specimen with two strands at 40 mm from the exposed side, minor horizontal cracks were calculated after the vertical cracks had formed at the level of the smallest web width, see fig. 7.11. The horizontal cracks are the result of the transfer from the shear stresses between the vertical cracks. After all, splitting stresses around the strands can not be calculated in the FE model of the entire slab, nor stresses that develop due to incompatibility of thermal strains in the transverse direction. High vertical compressive stresses are calculated in the vertical cracks parallel to the crack plane, see fig. 7.18. These compressive stresses are balanced by vertical tensile stresses in the concrete zones between the vertical cracks, which exceed at some point the tensile strength.

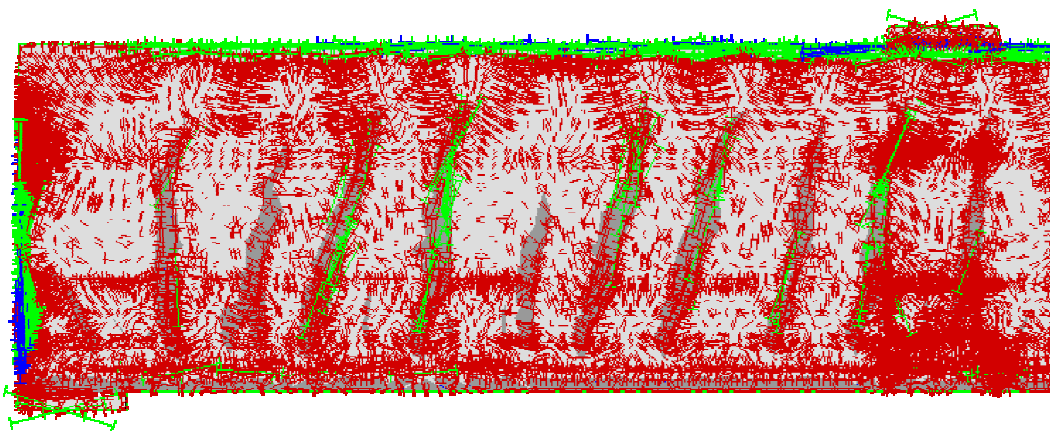


Figure 7.18: Crack pattern in grey scale after 60 minutes plus principal compressive stresses with vectors. The length of the lines indicates the size, the blue lines indicate the highest compression, the red lines the lowest.

In conclusion, horizontal cracks as observed in the fire tests along the strands were successfully simulated with the FE models, both in terms of the time of crack initiation and in terms of crack orientation. The cracks are the result of incompatible thermal strains in the transverse direction, splitting stresses and shear stresses. The simulations are successful, despite the fact that the effects of splitting stresses, calculated with the cross sectional models and shear stresses, calculated with the model of the entire slab, can not be combined in one simulation.

### 7.3.3.3 XB200 restrained

A splitting crack suddenly developed horizontally through the end of the web of the restraint XB200 rib specimen in the fire test after 117 minutes (test reference R-XB200-R), due to the introduction of the restraining force. This splitting crack did not cause failure. The latter crack was also observed in the simulation of the restraint XB200 specimen. The first simulation of the restraint specimen diverged after 28 minutes due to the development of a horizontal splitting crack at the point of the introduction of the restraining force. This early crack propagation was attributed to the too small steel plate that was modelled at the sawn end of the slab to introduce

the restraining force. Hereafter, the simulation was carried out again, but this time, the restraining force was introduced in a smoother way, using a larger steel plate at the sawn end of the slab with a soft interface layer in between the steel plate and the slab end. In the new simulation, no splitting cracks were calculated.

### 7.3.4 Slip development and failure behaviour

#### 7.3.4.1 HVP260-40/40

In this paragraph, the slip development is presented that was obtained with the model of the fire test R-HVP260S-11. The model was discussed in §7.3.2.1 concerning the calculated crack pattern. With this model, an additional simulation was made with a modified loading to simulate the fire test R-HVP260S-23 (23 % shear load instead of 11 % relative to the actual load bearing capacity at ambient conditions).

All simulations resulted in anchorage failure. The calculated slip development was in very good agreement with the measurements up to the time the strands are pulled out, see fig. 7.19. Like in the tests, the slip development is barely influenced by the load level, but the time to pull out failure is influenced considerably.

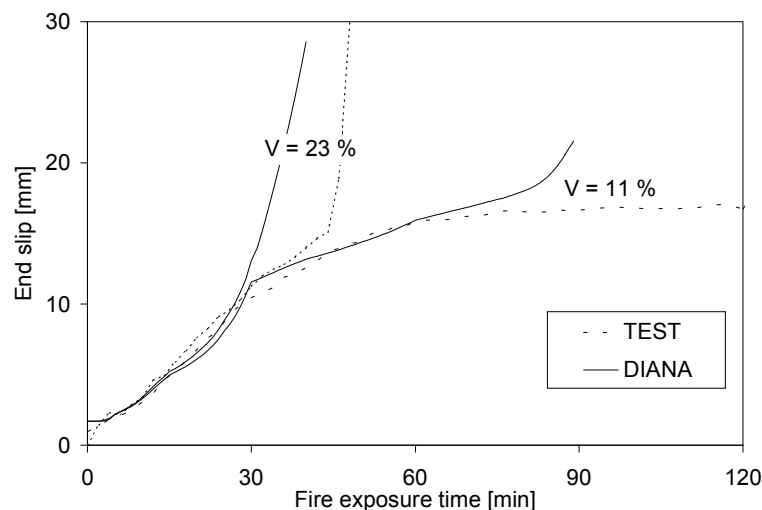


Figure 7.19: Slip comparison between the FE model and the fire tests on the R-HVP260S specimens with 11 and 23 % shear loading respectively.

In fig. 7.20, it is further illustrated that the slip increase at the onset of failure is caused by pull out failure. The figure shows that the strand is only pulled out over the zone from the support to the point load. Up to approximately 20 minutes the slip development of the simulation with 11 % and 23 % shear loading is very similar.

However, pull out is calculated too early, i.e. after 90 minutes instead of 123 minutes for the test with 11 % shear loading and after 40 minutes instead of 48 minutes for the test with 23 % shear loading. The discrepancy between the calculated and measured time to failure is attributed to the sensitivity of the failure time to various influence parameters. In chapter 8, it will be shown that

small changes in the fracture energy and the thermal expansion have a huge influence on time to failure. Moreover, in the R-HVP260S specimen one  $\varnothing$  9.3 mm strand was placed in the upper flange, which was assumed to have the same bond characteristics as the bottom strands in the simulations for the sake of simplicity. In doing so, the contribution of this strand was underestimated, especially in the fire test with only 11 % shear load.

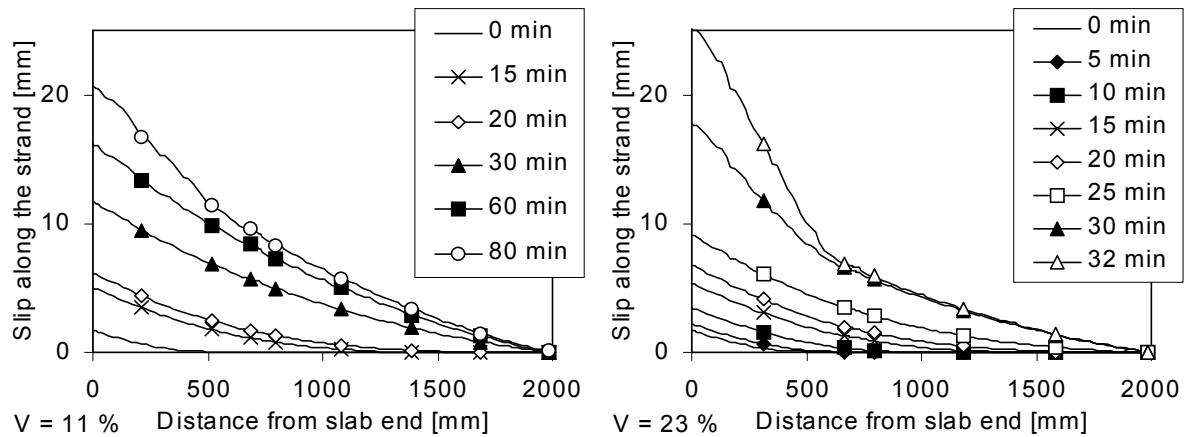


Figure 7.20: Slip development along the strands in the simulations of the R-HVP260S fire tests with 11 % shear loading (left) and 23 % (right).

With the axial FE model, it is possible to monitor the steel stress along the strands, see fig. 7.21. It appears that the transfer length increases rapidly right after the start of the fire, which is caused by the decrease of the bond strength, i.e. the slope of the curve of the steel stress along the strand is determined by the bond stress. Nevertheless, the steel stress at mid span increases beyond the initial prestress value due to the incompatible thermal strains. In longer spans, the steel stress can easily reach the yield strength. However, this would not lead to direct failure, since it is caused by imposed deformations rather than by imposed stresses. Once the strand starts to yield, the imposed deformation would be counteracted. Moreover, the bond strength would locally decrease over the zone of yielding of the strand, leading to a lower stress increase.

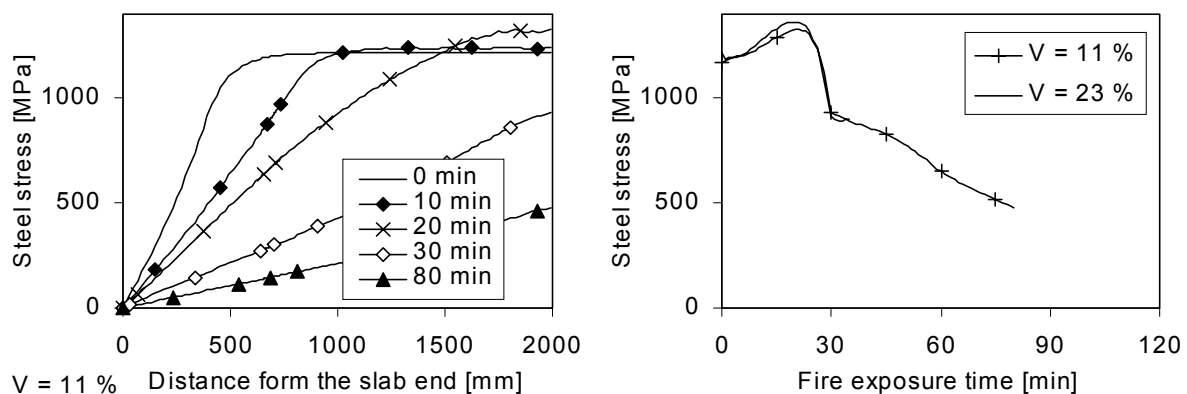


Figure 7.21: Steel stress development along the strand (left) in the simulation of the R-HVP260S-11 fire test and during fire exposure at mid span (right) of the R-HVP260S -11 and -23 fire tests.

With the model it is proven that the adhesion has a minor effect on the anchorage behaviour of fire exposed HC slabs: The contributions of the friction and the adhesion to the bond strength are

evaluated. In fig. 7.22, the bond strength and the adhesion are shown along the strand. Clearly, the contribution of the adhesion vanishes almost completely after 20 minutes and only the frictional part remains.

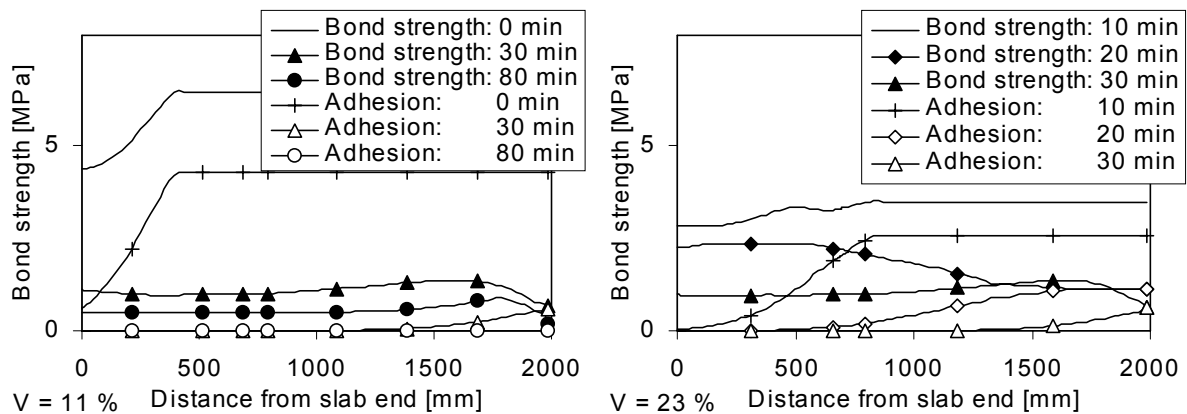


Figure 7.22: Bond strength and contribution of the adhesion along the strand at various times of fire exposure for R-HVP260S fire tests with 11 % shear loading (left) and 23 % shear loading (right).

Furthermore, it is concluded that the decrease of the pull out resistance during the fire depends only to a minor extent on the shear loading during fire exposure: The bond strength after 30 minutes is almost identical over the entire length of the strand for the simulation with 11 % shear loading and 23 % shear loading, see fig. 7.22. So, the applied loading does barely contribute to the decrease of the anchorage capacity. Also the radial expansion along the strand is almost identical after 30 minutes for both loading situations, see fig. 7.23, leading to the same conclusion.

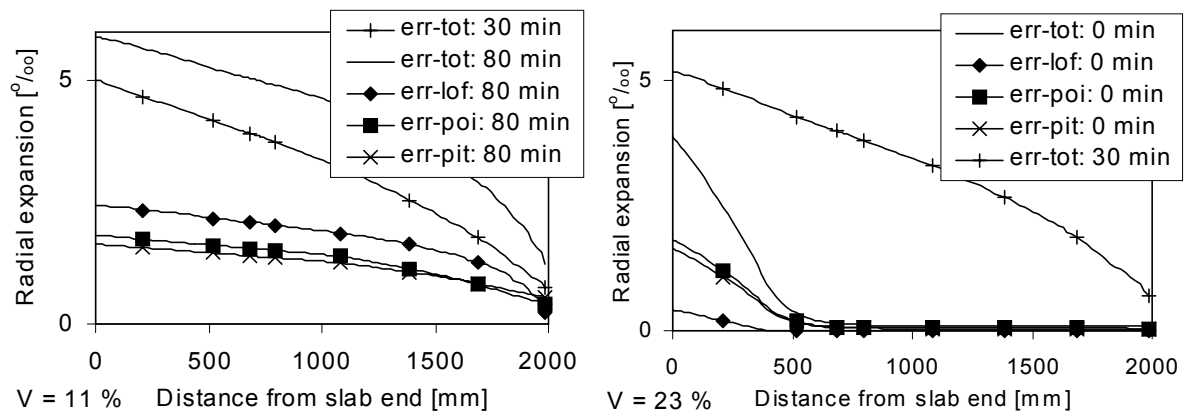


Figure 7.23: Calculated fictitious radial expansion of the strand and the contributions of the lack of fit effect, the Poisson effect and the pitch effect along the strand after various times of fire exposure. Left: the specimen loaded at 11 % of the ambient shear capacity. Right: loaded at 23 %.

### 7.3.4.2 XB200 restrained vs unrestrained

The slip development in the restrained fire test R-XB200-R on the double rib specimen out of a XB200 slab was significantly smaller than the slip development in the unrestrained fire test R-XB200. This observed behaviour was simulated with the model of the XB200 slab that was already discussed in §7.3.2.2.

The calculated and measured slip are compared in fig. 7.24. The slip development of both the restrained and the unrestrained specimen increases too rapidly in the beginning of the fire. The axial elongation of the concrete at the location of the strand is in relatively good agreement with the measurements, see also fig. 7.24.

As will be shown in the sensitivity study in chapter 8, the early slip can be attributed to the loss of bond rather than to the axial elongation of the concrete cross section. Therefore, the discrepancy between the measured and calculated slip is attributed to an underestimation of the fracture energy. Also, the discrepancy in the axial elongation of the concrete near failure must be attributed to an underestimation of the fracture energy, because the too rapid increase of the axial elongation near failure in the simulation is caused by the opening of the failure crack, rather than an error in the thermal expansion. The fracture energy was taken from the calibration tests which were carried out using the concrete mix related to the HVP260 specimens rather than the current XB200 specimens. So, it is well possible that the fracture energy of the concrete applied in the XB200 specimens was actually higher than the assumed  $40 \text{ J/m}^2$ . In the sensitivity study it will also be shown that the underestimation of the fracture energy can also explain the underestimation of the time to pull out failure, as a higher fracture energy would lead to an improved confining action and a substantial increase of the time to failure.

Nevertheless, the calculated effect of the axial restraint is fairly consistent with the measurements. Like in the tests, the slip and the axial elongation of concrete in the restrained specimen is substantially smaller than the slip respectively the axial elongation of concrete in the unrestrained specimen.

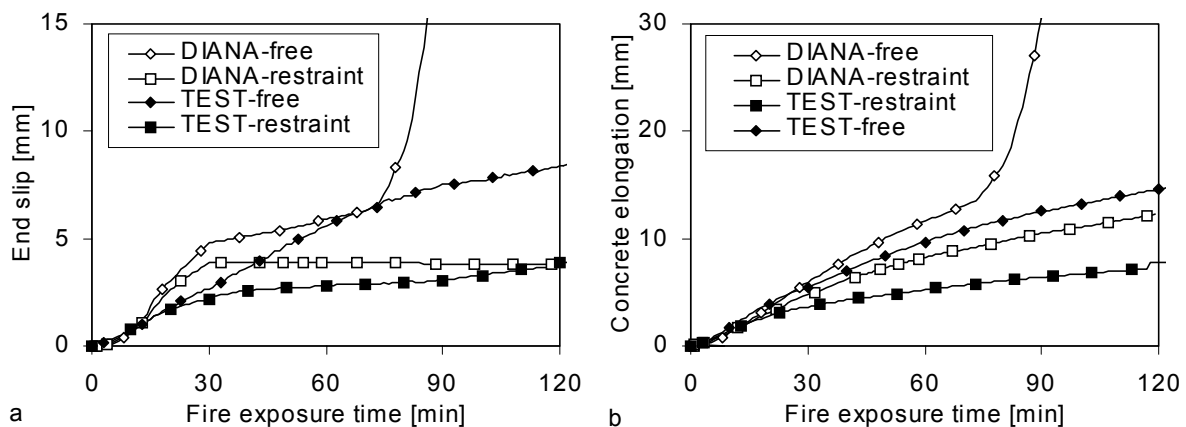


Figure 7.24: Comparison between the fire tests and the FE simulations for the R-XB200 and R-XB200-R specimens. a: Slip development, b: Axial elongation of the concrete at the location of the strand.

### 7.3.5 Conclusions

The FE models can describe the introduction of the prestress and the shear and anchorage behaviour at ambient conditions very well. The transfer length is calculated in good agreement with the Model Code formulation [CEB-FIB: 1991]. The failure load for shear tension failure is in accordance with the value obtained in tests. The failure load for anchorage failure differs some 20 % with the measured values, which is attributed to different bond characteristics obtained in the small scale calibration tests compared to those for the precast HC slab.

More important, the FE models can also describe the slip development, the crack pattern and the shear and anchorage behaviour of fire exposed HC slabs very well. The effect of restraining support conditions could adequately be simulated as well. Also the effect of the applied load on the slip development, crack pattern and time to failure is consistent with the test results. However, the time to failure could not perfectly be matched which is attributed to the uncertainty for the estimation of the dominant input parameters as will be shown in the next chapter.

As the FE models describe the shear and anchorage behaviour adequately, the FE models provide a proper basis for the conduction of a sensitivity study in order to determine the relevance of the various design parameters and to provide recommendations for design.



# 8 Evaluation

## 8.1 INTRODUCTION

A sensitivity study was carried out to investigate the effect of various influencing parameters were evaluated on the time to failure, the slip development and the crack development. The bond model parameters, except for the friction coefficient were not analysed with the FE models, because it was proven by theoretical considerations in chapter 6 that these parameters have a minor effect on the shear and anchorage behaviour of fire exposed HC slabs. They only effect the behaviour at ambient conditions. As an example, this paragraph starts with the demonstration of effect of the bond model parameters n the transfer length.

With respect to fire exposed HC slabs, the influence parameters are subdivided into three classes:

- External conditions
- Material properties
- Geometrical properties

Their effect on the shear and anchorage behaviour of fire exposed HC slabs is discussed in §8.3. This chapter ends with the evaluation of the consequences of the findings for the design of HC slabs.

## 8.2 PARAMETRIC STUDY ON THE TRANSFER LENGTH

In order to evaluate the parameter importance on the transfer length after the release of the prestress, each bond model parameter was varied around it's calibrated value as obtained with the calibration tests. While one parameter is varied, all other parameters were kept at the

calibrated values. The values were varied around the calibrated values in order to show the sensitivity of the confinement curve to these parameters in a relevant range.

The tensile strength  $f_{ct}$ , the fracture energy  $G_F$ , and the interface stiffness  $K_i$  were varied in determining the confining stress curves. The calibrated values,  $f_{ct} = 6.0$  MPa,  $G_F = 40$  J/m<sup>2</sup> and  $K_i = 3900$  N/mm, were obtained after 28 days of maturing, while the prestress is released a few hours after casting. Therefore, the calibrated value of the tensile strength and interface stiffness were reduced according to the strength development during maturing as given in fig. D.1 on page 255. The tensile strength was reduced within the concrete model to 3.86 MPa. The calibrated interface stiffness was reduced to 1300 N/mm. The final crack pattern as shown in fig. 7.1 appeared to be fairly independent of the material's properties.

The tensile strength mainly affects the peak stress and the radial expansion at the peak stress of the confinement curve, see fig. 8.1. The post-cracked branch is hardly affected by the tensile strength. The fracture energy has an important effect on the post-cracked branch, see fig. 8.2. The observations of the calculated confining stress curves are in accordance with the findings of chapter 6, which were based on the thick-walled cylinder model of Den Uijl.

The interface stiffness mainly affects the slope of the ascending branch of the confinement curve and the radial expansion at the peak stress. The effect on the peak stress and the post-cracked branch is negligible. As a result, the interface stiffness will have a substantial effect on the occurrence of splitting cracks, but the influence on the anchorage behaviour after splitting cracks developed will be small.

The confining stress curve is just an intermediate result. Therefore, the effect of the bond parameters was further explored using the FE model of the entire slab, in which the confining stress curves were used as input. Also the other bond model parameters were analysed with the model of the entire slab.

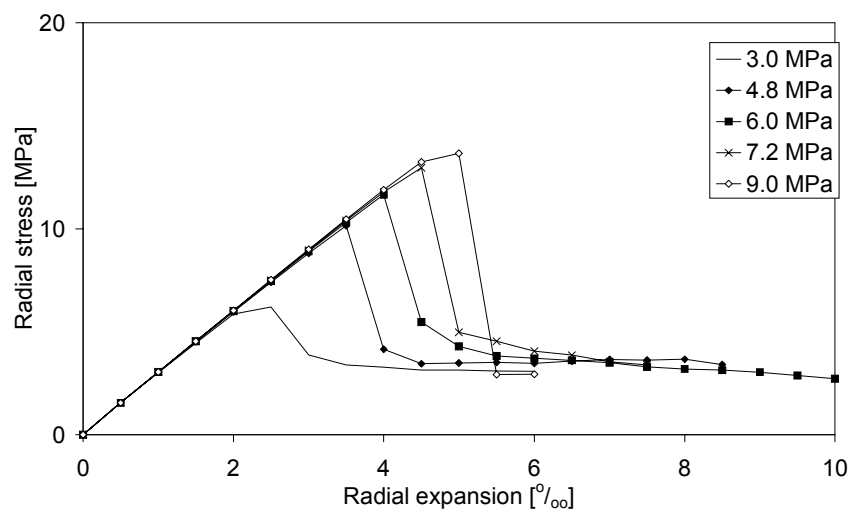


Figure 8.1: Confining stress curves for the HVP260 specimen at the time of the release of the prestress, for different values of  $f_{ct}$  after 28 days.

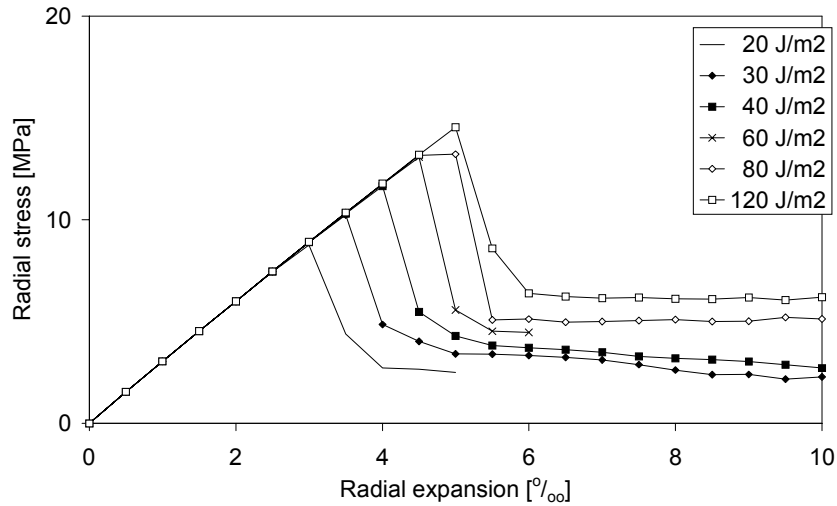


Figure 8.2: Confining stress curves for the HVP260 specimen at time of the release of the prestress, for different values of  $G_F$ .

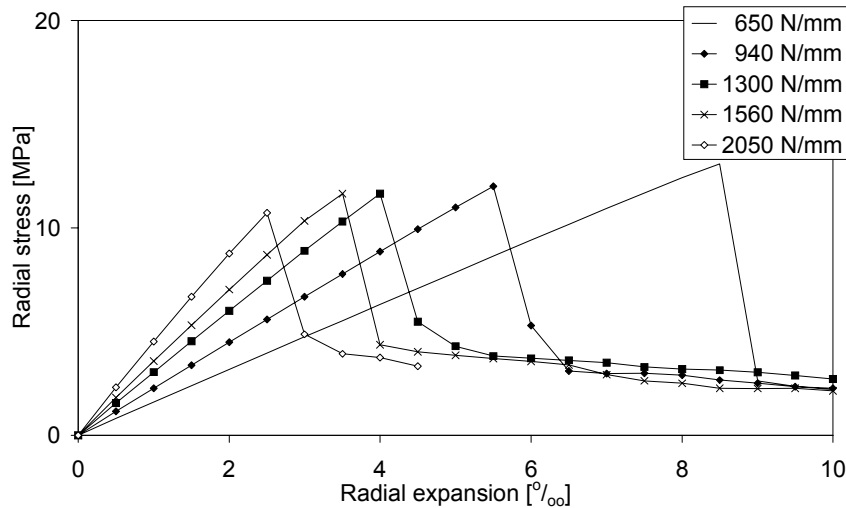


Figure 8.3: Confining stress curves for the HVP260 specimen at time of the release of the prestress, for different values of  $K_i$ .

In the left picture of fig. 8.4, the prestress development near the end of the slab is shown, as derived on the basis of the calibrated values. Also the initial prestress level of 1250 MPa in the strand before release is shown. After the prestress is released a maximum prestress of 1217 MPa remains at mid span, which corresponds to 3 % direct losses (excluding time dependent losses). The variation of the prestress development is shown for a variation of the interface stiffness between 50 and 150 % of the calibrated value. Remarkably, the calibrated value of the interface stiffness appears to result in a smaller transfer length than either a larger or a smaller value. In case a higher stiffness is chosen, the confinement curve is more brittle and larger splitting cracks are calculated, leading to a decreased bond strength over a larger length near the slab end and thus an increased transfer length. In case a smaller interface stiffness is applied, the confinement stress that belongs to a certain radial expansion over the ascending branch is lower than for the calibrated values and consequently a lower bond strength and an increased transfer length is obtained.

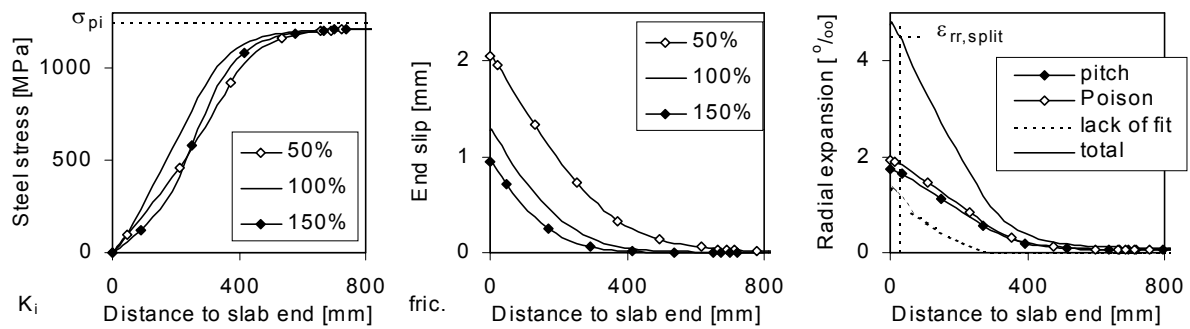


Figure 8.4: Left: Development of the prestress along the strand, varied for three values of the interface stiffness  $K_i$ . Middle: Development of the slip along the strand for various friction coefficients. Right: Development of the fictitious radial expansion along the strand and the separate contributions of the lack of fit effect, the Poisson effect and the pitch effect.

In the middle picture of fig. 8.4 the slip development is shown. The slip development was plotted for three values of the friction coefficient, relative to the calibrated value. Clearly, the friction coefficient has a substantial effect on the slip development. In the right picture of fig. 8.4, the radial expansion is presented as calculated with the calibrated values for the bond model parameters. The radial expansion is the sum of the contributions of the lack of fit, the Poisson effect and the pitch effect. For the calibrated case, the frictional part of the bond strength is dominated more by the change in the steel stress (the Poisson effect and the pitch effect) than by the slip (lack of fit effect).

In fig. 8.5 the variation of the transfer length is shown for various bond model parameters. Clearly, the adhesion and friction coefficient, together with the tensile strength dominate the transfer length, (compare the left to the middle picture of fig. 8.5).

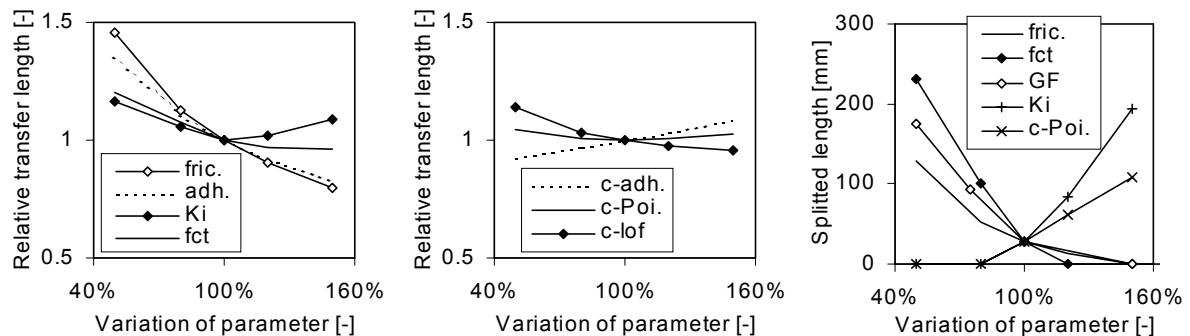


Figure 8.5: Relative variation of the transfer length and length of the splitting cracks in function of the basic model parameters.

The length of the fully developed splitting cracks is also shown in fig. 8.5. For the calibrated values, the peak of the confining stress is reached at  $4 \text{ ‰}$  radial expansion. For the calculation of length of the splitting cracks, it is assumed that the splitting cracks are fully developed at a radial expansion of  $4.5 \text{ ‰}$ . With the calibrated values splitting cracks develop over some 30 mm. In practice, splitting cracks that can be observed clearly, are not allowed and producers adapt the maturing time to prestress release in such a way that splitting cracks are just avoided. The

discrepancy between model and practise can be explained by the fact that only a 20 % increase of for instance the tensile strength or a 20 % decrease of the interface stiffness is sufficient to avoid splitting cracks. It can reasonably well be expected that the calibrated values obtained from small test specimens differ this much from the values in the production plant.

In conclusion, the adhesion strength and the friction coefficient are the most dominant bond model parameters regarding the transfer length. The importance of the adhesion is expected to vanish during fire while slip increases. The tensile strength, the fracture energy and the interface stiffness have a substantial effect on the occurrence and propagation of splitting cracks. The effect of the fracture energy and the interface stiffness on the transfer length is small.

## **8.3 PARAMETRIC STUDY ON FIRE EXPOSED HC SLABS**

### **8.3.1 External conditions**

#### *8.3.1.1 Introduction*

External conditions can be split into the thermal and mechanical loading and the support conditions.

As thermal loading, the standard fire curve was assumed so far. Obviously, in reality the range of fires that can occur is large. It could be evaluated using for instance the parametric fire curves of Eurocode 1 [PREN 1991-1:2002] or more recently developed fire models. These curves are characterised by a heating phase and a cooling phase. However, the constitutive models were not validated for the cooling phase and the material properties were not calibrated for this case. Therefore, other fire conditions than the standard fire curve were not analysed in the thesis. Nevertheless, it must be expected that another fire curve will affect the thermal gradient and the development of the incompatible thermal strains in the slab and consequently the formation of the thermal cracks, the slip development and the final failure behaviour. However, as the models developed in this thesis are very generic, they have the potential to cover these fire conditions as well.

The mechanical loading concerns the loading configuration (point load and it's location or uniformly distributed load) and the degree of utilization. In the sensitivity study, only the degree of utilization was evaluated. The loading configuration of the fire tests of chapter 4 was used in the sensitivity study.

With regard to the support conditions, the effect of restraining boundaries in the axial and transverse direction was analysed briefly.

#### *8.3.1.2 Shear loading*

One of the major uncertainties in the design is the actual shear load that will be present during fire. As already shown in the fire tests R-HVP260S-11 and R-HVP260S-23 and the simulation of these tests, the time to failure strongly depends on the shear loading while the slip development and is barely influenced by it until the onset of failure. An additional simulation

was made of R-HVP260S-11 with 12.2 kN instead of 11.1 kN shear load during fire exposure and of R-HVP260S-23 with 24.4 kN instead of 22.8 kN. The time to failure decreases from 40 to 32 minutes for fire test R-HVP260S-23 and from 91 to 80 minutes for fire test R-HVP260S-11.

In fig. 8.12 on page 197, the effect of the shear loading on the crack development is given. Similar to the observations in the fire tests, barely any influence of the shear loading on the crack propagation is found.

Finally, additional simulations were made with the FE model of the entire slab in order to determine the ultimate load bearing capacity after some characteristic time points. In these simulations the load is increased up to failure after distinct durations of fire exposure. The simulations start with a stored state of the internal stresses and damage of a simulation in the time domain with constant load. The results are given in fig. 8.6. The load bearing capacity is also presented for a HC slab for which it was assumed that the thermal expansion of concrete was zero. For this case, the calculation sequence to obtain the decrease of the load bearing capacity is illustrated: the horizontal line indicated the load level during heating, the vertical lines indicate the increasing load up to failure after the distinct periods of fire exposure.

The anchorage capacity decreases rapidly after the start of the fire. Beyond 30 minutes, the further decrease is limited.

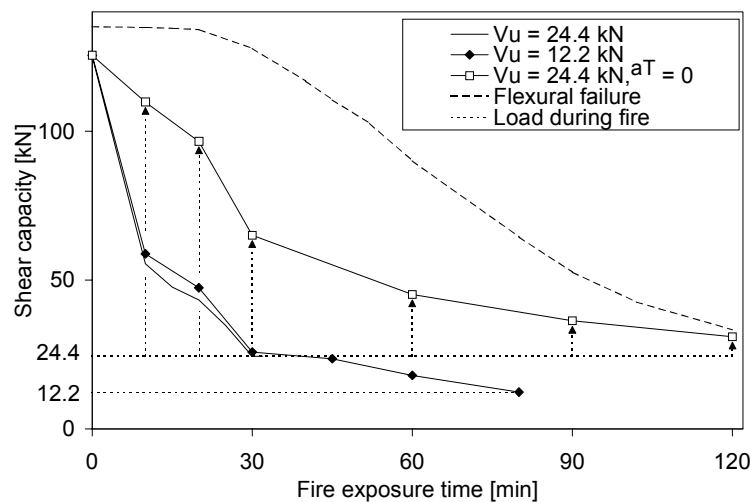


Figure 8.6: Calculated decrease of the anchorage and flexural capacity during fire exposure of the R-HVP260S specimen, depending on the shear load during fire exposure and the thermal expansion of concrete.

The comparison of the anchorage capacity of the simulation with 12.2 and 24.4 kN shear load during fire shows that the shear load during fire has only a small effect on the ultimate capacity that remains. It means that the load does not need to be taken into account in the calculation of the anchorage capacity.

From the simulations with the increasing load after a certain time of fire exposure, the actual failure behaviour is better understood.

After 10 minutes fire exposure, vertical thermal cracks already formed. When the load is increased, some of these cracks in the middle between the point load and the support grow into flexural cracks, see fig 8.7. In this figure, the cracks are presented that are beyond a plastic strain of 10 ‰, which corresponds approximately to a crack opening of 0.02 mm. After the flexural cracks formed, the strands are directly pulled out. After 25 minutes fire exposure, a similar type of failure is obtained, however, the flexural crack develops even closer to the support. After 60 minutes fire exposure, the flexural crack develops rapidly already at an increase of the shear load from 12.2 to 15.8 kN. Hereafter, the load can still be increased until pull out failure is reached at 18.0 kN. Moreover, the flexural crack that opens at failure is located closer to the point load, see fig. 8.7.

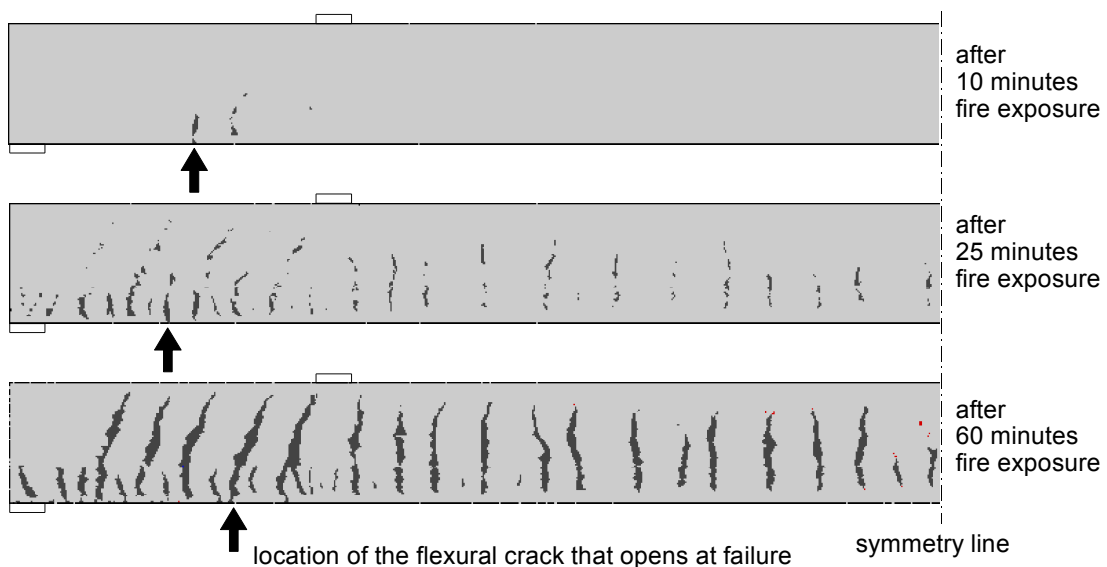


Figure 8.7: Flexural crack development due to an increasing shear load after various times of fire exposure.

Anchorage failure is limited by the maximum value of the cracking moment capacity and the pull out capacity. In the early stage of the fire, the splitting cracks cause a rapid decrease of the pull out capacity. The vertical cracks cause rapid decrease in the cracking moment capacity. For the current R-HVP260S specimen, (with 2 strands at 40 mm from the exposed side) the pull out capacity decreases faster within the first 10 minutes than the cracking moment capacity and the cracking moment remains larger from 10 up to 30 to 60 minutes. As a result, failure is relatively brittle if it occurs in this period and the flexural cracks are located closer to the support than at ambient conditions. As a consequence, the cracks are inclined and look more like shear cracks. The crack propagation is driven by a combination of bending and shear stresses. Therefore, it could also be defined as shear failure. Especially, for the R-HVP260A specimens (with one strand at 76 mm from the exposed side near the web and one strand at 40 mm from the exposed side), the development of the horizontal splitting cracks through the web yields a failure crack pattern of flexural cracks connected to the horizontal cracks and failure looks even more like shear failure.

Beyond 30 minutes, the pull out capacity of the R-HVP260S barely decreases while the cracking moment does due to the gradual loss of the prestress and the growth of the vertical thermal

cracks. As a result, after 60 minutes, the pull out capacity becomes larger than the cracking moment capacity again. Failure is relatively ductile if it occurs after more than 60 minutes fire exposure.

In conclusion, the decrease of the load bearing capacity of HC slabs is only slightly dependent on the degree of utilization during fire exposure. The anchorage failure is limited by the highest value of the cracking moment capacity and the pull out capacity, which can alternate during the fire. As the flexural cracks can open closely to the support and grow together with horizontal cracks, also shear failure can govern the behaviour in some stage of the fire exposure.

### 8.3.1.3 Restraining boundaries

In practical situations, the thermal expansion of fire exposed HC slabs will partly be restrained. As already outlined in chapter 3, effects of restraint often overshadow the other factors that determine the fire behaviour. From the experiments, it was concluded that restraining boundaries can substantially improve the fire resistance. With the axial model of the R-XB200 and R-XB200-R fire test, it was shown in §7.3.4.2 that the vertical thermal cracks opens less and the slip remains smaller if axial restraining is applied.

The effect of restraint in direction perpendicular to the span of the slab was evaluated with the cross sectional models. This direction is further referred to as the transverse direction. As shown in §7.3.3.1, transverse restraint causes a completely different distribution of the thermal stresses over the cross section of the VX265 slab. When this slab is restrained, no horizontal crack develops through the web at the smallest section. If no transverse restraint is applied, the thermal curvature of the lower flange in the transverse direction causes bending stresses in the web and the horizontal crack develops, leading to a rapid failure.

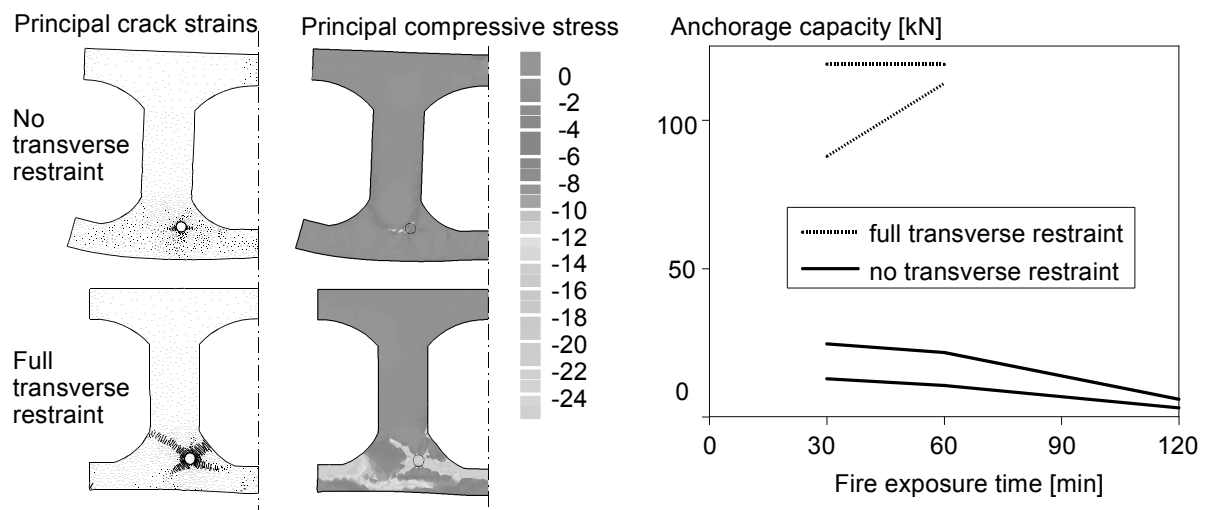


Figure 8.8: Effect of the transverse restraint on the confining action of the concrete cover and the resulting pull out resistance.

The transverse restraint has also a beneficial effect on the concrete confinement. This was quantified with the validated model of the R-HVP260S specimen. In fig. 8.8, the crack pattern

and the principal compressive stress are shown after 30 minutes and 5 ‰ fictitious radial expansion of the strand. The splitting cracks open far more in the restrained case than in the unrestrained case. Despite the larger crack openings, the compressive forces are also much larger. In addition to the circumferential tensile stresses the external compressive forces caused by the restraint contribute to the confinement.

The confining stress curves can directly be used to estimate the maximum shear force that can be transferred during fire without pull out failure. After 30 minutes, the adhesion vanishes and the bond strength is fully determined by the frictional part only. As already shown in fig. 7.17 on page 177, the confining stress curves after 30 minutes and beyond correspond to the cracked stage of the confining concrete cover. This means that the confining stress is almost independent of the actual radial expansion, especially between 4-8 ‰ of radial expansion. In fig. 7.23 on page 181, it was shown that over the zone between the support and the point load where the steel stress must be transferred, the radial expansion exceeds 4 ‰ after 30 minutes and beyond. So, for fire exposure times of 30 minutes and more, the confining stress is approximately independent of the actual slip and actual steel strain. As a result, the maximum steel stress that can be developed below the point load can be calculated directly from the confining stress curves and the friction coefficient. Once the maximum steel stress is known, the anchorage capacity can be calculated using an estimated internal lever arm of 215 mm for this type of HC slab.

The average value of two confining stress curves at each time of fire exposure was used. One was based on the assumption of no initial radial expansion during the release of the prestress, representing cross sections near the point load. The other was based on the assumption that already 4 ‰ radial expansion occurred during the release of the prestress, representing cross sections near the end of the slab. The descending branch of the confining stress curves is generally not a straight line, but show some waves, due to the unstable nature of the simulation of concrete with multiple crack localisation zones. In order to estimate the anchorage capacity, the lowest and highest values between 4-8 ‰ radial expansion are taken. Consequently, the pull out resistance varies within a range.

The resulting pull out resistance, calculated on the basis of the confining stress curves only, was compared, see fig. 8.8. It is shown that the transverse restraint causes a huge increase in the pull out resistance. After 30-60 minutes of fire exposure, the pull out resistance is even larger than at ambient conditions, which equals 125 kN in the simulations with the FE model of the entire slab, see §7.2.3. The restraining effect indeed overshadows other influencing parameters, like the coefficient of thermal expansion and the fracture energy of concrete. However, in practical applications, full transverse restraint will probably never be realised. In that respect, the calculated pull out resistance of the fully restrained slab must be considered as an upper bound, while the unrestrained slab is a lower bound. In principle, the FE models are suitable to determine the effect of any type of restraining condition on the anchorage capacity by a proper modification of the boundary conditions.

### **8.3.2 Material properties**

Regarding the bond model parameters, only the friction coefficient is assumed to have an influence on the anchorage behaviour. As already discussed in chapter 6, the influence of the

bond model parameters that set the relation between the slip and the steel strain to the fictitious radial expansion of the strand, vanishes within 30 minutes of fire exposure because the confining stress becomes fairly independent of the actual radial expansion. In the calibration process, it was further shown that the adhesion diminishes beyond a strand temperature of 150 °C, which is commonly reached within some 30 minutes. Moreover, over the zone where the steel stress must be transferred to the concrete cross section, substantial slip develops within the first 30 minutes of fire exposure in all tests, leading to a further decrease of the adhesion.

It is further expected that the interface stiffness in the cross sectional model has a minor effect on the fire behaviour since the descending branch of the confining stress curves related to the fully cracked stage, is almost unaffected. It only affects the ascending branch of the confining stress curves at ambient conditions and even at ambient conditions the effect on the anchorage behaviour is small.

The concrete properties will affect the anchorage behaviour, since the frictional part of the bond strength depends fully on the concrete confinement that is determined by the tensile properties of concrete, like the fracture energy and the tensile strength. The influence of these parameters will be demonstrated below. The compressive behaviour of concrete will affect the development of thermal stresses and vertical thermal cracks, because the heated lower side of the slab will be compressed due to the rise of the incompatible thermal strains. Since the elastic strains are negligible compared to the plastic strains and the transient creep strains, it is expected that the compressive strength and Young's modulus have a small effect on the vertical crack development compared to the transient creep value and the ductility of the stress-strain relation. Therefore, the latter two parameters were investigated rather than the compressive strength and Young's modulus. Finally, on the basis of the fire tests of chapter 4, it was concluded that the thermal expansion of concrete drives the formation of the thermal cracks and the slip of the strands. Obviously, the influence of the thermal expansion of concrete was also evaluated.

### *8.3.2.1 Aggregate type: thermal expansion and thermal properties*

According to Eurocode 2 [PREN 1992-1-2:2002], the aggregate type has an effect on both the thermal expansion and the thermal properties of concrete. Siliceous and calcareous aggregate types are distinguished. The differences in thermal expansion between siliceous and calcareous aggregate are much larger than the differences in the temperature profiles that result from the differences in the thermal properties, see fig. 8.9. It shows that the temperature profiles over the depth of the R-HVP260S specimen are only slightly dependent on the thermal properties, while the differences in thermal strains over the depth are considerable. So, differences in the fire behaviour between aggregate types must be attributed to differences in the thermal expansion. In the simulations that are presented below, the thermal expansion and the thermal properties were not evaluated separately. The structural behaviour was always assessed on the basis of the temperature field that corresponds to the same aggregate type.

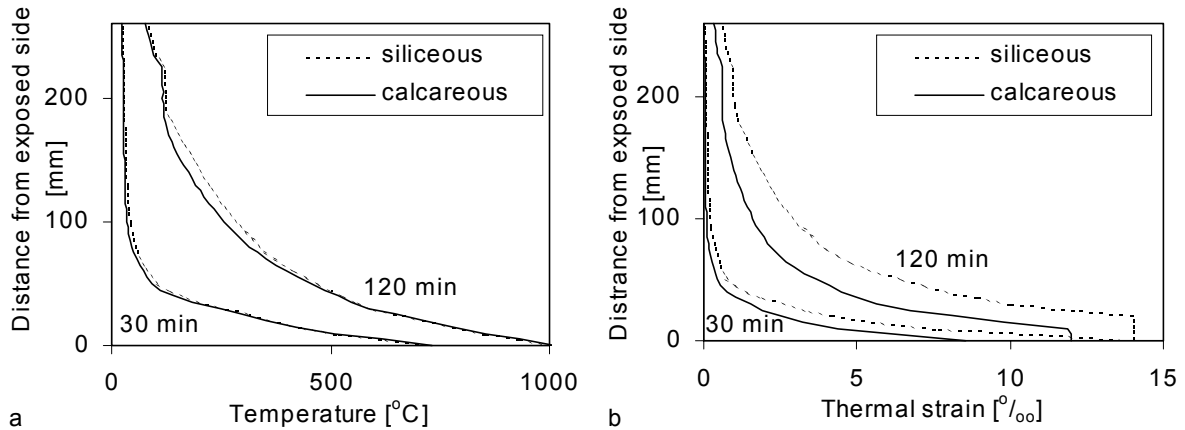


Figure 8.9: Averaged temperature distribution over the depth of the R-HVP260S slab (a) and resulting thermal strains (b) for siliceous and calcareous aggregate.

In order to assess the effect of the aggregate type of concrete on the slip development, the crack development and the time to failure, the R-HVP260S-11 test was simulated again assuming the thermal expansion of calcareous aggregate concrete according to Eurocode 2 [PREN 1992-1-2: 2002]. The R-HVP260S-23 test was also simulated again with the thermal expansion of siliceous aggregate. In addition, the latter test was simulated again under the extreme assumption that concrete does not expand at all at elevated temperature.

The thermal expansion of concrete effects the results of the cross section model and those of the model of the entire slab.

The confining stress curves are affected by the thermal expansion. This can be demonstrated using the cross sectional model only. The confining stress curves for fire test R-HVP260S-11 and R-HVP260S-23 are identical since these curves are independent of the shear loading. In fig. 8.10, the decrease of the pull out capacity is given for the R-HVP260S cross section, assuming various values of the thermal expansion. The actual anchorage capacity at ambient conditions was 99 kN.

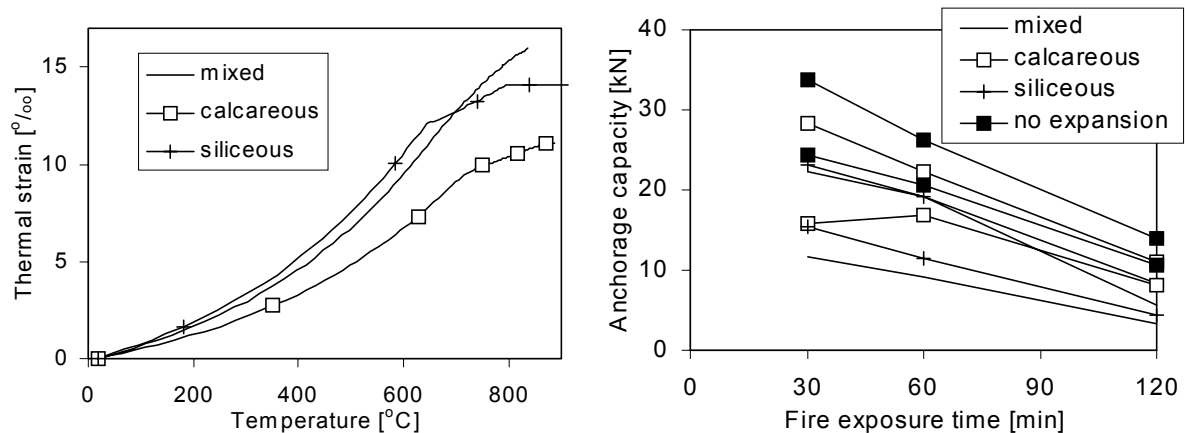


Figure 8.10: Assumed thermal expansion (left) and range of the anchorage capacity after 30 minutes of fire exposure and beyond (right), estimated on the basis of the confining stress curves.

As fig. 8.10 shows, the anchorage capacity decreases more for siliceous aggregate than for calcareous aggregate due to the larger thermal expansion. Assuming no thermal expansion at all,

the highest anchorage capacity was calculated. The anchorage capacity of a HVP260 slab with mixed aggregate is fairly similar to the one with siliceous aggregate, although the decrease of the upper bound value after 120 minutes is stronger. There is no fundamental explanation for this stronger decrease. Probably, the unstable nature of the crack localisation phenomenon caused the variation in the results. Moreover, the assumed difference in the thermal expansion is only limited, see fig. 8.10. According to Eurocode 2 [PREN 1992-1-2: 2002], concrete of siliceous aggregate does not expand beyond 700 °C and concrete of calcareous aggregate beyond 800 °C. The input in the simulation however, was smoothed in order to avoid numerical difficulties in the calculation of the strain field within the elements that are partly beyond this transition point. The actual thermal expansion at these high temperatures is rather irrelevant, because the strength and stiffness of the hot area are limited and the effect on the equilibrium is small.

The vertical crack propagation and the slip development is affected by the thermal expansion. This was demonstrated using the FE model of the entire slab.

The simulation of R-HVP260S-23 with the thermal expansion of siliceous aggregate leads to almost the same slip development as for the validated case with mixed aggregate. The shear loading was kept at 24.4 kN so the result must be compared with the simulation of the previous paragraph with the same shear loading. Failure is simulated after 42 minutes instead of 32 minutes for the case with mixed aggregate, see fig. 8.11. This is in contradiction with the expectation that concrete slabs consisting of aggregates with lower thermal expansion (the mixed siliceous-calcareous one) develop less slip and reach a higher fire resistance than concrete slabs consisting of aggregates with higher thermal expansion (siliceous). However, the temperature of the strands rises faster in the siliceous aggregate concrete than in the mixed aggregate concrete. As a result, the friction coefficient exceeds the lowest calibrated value at 150 °C after 25 minutes in the simulation with siliceous aggregate and only after 30 minutes in the simulation with the mixed aggregate. In the latter simulation, both the confining action and the friction coefficient decrease between 20-30 minutes and pull out is calculated. On the contrary, in the simulation of the siliceous aggregate, the decrease in the confining action between 20-30 minutes is counteracted by the increase of the friction coefficient. Beyond 30 minutes, the decrease in the confining action is much slower than between 20-30 minutes. Pull out after 30 minutes is just being avoided and 12 more minutes are gained until failure occurs after 42 minutes. Besides, the assumed difference in the thermal expansion is limited, see fig. 8.10.

The R-HVP260S-23 test was also simulated again with 24.4 kN shear loading, assuming no thermal expansion of concrete, see also fig. 8.11. In this simulation no failure occurs within 120 minutes, despite the fact that the upper bound calculated by the confining stress curve is only 16.3 kN after 120 minutes. Actually, no vertical thermal cracks develop and the cracking moment capacity rather than the pull out capacity limits the anchorage capacity. The slip increases a few millimetres in the beginning of the fire, as the bond strength decreases. However, after approximately 30 minutes, the slip remains constant as the thermal expansion of the steel would rather lead to a decreasing slip, which would only occur once a bond stress develops in the opposite direction that reaches the yield strength.

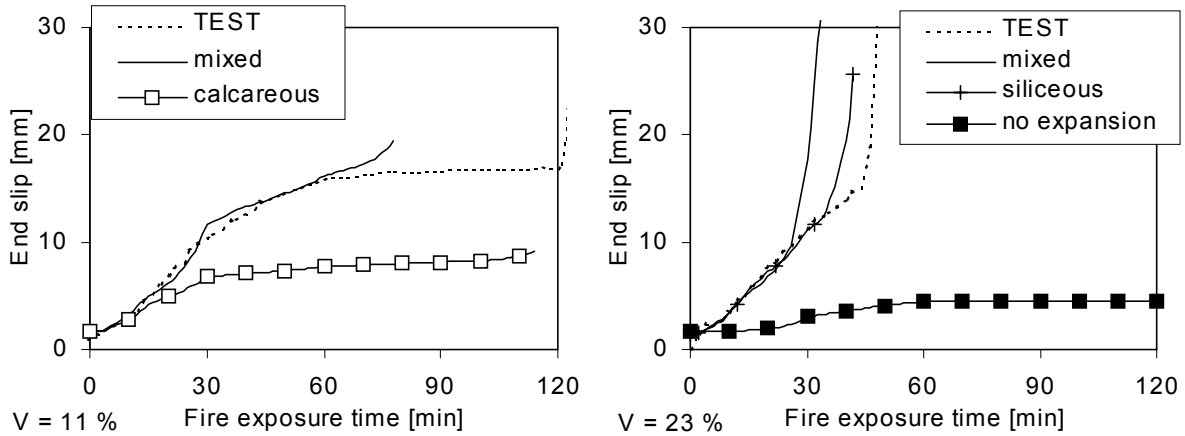


Figure 8.11: Effect of the assumed thermal expansion of the slip development and the time to failure for the R-HVP260S-11 and R-HVP260S-23 fire tests.

The fire test with 11 % shear loading was simulated again assuming the thermal expansion of calcareous aggregate instead of mixed aggregate. The shear loading was kept at 12.2 kN, so a comparison was made with the simulation of the previous paragraph with the same shear loading. Due to the lower thermal expansion, failure is postponed from 80 minutes to 114 minutes, see fig. 8.11. Moreover, the slip development is substantially smaller than the slip calculated for the mixed aggregate. Also the vertical cracks remain smaller, see fig. 8.12. In this figure, the deformation is scaled by a factor 5 and the principal plastic tensile strains beyond 5 ‰ are presented.

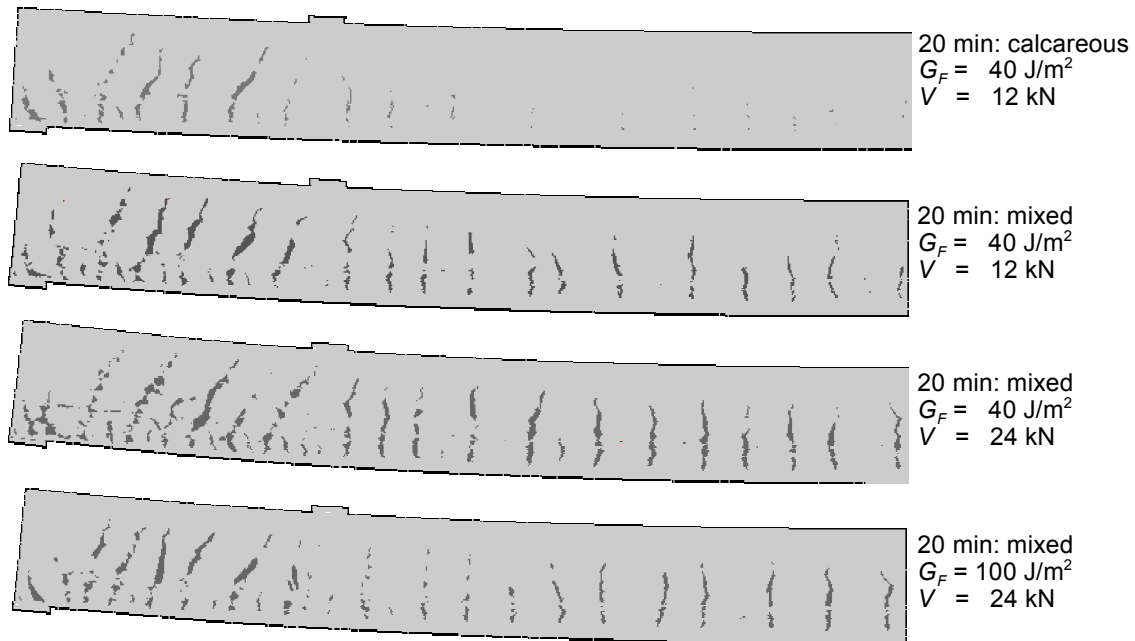


Figure 8.12: Crack pattern after 20 minutes in the R-HVP260S specimen depending on the thermal expansion (calcareous vs mixed aggregate), the fracture energy and the shear loading.

In conclusion, the comparison between the simulations with mixed and siliceous aggregate shows that small changes in the input values have a huge effect on the time to failure. The comparison with the extreme case of no thermal expansion of concrete proves that the thermal expansion is

one of the most important parameters that determines the slip development and the time to failure. No vertical cracks develop in that case and the cracking moment capacity rather than the pull out capacity limits the anchorage capacity. It underlines once more the necessity to incorporate the thermal expansion in the evaluation of the anchorage capacity of fire exposed HC slabs. Furthermore, on the basis of this comparison, it is recommended to use concrete mixes with low thermal expansion as it improves the anchorage capacity during fire exposure.

### 8.3.2.2 Fracture energy of concrete

Since the confining stress curves after 30 minutes all relate to the stage of fully developed splitting cracks, it is expected that the fracture energy has a substantial effect on the bond strength. This was evaluated with the cross sectional model.

The fracture energy also determines the opening of the vertical thermal cracks and in this way, the fracture energy affects the growth of the vertical thermal cracks through the lower flange of the slab into flexural cracks. In this way the fracture energy influences the cracking moment capacity. As shown in the previous paragraph, the cracking moment capacity can determine the load bearing capacity, especially when the vertical thermal cracks have not yet grown into flexural cracks.

The effect of the fracture energy on the confining stress curves is illustrated in fig. 8.13. The confining stress curves at various characteristic times of fire exposure were calculated for the R-HVP260S specimen. Typically, the ascending branch is independent of the fracture energy of concrete. However, with increasing fracture energy, a larger radial expansion can be withstood without the occurrence of a fully propagated splitting crack. The fracture energy has a large effect on the remaining confining stress in the fully cracked stage. As the splitting cracks are already present after 15 minutes, a large difference between the confining stress curves beyond this time point exist, like for instance after 60 minutes as shown in the left picture of fig. 8.13.

In the right picture of fig. 8.13, the effect of the fracture energy of concrete on the remaining pull out capacity is shown. The anchorage capacity was manually calculated on the basis of the confining stress curves with the method outlined in §8.3.2.1.

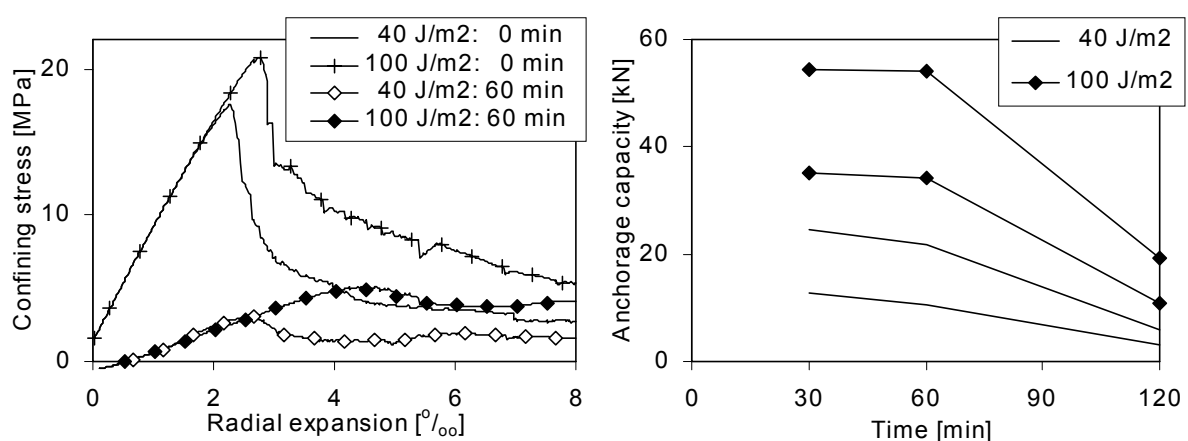


Figure 8.13: Effect of the fracture energy on the confining stress curve (left) and the resulting upper and lower bound values of the pull out capacity (right).

An increased fracture energy from 40 to 100 J/m<sup>2</sup> leads to an increase in the anchorage capacity over the time domain from 30-120 minutes with a factor 2.

After the simulations with the cross sectional model, the confining stress curves at various characteristic times of fire exposure were used in the FE model of the entire slab, to observe the effect of the fracture energy on the crack development and the slip development.

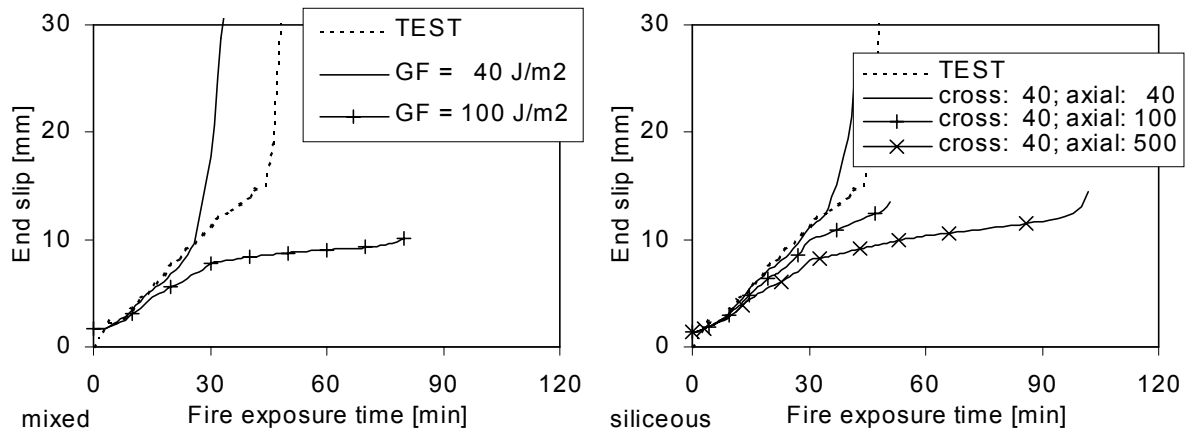


Figure 8.14: Effect of the fracture energy of concrete on the slip development and time to failure, calculated with the axial model of the R-HVP260S-23 fire test.

For that purpose, the fire test R-HVP260S-23 with 23 % shear loading was simulated again, assuming an increased fracture energy to 100 J/m<sup>2</sup>, see the left picture of fig. 8.14. The applied shear load was 24.4 kN and the slip development was compared with the simulation on the basis of the calibrated values with the same shear load.

With the increased fracture energy, the time to failure increased from 32 to 80 minutes. The variation of the fracture energy from 40 to 100 J/m<sup>2</sup> must be considered as a practical one, see for instance, measurements given in fig. 3.2 on page 62 [DARWIN et al.: 2001]. So, the scatter of the fracture energy must be considered as a major cause of the scatter in the time to failure as obtained in fire tests.

In order to further analyse whether the increased time to failure must fully be attributed to the increased confining stress curve or not, additional simulations were performed, in which the fracture energy of concrete was only varied in the FE model of the entire slab between 40 to 500 J/m<sup>2</sup>. In all these simulations, the applied confining stress curves were obtained with a fracture energy of 40 J/m<sup>2</sup>. The simulations were made assuming the thermal expansion of siliceous aggregate. The results are given in the right picture of fig. 8.14.

It appears that even an increase in the time to failure can be reached from 42 to 52 minutes, just by the increase of the fracture energy in the axial model from 40 to 100 J/m<sup>2</sup>. It is because the vertical cracks remain smaller for larger fracture energy values and consequently, the cracking moment resistance decreases slower, which is limiting the failure behaviour in this stage of fire exposure. Failure occurs once the vertical cracks grow through the lower flange into flexural cracks as the pull out resistance is too limited to take over the released stresses in the flexural crack. If the fracture energy is further increased to 500 J/m<sup>2</sup>, failure is even postponed to 102 minutes. Such a value for the fracture energy is out of reach for normal concrete, unless measures are taken to enhance the fracture energy.

The analysis demonstrates that the fracture energy is a dominant parameter for the anchorage capacity of HC slabs. As the anchorage behaviour improves with increasing fracture energy, it is recommended to apply concrete mixes with a large fracture energy, for instance by adding fibres in the concrete mix.

The effect of fracture energy of concrete in compression was also investigated. The compressive stresses in the concrete zone at the exposed side are in equilibrium with the tensile stresses that cause the thermal cracks. In this way, the ductility of concrete in compression affects the crack propagation and the slip development. Therefore, an additional calculation was made with the validated FE model of the entire slab to simulate the test with 22.8 kN shear load, with a fracture energy of concrete in compression of 10 kJ/m<sup>2</sup> instead of 20 kJ/m<sup>2</sup> which was used for all other calculations.

The effect on the slip development is given in fig. 8.15. The effect on both the slip development and the time to failure is negligible.

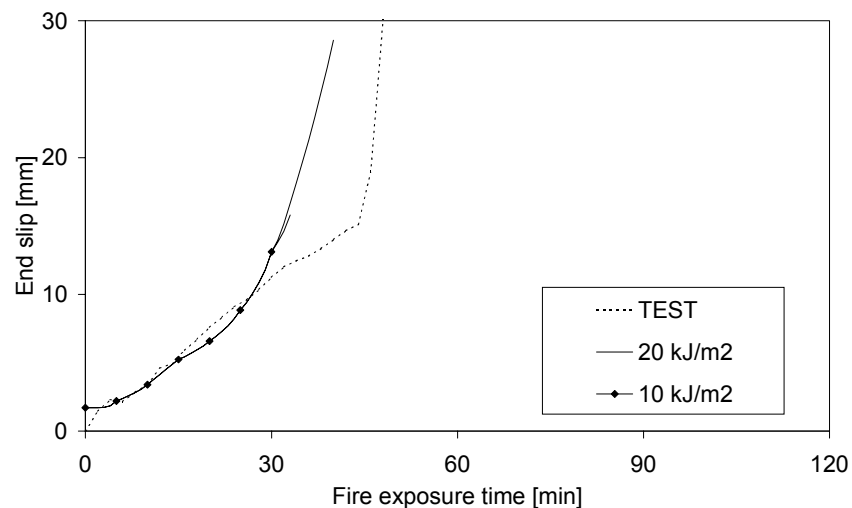


Figure 8.15: Effect of the fracture energy of concrete in compression on the slip development of the R-HVP260S-23 test.

### 8.3.2.3 Concrete tensile strength

The concrete tensile strength affects the shear and anchorage behaviour in two ways. In the first place, the peak stress of the response curve of the concrete confinement to radial expansion of the strand is mainly determined by the tensile strength, see fig. 8.1 on page 186. However, in the fully cracked stage, i.e. the horizontal branch of the confining stress curve, the response is almost completely independent of the tensile strength. The resulting effect of the tensile strength on the pull out resistance after 30 minutes of fire exposure and beyond was evaluated for the R-HVP260S specimen with a new simulation in which the tensile strength was reduced from the measured value for HVP260 specimen of 6.0 MPa to 4.0 MPa. It appears that the tensile strength has no significant influence on the pull out resistance after 30 minutes and beyond, see fig. 8.16.

Secondly, the tensile strength has an effect on the vertical crack development and the cracking moment resistance. In §8.3.1.2, it was outlined that the cracking moment resistance can exceed the pull out resistance during some stages of fire exposure. During these periods, anchorage failure occurs immediately once the vertical thermal cracks grow through the lower flange in a flexural crack. With an increased tensile strength, higher tensile bending stresses can be resisted in the lower flange and the cracking moment capacity is increased. For the R-HVP260S slab, the cracking moment capacity exceeds the pull out resistance between 10 and 30 to 60 minutes. Hereafter the pull out resistance is larger than the cracking moment capacity. So for practical fire resistance requirements of 60-120 minutes, the cracking moment capacity is not very relevant.

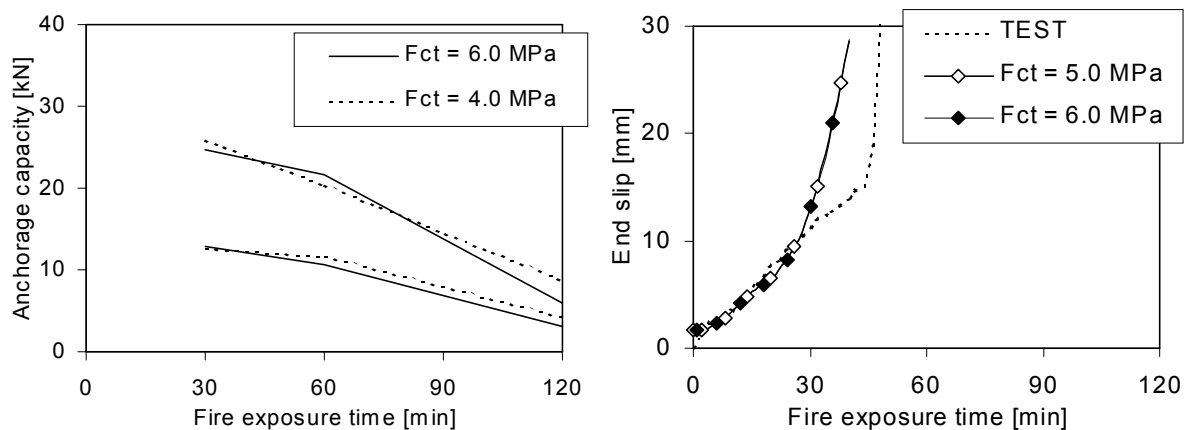


Figure 8.16: Effect of the concrete tensile strength on the upper and lower bound of the pull out capacity of the R-HVP260S specimen on the basis of variations of the concrete confinement (left) and on the basis of the FE model of the entire slab only(right).

To show that the effect of the tensile strength on the slip development is negligible, the slip development was calculated in the FE model of the entire slab on the basis of a tensile strength of 5.0 or 6.0 MPa, both simulations based on the confinement curves derived for a tensile strength of 6.0 MPa. The slip was identical over the entire time of fire exposure, see fig. 8.16.

In conclusion, the influence of the concrete tensile strength on the anchorage behaviour of HC slabs is only relevant until approximately 30 minutes of fire exposure.

#### 8.3.2.4 Friction coefficient

The friction coefficient can directly be related to the pull out resistance during fire, at least beyond 30 minutes of fire exposure. After 30 minutes, the adhesion vanishes completely and the confining stress is almost independent of the actual radial expansion of the strand. So the friction coefficient directly determines the frictional part of the bond strength.

With the calibration tests, the friction coefficient and the variation of the friction coefficient was determined, see fig. 6.17 on page 160. The variation of the friction coefficient leads to a variation of the pull out resistance. This variation comes on top of the variations in the softening branch of the confining stress curves, which is attributed to the unstable character of the simulations of the fully cracked stage when several crack localisation zones are calculated. In fig. 8.17, the

consequences of the variation of the friction coefficient on the pull out resistance are presented.

The scatter in the friction coefficient leads to a substantial increase of the range in which pull out failure must be expected.

The calibrated friction coefficient was temperature dependent. The highest value of 0.61 was found at 400 °C, and a low value of 0.49 at 150 °C. As a result, a scatter in the strand temperature leads also to a scatter in the pull out resistance. Besides, a different temperature field will lead to another confining action of the concrete cover. In the right picture of fig. 8.17, the effect of a 50 °C higher and lower strand temperature on the pull out resistance is shown, based on a different friction coefficient only. Given the facts that the lowest friction coefficient was found at 150 °C and the strand temperature after 30 minutes was about 150 °C, both a higher and a lower temperature lead to an increased pull out resistance. The effect of a different strand temperature on the pull out resistance is small.

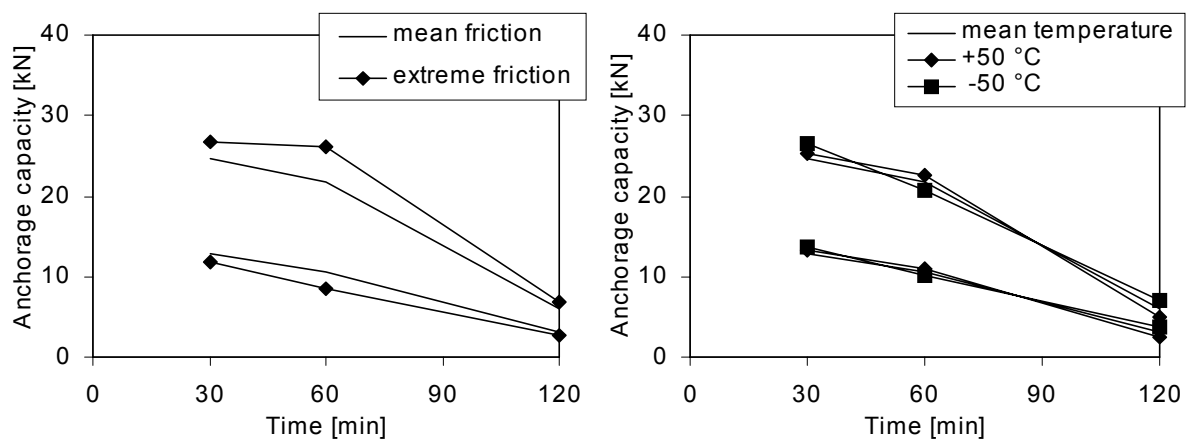


Figure 8.17: Comparison of the upper and lower bound of the pull out capacity based on the mean calibrated friction coefficient and the 5-95 % characteristic values of the friction coefficient (left). Right: Effect of a temperature variation of the strand of  $\pm 50$  °C on the pull out capacity through the friction coefficient only.

As the friction coefficient dominates the bond strength after 30 minutes of fire exposure, it is recommended to improve the pull out capacity of HC slabs through the use of strands with an increased friction, like for instance strands with indentations.

### 8.3.2.5 Transient creep

As stated in chapter 5, two different concrete models were developed. The first model includes transient creep and the dependency of the stress-strain curves on the compressive loading during heating. The second model is based on Eurocode 2 [PREN 1992-1-2:2002]. In this model transient creep is implicitly taken into account by an increased ductility of the stress-strain relations at elevated temperatures. The strain that corresponds to the maximum compressive stress is prescribed by Eurocode 2. The stress-strain curves are independent of the loading history during heating.

The effect of the choice of the model was evaluated by the simulation of R-HVP260S-11 and R-HVP260S-23 fire test. The simulation including transient creep was compared with a simulation without transient creep.

In the simulation without transient creep, the slip development is overestimated, see fig. 8.18. Also the crack propagation is overestimated. So, for a proper simulation, the transient creep must be taken into account including the dependency of the stress-strain relations on the loading history during heating.

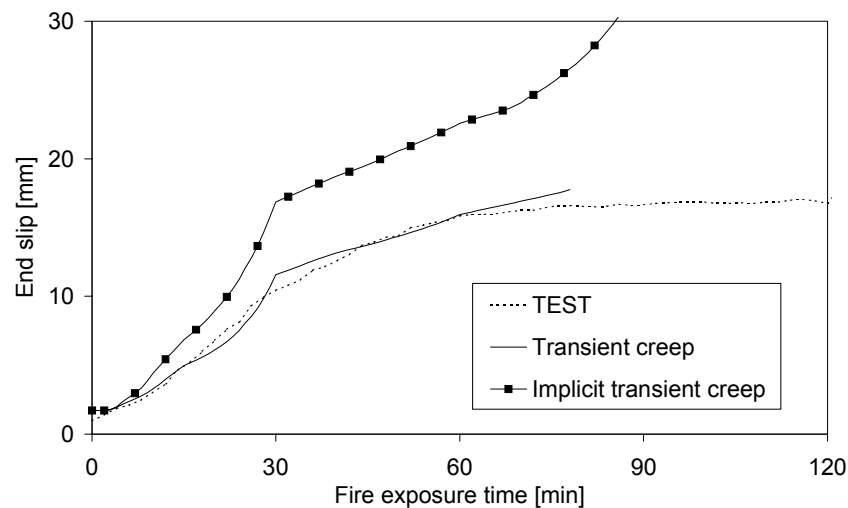


Figure 8.18: Effect of transient creep formulation in the concrete model on the slip development in fire test R-HVP260S-11.

### 8.3.3 Geometrical properties

The geometrical properties concern the shape of the cross section of the HC slab, the position of the strands and the span of the slab. In the sensitivity study, only the effect of the position of the strands was analysed. In all simulations the span was 4 m, which is relatively short compared to practical spans. Due to the increasing ratio between bending moment and shear force for increasing spans, flexural failure tends to dominate over shear and anchorage failure for longer spans. Therefore, the short span is considered as a worst case for shear and anchorage failure.

The position of the strand in the cross section has an effect on the orientation of the splitting cracks. The strand temperature and remaining concrete confinement after the occurrence of splitting cracks are affected by the strand position. The strand position also determines the slip development and consequently the increase of the fictitious radial expansion during fire. The effect of the strand position on the pull out capacity is given on the basis of the cross sectional analyses only. The effect of the slip development on the pull out capacity through the increase of the radial expansion caused by the slip, is neglected. This effect is assumed to be limited, since the confining stress is relatively independent of the actual radial expansion.

The pull out resistance of the HVP260 slab with three different positions of the strand were compared:

- a* in the centre of the rib at 76 mm from the exposed side;
- b* in the centre of the rib at 40 mm from the exposed side;
- c* eccentrically positioned in the rib at 40 mm from the exposed side, 20 mm outside the centre from the rib.

Fig. 8.19 presents the effect of the strand position in the HVP260 slab on the pull out resistance. Also the strand temperature and corresponding friction coefficient are given. The pull out resistance of strand position *b* equals approximately that of strand position *c*, despite of the increased concrete cover. Also the strand temperature is barely affected by the horizontal position of the strand. After 50 minutes the maximum temperature difference between strand position *b* and *c* reaches 10 °C. Therefore the temperature of the strand at position *b* was omitted in fig. 8.19.

The pull out resistance of the strand increases when the axis distance is increased from 40 mm to 76 mm, especially after 120 minutes. However, no definite conclusions can be drawn from this picture because the interaction between the shear stresses and splitting stresses can not be taken into account, which is especially relevant for the strand at 76 mm from the exposed side. In order to accurately judge this interaction a combined 3D model would be required, which is out of scope with the current computer power.

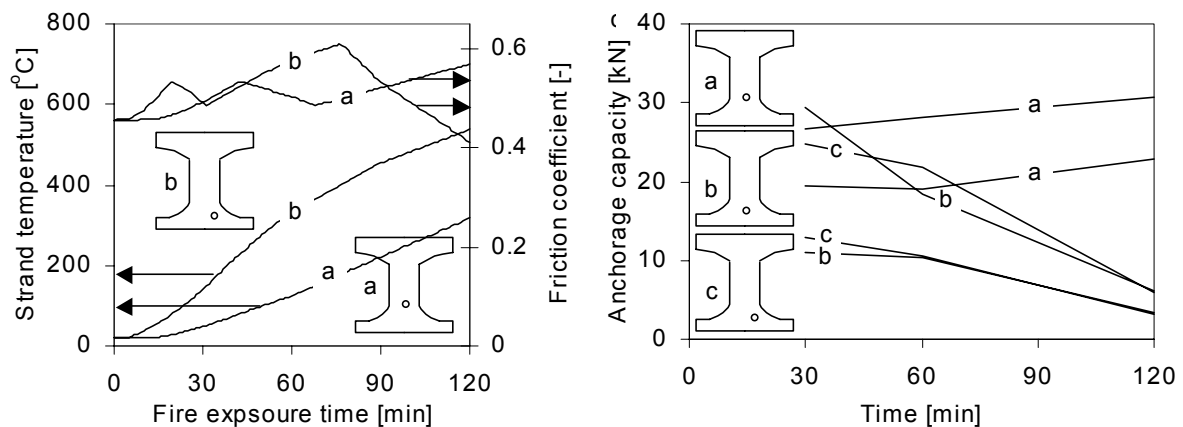


Figure 8.19: Effect of the strand position of the pull out failure. Left, the strand temperature and corresponding the friction coefficient are presented, right the resulting upper and lower bounds of the pull out capacity.

## 8.4 FIRE SAFE DESIGN OF HC SLABS

Structural fire resistance design is currently based on meeting a desired fire resistance time. Safety considerations are taken into account in an implicit manner [FELLINGER & BOTH: 2000]. To take into account the incidental character of a fire, the partial safety factors for load and resistance are relieved compared to room temperature design, and the combination of extreme loads and fire is not considered. To account for the large variation in possible fires and the

uncertainty of the evaluation of the structural fire resistance on an element level instead of a system level, the fire resistance requirements are expressed in time classes with large intervals of 30 minutes up to 120 minutes and beyond in combination with the standard fire curve.

The required fire resistance time depends partly on the expected damage in case of failure. In the Netherlands for offices and dwellings a requirement of 30 minutes fire resistance is mainly related to rescue and egress times, the requirement of 60 minutes is mainly related to the fulfilment of the separating function while higher requirements are mainly set to obtain an increased safety. The idea is generally accepted that the fire brigade is capable to control a fire within 60 minutes or a fire extinguishes naturally within 60 minutes simply by lack of combustibles [BIZA: 1996]. Therefore, a fire resistance requirement of 90 minutes and above is mainly meant as an increase of safety.

However, the formulation of the fire resistance in the time domain is not appropriate for shear and anchorage failure of HC slabs. In the previous paragraph, the huge impact was demonstrated of various parameters on the time to failure of fire exposed HC slabs. All these parameters are characterised by a stochastic distribution. As a direct consequence of the huge effect of some stochastic parameters on the time to failure, the actual safety level of the slab designed for 30 minutes fire resistance would almost coincide with a slab designed for 90 or 120 minutes. For instance, the double rib specimen R-HVP260S, with the properties as calibrated in chapter 6, would reach 90 minutes with a degree of utilization of 11 %. With a small change in the shear load to 25 %, or another detrimental change in some of the other parameters, failure would occur within 30 minutes.

For reasons of comparison, the allowable shear load for a 30,60,90 and 120 minutes fire safe design regarding flexural failure are plotted in figure 8.6 on page 190. Clearly, the decrease in the allowable degree of utilization between 30, 60, 90 and 120 minutes is much larger than for anchorage failure. Moreover, the most important parameter determining the flexural resistance is the axis distance, i.e. the distance from the centroid of the steel strands to the exposed side. The axis distance can much better be controlled than the influence factors for anchorage failure, like the fracture energy and thermal expansion of concrete, the friction coefficient of the strands and the amount of axial and transverse restraint. As a result, for flexural failure, an increased time to failure under standard fire conditions corresponds to an increased safety level in reality. So, for flexural failure, the current approach using fire resistance requirements in the time domain does lead to an adequate safety level.

Alternatively, it is recommended to ensure the fire safety of HC slabs regarding shear and anchorage failure by a limitation of the allowable shear load. In principle, the maximum shear load could be adapted to a desired safety level [Fellinger & Both: 2000], but it is more practical to limit the shear load to such an extent that flexural failure will dominate over shear and anchorage failure. The allowable shear load for each type of HC slab can be determined with reliability analyses using the FE models developed in this thesis. Since the decrease in the shear and anchorage capacity during fire is almost independent of the load level during heating, the resistance can be determined without consideration of the solicitation.

The shear and anchorage capacity depend on the stochastic influence parameters. The decrease of the shear and anchorage capacity during fire is therefore also subject to statistical variations.

In the design of the HC slabs, some of influence parameters are commonly monitored and controlled in a narrow range, like the geometrical parameters. Obviously, these parameters are taken into account in the design process. Others can not be controlled in the design stage, like the fire load and shear load. The rest of the parameters could be controlled, but currently that is not common practice, like the thermal expansion of concrete.

In order to minimise the expected variation in the shear and anchorage capacity in the design, the important influence parameters must be monitored and controlled, if possible. Notably, it is recommended to control the fracture energy and thermal expansion of concrete and the friction coefficient of the strands. After all, the range in which the shear and anchorage capacity decreases during fire for a HC slab out of concrete with an unknown fracture energy is much larger than for a known value of the fracture energy. Consequently, the safety margin between the allowable shear load and the mean shear and anchorage capacity can be much smaller in the latter case.

In table 8.1, the influence of various parameters on the shear and anchorage behaviour is summarised. The table is partly based on the fire tests and partly on the FE models and for some parameters only on theoretical considerations.

**Table 8.1** Summary of relevance of input parameters on the shear and anchorage behaviour of fire exposed HC slabs.

Type	Parameter	effect on:				based on:			
		thermal cracks		slip	time to failure	fire tests	FE model		theory
		vertical	splitting				cross	axial	
external factors	fire conditions	?	?	?	?				X
	degree of utilization	-	0	-	++	X		X	
	axial restraint	++	0	++	++	X		X	
	transverse restraint	?	+	++	++		X		
concrete properties	thermal properties	0	0	0	+			X	X
	thermal expansion	++	++	++	++		X	X	
	fracture energy	+	+	++	++		X	X	
	tensile strength	-	-	--	--		X	X	
	compressive strength	--	--	--	--				X
	Young's modulus	--	--	--	--				X
	transient creep	++	0?	++	-			X	
bond model	friction coefficient	0	0	+	++		X		
	adhesion	-	-	-	--				X
	adhesion coefficient	--	--	--	--				X
	lack of fit coefficient	--	--	--	--				X
	slip coefficient	--	--	--	--				X
	Poisson coefficient	--	--	--	--				X
	pitch coefficient	--	--	--	--				X
	interface stiffness	--	--	--	--				X
	Gliding modulus	--	--	--	--				X
geometrical properties	strand position	-	++	++	++	X	X	X	
	shape of the HC slab	++	++	++	++	X	X	X	



# 9 Conclusions and recommendations

## 9.1 CONCLUSIONS

### 9.1.1 Based on tests

#### 9.1.1.1 *Ambient conditions*

On the basis of an assessment of 253 tests on HC units at ambient conditions, it is concluded that the load bearing behaviour can well be distinguished into four failure modes, i.e. flexural failure, anchorage failure, shear tension failure and shear compression failure. Also combinations of anchorage failure with either flexural, shear tension or shear compression failure can occur. The load bearing capacity is never limited by the brittle cracking moment capacity, unless the bond capacity of the strands was downgraded intentionally. The data base of tests is representative for the current practice, as it covers a wide range of types of HC slabs, production methods, years and countries of production, concrete strengths and loading configurations in the test.

#### 9.1.1.2 *Fire conditions*

Flexural failure, anchorage failure and shear failure can be distinguished for HC slabs exposed to fire. No distinction between shear tension and shear compression failure can be made, because the failure crack starts in the web like for shear tension failure, but the load can be beared after formation of the crack, like for shear compression failure. Similar to the tests at ambient conditions, combinations of anchorage failure with either shear or flexural failure can occur.

Shear and/or anchorage failure must be taken into account in the design of the slabs, because such a failure can occur within 20-130 minutes when a practical load level is applied during fire: shear and anchorage failure were observed in tests in which the calculated degree of utilization was as low as 30-50 % regarding anchorage failure, 10-25 % regarding shear tension failure and

15-40 % regarding shear compression failure. Compared to a common degree of utilization of 40-70 % for the dominating failure mode, which is generally flexural failure, the degree of utilization regarding anchorage and shear failure in the tests can be considered as realistic.

Vertical thermal cracks develop in the webs at regular distance over the entire length of the slab within 14-16 minutes of standard fire exposure, irrespective to the geometry of the slab, the prestress level, or the loading configuration. Axial restraint reduces the size of the vertical thermal cracks and improves the fire resistance.

Thermal cracks along the strands and horizontally through the webs can develop within 20-22 minutes, depending on the geometry of the slab, see chapter 4. Axial restraint does not reduce the development of these cracks and consequently does not improve the fire resistance in this case.

Thermal cracks do not lead to a direct failure, provided that the applied loading can be taken by the cracked specimen. There is a tendency for larger cracks with increasing slab height. This is in accordance with the assessment of the fire tests found in literature, in which an increasing sensitivity to shear and anchorage failure was found with increasing slab height.

Test results can well be reproduced provided that the specimens originate from the same production batch. The scatter in results found in literature is attributed to the influencing parameters discussed below.

The effect of the degree of utilization on the shear and anchorage behaviour is a paradox. On one hand, the loading barely influences the observed thermal crack propagation and slip development. On the other, it has significant influence of the time to failure. Failure within 1 hour is driven by a combination of applied loading and thermal stresses. If the specimen survives the first hour, the thermal stresses vanish and failure is caused by a combination of the applied loading and a loss of the mechanical properties.

Shear or anchorage failure can not be related to the temperature of the strands, nor to the evaporation of moisture in concrete that escapes the slab along the strand, since such a failure was reported in cases with a strand temperature well below 100 °C at failure while no such a failure was reported with strand temperatures over 600 °C for slabs with about the same anchorage loading.

Axial restraint of thermal expansion improves the fire resistance with respect to shear and anchorage failure significantly. However, the contribution of the restraint to the fire resistance strongly depend on support detail through the vertical position of the restraining force. The improvement can only be obtained provided that the restraining force acts on the bottom of the slab. A transverse restraint by means of a reinforced concrete beam at the sawn edge of the HC slabs with reinforcement that is well anchored behind the HC slabs, only marginally improves the shear and anchorage behaviour.

Based on the assessment of the fire tests found in literature, it is concluded that filling some of the cores over the transfer length with reinforced cast-in-place concrete does not significantly improve the shear and anchorage behaviour. Moreover, in fire tests on specimens with concrete core filling carried out in scope of this thesis, the shear and anchorage behaviour was not

improved by it. No composite action developed between the core filling and the HC slab due to insufficient bond, even though the cores were properly filled after removal of the upper flange over the filling length. Unless adequate bond between the core filling and the precast unit can be ensured, the core filling moves freely in the core, thermal stresses are not spread out over the composite cross section, and vertical thermal cracks still develop in the precast part of the slab leading to a similar reduction in the shear and anchorage capacity as for slabs without a core filling.

A substantial improvement in the shear and anchorage behaviour is obtained by insulation of the support over the transfer length of the prestress. None of the 20 test specimens that were insulated over at least 500 mm failed by loss of anchorage or shear capacity, despite sometimes relatively high degrees of utilization. No significant improvement is obtained if the insulation is only extended over the support length of 100 mm.

The effect of flexible supports on the shear and anchorage behaviour of fire exposed HC slabs is overshadowed by the scatter in the results of fire tests on HC slabs.

## **9.1.2 Regarding the quality of the models**

### *9.1.2.1 Analytical models*

The analytical formulations as given in chapter 2 correspond satisfactorily to the actual load bearing capacity for the four failure modes. The ratio between the actual capacity and the calculated capacity can well be described by a normal distribution, for all failure mechanisms, with a coefficient of variation of approximately 20 % for anchorage, shear tension and shear compression and only 10 % for flexural failure. None of the ratios depend substantially on one of the influencing parameters, indicating that the models take the relevant parameters into account in an adequate way.

The database of HC slabs tested at ambient conditions is not suitable for the adjustment of the formulations of the ultimate capacity of these four failure mechanisms because for many specimens more than one failure mode could be expected. Tests that fail in one mode provide insufficient information with respect to the other failure modes.

The flexural capacity can well be predicted with the plastic cross sectional model of chapter 2. On average, the flexural capacity is underestimated with 7 %. The difference is primarily attributed to the fact that the actual steel strength was not measured and estimated on the basis of the design value.

The linear elastic shear tension model of chapter 2 overestimates the actual capacity 6-8 %, with a slight tendency that the difference increases for higher concrete tensile strengths. However, there is no need to modify the model since there is a very large margin between the mean model value and the design value of ranging from 1.5 for lower strength up to 2.5 for higher strengths. The relatively large coefficient of variation of 21 % is attributed to the large variation in the origin and type of the slabs. Within one series of tests on specimens obtained from one producer, the scatter is much smaller, down to 9 %.

The model of Hedman and Losberg [1978] overestimates the actual shear compression capacity

only 4 % and the coefficient of variation obtained in with the current data base corresponds satisfactorily with their model factors to obtain a characteristic lower bound. Although, their model was mainly derived for beams with well anchored reinforcement using hooks, anchors or strands with very small diameters, it can satisfactorily being applied to HC slabs.

The anchorage model of the Model Code [CEB-FIB: 1991] is rather conservative as it underestimated the actual anchorage capacity with 25 %. An optimal agreement between the experimental data and the design formulation of the transfer length according to the Model Code is obtained using a mean value for the model factor  $\alpha_s$  of 0.6. Given the recommended range by the Model Code for  $\alpha_s$  of 0.5-1.0 regarding the control of splitting and bursting cracks respectively regarding pull out, the average value of 0.6 implies that the safety margin for pull out is larger than for splitting and bursting. This is justified by the fact that splitting and bursting cracks can directly be observed after the release of the prestress when the HC units can be rejected.

### 9.1.2.2 *FE models*

The thermal and structural behaviour of fire exposed HC slabs was successfully simulated with FE models that follows fundamental kinematic, constitutive and equilibrium equations.

The thermal response could successfully be simulated using the Eurocode 2 [ENV 1992-1-2:1995] thermal properties in combination with the measured moisture content and boundary conditions according Eurocode 1 [PREN 1991-1-2: 2002]. The comparison between the measured and the calculated temperatures was made for the average temperature gradient over the height of the HC slab. The differences between the two gradients remain within 50 °C over the entire depth over the entire time domain for all types of HC slabs that were tested in the scope of the thesis, which is of the same magnitude as the maximum standard deviation of the temperature readings.

The simulation of the structural behaviour of fire exposed slabs matches satisfactory the crack development, the slip of the strands and the shear and anchorage failure. The simulations were carried out using the calibrated values of the parameters of the bond model and the concrete model.

Also the behaviour of HC slabs at ambient conditions was successfully simulated, regarding the introduction of the prestress, the development of splitting cracks, and the shear tension and anchorage failure. The model simulates the observed phenomena correctly, but no investigations into the accuracy of the model were performed.

The vertical, horizontal and splitting cracks were calculated in accordance with the test observations, with respect to the time of initiation, the orientation and the propagation during fire. Vertical cracks are driven by the incompatible thermal strains acting in the direction of the span of the slab. The incompatible thermal strains acting in the transverse direction cause the horizontal cracks through the webs and the splitting cracks along the strand. Also the transfer of shear stresses and the introduction of the prestress contribute to the development of splitting cracks.

Regarding the slip of the strands, the simulation of the R-HVP260S-11 and R-HVP260S-23

specimens was matched within 3 mm over the entire exposure time up to the onset of failure.

In regard to the anchorage failure, pull out failure of the strands was simulated like in the tests. However, the time to failure was underestimated, which is attributed to the sensitivity to various input parameters.

During fire, anchorage failure is either limited by the cracking moment resistance or the pull out resistance. The cracking moment exceeds the pull out resistance for the R-HVP260S between 10 and 30 to 60 minutes of fire exposure. If the load is increased in this period, failure is relatively brittle and the vertical thermal crack that grows into a flexural crack is located close to the support. Due to the existence of the additional horizontal cracks near the support, the distinction with shear failure is hard to make.

In order to obtain the successful simulation of fire exposed slabs, the FE models had to include the following features:

The bond model needs to allow for a slip that is irreversible during fire exposure and during maturing of the HC slab.

In order to allow for the simulation of both anchorage failure and the introduction of the prestress, the bond model needs to consider a lower bond strength in case the strands are pulled out than in case the prestress is released. The introduction of the prestress needs to be covered in order to allow for a proper calculation of the cracking moment, the shear tension capacity and the development of splitting cracks. In order to cover both the pull out behaviour and the transfer of the prestress, the separate effects of lack of fit during slip and the Poisson contraction of the strand and change of pitch during straining of the strand need to be included in the calculation of the part of the bond strength caused by frictional stresses.

The steel model needs to include plasticity in order to allow for the calculation of flexural failure and to allow for a reduced radial expansion on the concrete cover during yielding, which leads to a drop in the bond strength and consequently affects the anchorage behaviour.

The steel and concrete model need to include thermal expansion, since the thermal expansion dominates the failure behaviour and drives the slip development and crack propagation during fire exposure.

The bond model needs to account for the confining action of the concrete cover. Splitting cracks were observed within 20-22 minutes in many fire tests carried out in scope of the thesis and the literature survey into the bond behaviour of strands showed that splitting cracks diminish the bond strength. Since these splitting cracks start at such an early stage of the fire, the effect of thermal expansion on the confining action has to be taken into account as well.

The concrete model needs to include irreversible damage by cracking to account for the irreversible reduction of the confining strength and the shear strength after the formation of the thermal cracks. Moreover, cracking must be based on the fracture energy in order to obtain mesh objective crack localisations.

The concrete model needs to include irreversible damage in compression by plastic straining and transient creep, in order to properly calculate the compressive stresses at the bottom of the HC

slab resulting from the incompatible thermal strains. An error in these stresses would lead to an error in the balancing tensile stresses in the web and the strands and consequently in the prediction of the crack development, the slip development and the failure behaviour of the slab. For the same reason, the concrete stiffness and strength at elevated temperatures need to be dependent on the loading history during heating, since the stiffness and strength of unloaded concrete decreases during heating significantly more than of compressed concrete.

### **9.1.3 Based on the models**

The shear and anchorage behaviour of fire exposed HC slabs is dominated by the aggregate type in the concrete mix, through the thermal expansion and the fracture energy of concrete. With the FE models it is shown that these two parameters determine the decrease in the load bearing capacity during fire exposure and the time to failure. The fracture energy determines the shear and anchorage behaviour in terms of the propagation of the thermal cracks and the remaining confining capacity of the concrete cover around the strands after the development of splitting cracks. The thermal expansion drives the thermal crack propagation and the slip development. Moreover, the aggregate type determines the thermal response of concrete. However, the variation in the thermal response has a minor effect on the shear and anchorage behaviour compared to the effect of the aggregate type through the variations in the fracture energy and the thermal expansion. Concretes containing aggregates with low thermal expansion such as expanded slag or andesite perform better than concretes with high thermal expansion containing for instance siliceous aggregates. Concretes with aggregates with a high fracture energy have a better performance than concretes with a low fracture energy.

Furthermore, the friction coefficient of the strand has a large effect on the anchorage behaviour. Also axial and transverse restraint of the thermal expansion enhances the shear and anchorage behaviour. Transverse restraint dramatically increases the concrete confinement and the resulting bond strength. Axial restraint reduces the vertical crack propagation, slip development and can postpone the growth of vertical thermal cracks into flexural cracks.

The decrease in the shear and anchorage capacity during fire is barely affected by the shear load during heating. As a result, the resistance can be determined without consideration of the solicitation.

The anchorage capacity of HC slabs decreases rapidly within the first 30 minutes of fire exposure, due to the development of vertical and splitting thermal cracks. Beyond 30 minutes of fire exposure only a minor further decrease is calculated.

Due to the gradual decrease in the resistance after a dramatic drop in the first 30 minutes, the widely spread method to ensure structural fire safety in which a requirement in terms of a time to failure must be satisfied, is inappropriate regarding shear and anchorage failure of HC slabs. Small variations in some of the influencing factors cause large variations in the time to failure. Alternatives are provided in the next paragraph.

## 9.2 RECOMMENDATIONS

### 9.2.1 Testing

In order to avoid an effect of the thermal stresses on the measured strength of concrete, it is recommended to limit the rate of heating to 0.2 °C/min, when conducting splitting tensile strength tests at elevated temperatures on specimens with a size of 75 mm diameter.

When the concrete properties need to be tested at elevated temperatures, using a minimum number of temperature levels, it is recommended to carry out tests at elevated temperatures at 80 and 150 °C in order to cover the trough in the strength that was reported by various researchers. Furthermore, tests at 400 °C are recommended, as the dehydration of the calcium hydroxide starts just beyond this temperature. And tests at 600 °C are recommended as the calcium hydroxide has fully dehydrated at that temperature and the quartz in siliceous particles in the concrete transform from  $\alpha$ -quartz to  $\beta$ -quartz at 573 °C, leading to an instantaneous expansion and internal damage.

There is a strong need for test data regarding the fracture energy of concrete at room temperature and elevated temperature. Because large variations and different influencing parameters were found in literature, while the fracture energy has a significant effect on the shear and anchorage behaviour of HC slabs at fire conditions.

### 9.2.2 Modelling

The temperature readings of the strands in HC slabs show great scatter and the use of these readings for the calibration of FE models is dissuaded.

For the modelling of the structural response of failure modes that are affected by incompatible thermal strains, it is recommended to include all the constitutive model features as described in §9.1.2.2.

### 9.2.3 Design

Regarding the concrete composition, the shear and anchorage capacity of fire exposed HC slabs can strongly be increased using a concrete mix with a high fracture energy, for instance through the addition of plastic or steel fibres in the mix. Also concrete with a low thermal expansion has a better performance than concrete with high thermal expansion. In order to limit the variations in the shear and anchorage capacity of HC slabs at fire conditions, it is recommended to monitor and control the thermal expansion and fracture energy of concrete and the friction of the strands.

Shear and anchorage failure can be effectively be avoided by insulation of the HC slabs over the transfer length of the prestress. Insulation over a shorter length does not adequately improve the behaviour.

Filling of the cores near the support with reinforced concrete is dissuaded, unless adequate bond

between the cast-in-place concrete and the precast product can be guaranteed.

It is dissuaded to rely on the beneficial effect of axial restraint at the supports of the HC slabs while sufficient axial restraint can not be ensured in the design. After all, the required amount of restraint is unknown in order to avoid shear and anchorage failure. Moreover, the actual restraining action provided by the cold structure surrounding the fire exposed HC slabs outside the fire compartment is generally unknown.

It is recommended to limit the allowable shear load on HC slabs in fire conditions to such an extent that shear and anchorage failure under fire conditions are avoided and flexural failure dominates the behaviour. For each HC slab on the market, the maximum shear load can be determined in a reliability analysis in which the properties of the slab should be varied systematically, within their variations. In order to limit the variations in the resistance, it is recommended to monitor and control the thermal expansion and fracture energy of concrete and the friction of the strands. Also the fire conditions should actually be varied, since variations in the development of the fire are expected to influence the thermal gradients over the depth of the slabs and consequently the incompatible thermal strains.

#### **9.2.4 Future research**

As the tests on the HC units reached a lower fire resistance than the comparable HC ribs, further research is recommended into load distribution between ribs, torsion, flexible supports and the effects of transverse restraint on the horizontal cracks at mid depth in the VX265 slab. Moreover, it is recommended to investigate the effect of moisture flow and cracking on the heat flow.

For each HC slab on the market, the maximum shear load can be determined for which flexural failure will dominate the behaviour at fire conditions, through a reliability analysis of each HC slab with the FE models presented in this thesis. The study can lead to a modification of the well known load-span interaction diagrams that are commonly used by the concrete industry. In the reliability analysis, the properties of the slab should be varied systematically, within their variations. Also the fire conditions should actually be varied, since variations in the development of the fire are expected to influence the thermal gradients over the depth of the slabs and consequently the incompatible thermal strains.

In order to allow for the inclusion of the beneficial effect of axial restraint in the design, it is recommended to incorporate restraining effects in the reliability study to determine the required amount of restraint in relation to the allowable shear load for which flexural failure dominates the behaviour. In addition, further studies into the restraining capabilities of cold surrounding structures need to be carried out, both experimental and with models. In doing so, it is recommended to conservatively assume that the fire will be fully developed in the entire fire compartment rather than in single room separated by interior walls without a fire separating function.

# Notation

## Greek Upper case

$\Phi$	strand diameter
$\Psi$	non-dimensional transfer length parameter [-]

## Greek lower case

$\alpha_{con}$	convection coefficient representing contribution of convective heat flux [W/m <sup>2</sup> K]
$\alpha_{rad}$	convection coefficient representing contribution of radiative heat flux [W/m <sup>2</sup> K]
$\alpha_{tot}$	convection coefficient representing total heat flux [W/m <sup>2</sup> K]
$\alpha_{cp}$	reduction factor for prestress in critical point [-]
$\alpha_E$	reduction factor for the Young's modulus of concrete depending on load history [-]
$\alpha_f$	reduction factor for the concrete compressive strength depending on load history [-]
$\alpha_{f2a}$	compressive yield contour factor [-]
$\alpha_{f2b}$	compressive yield contour factor [-]
$\alpha_T$	coefficient of thermal elongation [°C <sup>-1</sup> ]
$\alpha_t$	fictitious coefficient of thermal elongation to represent time dependent creep [°C <sup>-1</sup> ]
$\beta$	reliability index and standard normal deviate [-]
$\beta_1$	distance from the centroid of the compressive to from top of the slab, relative to the total height of the compressive zone [-]
$\beta_2$	shape factor for the compressive zone [-]
$\beta_{cc}$	reduction factor for maturing influence on concrete strength properties [-]
$\beta_f$	reduction factor for concrete creep coefficient depending on the concrete strength [-]
$\beta_{RHT}$	reduction factor for the influence of ambient conditions on concrete shrinkage [-]
$\beta_t$	reduction factor for concrete creep coefficient depending on time [-]
$\beta_{t0}$	reduction factor for concrete creep coefficient depending on start time of loading [-]
$\gamma_c$	partial safety factor for concrete [-]
$\gamma_{SC1}$	partial safety factor for shear compression model [-]
$\gamma_{SC2}$	partial safety factor for shear compression model [-]
$\gamma_{ST}$	partial safety factor for shear tension model [-]
$\delta$	total slip [mm]
$\delta_{el}$	elastic slip [mm]
$\delta_{pl}$	plastic slip [mm]
$\delta_{tol}$	ultimate allowable slip after prestress release for quality control [mm]
$\eta$	degree of utilization [-]
$\varepsilon$	strain component [-] or emission coefficient [-]
$\boldsymbol{\varepsilon}$	strain tensor
$\varepsilon_{auto}$	autogenous shrinkage strain [-]

$\varepsilon_{cas0}$	notional autogenous shrinkage strain [-]
$\varepsilon_{cs}$	notional drying shrinkage strain [-]
$\varepsilon_c$	concrete strain [-]
$\varepsilon_{c1}$	concrete compressive strain at peak stress [-]
$\varepsilon_{cr}$	crack strain [-]
$\varepsilon_{crp}$	creep strain [-]
$\varepsilon_{dry}$	drying shrinkage strain [-]
$\varepsilon_{el}$	elastic strain [-]
$\varepsilon_M$	mechanical strain [-]
$\varepsilon_p$	axial prestressing steel strain [-]
$\varepsilon_{p,0}$	initial axial prestressing steel strain due to prestressing [-]
$\varepsilon_{p,v}$	transverse strain of prestressing steel [-]
$\varepsilon_{p,v,0}$	initial transverse strain of prestressing steel due to prestressing [-]
$\varepsilon_{p,T}$	thermal strain of prestressing steel [-]
$\varepsilon_{pl}$	plastic strain [-]
$\varepsilon_{pl,1}$	maximal principal plastic strain [-]
$\varepsilon_{pl,2}$	minimal principal plastic strain [-]
$\varepsilon_{rr}$	radial expansion strain [-]
$\varepsilon_{rr,v}$	radial expansion strain due to the Poisson effect [-]
$\varepsilon_{rr,lof}$	radial expansion strain due to the lack of fit effect [-]
$\varepsilon_{rr,pit}$	radial expansion strain due to the pitch effect [-]
$\varepsilon_s$	shrinkage strain [-]
$\varepsilon_T$	thermal strain [-]
$\varepsilon_{tot}$	total strain [-]
$\varepsilon_{tr}$	transient strain tensor
$\varepsilon_{tr}$	transient creep strain [-]
$\varepsilon_{tr,eq}$	equivalent transient creep strain [-]
$\varepsilon_{tr,t}$	fictitious time dependent transient creep strain [-]
$\varphi$	concrete friction angle [-]
$\varphi_{cr,t}$	time dependent concrete creep coefficient [-]
$\varphi_{cr,tm}$	concrete creep coefficient at time of changing maturing conditions [-]
$\varphi_{cr,t0i,t}$	concrete creep coefficient at time $t$ due to loading at time $t_{0i}$ [-]
$\varphi_{RHT}$	notional creep coefficient depending on the ambient conditions [-]
$\phi$	rotation [-]
$\kappa$	curvature [ $\text{mm}^{-1}$ ]
$\kappa_c$	hardening parameter for concrete in compression [-]
$\kappa_{ce}$	hardening parameter value at peak concrete compressive stress [-]
$\kappa_{cu}$	ultimate hardening parameter value for concrete in compression [-]
$\kappa_{ce}$	hardening parameter value at peak compressive stress [-]
$d\kappa_{ro}$	hardening increment to round off softening curve of concrete in tension [-]
$\kappa_s$	hardening parameter for slip [mm]
$\kappa_t$	hardening parameter for concrete in tension [-]
$\kappa_{te}$	hardening parameter value at peak concrete tensile stress [-]
$\kappa_{tu}$	ultimate hardening parameter value for concrete in tension [-]

$\kappa_{u0}$	hardening parameter value related to reduced concrete tensile strength [-]
$\lambda$	thermal conduction coefficient [W/mK]
$\lambda_{ST}$	ratio between calculated shear stress and shear stress at failure [-]
$\lambda_{flex}$	ratio between shear tension capacity of HC slab on flexible and rigid supports [-]
$\mu$	friction coefficient [-] or mean value
$\nu$	Poisson constant [-]
$\mathbf{v}$	nodal test function vector
$\rho$	density [kg/m <sup>3</sup> ]
$\sigma$	stress component [MPa] or standard deviation or Stefan-Boltzmann coefficient [-]
$\boldsymbol{\sigma}$	stress tensor
$\sigma_c$	concrete stress [MPa]
$\sigma_I$	maximum principal stress [MPa]
$\sigma_{c,tot}$	concrete stress at the top of the slab [MPa]
$\sigma_p$	prestress [MPa]
$\sigma_{p0}$	initial prestress before release [MPa]
$\sigma_{pi}$	prestress after immediate losses [MPa]
$\sigma_{p\infty}$	prestress after time dependent losses [MPa]
$\sigma_{rr}$	confining stress [MPa]
$\sigma_{spl}$	splitting stress [MPa]
$\sigma_T$	normal thermal stress [MPa]
$\Delta\sigma_{t0i}$	stress increment at time $t_{0i}$ [MPa]
$\theta$	temperature [°C]
$\boldsymbol{\theta}$	nodal temperature vector [°C]
$\theta_0$	initial temperature [°C]
$\theta_E$	external temperature [°C]
$\theta_{fic}$	fictional temperature to include the maturing time in the concrete model [°C]
$\theta_S$	temperature at boundary surface $S$ [°C]
$\tau$	bond stress or shear stress [MPa]
$\tau_0$	initial bond strength [MPa]
$\tau_I$	principal shear stress [MPa]
$\tau_{el}$	bond stress related to elastic slip [MPa]
$\tau_{ini}$	adhesion part of yield bond strength [MPa]
$\tau_{pas}$	assumed bond stress beyond passive end in pull out test [MPa]
$\tau_{pl}$	bond stress related to plastic slip [MPa]
$\tau_T$	thermal shear stress [MPa]
$\tau_y$	yield bond strength [MPa]
$\chi$	ratio between calculated value with a model and value obtained in a test [-]

### Latin Upper case

$A$	cross sectional area [mm <sup>2</sup> ]
$A_{cp}$	cross sectional area of above the critical point [mm <sup>2</sup> ]
$A_p$	cross sectional area of prestressing steel [mm <sup>2</sup> ]

<b>B</b>	differential matrix
<b>C</b>	heat capacity matrix
<b>D</b>	constitutive relations matrix
$E_c$	Young's modulus of concrete [MPa]
$E_{c,20}$	Young's modulus of concrete at ambient conditions [MPa]
$E_{c,t0i}$	Young's modulus of concrete at time $t_{0i}$ during maturing [MPa]
$E_p$	Young's modulus of prestressing steel [MPa]
$E_{c,t}$	time dependent Young's modulus of concrete [MPa]
$EI$	bending stiffness [Nmm <sup>2</sup> ]
$F()$	standard normal cumulative distribution function
<b>F</b>	external force vector
$F_a$	applied load [kN]
$F_c$	resultant force in concrete cross section [kN]
$F_p$	resultant force in prestressing strands [kN]
$F_s$	support reaction [kN]
$F_{spl}$	splitting load [kN]
$GA$	shear stiffness [N]
$G_{el}$	elastic bond stiffness [N/mm]
$G_{tan}$	tangential bond stiffness [N/mm]
$G_F$	fracture energy for concrete in tension [J/m <sup>2</sup> ]
$G_{Fc}$	fracture energy for concrete in compression [J/m <sup>2</sup> ]
$I_1, I_2, I_3$	first stress invariants
$I_z$	second moment of inertia around the z-axis [mm <sup>4</sup> ]
$J$	compliance function
<b>K</b>	conductivity matrix
$K_i$	interface stiffness [N/mm]
$K_s$	spring stiffness [N/mm]
<b>L</b>	differential operator matrix
$M$	bending moment [kNm]
$M_a$	applied bending moment [kNm]
$M_A$	anchorage moment capacity [kNm]
$M_0$	decompression moment [kNm]
$M_c$	bending moment in the concrete part of the cross section [kNm]
$M_{c0}$	decompression moment in the concrete part of the cross section [kNm]
$M_{cr}$	cracking moment capacity [kNm]
$M_F$	flexural bending moment capacity [kNm]
$M_q$	bending moment due to applied uniform load [kNm]
$M_t$	bending moment at the root of the concrete tooth [kNm]
$M_{ta}$	tied arch moment capacity [kNm]
$M_{u,hog}$	hogging moment capacity [kNm]
$M_{u,sag}$	sagging moment capacity [kNm]
<b>N</b>	interpolation function matrix
$N$	normal force [kN]
$N_p$	normal force in the prestressing strands [kN]
$N_{pas}$	normal force in the prestressing strands at passive end in pull out tests [kN]
$N_c$	normal force in the concrete part of the cross section [kN]

$O_p$	perimeter of the steel strand [mm]
$\mathbf{Q}$	external flux vector
$R$	resistance
$\mathbf{R}$	radiative heat exchange factors matrix
$R^2$	correlation coefficient [-]
$S$	boundary surface [m <sup>2</sup> ] or solicitation
$S_t$	boundary surface with prescribed tractions
$S_u$	boundary surface with prescribed displacements
$S_z$	first moment of inertia around the z-axis [mm <sup>3</sup> ]
$V$	shear force [kN] or volume [m <sup>3</sup> ]
$V_{SC}$	shear compression capacity [kN]
$V_{ST}$	shear tension capacity [kN]
$V_{ST,flex}$	shear tension capacity including effect of flexible supports [kN]
$V_{test}$	shear load in a test [kN]
$W$	Section modulus [mm <sup>3</sup> ]
$W_0$	Section modulus of the total cross section including strands [mm <sup>3</sup> ]
$W_c$	Section modulus of the concrete cross section [mm <sup>3</sup> ]

### Latin lower case

$a$	shear span [m]
$b$	breadth [mm]
$b_{eff}$	effective breadth of composite beam [mm]
$b_w$	web breadth [mm]
$\Sigma b_w$	total web breadth of a HC unit [mm]
$c$	axis distance, i.e. distance from strand axis to the bottom of the slab [mm]
$c_1$	parameter in softening rule of Hordijk [1991]
$c_2$	parameter in softening rule of Hordijk [1991]
$c_{eff}$	effective concrete cover [mm]
$c_{ini}$	adhesion decrease coefficient [mm <sup>-1</sup> ]
$c_{lof}$	lack of fit coefficient for contribution to radial expansion [-]
$c_v$	Poisson effect coefficient [-]
$c_p$	heat capacity [J/kgK]
$c_{pit}$	pitch effect coefficient [-]
$c_{slip}$	slip coefficient for contribution to radial expansion by of lack of fit [mm <sup>-1</sup> ]
$c_y$	yield value of concrete cohesion [MPa]
$c_{y,max}$	maximum yield value of concrete cohesion [MPa]
$d$	distance from the centroid of the tensile force to the top of the slab [mm]
$df_{ro}$	stress increment to round off softening curve of concrete in tension [MPa]
$d_i$	interface thickness [mm]
$e$	eccentricity of the strand to the neutral axis of the cross section [mm]
$e_c$	eccentricity of the strand to the neutral axis of the concrete cross section [mm]
$f$	yield function
$f_c$	concrete compressive strength [MPa]
$f_{c,20}$	concrete compressive strength at ambient conditions [MPa]

$f_{ck}$	characteristic concrete compressive strength [MPa]
$f_{cm}$	mean concrete compressive strength [MPa]
$f_{cmi}$	mean concrete compressive strength at time of prestress release [MPa]
$f_{cp}$	proportional limit of concrete in compression [MPa]
$f_{ct}$	concrete tensile strength [MPa]
$f_{ctd}$	design concrete tensile strength [MPa]
$f_{ctf}$	concrete flexural tensile strength [MPa]
$f_{ctk}$	characteristic 5% lower bound concrete tensile strength [MPa]
$f_{ctm}$	mean concrete tensile strength [MPa]
$f_{ctmi}$	mean concrete tensile strength at time of prestress release [MPa]
$f_{ctp}$	proportional limit of concrete in tension [MPa]
$f_{c,t}$	time dependent concrete compressive strength [MPa]
$f_{ct,t}$	time dependent concrete tensile strength [MPa]
$f_p$	tensile strength of prestressing steel [MPa]
$f_{yt}$	yield value of concrete in tension [MPa]
$f_{yt,max}$	maximum yield value of concrete in tension [MPa]
$\mathbf{g}$	volume forces vector
$g_{pl}$	function for the plastic strain of concrete in compression [-]
$g_{ic}$	function for the transient creep strain of concrete in compression [-]
$h$	height of the slab [mm]
$h_c$	numerical crack band width [mm]
$h_x$	height of the compressive zone [mm]
$k_E$	reduction factor for the Young's modulus depending on temperature [-]
$k_s$	scale factor [-]
$k_{ster}$	reduction factor on shrinkage strain for tensile creep effects [-]
$k_{ta}$	scale factor for the tied arch effect [-]
$k_{tr}$	transient creep factor [-]
$l$	length of the slab [m]
$l_b$	length of the beam [m]
$l_d$	development length [m]
$l_{cr}$	critical length [m]
$l_s$	span [m]
$l_t$	transfer length [m]
$l_{tm}$	transmission length [m]
$q$	uniformly distributed load [kN/m <sup>2</sup> ] or flux component [J/m <sup>2</sup> s]
$\mathbf{q}$	heat flux vector [J/m <sup>2</sup> s]
$q_{con}$	heat flux through convection [J/m <sup>2</sup> s]
$q_{rad}$	heat flux through radiation [J/m <sup>2</sup> s]
$q_S$	heat flux at boundary surface S [J/m <sup>2</sup> s]
$q_V$	heat production [J/m <sup>3</sup> s]
$r$	radius [mm]
$\mathbf{r}_{ij}$	distance vector between point $i$ and $j$ [m]
$r_p$	radius of the strand [mm]
$s_i s_j$	mutual radiative heat exchange factor among surface $i$ and $j$ [m <sup>2</sup> ]
$t$	time [min]
$\mathbf{t}$	surface tractions vector

$t_0$	start time [min]
$t_m$	time of changing maturing conditions [min]
$t_s$	start time of drying period [min]
$t_T$	equivalent time depending on temperature history [min]
$u$	displacement component [mm]
$\mathbf{u}$	nodal displacement vector
$w$	deflection [mm]
$w_u$	ultimate crack opening [mm]
$\mathbf{w}$	gross incoming radiative flux vector [ $\text{J}/\text{m}^2\text{s}$ ]
$x$	perimeter along slab axis [mm]
$z$	inner lever arm [mm]



# References

- ABRAMS, M.S.: 1971, *Compressive Strength of Concrete At Temperatures to 1600 F*, Temperature and Concrete, ACI Special Publications SP25, Detroit, USA, pp 33-58.
- ABRAMS, M.S.: 1976, *Fire Tests of Hollow Core Specimen with and Without Roof Insulation*, PCI Journal, Jan./Feb. 1976 page 40-49, PCA Skokie, Ill., USA.
- VAN ACKER, A.: 2000, *Dwarskrachtsterkte van voorgespannen holle vloeren bij brand*, Beton, Tijdschrift van het Prefab beton, Oct. 2000, FeBe, Brussels, Belgium (in Dutch).
- ALTOUBAT, S.A.; LANGE, D.A.: 2001a, *Creep, Shrinkage and Cracking of restrained concrete at early age*, ACI Materials Journal, Volume 98, No. 4, July-August 2001, USA.
- ALTOUBAT, S.A.; LANGE, D.A.: 2001b, *Tensile basic Creep: Measurement and behaviour at early age*, ACI Materials Journal, Volume 98, No. 5, September-October 2001, USA.
- ANDERBERG, Y.; THELANDERSSON, S.: 1976, *Stress and Deformation Characteristics of Concrete at High Temperatures, Part 2, Experimental Investigation and Material Behaviour Model*, Lund University of Technology, Div. Of Structural Mechanics and Concrete Construction - Bulletin 54, Sweden.
- ANDERSEN, N.E.; LAURIDSEN, D.H.: 1999, *Hollow Core Concrete Slabs*, DIFT, technical report X52650, Hvidovre, Danmark
- ARTHUR, P.D.: 1965, *The shear strength of pretensioned I-beams with unreinforced webs*, Magazine of Concrete Research, Vol 17, Nr. 53.
- BAZANT Z.P.; KAPLAN, M.F.: 1996, *Concrete At High Temperatures*, Longman Scientific and Technical, UK
- BECKER, R.J., BUETTNER, D.R.: 1985, *Shear Tests of Extruded Hollow Core Slabs*, PCI Journal, March April, pp 40-54.
- BIGAJ, A.J.; DEN UIJL, J.A.: 1996, *Tension stiffening simulation with confinement based bond model*, Progress in Concrete Research, Vol.5, Delft University of Technology
- BIGAJ, A.J.: 1999, *Structural Dependence of Rotation Capacity of Plastic Hinges in RC Beams and Slabs*, Ph.D. Thesis, Delft University of Technology
- BIZA: 1996: *Fire Safety Concepts Offices and Education Buildings*, Ministry of internal affairs, The Hague, the Netherlands. (In Dutch)
- BLUNDELL, R.; DIAMOND, C.; BROWNE, R.G.: 1976, *The Properties of concrete subjected to elevated temperatures*, Technical note No 9, CIRIA Underwater Engineering Group, London, UK.
- BORGOGNO, W.; FONTANA, M.: 1995, *Brandversuch an einer Slim Floor Decke*, IBK interner Bericht 95-1, ETH, Zurich, Switzerland (in German)
- BORGOGNO, W.; FONTANA, M.: 1996, *Versuche zum Tragverhalten von Betonhohlplatten mit Flexibeler Auflagerung bei Raumtemperaturen und Normbrandbedingungen*, IBK Bericht 219, ETH Zurich, Birkhäuser Verlag Basel, Switzerland (in German)
- BORGOGNO, W.: 1997, *Tragverhalten von Slim Floor Deckes mit Betonhohlplatten bei Raumtemperatur und Brandeinwirkungen*, IKB Bericht No. 233, Birkhäuser Verlag Basel, Switzerland. (in German)
- DE BORST, R.: 1991, *Computational Methods in Non Linear Solid Mechanics, Part 2: Physical Non-linearity*, Delft UT report 25-3-91-2-06, TNO report BI-91-043, Delft, the

- Netherlands.
- BRANDER, M.E.; PARKS, R.L.: 1968, *Floor or Roof and Ceiling Construction Consisting of Prestressed Pretensioned Concrete Hollow-Core Flat Slabs*, Underwriters' Laboratories, File R5558, Chicago, Ill. USA.
- BREKELMANS, J.W.P.M.; FELLINGER, J.H.H.; HOVE, VAN, B.W.E.M.: 1999, *Aanbevelingen voor het ontwerp, de vervaardiging en toetsing van vloeren bestaande uit kanaalplaten met geïntegreerde stalen liggers*, CUR VC53 / SG TC 11 - WG1, Gouda (in Dutch)
- BREUNESE, A.J.: 2001, *Tensile Properties of Concrete during Fire*, Delft University of Technology - TNO Centre for Fire Research report 2001-CVB-R04634, Rijswijk ZH, the Netherlands
- BRUGGEMAN, D.A.G.: 1936, *Über Die Geltungsbereiche Und Die Konstantwerte Der Verschiedenen Mischkorperformeln Lichteneckers*, Physikalische Zeitschrift 37: 906 (in German)
- BRUNAUER S.; GREENBERG, S.A.: 1962, *The Hydration of Tricalcium Silicate and  $\beta$ -Dicalcium Silicate At Room Temperature*. Chemistry of Cement, Vol. I, Proc. of the 4<sup>th</sup> Int. Symp., 2-7 Oct. 1960, Washington Dc, Nat. Bureau of Standards Monograph 43 - Vol I, Us Government Printing Office, P. 135
- CAFLISCH, R.; THÜRLIMANN, B.: 1970, *Schubversuche an Teilweise Vorgespannten Betonbalken, Serie A & B*, Bericht 6504-02 Institut für Bautechnik ETH Zurich, Switzerland. (In German)
- CAFLISCH, R.; KRAUS, R.; THÜRLIMANN, B.: 1971, *Biege- und Schubversuche an Teilweise Vorgespannten Betonbalken, Serie C*, Bericht 6504-03 Institut für Bautechnik ETH Zurich, Switzerland.(In German)
- Carlson, C.C., Selveggio, S.L., Gustafarro, A.H.: 1965, *A Review of Studies of the Effect of Restraint on the Fire Resistance of Prestressed Beams*, Bulletin 206, Research Department, PCA, Skokie, Ill. USA
- CBR: 1977, *Fire Resistance of Spiroll Slabs*, Test- Survey in Different Countries, Calculation of Fire Resistance, SRP. 033, CBR, Lier, Belgium.
- CEB-FIP: 1991, *Model Code 1990 - Design Code for Concrete Structures*, Thomas Telford, Trowbridge
- CEDERWALL, K.; HEDMAN, O.; LOSBERG, A.: 1974, *Shear strength of partially Prestressed Beams with Pretensioned Reinforcement of High Grade Deformed Bars*, in ACI Publication SP-42 Shear in Reinforced Concrete, Detroit, USA.
- CIB W14: 1983, *A Conceptual Approach Towards a Probability Based Design Guide on Structural Fire Safety*, Workshop report in Fire Safety Journal, Vol. 6 No. 1, Elsevier Sequoia S.A., Lausanne, Switzerland
- CIB W14: 1986, *Design Guide Structural Fire Safety*, Fire Safety Journal, Vol. 10 No. 2, Elsevier Sequoia S.A., Lausanne, Switzerland
- CUR : 1958, *Brandproeven op Voorgespannen betonliggers*, CUR rapport 13, Gouda, the Netherlands. (in Dutch)
- DANTUMA, W.F.: 1987, *De Invloed van Dwarscontractie op het Aanhechtgedrag van Voorspanstrengen*, Graduation report, TU Delft, the Netherlands
- DARWIN, D.; BARHAM, S.; KOZUL, R.; LUAN, S.: 2001, *Fracture energy of High Strength Concrete*, ACI Material's Journal, Vol. 98, Title 98-M45, Sep./Oct., USA, pp 410-417
- DEATHERAGE, J.H.; BURDETTE, E.G.; CHEW, C.K.: 1994, *Development Length and lateral*

- Spacing Requirements of Prestressed Strands for Prestressed Concrete Bridge Girders*, PCI Journal Jan-Feb, pp 76-84
- DEN UIJL, J.A.: 1992, *Bond and Splitting Action of Prestressing Strand*. International Conference on Bond in Concrete, October 15-17, Riga, Estonia.
- DEN UIJL, J.A.: 1995, *Transfer length of Prestressing Strand in HPC*, Progress in Concrete Research, Vol. 4, Delft University of Technology.
- DEN UIJL, J.A.: 1998, *Bond Modelling of Prestressing Strand*, ACI Special Publication 180, pp 145-169, Michigan USA.
- DEN UIJL, J.A.: 2001, *Zelfverdichtend Beton, Deel 7: Aanhechting Strengen*, TU Delft report 25.5.01-02, the Netherlands (in Dutch)
- DIAS, W.P.S.: 1986, *Time Dependent Deformations of Hardened Cement Paste From 20 °C to 725 °C*. Ph.D. Thesis, University of London.
- DIEDERICHS, U., SCHNEIDER, U.: 1981, *Bond Strength At High Temperature*, Magazine of Concrete Research, Vol 33, No 115. June 1981, pp 75-84.
- DIEDERICHS, U., SCHNEIDER, U.: 1982, *Changes in Bond Behaviour due to Elevated Temperatures*, Proc. of the Int. Conf. On Bond in Concrete, Paisley College, Scotland
- DIEDERICHS, U.; EHM, C.; HINRICHSMEYER, K.; SCHNEIDER, U.; WYDRA, W.: 1987, *Hochtemperatur-verhalten von Festbeton*, Sonderforschungsbericht 148, Brandverhalten von Bauteilen, Arbeitsbericht 1984-1986, Teil II, Projectbereich B3, TU Braunschweig, Germany. (in German)
- EHM, C.: 1986, *Versuche Zur Festigkeit und Verformung von Beton under Zweiaxialer Beanspruchung und Hoher Temperaturen.*, iBMB, TU Braunschweig, Heft 71 (in German)
- VAN ELTEREN, J.F.: 1972, *De Bepaling van de Brandwerendheid van een Vloer Samengesteld uit 2 Voorgespannen Kanaalplaten (SP-platen)*. TNO Centrum voor Brandveiligheid, report BV-72-13, Rijswijk ZH, the Netherlands (In Dutch)
- ENV 1992-1-2: 1995, *Eurocode 2: Design of Concrete Structures, Part 1.2: General Rules. Structural Fire Design*, CEN, Brussels
- ECCS/IPHA: 1998, *Guidelines for the Application of Prestressed Hollow Core Slabs Supported on Built-in Beams*, ECCS Publication 103
- FEENSTRA, P.H.: 1993, *Computational Aspects of Biaxial Stress in Plain and Reinforced Concrete*. Ph.D. Thesis, Delft University of Technology
- FEENSTRA, P.H.; BORST DE, R.: 1993, *Aspects of Robust Computational Modeling for Plain and Reinforced Concrete*, Heron, Vol. 38 - No. 4, Delft, the Netherlands
- FELICETTI, R.; GAMBAROVA, P.G.: 1998, *On the Residual Properties of High Performance Siliceous Concrete Exposed to High Temperature*, Proc. Of the Int. Workshop in Honor of Z.P. Bažant's 60 anniversary, Prague, Czech Rep.
- FELICETTI, R.; GAMBAROVA, P.G.: 1999, *On the Residual Tensile Properties of High Performance Siliceous Concrete Exposed to High Temperature*, From Mechanics of Quasi brittle materials and Structures
- FELLINGER, J.H.H.: 1998, *Shear and Anchorage Behaviour of Fire Exposed HC Slabs, second Interim report*, TNO Building and Construction research, Delft University of Technology, Technology Foundation STW, Delft
- FELLINGER, J.H.H.: 1999a, *Shear and Anchorage Behaviour of Fire Exposed HC Slabs, Third interim report*, TNO Building and Construction research, Delft University of Technology, Technology Foundation STW, Delft

- FELLINGER, J.H.H.: 1999b, *Shear and Anchorage Behaviour of Fire Exposed HC Slabs, Test report: Fire tests on double ribs sawn out of HC slabs*, TNO Building and Construction Research, Delft University of Technology, Technology Foundation STW, Delft
- FELLINGER, J.H.H.: 2000a, *Shear and Anchorage Behaviour of Fire Exposed HC Slabs, Test report: Fire Test on Double Rib of HC Slab with Concrete Filled Cores*, TNO Building and Construction Research, Delft University of Technology, Technology Foundation STW, Delft
- FELLINGER, J.H.H.: 2000b, *Shear and Anchorage Behaviour of Fire Exposed HC Slabs, Test report: Fire Tests on Bare HC Units*, TNO Building and Construction Research, Delft University of Technology, Technology Foundation STW, Delft
- FELLINGER, J.H.H.; BOTH, C.: 2000, *Fire Resistance: Reliability vs. Time Analyses*, Proc. of the Int. Conf. on Composite Structures, Banff, Canada.
- FELLINGER, J.H.H.: 2001a, *Shear and Anchorage Behaviour of Fire Exposed HC Slabs, Test Report: Fire Test on Bare HC Ribs with Varying Shear Loading*, TNO Building and Construction Research, Delft University of Technology, Technology Foundation STW, Delft
- FELLINGER, J.H.H.: 2001b, *Shear and Anchorage Behaviour of Fire Exposed HC Slabs, Test report: Fire Test on Concrete Filled HC Ribs with Varying Shear Loading*, TNO Building and Construction Research, Delft University of Technology, Technology Foundation STW, Delft
- FELLINGER, J.H.H.: 2001c, *Shear and Anchorage Behaviour of Fire Exposed HC Slabs, Test Report: Fire Test on Symmetrical HC Ribs with Varying Shear Loading*, TNO Building and Construction Research, Delft University of Technology, Technology Foundation STW, Delft
- FIB: 1999, *Structural Concrete, Textbook on Behaviour, Design and Performance*, fib manual, Bulletin 1, Lausanne, Switzerland.
- FIB: 2000, *Bond of Reinforcement in Concrete, fib State of the Art Report*, Bulletin 10, Chapter 6, Task Group Bond Models, Working Party 6, Lausanne, Switzerland
- FIP: 1988, *Precast Prestressed Hollow Core Floors*, FIP Recommendations, Thomas, Telford, London
- GANTVOORT, G.J.: 1981, *Brandwerendheid van Holle Vloerplaten*, TNO Centrum voor Brandveiligheid, Report B-81-106/62.6.0909, Rijswijk ZH, the Netherlands (in Dutch)
- GRAIGNER, B.N.: 1980, *Private Communication*, Central Electricity Research Laboratories, UK
- HAMILTON, R.L.; CROSSER, O.K.: 1962, *Thermal Conductivity of Heterogenous Two-component Systems*, Industrial & Engineering Chemistry Fundamentals (American Chemical Society) 411: 187
- HARMATHY, T.Z.; BERNDT, J.E.: 1966, *Hydrated Portland Cement and Light Weight Concrete at Elevated Temperatures*. Journal of the American Concrete Institute, Vol 63 No 1, Detroit, USA, pp 93-111.
- HARMATHY, T.Z.: 1970, *Thermal Properties of Concrete At Elevated Temperatures*, ASTM Journal of Materials 5:47
- HARMATHY, T.Z.: 1993, *Fire Safety Design and Concrete*, Longman Scientific and Technical, UK.
- HEDMAN, O.; LOSBERG, A.: 1978, *Design of Concrete Structures with regard to Shear Forces*,

- Bulletin d'Information CEB No. 126, Lausanne, Switzerland
- HERTZ, K.: 1982, *The Anchorage Capacity of Reinforcing Bars at Normal and High Temperatures*, Magazine of Concrete Research, Vol 34 No 121, pp 213-220
- HIETANEN, T.: 1992, *Fire Tests For Finnish Hollow Core Slabs*, Association of the Concrete Industry Finland, Finland (confidential)
- HORDIJK, D.A.: 1991, *Local Approach to Fatigue of Concrete*, Ph.D. Thesis, Delft University of Technology
- HUYGHE, G.F., WALRAVEN, J.C., STROBAND, J.: 1980, *Research on Extruded Prestressed Concrete Hollow Core Slabs*, TU Delft Report 5-80-2, TU Delft, Stevin Laboratory Concrete Structures, Delft the Netherlands.
- ISO 834-1: 1999, *Fire-Resistance Tests - Elements of Building Construction - Part 1: General Requirements*, ISO, Geneva, Switzerland
- JOHNSON, O.F.; PARKS, R.L.: 1966, *Floor or Roof and Ceiling Construction Consisting of Prestressed Pretensioned Concrete Hollow-Core Flat Slabs*, Underwriters' Laboratories, File R5309-4, Chicago, Ill. USA.
- KAMERLING, J.W.; FIJNEMAN, H.J.: 1980, *Onderzoek Holle Prefab. Vloerplaten. Deel 1,2, & 3*, TU Eindhoven, afd. Bouwkunde, Vakgroep Constructief Ontwerpen. (in Dutch)
- KHOURY, G.A.; GAINGER, B.N.; SULLIVAN, P.J.E.: 1985, *Strain of Concrete During First Heating to 600 °C Under Load*, Magazine of Concrete Research, Vol 37, No. 133, pp 195-215
- KHOURY, G.A.: 1992, *Compressive Strength of Concrete At High Temperatures: A Reassessment*, Magazine of Concrete Research, Vol 44, No. 161, pp 291-309
- KINGERY, W.D.: 1959, *Property Measurement At High Temperatures*, John Wiley & Sons, New York, USA.
- KLEIN HOLTE, R.: 1998, *Collection of Standard Shear Tests on HC Units*, Internal correspondence, VBI, Huissen, the Netherlands (Confidential)
- KOK, A.W.M.: 1991, *Numerical Mechanics, the Displacement Method*, Reader B18, TU Delft, the Netherlands
- LANKARD, D.R.: 1970, *The Dimensional Stability of Heated Portland Cement Concrete*, Ph.D. Thesis, Ohio State University, Cleveland, Ohio
- LEA, F.C.: 1920, *The Effect of Temperature on Some of the Properties of Materials*, Engineering, Vol. 110, UK, pp. 293-298
- LEA, F.C. & STRADLING, R.: 1922, *The Resistance to Fire of Concrete and Reinforced Concrete*, Engineering, Vol 114, No 2959, UK, pp. 341-344 and 380-383
- LEBORGNE, H.; FRÉCHET, O.: 1996a, *Plancher Béton Comprenant une Dalle en Béton Alvéolée Précontrainte et Deux Poutres d'Extrémité en PRS*, CTICM report 96-U-349, Metz, France (in French)
- LEBORGNE, H.; FRÉCHET, O.: 1996b, *Plancher Béton Comprenant une Dalle en Béton Alvéolée Précontrainte et Deux Poutres d'Extrémité en Béton Armé*, CTICM report 96-U-350, Metz, France (in French)
- LEONHARDT, F.; KOCH, R.; ROSTÁSY, F.S.: 1973, *Schubversuche an Spannbetonträgern*. Deutscher Ausschuß für Stahlbeton ; Heft 227, Ernst, Berlin Germany. ISBN 3-433-00629-6. (In German)
- LESKALÄ, M.V.: 1991a, *The shear Failure Condition in Hollow Core Slab Units Loaded by Vertical and Transverse Shear Force Components*. Journal of Structural Mechanics, Vol. 24, No. 2 Finnish Association for Structural Mechanics, Finland pp 22-29.

- LESKALÄ, M.V.: 1991b, *Strength Reduction in Hollow Core Slabs when Supported by Beams and Girders*. Nordic Concrete Research Publication 10, Nordic Concrete Federation, pp 105-120
- LIE, T.T.: 1965, *Insulation Materials and Building Constructions Exposed to Fire*, Heron Vol. 13 - No. 2, Delft, the Netherlands. [in Dutch]
- LOIKKANEN, P.; JUMPPANEN, U-M.: 1984a, *Burning test on an Variax 5 Hollow Slab*, VTT Technical Research Centre, Report PAL 4437, Espoo, Finland (in Finnish, confidential)
- LOIKKANEN, P.; JUMPPANEN, U-M.: 1984b, *Burning test on a Loaded Variax 5 Hollow Slab*, VTT Technical Research Centre, Report PAL 4450, Espoo, Finland (Confidential)
- LOIKKANEN, P.; JUMPPANEN, U-M.: 1984c, *Burning test on an Unloaded Variax 5 Hollow Slab*, VTT Technical Research Centre, Report PAL 4452, Espoo, Finland (Confidential)
- LOIKKANEN, P.; JUMPPANEN, U-M.: 1984d, *Burning test on an Variax 5 Hollow Slab*, VTT Technical Research Centre, Report PAL 4453, Espoo, Finland (in Finnish, Confidential)
- LOIKKANEN, P.; JUMPPANEN, U-M.: 1985a, *The Determination of the Fire Resistance of a Variax 6 Hollow Core Slab*, VTT Technical Research Centre, Report PAL 566a, Espoo, Finland (Confidential)
- LOIKKANEN, P.; JUMPPANEN, U-M.: 1985b, *The Determination of the Fire Resistance of a Parma 5 Hollow Core Slab*, VTT Technical Research Centre, Report PAL 566b, Espoo, Finland (Confidential)
- LOIKKANEN, P.; KAJASTILA, R.: 1990a, *Fire Test on an Unloaded L4 A120 Hollow Core Slab*, VTT Technical Research Centre, Report PAL 360a, Espoo, Finland (in Finnish, Confidential)
- LOIKKANEN, P.; KAJASTILA, R.: 1990b, *Fire Test on a Loaded L4 A120 Hollow Core Slab*, VTT Technical Research Centre, Report PAL 360b, Espoo, Finland (Confidential)
- LOIKKANEN, P.; KAJASTILA, R.: 1991, *Fire Test on a Loaded L4 A60 Hollow Core Slab*, VTT Technical Research Centre, Report PAL 1127, Espoo, Finland (Confidential)
- MAGNUSSON, S.E.: 1974, *Probabilistic Analysis of Fire Exposed Steel Structures*, Bulletin 27, Lund Institute of technology, Div. Of Structural Mechanics and Concrete Construction, Lund, Sweden
- MAGNUSSON, S.E.; PETTERSON, O.: 1974, *Functional Approaches - An Outline*, Bulletin 27, CIB Symposium on Fire Safety in Buildings: Needs and Criteria, CIB Publ. 48, pp.120-145.
- MALHOTRA, H.L.: 1969, *A Standard Fire Resistance Test on a Floor of Prestressed Concrete 'Spiroll' Units*. Ministry of Technology and Fire Offices' Committee Joint Fire research Organisation, F.R.O.S.I. 4904, UK.
- MARTIN, H.: 1973, *Relation between Surface Characteristics, Bond and Splitting Action of Reinforcement Under Short Term Loading*. (In German) Heft 228 Deutscher Ausschuss für Stahlbeton, Verlag, Wilhelm Ernst & Sohn, Berlin, Germany
- MAXWELL, J.C.: 1904, *A Treatise on Electricity and Magnetism*, Vol. 1, 3<sup>rd</sup> Ed. Clarendon Press, Oxford, UK, p 440
- MORLEY, P.D., ROYLES, R.: 1979, *The Influence of High Temperature on the Bond in Reinforced Concrete*, Fire Safety Journal 2 ( 1979/1980) pp. 243-255, Elsevier Sequoia S.A. Lausanne, Switzerland.
- MORLEY, P.D., ROYLES, R.: 1983, *Response of the Bond in Reinforced Concrete to High*

- Temperatures*, Magazine of Concrete Research Vol. 35, No 123, pp. 67-74.
- NOAKOWSKI, P.: 1978, *The Reinforcement of Composite Steel Concrete Structures Under Temperature Loading*. Heft 296 Deutscher Ausschuss für Stahlbeton, Verlag, Wilhelm Ernst & Sohn, Berlin, Germany, (In German)
- NEN 6072: 1991, *Determination by Calculation of the Fire Resistance of Building Elements, Steel structures*, NNI, Delft, the Netherlands. [In Dutch]
- NOWAK, A.S. COLLINS, K.R.,: 2000, *Reliability of Structures*, McGraw Hill Higher Education, USA
- OLESEN, S.Ø.; SOZEN, M.A.; SIESS, C.P.: 1967, *Investigation of Prestressed Reinforced Concrete for Highway Bridges, Part IV: Strength in Shear of Beams with Web Reinforcement*, Engineering Experiment Station Bulletin 493, University of Illinois, USA.
- OTTOSEN, N.S.: 1977, *A Failure Condition for Concrete*, in ASCE Journal of the Engineering Mechanics Division, Vol. 103, No. EM4.
- PAJARI, M.: 1995a, *Shear Resistance of Prestressed Hollow Core Slabs on Flexible Supports*, VTT Technical Research Centre of Finland Publication No. 228, Espoo: Finland.
- PAJARI, M.: 1995b, *Design Recommendations for Hollow Core Slabs Supported on Beams*, VTT Report RTE37-IR-2/1995, Espoo, Finland.
- PAJARI, M.; KOUKKARI, H.: 1998, *Shear Resistance of PHC Slabs Supported on Beams, Part I, Tests*, ASCE Journal of Structural Engineering, pp. 1050-1061
- PAJARI, M.: 1998, *Shear Resistance of PHC Slabs Supported on Beams, Part II, Analysis*, ASCE Journal of Structural Engineering, pp. 1062-1073
- PEHERSTORFER, H.; MOSER, K.: 1983, *Prüfbericht: Spannbetonhohldielen-Decke System "VSD" 9-16*, IBS, Report BV 2311/83, Linz, Austria (In German)
- PEHERSTORFER, H.; MOSER, K.: 1987, *Prüfzeugnis: Spannbetonhohldielen-Decke System "VSD" 26,5 D - "VSD" 40 D*, IBS, Report BV 2697/87, Linz, Austria (In German)
- PEHERSTORFER, H.; MOSER, K.: 1993, *Prüfzeugnis: Spannbetonhohldeckenelemente V6/20*, IBS, Report BV 3391/93Z, Linz, Austria (In German)
- PISANTY, A.: 1992, *The Shear Strength of Extruded Hollow Core Slabs*, Materials and Structures, Vol 25, pp. 224-230
- POPOVICS, S.: 1973, *A Numerical Approach to the Complete Stress-strain Curve of Concrete*, Cement and Concrete Research, 3, pp 583-599
- POWERS, T.C.: 1949, *The Non Evaporable Water Content of Hardened Portland Cement Paste - its Significance for Concrete Research and Methods of Determination*. ASTM Bulletin, No. 158, Pp 68; Bulletin 29, Research and Development Laboratories of the Portland Cement Association, Skokie Ill. USA
- POWERS, T.C.: 1958, *Structure and Physical Properties of Hardened Portland Cement Paste*. Journal of the American Ceramic Society 41: 1, Bulletin 94, Research and Development Laboratories of the Portland Cement Association, Skokie Ill. USA.
- POWERS, T.C.: 1962, *Physical Properties of Cement Paste*. In *Chemistry of Cement*, Vol. II, Proc. of 4<sup>th</sup> Int. Symp. 2-7 Oct 1960, Nat. Bureau of Standards Monograph 43 - Vol II, US Government Printing Office, Washington DC, USA, p. 577
- PREN 1168-1: 1997: *Precast Concrete Products - Hollow Core Slabs for Floors - Part 1: Prestressed Slabs*, CEN, Brussels, Belgium
- PREN 1991-1-2: 2002, *Eurocode 1: Basis of Design and Action on Structures, Part 2.2: Actions on Structures Exposed to Fire*, CEN, Brussels, Belgium
- PREN 1992-1-1: 2002: *Eurocode 2, Design of Concrete Structures, Part 1.1: General Rules and*

- Rules for Buildings*, CEN, Brussels, Belgium
- PREN 1992-1-2: 2002: *Eurocode 2, Design of Concrete Structures, Part 1.2: General Rules - Structural Fire Design*, CEN, Brussels, Belgium
- PURKISS, J.A.; BALI, A.: 1988, *The Transient Behaviour of Concrete At Temperatures Up to 800 °C*, Proceeding of the 10<sup>th</sup> Ibausul, Weimar 1988, Hochschule Für Architektur Und Bauwesen, Weimar, Section 2/1, Pp 234-239.
- PURKISS, J.A.: 1996, *Fire Safety Engineering, Design of Structures*, Butterworth Heinemann, Oxford.
- REINHARDT, H.W.: 1998, *Beton als Constructiemateriaal, Eigenschappen en Duurzaamheid*, Delftse Universitaire Pers, Delft (in Dutch)
- ROSTÁSY, F.S., NEISECKE, J., BUDELMANN, H., SAGER, H.: 1980: Bond Behaviour of Reinforcing and Prestressing Steels At Elevated Temperatures,, Sonderforschungsbereich 148: Brandverhalten von Bauteilen Teilproject B5: Förderungsantrag 1980, pp. 157-176 (in German)
- ROSTÁSY, F.S.; SAGER, H.: 1985, *Hochtemperaturverhalten von Beton- und Spannstählen*, Sonderforschungsbereich 148, Schlussbericht des Teilproject B5, TU Braunschweig, Germany, (in German)
- ROYLES, R., MORLEY, P.D., KHAN, M.R.: 1982: *The Behaviour of Reinforced Concrete At Elevated Temperatures with Particular Reference to Bond Strength*, Proc. Of the Int. Conf. On Bond in Concrete, Paisley College, Scotland
- RUSSELL, B.W.; BURNS, N.H.: 1993, *Design Guidelines for Transfer, Development and Debonding of Large Diameter 7 wire Strands in Pretensioned Concrete Girders*, University of Texas, Center for Transportation Research, Report 1210-5F, USA
- SAGER, H., ROSTÁSY, F.S.: 1982, *The Effect of Elevated Temperature on the Bond Behaviour of Embedded Reinforcing Bars*, Proc. Of the Int. Conf. On Bond in Concrete, Paisley College, Scotland
- Sager, H.: 1985: *About the Influence of Elevated Temperatures on the Bond Behaviour of Reinforcement in Concrete*. (In German) Heft 68, iBMB, Braunschweig UT, Braunschweig, Germany.
- SARSHAR, R.: 1989, *Effect of Elevated Temperature on the Strength of Different Cement Pastes and Concretes*, Ph.D. Thesis DX187706, Dep. Of Civil Engineering, Imperial College of Science, Technology and Medicine, London University, London.
- SCHEPPEL, L. LANGSTRUP PETERSEN, P., ANDERSEN, N.E.: 2000, *Fire Test of Deck Elements*, DIFT + COWI, Technical Report PG 10724, Hvidovre, Denmark
- SCHNEIDER, U.: 1982, *Creep effects under Transient Temperature Conditions, in Fundamental Research on Creep and Shrinkage of Concrete*, edited by Wittmann, F.H., Martinus
- SCHNEIDER, U.: 1985, *Properties of Materials at High Temperatures - Concrete*, RILEM Committee 44 - PHT, GhK, Kassel, Germany.
- SCHNEIDER, U.: 1988, *Concrete At High Temperatures - A General Review*, Fire Safety Journal 13, Elsevier Sequoia, the Netherlands, pp 55-68
- SOZEN, M.A.; ZWOYER, E.M.; SIESS, C.P.: 1959, *Investigation of Prestressed Concrete for Highway Bridges*, Part I: Strength in Shear of Beams without Web Reinforcement, Engineering Experiment Station Bulletin 452, University of Illinois.
- SPANBETON: 1998, *Default Shear Test Sheets*, Spanbeton, Koudekerk a/d/ Rijn, the Netherlands. (Confidential)
- STOCKER, M.F.; SOZEN, M.A.: 1969, *Investigation of Prestressed Reinforced Concrete for*

- Highway Bridges, Part VI, Bond Characteristics of Prestressing Strand*, University of Illinois, Structural Research Series, NO 344, USA
- TEIRLINCK, S; VANDEVELDE, P.: 1999a, *Oriëntatieproef Betreffende de Weerstand tegen Brand van een Belaste Vloer*, Laboratorium voor Aanwending van Brandstoffen en Warmteoverdracht, verslag Nr. 8871, Universiteit Gent, Belgium, (in Dutch)
- TEIRLINCK, S; VANDEVELDE, P.: 1999b, *Oriëntatieproef Betreffende de Weerstand tegen Brand van een Belaste Vloer*, Laboratorium voor Aanwending van Brandstoffen en Warmteoverdracht, verslag Nr. 8872, Universiteit Gent, Belgium, (in Dutch)
- TEIRLINCK, S; VANDEVELDE, P.: 2000a, *Oriëntatieproef Betreffende de Weerstand tegen Brand van een Belaste Vloer*, Laboratorium voor Aanwending van Brandstoffen en Warmteoverdracht, verslag Nr. 9157, Universiteit Gent, Belgium, (in Dutch)
- TEIRLINCK, S; VANDEVELDE, P.: 2000b, *Oriëntatieproef Betreffende de Weerstand tegen Brand van een Belaste Vloer*, Laboratorium voor Aanwending van Brandstoffen en Warmteoverdracht, verslag Nr. 9158, Universiteit Gent, Belgium, (in Dutch)
- TEPFERS, R.: 1979, *Cracking of Concrete Cover along Anchored Deformed Reinforcing Bars*, magazine of Concrete research Vol31, No 106, pp 3-12
- TIMOSHENKO, S.: 1956, *Strength of Materials, Part II, Advanced Theory and Problems*, 3<sup>th</sup> Ed., Van Nostrand Reinhold Company, New York, USA, § 40.
- ULM, F-J.; COUSSY, O.; BAZANT, Z.P.: 1999, *The "Chunnel" Fire I: Chemoplastic Softening in Rapidly Heated Concrete*, Journal of Engineering Mechanics, Vol. 125, No. 3, pp 272-282
- VANDEVELDE, P.; ODOU, M.; MINNE, R.: 1983, *Verslag van Proeven - Vloerplaat in Voorgespannen Beton*, Laboratorium voor Aanwending der Brandstoffen en Warmteoverdracht, report 4514, Gent, Belgium (in Dutch).
- VEEN, VAN DER, C.: 1990, *Theoretical and Experimental Determination of Crack Width in Reinforced Concrete at Very Low Temperature*, Heron Vol. 35 - No 2, Delft, the Netherlands
- VERBECK, G.; COPELAND L.E.: 1972, *Some Physical and Chemical Aspects of High Pressure Steam Curing*, Menzel Symp. On High Pressure Steam Curing, ACI publ. SP-32, pp. 1-13
- VERMEULEN, G.: 1978, *Resistance au Feu des Dalles SP*, CBR Departement Technique, Report S.R.78/85, Lier, Belgium (in French)
- VONK, R.A.: 1992, *Softening of Concrete Loaded in Compression*, Ph.D. Thesis, Delft University of Technology
- VOS, E.: 1983, *Influence of Loading Rate and Radial Pressure on the Bond in Reinforced Concrete; a Numerical and Experimental Approach*, Ph.D. Thesis, Technische Universiteit Delft, the Netherlands.
- DE VRIES, D.A.: 1952, *The Thermal Conductivity of Granular Materials*, Problems Relating to Thermal Conductivity, Bulletin De L'institut International De Froid, Annexe 1952-i, Leuven, Belgium, P.115
- VROUWENVELDER, A.C.W.M.: 1977, *Optimum Fire Resistance*, Heron Vol. 22 - No. 3, Delft, the Netherlands.
- WAARTS, P.H.: 2000, *Structural Reliability Using Finite Elements Methods*, Ph.D. Thesis, Delft University of Technology, Delft, the Netherlands
- WALRAVEN, J.C.; MERCX, P.: 1983, *The Bearing Capacity of Prestressed Hollow Core Slabs*, Heron Vol. 28 - No. 3, Delft, the Netherlands

- WESCHE; NAUSE, P.: 1993, *Prüfzeugnis: Prüfung von Zwei Verbundträgern DELTA 3-400 in Verbindung mit Angrenzenden 260 mm Dicken Spannbetonhohldielen auf Brandverhalten*. IBMB, Report 3731/5353, Braunschweig, Germany (In German)
- DE WITTE, F.C.: 1999, *DIANA User's Manual, Release 7.2*, TNO Building and Construction Research, Delft, the Netherlands
- YANG, L.: 1994, *Design of Prestressed Hollow Core Slabs with Reference to Web Shear Failure*, ASCE Journal of Structural Engineering, Vol 120, No. 9, pp 2675-2696
- ZHAO, B.: 1993, *Analyse des Résultats d'un Essai de Résistance au Feu d'un Plancher Constitué de Poutres à Talon et Dalles Alvéolées en Béton Précontraint*, CTICM, report INC-93/204, Metz, France (in French)
- ZHAO, B.: 1995a, *Plancher mixte à Dalles Alvéolées Précontraintes et de Poutres à Talon Métallique*, CTICM, report 95-E-467, Metz, France (in French)
- ZHAO, B.: 1995b, *Plancher mixte à Dalles Alvéolées Précontraintes et de Poutres à Talon Métallique*, CTICM, report 95-E-533, Metz, France (in French)

# Appendix A: HC tests at ambient conditions

Database of tests on HC slabs on rigid supports at ambient conditions.

In the second column, the reference number is given which corresponds to the following researchers:

- [0] [Kamerling & Fijneman: 1980]
- [1] [Walraven & Mercx: 1982]
- [2] [Becker & Buettner: 1985]
- [3] [Pisanty: 1992]
- [4] [Pajari & Koukari: 1998]
- [5] [Test Sheets Spanbeton: 1998]
- [6] [Borgogno & Fontana: 1996]
- [7] [Fellinger: 1999 & 2000]

year	Ref.	Test results			Ratio test/theory				loading			Geometry						
		fail. mode	Vu kN	Mcr kNm	F [-]	A [-]	ST [-]	SC [-]	Mcr [-]	span m	a m	s mm	h mm	b mm	bw mm	hct mm	ec mm	
1979	[0]	1	A	176.3		1.05	1.25	0.83	1.06		4.0	0.95	100	265	1200	229	0	132
1979	[0]	2	F	188.3		1.12	1.34	0.89	1.13		4.0	0.95	100	265	1200	229	0	132
1979	[0]	4	F	170.6		1.30	1.54	0.81	1.15		5.0	1.21	100	265	1200	229	0	132
1979	[0]	5	F	160.3		1.21	1.45	0.76	1.08		5.0	1.21	100	265	1200	229	0	132
1979	[0]	6		129.9		1.17	1.31	0.60	0.93		5.9	1.43	100	265	1200	229	0	132
1979	[0]	7		128.6		1.17	1.30	0.59	0.93		6.0	1.45	100	265	1200	229	0	132
1979	[0]	8	F	128.4		1.16	1.30	0.59	0.92		6.0	1.45	100	265	1200	229	0	132
1979	[0]	9	SC	243.7		1.13	1.41	1.07	1.11		6.0	1.45	100	265	1200	229	0	132
1979	[0]	10	ST	225.2		0.86	1.19	0.99	0.92		5.0	1.19	100	265	1200	229	0	132
1979	[0]	11	A	233.2		0.90	1.24	1.03	0.96		5.0	1.20	100	265	1200	229	0	132
1979	[0]	12	ST	229.2		0.88	1.21	1.01	0.94		5.0	1.20	100	265	1200	229	0	132
1979	[0]	13	ST	230.4		0.89	1.22	1.02	0.94		5.0	1.20	100	265	1200	229	0	132
1979	[0]	14	ST	257.8		0.99	1.37	1.14	1.06		5.0	1.20	100	265	1200	229	0	132
1979	[0]	15	F	115.6		1.00	0.83	0.51	0.70		11.0	2.70	100	265	1200	229	0	132
1979	[0]	16	F	118.6		1.03	0.86	0.52	0.72		11.0	2.70	100	265	1200	229	0	132
1979	[0]	17	F	138.9		1.07	1.24	0.54	0.87		6.0	1.45	100	305	1200	234	0	152
1979	[0]	18	F	111.6		1.01	1.10	0.43	0.75		7.0	1.69	100	305	1200	234	0	152
1979	[0]	19	A	146.4		0.63	0.96	0.55	0.60		4.0	0.95	100	200	1200	338	0	100
1979	[0]	20	A	146.0		0.62	0.95	0.55	0.60		4.0	0.95	100	200	1200	338	0	100
1979	[0]	21	A	147.0		0.80	1.07	0.56	0.68		5.0	1.20	100	200	1200	338	0	100
1979	[0]	22	A	156.7		0.84	1.13	0.60	0.73		5.0	1.19	100	200	1200	338	0	100
1979	[0]	23	FC	164.6		1.08	1.30	0.63	0.83		6.0	1.45	100	200	1200	338	0	100
1979	[0]	24	FC	161.0		1.05	1.27	0.61	0.81		6.0	1.45	100	200	1200	338	0	100
1979	[0]	25	F	41.7		1.06	0.71	0.19	0.46		4.0	0.95	100	200	1200	338	0	100
1979	[0]	26	F	46.1		1.18	0.79	0.20	0.50		4.0	0.95	100	200	1200	338	0	100
1979	[0]	27	A/F	39.8		1.28	0.86	0.18	0.45		5.0	1.20	100	200	1200	338	0	100
1979	[0]	28	F	40.1		1.29	0.86	0.18	0.46		5.0	1.20	100	200	1200	338	0	100
1979	[0]	29	A/F	33.3		1.30	0.87	0.15	0.39		6.0	1.45	100	200	1200	338	0	100
1979	[0]	30	F	34.4		1.34	0.90	0.15	0.40		6.0	1.45	100	200	1200	338	0	100
1979	[0]	33	ST	241.9		0.73	0.80	0.90	0.82		4.0	0.95	100	265	1200	229	0	132
1979	[0]	34	ST	231.8		0.71	1.07	1.02	0.82		4.0	0.95	100	265	1200	229	0	132
1979	[0]	35	ST	245.1		0.75	1.13	1.08	0.87		4.0	0.95	100	265	1200	229	0	132
1979	[0]	35	SC	213.9		0.72	0.62	0.66	0.73		5.8	1.41	100	305	1200	234	0	152
1979	[0]	37	SC	187.3		0.89	0.59	0.57	0.76		8.1	1.98	100	305	1200	234	0	152
1979	[0]	38	SC	183.2		0.72	0.55	0.56	0.68		6.7	1.63	100	305	1200	234	0	152
1979	[0]	39	SC	166.3		0.90	0.72	0.61	0.75		7.0	1.70	100	265	1200	229	0	132
1979	[0]	40	SC	182.0		0.98	0.79	0.67	0.83		7.0	1.70	100	265	1200	229	0	132
1979	[0]	41	SC	181.0		0.83	0.75	0.67	0.76		6.0	1.45	100	265	1200	229	0	132
1979	[0]	42		168.5		0.77	0.70	0.62	0.71		6.0	1.45	100	265	1200	229	0	132
1979	[0]	43	SC	217.7		1.00	0.90	0.80	0.92		6.0	1.45	100	265	1200	229	0	132
1979	[0]	44	SC	201.2		0.93	0.83	0.74	0.85		6.0	1.45	100	265	1200	229	0	132
1979	[1]	I-1	F	61.7	84.6	1.04	0.80	0.19	0.51	0.98	5.4	1.80	150	200	1200	370	0	100
1979	[1]	I-10	F	29.7	82.3	0.99	0.45	0.09	0.26	0.95	7.2	3.60	150	200	1200	370	0	100
1979	[1]	I-11	F	30.9	83.6	1.03	0.47	0.10	0.27	0.97	7.2	3.60	150	200	1200	370	0	100
1979	[1]	I-12	F	44.5	79.2	0.99	0.62	0.14	0.37	0.92	7.2	2.40	150	200	1200	370	0	100
1979	[1]	I-2	F	44.0	90.6	1.02	0.62	0.14	0.39	1.05	7.2	2.50	150	200	1200	370	0	100
1979	[1]	I-3	F	36.0	93.0	1.01	0.53	0.11	0.33	1.08	9.0	3.00	150	200	1200	370	0	100
1979	[1]	I-4	F	78.1	90.4	1.09	0.95	0.24	0.60	1.05	6.0	1.50	150	200	1200	370	0	100
1979	[1]	I-5	F	113.2	93.2	1.05	1.17	0.35	0.76	1.08	5.0	1.00	150	200	1200	370	0	100
1979	[1]	I-6	F	151.1	92.0	1.05	1.31	0.47	0.90	1.06	4.5	0.75	150	200	1200	370	0	100
1979	[1]	I-7	F	221.0	91.5	1.03	1.28	0.69	1.08	1.06	4.0	0.50	150	200	1200	370	0	100
1979	[1]	I-8	F	314.0	114.5	1.01	1.49	0.93	1.20	1.09	4.0	0.50	150	200	1200	370	0	100
1979	[1]	I-9	F	276.5	94.3	0.96	1.25	0.86	1.02	1.14	3.8	0.38	150	200	1200	370	0	100
1982	[1]	II-1a	A*	139.3	63.5	0.28	0.52	0.49	0.34	0.52		0.46	100	255	1200	294	0	128
1982	[1]	II-1b	A	204.0	138.0	0.72	1.04	0.72	0.80	0.87		0.81	100	255	1200	294	0	128
1982	[1]	II-2	A*	66.3	97.8	0.43	0.52	0.24	0.36	0.62		1.48	100	255	1200	294	0	128
1982	[1]	II-3	A*	75.3	83.7	0.37	0.53	0.27	0.36	0.53		1.15	100	255	1200	294	0	128
1982	[1]	II-4a	ST	284.3		0.36	0.78	0.93	0.46			0.46	100	255	1200	294	0	128

Ac	I	S	Strands										Concrete		Steel		
			#1	Dia 1	c1	spl 1	#2	Dia 2	c2	spl 2	#3	Dia 3	c3	spl 3	fcm	ftcm	fpu
10 <sup>3</sup> mm <sup>2</sup>	10 <sup>8</sup> mm <sup>4</sup>	10 <sup>6</sup> mm <sup>3</sup>		mm	mm	MPa		mm	mm	MPa		mm	mm	MPa	MPa	MPa	MPa
172.3	15.1	7.6	4	12.5	35	1395	2	9.3	230	1395					65.3	4.28	1900
172.3	15.1	7.6	4	12.5	35	1395	2	9.3	230	1395					65.3	4.28	1900
172.3	15.1	7.6	4	12.5	35	1395	2	9.3	230	1395					65.3	4.28	1900
172.3	15.1	7.6	4	12.5	35	1395	2	9.3	230	1395					65.3	4.28	1900
172.3	15.1	7.6	4	12.5	35	1395	2	9.3	230	1395					68.4	4.37	1900
172.3	15.1	7.6	4	12.5	35	1395	2	9.3	230	1395					68.4	4.37	1900
172.3	15.1	7.6	4	12.5	35	1395	2	9.3	230	1395					68.4	4.37	1900
172.3	15.1	7.6	8	12.5	35	1395	2	9.3	230	1395					67.6	4.34	1900
172.3	15.1	7.6	8	12.5	35	1395	2	9.3	230	1395					67.6	4.34	1900
172.3	15.1	7.6	8	12.5	35	1395	2	9.3	230	1395					67.6	4.34	1900
172.3	15.1	7.6	8	12.5	35	1395	2	9.3	230	1395					67.6	4.34	1900
172.3	15.1	7.6	8	12.5	35	1395	2	9.3	230	1395					67.6	4.34	1900
172.3	15.1	7.6	8	12.5	35	1395	2	9.3	230	1395					67.6	4.34	1900
172.3	15.1	7.6	8	12.5	35	1395	2	9.3	230	1395					67.6	4.34	1900
172.3	15.1	7.6	8	12.5	35	1395	2	9.3	230	1395					67.6	4.34	1900
172.3	15.1	7.6	8	12.5	35	1395	2	9.3	230	1395					67.6	4.34	1900
172.3	15.1	7.6	8	12.5	35	1395	2	9.3	230	1395					67.6	4.34	1900
172.3	15.1	7.6	8	12.5	35	1395	2	9.3	230	1395					67.6	4.34	1900
186.6	21.9	9.5	4	12.5	35	1395	2	9.3	270	1395					69.8	4.40	1900
186.6	21.9	9.5	4	12.5	35	1395	2	9.3	270	1395					69.8	4.40	1900
145.2	6.8	4.6	8	12.5	35	1395	2	9.3	165	1395					80.9	4.68	1900
145.2	6.8	4.6	8	12.5	35	1395	2	9.3	165	1395					80.9	4.68	1900
145.2	6.8	4.6	8	12.5	35	1395	2	9.3	165	1395					76.9	4.58	1900
145.2	6.8	4.6	8	12.5	35	1395	2	9.3	165	1395					76.9	4.58	1900
145.2	6.8	4.6	8	12.5	35	1395	2	9.3	165	1395					76.9	4.58	1900
145.2	6.8	4.6	8	12.5	35	1395	2	9.3	165	1395					76.9	4.58	1900
145.2	6.8	4.6	8	12.5	35	1395	2	9.3	165	1395					76.9	4.58	1900
145.2	6.8	4.6	4	7.5	35	1395	2	7.5	165	1395					65.8	4.29	1900
145.2	6.8	4.6	4	7.5	35	1395	2	7.5	165	1395					65.8	4.29	1900
145.2	6.8	4.6	4	7.5	35	1395	2	7.5	165	1395					65.8	4.29	1900
145.2	6.8	4.6	4	7.5	35	1395	2	7.5	165	1395					65.8	4.29	1900
145.2	6.8	4.6	4	7.5	35	1395	2	7.5	165	1395					65.8	4.29	1900
145.2	6.8	4.6	4	7.5	35	1395	2	7.5	165	1395					65.8	4.29	1900
172.3	15.1	7.6	8	12.5	35	1395	2	9.3	230	1395					86.7	4.81	1900
172.3	15.1	7.6	8	12.5	35	1395	2	9.3	230	1395					67.6	4.34	1900
172.3	15.1	7.6	8	12.5	35	1395	2	9.3	230	1395					67.6	4.34	1900
186.6	21.9	9.5	9	12.5	35	1395	2	9.3	270	1395					86.7	4.81	1900
186.6	21.9	9.5	9	12.5	35	1395	2	9.3	270	1395					86.7	4.81	1900
186.6	21.9	9.5	9	12.5	35	1395	2	9.3	270	1395					86.7	4.81	1900
172.3	15.1	7.6	8	12.5	35	1395	2	9.3	230	1395					93.3	4.95	1900
172.3	15.1	7.6	8	12.5	35	1395	2	9.3	230	1395					93.3	4.95	1900
172.3	15.1	7.6	8	12.5	35	1395	2	9.3	230	1395					93.3	4.95	1900
172.3	15.1	7.6	8	12.5	35	1395	2	9.3	230	1395					93.3	4.95	1900
172.3	15.1	7.6	8	12.5	35	1395	2	9.3	230	1395					93.3	4.95	1900
172.3	15.1	7.6	8	12.5	35	1395	2	9.3	230	1395					93.3	4.95	1900
172.3	15.1	7.6	8	12.5	35	1395	2	9.3	230	1395					93.3	4.95	1900
157.0	7.1	4.7	7	9.3	40	1240									65.1	5.10	1900
157.0	7.1	4.7	7	9.3	40	1240									74.1	5.10	1900
157.0	7.1	4.7	7	9.3	40	1240									75.1	5.10	1900
157.0	7.1	4.7	7	9.3	40	1240									76.1	5.10	1900
157.0	7.1	4.7	7	9.3	40	1240									66.1	5.10	1900
157.0	7.1	4.7	7	9.3	40	1240									67.1	5.10	1900
157.0	7.1	4.7	7	9.3	40	1240									68.1	5.10	1900
157.0	7.1	4.7	7	9.3	40	1240									69.1	5.10	1900
157.0	7.1	4.7	7	9.3	40	1240									70.1	5.10	1900
157.0	7.1	4.7	7	9.3	40	1240									71.1	5.10	1900
157.0	7.1	4.7	7	9.3	40	1240	4	9.3	67.5	1240					72.1	5.10	1900
157.0	7.1	4.7	7	9.3	40	1240									73.1	5.10	1900
171.0	13.4	6.6	6	12.5	35	1240									63.2	4.22	1900
171.0	13.4	6.6	6	12.5	35	1240									63.2	4.22	1900
171.0	13.4	6.6	6	12.5	35	1240									63.2	4.22	1900
171.0	13.4	6.6	6	12.5	35	1240									63.2	4.22	1900
171.0	13.6	6.6	10	12.5	35	1240									63.2	4.22	1900

year	Ref.	Test results		Ratio test/theory				loading			Geometry									
		fail. mode	Vu kN	Mcr kNm	F [-]	A [-]	ST [-]	SC [-]	Mcr [-]	span m	a m	s mm	h mm	b mm	bw mm	hct mm	ec mm			
1982	[1]	II-4b	ST	268.3			0.59	0.95	0.88	0.71			0.81	100	255	1200	294	0	128	
1982	[1]	II-5a	ST	286.3			0.36	0.79	0.94	0.46			0.46	100	255	1200	294	0	128	
1982	[1]	II-5b	ST	252.1	240.4		0.78	1.09	0.83	0.84	1.06		1.15	100	255	1200	294	0	128	
1982	[1]	II-6	ST/L	213.3	249.7		0.86	1.04	0.70	0.82	1.10		1.50	100	255	1200	294	0	128	
1982	[1]	II-7a	ST	216.0			0.51	0.76	0.84	0.58			0.54	100	300	1200	250	0	150	
1982	[1]	II-7b	ST	231.5	186.9		0.94	1.22	0.90	1.01	1.04		0.95	100	300	1200	250	0	150	
1982	[1]	II-8a	A	171.5	151.3		0.70	0.90	0.66	0.75	0.84		0.95	100	300	1200	250	0	150	
1982	[1]	II-8b	ST	181.6			0.35	0.57	0.70	0.39			0.44	100	300	1200	250	0	150	
1982	[1]	II-9	A/F	156.6	190.7		1.00	1.23	0.61	0.86	1.06		1.50	100	300	1200	250	0	150	
1982	[1]	II-10a	ST	208.5			0.26	0.56	0.83	0.35			0.54	100	300	1200	250	0	150	
1982	[1]	II-10b	A	151.1	140.6		0.33	0.53	0.57	0.42	0.52		0.95	100	300	1200	250	0	150	
1982	[1]	II-11a	ST	224.6			0.49	0.78	0.85	0.62			0.95	100	300	1200	250	0	150	
1982	[1]	II-11b	ST	239.3			0.30	0.64	0.90	0.40			0.54	100	300	1200	250	0	150	
1982	[1]	II-12	ST	226.2	264.8		0.77	1.01	0.85	0.84	0.98		1.50	100	300	1200	250	0	150	
1982	[1]	II-13	F	161.0	149.0		1.05	1.28	0.57	0.88	0.94		1.50	100	255	1200	294	0	128	
1982	[1]	II-14	A/F	168.0	160.0		0.94	1.18	0.60	0.81	1.01		1.15	100	255	1200	294	0	128	
1982	[1]	II-15a	ST	234.0	160.6		0.83	1.19	0.83	0.92	1.01		0.81	100	255	1200	294	0	128	
1982	[1]	II-15b	ST	258.3			0.53	0.97	0.92	0.63			0.46	100	255	1200	294	0	128	
1982	[1]	II-16a	ST	245.9	162.5		0.87	1.25	0.87	0.97	1.03		0.81	100	255	1200	294	0	128	
1982	[1]	II-16b	ST	282.0			0.57	1.05	1.00	0.68			0.46	100	255	1200	294	0	128	
1982	[1]	II-17	F	190.9	192.8		1.35	1.38	0.76	1.12	1.21		1.50	100	265	1200	260	0	133	
1982	[1]	II-18	ST	240.6	198.5		1.32	1.56	0.96	1.24	1.25		1.15	100	265	1200	260	0	133	
1982	[1]	II-19a	ST	276.3	200.6		1.06	1.40	1.11	1.17	1.26		0.81	100	265	1200	260	0	133	
1982	[1]	II-19b	ST	263.9			0.58	0.84	1.06	0.67			0.46	100	265	1200	260	0	133	
1982	[1]	II-20	A/F	240.8	200.6		1.33	1.52	0.95	1.24	1.26		1.15	100	265	1200	260	0	133	
1985	[2]	10-1	SC	129.1			0.73	1.03	0.85	0.74		4.6	0.76	76	254	1016	338	100	127	
1985	[2]	10-10	SC	223.8			0.93	1.30	1.42	0.97		4.6	1.14	76	254	1016	338	100	127	
1985	[2]	10-11	A	186.0			0.77	1.08	1.18	0.81		4.6	1.14	76	254	1016	338	100	127	
1985	[2]	10-12	ST	191.8			0.46	0.72	1.16	0.56		10.4	0.92	76	254	1016	338	100	127	
1985	[2]	10-13	SC	149.5			0.71	0.77	0.90	0.65		10.4	1.83	76	254	1016	338	100	127	
1985	[2]	10-2	A	160.2			0.91	1.27	1.05	0.92		4.6	0.76	76	254	1016	338	100	127	
1985	[2]	10-3	A	116.1			0.98	1.10	0.76	0.80		4.6	1.14	76	254	1016	338	100	127	
1985	[2]	10-4	A	113.9			0.97	1.08	0.75	0.79		4.6	1.14	76	254	1016	338	100	127	
1985	[2]	10-5	A	212.3			0.91	1.41	1.39	1.01		4.6	0.76	76	254	1016	338	100	127	
1985	[2]	10-6	A	137.5			0.88	1.12	0.90	0.81		4.6	1.14	76	254	1016	338	100	127	
1985	[2]	10-7	A	141.1			0.90	1.15	0.92	0.83		4.6	1.14	76	254	1016	338	100	127	
1985	[2]	10-8	ST	249.2			0.69	1.16	1.58	0.85		4.6	0.76	76	254	1016	338	100	127	
1985	[2]	10-9	ST	257.7			0.72	1.20	1.63	0.88		4.6	0.76	76	254	1016	338	100	127	
1985	[2]	8-1	-	144.2			1.09	1.51	0.96	0.94		4.6	0.76	76	200	1016	432	70	100	
1985	[2]	8-10	SC	114.4			0.97	1.24	0.76	0.75		4.6	1.14	76	200	1016	432	70	100	
1985	[2]	8-11	ST	115.3			0.98	1.25	0.76	0.76		4.6	1.14	76	200	1016	432	70	100	
1985	[2]	8-12	SC	96.1			0.81	1.04	0.64	0.63		4.6	1.14	76	200	1016	432	70	100	
1985	[2]	8-13	SC	93.9			0.79	1.02	0.62	0.62		4.6	1.14	76	200	1016	432	70	100	
1985	[2]	8-14	ST	271.9			1.01	1.70	1.74	1.09		4.6	0.76	76	200	1016	432	70	100	
1985	[2]	8-15	ST	249.2			0.93	1.56	1.60	1.00		4.6	0.76	76	200	1016	432	70	100	
1985	[2]	8-16	ST	133.5			0.50	0.83	0.85	0.54		4.6	0.76	76	200	1016	432	70	100	
1985	[2]	8-17	SC	178.0			0.99	1.38	1.14	0.89		4.6	1.14	76	200	1016	432	70	100	
1985	[2]	8-18	SC	172.7			0.96	1.34	1.11	0.86		4.6	1.14	76	200	1016	432	70	100	
1985	[2]	8-19	SC	146.4			0.81	1.14	0.94	0.73		4.6	1.14	76	200	1016	432	70	100	
1985	[2]	8-2	-	142.4			1.07	1.49	0.95	0.93		4.6	0.76	76	200	1016	432	70	100	
1985	[2]	8-3	SC	122.8			0.92	1.29	0.82	0.80		4.6	0.76	76	200	1016	432	70	100	
1985	[2]	8-4	-	87.2			0.97	1.09	0.58	0.66		4.6	1.14	76	200	1016	432	70	100	
1985	[2]	8-5	SC	88.1			0.98	1.10	0.59	0.67		4.6	1.14	76	200	1016	432	70	100	
1985	[2]	8-6	SC	88.1			0.98	1.10	0.59	0.67		4.6	1.14	76	200	1016	432	70	100	
1985	[2]	8-7	SC	111.7			1.25	1.40	0.74	0.85		4.6	1.14	76	200	1016	432	70	100	
1985	[2]	8-8	SC	169.5			0.96	1.51	1.12	0.93		4.6	0.76	76	200	1016	432	70	100	
1985	[2]	8-9	ST	155.8			0.89	1.38	1.03	0.85		4.6	0.76	76	200	1016	432	70	100	
1992	[3]	1	ST	178.5	167.9		0.51	0.74	0.61	0.51	0.80		1.9	0.97	70	300	900	327.5	150	150

Ac	I	S	Strands									Concrete		Steel		
			#1	Dia 1	c1	spl 1	#2	Dia 2	c2	spl 2	#3	Dia 3	c3	spl 3	fcm	ftcm
10 <sup>3</sup> mm <sup>2</sup>	10 <sup>8</sup> mm <sup>4</sup>	10 <sup>6</sup> mm <sup>3</sup>		mm	mm	MPa		mm	mm	MPa		mm	mm	MPa	MPa	MPa
171.0	13.6	6.6	10	12.5	35	1240								63.2	4.22	1900
171.0	13.6	6.6	10	12.5	35	1240								63.2	4.22	1900
171.0	13.6	6.6	10	12.5	35	1240								63.2	4.22	1900
171.0	13.6	6.6	10	12.5	35	1240								63.2	4.22	1900
199.0	21.8	9.7	5	12.5	35	1240								67.7	4.20	1900
199.0	21.8	9.7	5	12.5	35	1240								67.7	4.20	1900
199.0	21.8	9.7	5	12.5	35	1240								67.7	4.20	1900
199.0	21.8	9.7	5	12.5	35	1240								67.7	4.20	1900
199.0	21.8	9.7	5	12.5	35	1240								67.7	4.20	1900
199.0	22.3	9.7	8	12.5	35	1240	2	12.5	65	1240				51.7	3.72	1900
199.0	22.3	9.3	8	12.5	35	1240	2	12.5	65	1240				51.7	3.72	1900
199.0	22.3	9.3	8	12.5	35	1240	2	12.5	65	1240				51.7	3.72	1900
199.0	22.3	9.3	8	12.5	35	1240	2	12.5	65	1240				51.7	3.72	1900
199.0	22.3	9.3	8	12.5	35	1240	2	12.5	65	1240				51.7	3.72	1900
171.0	13.4	6.6	6	12.5	35	1240								63.2	4.22	1900
171.0	13.4	6.6	6	12.5	35	1240								62.2	4.19	1900
171.0	13.4	6.6	6	12.5	35	1240								63.2	4.22	1900
171.0	13.4	6.6	6	12.5	35	1240								63.2	4.22	1900
171.0	13.4	6.6	6	12.5	35	1240								63.2	4.22	1900
171.0	13.4	6.6	6	12.5	35	1240								63.2	4.22	1900
178.0	15.5	7.7	9	9.3	25	1240								62.2	4.19	1900
178.0	15.5	7.7	9	9.3	25	1240								62.2	4.19	1900
178.0	15.5	7.7	9	9.3	25	1240								62.2	4.19	1900
178.0	15.5	7.7	9	9.3	25	1240								62.2	4.19	1900
178.0	15.5	7.7	9	9.3	25	1120								62.2	4.19	1900
165.8	12.2	9.3	14	6.3	24	1120								41.34	3.11	1756
165.8	12.2	9.3	14	9.3	24	1120								41.34	3.11	1756
165.8	12.2	9.3	14	9.3	24	1120								41.34	3.11	1756
165.8	12.2	9.3	20	9.3	24	1120								41.34	3.11	1756
165.8	12.2	9.3	20	9.3	24	1120								41.34	3.11	1756
165.8	12.2	9.3	14	6.3	24	1120								41.34	3.11	1756
165.8	12.2	9.3	14	6.3	24	1120								41.34	3.11	1756
165.8	12.2	9.3	14	6.3	24	1120								41.34	3.11	1756
165.8	12.2	9.3	14	6.3	24	1120								41.34	3.11	1756
165.8	12.2	9.3	12	7.9	24	1120								41.34	3.11	1756
165.8	12.2	9.3	12	7.9	24	1120								41.34	3.11	1756
165.8	12.2	9.3	12	7.9	24	1120								41.34	3.11	1756
165.8	12.2	9.3	14	9.3	24	1120								41.34	3.11	1756
165.8	12.2	9.3	14	9.3	24	1120								41.34	3.11	1756
140.6	6.3	6.2	14	6.3	24	1120								41.34	3.11	1756
140.6	6.3	6.2	12	7.9	24	1120								41.34	3.11	1756
140.6	6.3	6.2	12	7.9	24	1120								41.34	3.11	1756
140.6	6.3	6.2	12	7.9	24	1120								41.34	3.11	1756
140.6	6.3	6.2	12	7.9	24	1120								41.34	3.11	1756
140.6	6.3	6.2	14	9.3	24	1120								41.34	3.11	1756
140.6	6.3	6.2	14	9.3	24	1120								41.34	3.11	1756
140.6	6.3	6.2	14	9.3	24	1120								41.34	3.11	1756
140.6	6.3	6.2	14	9.3	24	1120								41.34	3.11	1756
140.6	6.3	6.2	14	9.3	24	1120								41.34	3.11	1756
140.6	6.3	6.2	14	9.3	24	1120								41.34	3.11	1756
140.6	6.3	6.2	14	9.3	24	1120								41.34	3.11	1756
140.6	6.3	6.2	14	9.3	24	1120								41.34	3.11	1756
140.6	6.3	6.2	14	6.3	24	1120								41.34	3.11	1756
140.6	6.3	6.2	14	6.3	24	1120								41.34	3.11	1756
140.6	6.3	6.2	14	6.3	24	1120								41.34	3.11	1756
140.6	6.3	6.2	14	6.3	24	1120								41.34	3.11	1756
140.6	6.3	6.2	14	6.3	24	1120								41.34	3.11	1756
140.6	6.3	6.2	14	6.3	24	1120								41.34	3.11	1756
140.6	6.3	6.2	14	6.3	24	1120								41.34	3.11	1756
140.6	6.3	6.2	12	7.9	24	1120								41.34	3.11	1756
140.6	6.3	6.2	12	7.9	24	1120								41.34	3.11	1756
150.4	13.9	6.1	8	12.5	25	1400								48	3.51	1770

year	Ref.	Test results			Ratio test/theory				loading			Geometry						
		fail. mode	Vu kN	Mcr kNm	F [-]	A [-]	ST [-]	SC [-]	Mcr [-]	span m	a m	s mm	h mm	b mm	bw mm	hct mm	ec mm	
1992	[3]	10	ST	57.3	53.5	0.64	0.95	0.88	0.67	0.99	1.9	0.97	70	300	257	74	150	150
1992	[3]	2	ST	172.5	158.3	0.49	0.72	0.59	0.49	0.76	1.9	0.97	70	300	900	329.5	150	150
1992	[3]	3	ST	174.0	155.8	0.49	0.73	0.59	0.50	0.74	1.9	0.97	70	300	900	328.5	150	150
1992	[3]	4	ST	173.5	147.2	0.49	0.72	0.59	0.50	0.70	1.9	0.97	70	300	900	325.5	150	150
1992	[3]	5	SC	47.5		0.53	0.78	0.43	0.48		1.9	0.97	70	300	321	126	150	150
1992	[3]	6	A	67.0	57.2	0.75	1.10	0.61	0.68	1.01	1.9	0.97	70	300	321	126.5	150	150
1992	[3]	7	A	78.0	58.4	0.87	1.28	0.71	0.79	1.02	1.9	0.97	70	300	321	126	150	150
1992	[3]	8	SC	53.8		0.60	0.88	0.49	0.55		1.9	0.97	70	300	321	124.5	150	150
1992	[3]	9	ST	47.0		0.53	0.78	0.72	0.55		1.9	0.97	70	300	257	74.5	150	150
1998	[4]	DE265-1	ST	288.8		0.88	1.12	1.28	0.97		5.9	1.00	60	265	1200	223	0	115
1998	[4]	DE265-2	ST	280.2		0.85	1.09	1.25	0.94		5.9	1.00	60	265	1200	223	0	115
1998	[4]	PC265C-1	ST	188.6		0.57	0.80	0.85	0.70		5.9	1.00	60	265	1200	223	0	115
1998	[4]	PC265C-2	ST	201.3		0.61	0.85	0.90	0.74		5.9	1.00	60	265	1200	223	0	115
1998	[4]	PC265E-1	ST	248.5		0.76	0.96	1.09	0.83		5.9	1.00	60	265	1200	223	0	115
1998	[4]	PC265E-2	ST	255.1		0.78	0.99	1.12	0.85		5.9	1.00	60	265	1200	223	0	115
1998	[4]	PC265N-1	ST	213.4		0.65	0.91	0.98	0.79		5.9	1.00	60	265	1200	223	0	115
1998	[4]	PC265N-2	ST	217.0		0.66	0.93	0.99	0.81		5.9	1.00	60	265	1200	223	0	115
1998	[4]	PC265N-3	ST	195.8		0.60	0.84	0.90	0.73		5.9	1.00	60	265	1200	223	0	115
1998	[4]	PC265N-4	ST	217.7		0.66	0.93	1.00	0.81		5.9	1.00	60	265	1200	223	0	115
1998	[4]	PC265T-1	ST	208.0		0.63	0.87	0.93	0.76		5.9	1.00	60	265	1200	223	0	115
1998	[4]	PC265T-2	ST	178.6		0.54	0.75	0.79	0.66		5.9	1.00	60	265	1200	223	0	115
1998	[4]	PC400-1	ST	494.0		0.91	1.00	1.03	0.98		7.1	1.26	80	400	1200	290	200	183
1998	[4]	PC400-2	ST	461.0		0.85	0.93	0.96	0.92		7.1	1.26	80	400	1200	290	200	183
1998	[4]	PC400-3	ST	487.0		0.90	0.98	1.02	0.97		7.1	1.26	80	400	1200	290	200	183
1998	[4]	PC400-4	ST	490.0		0.90	0.99	1.02	0.98		7.1	1.26	80	400	1200	290	200	183
1998	[4]	RC265-1	ST	225.5		0.69	0.95	1.01	0.83		5.9	1.00	60	265	1200	223	0	115
1998	[4]	RC265-2	ST	226.8		0.69	0.95	1.01	0.83		5.9	1.00	60	265	1200	223	0	115
1998	[4]	ST265-1	ST	250.2		0.76	0.99	1.15	0.85		5.9	1.00	60	265	1200	223	0	115
1998	[4]	ST265-2	ST	212.0		0.65	0.84	0.97	0.72		5.9	1.00	60	265	1200	223	0	115
1998	[4]	ST400-1	ST	499.8		0.92	1.02	1.07	1.00		7.1	1.26	80	400	1200	290	200	183
1998	[4]	ST400-2	ST	532.8		0.98	1.09	1.14	1.07		7.1	1.26	80	400	1200	290	200	183
1998	[5]	6994	ST	392.9		0.80	1.17	0.79	0.92		3.9	1.00	100	395	1200	311	200	204
1998	[5]	7008	ST	336.0	146.6	0.81	1.18	0.85	0.95	0.64	3.9	0.80	100	312.5	1200	312	200	160
1998	[5]	7086	ST	270.1		0.47	0.78	0.66	0.61		3.9	0.80	100	315.5	1200	309	150	160
1998	[5]	7089	ST	429.3		0.61	0.91	0.77	0.77		3.9	1.00	100	390	1200	332	200	204
1998	[5]	7099	ST	278.8		0.54	0.85	0.66	0.67		3.9	0.80	100	312	1200	321	150	160
1998	[5]	7105	ST	425.6		0.60	0.88	0.78	0.75		3.9	1.00	100	392	1200	321	200	204
1998	[5]	7114	ST	391.4		0.61	0.91	0.74	0.76		3.9	1.00	100	388	1200	320	200	204
1998	[5]	7121	ST	218.9	137.0	0.82	1.02	0.93	0.99	0.97	3.9	0.66	100	267.5	1200	224	0	133
1998	[5]	7124	ST	380.2		0.54	0.79	0.70	0.67		3.9	1.00	100	392	1200	321	200	204
1998	[5]	7133	ST	294.7		0.41	0.67	0.66	0.54		3.9	0.80	100	314	1200	323	150	160
1998	[5]	7143	ST	467.2	458.6	0.65	0.96	0.87	0.83	1.03	3.9	1.00	100	395.5	1200	316	200	204
1998	[5]	7168	ST	335.6		0.47	0.68	0.59	0.58		3.9	1.00	100	397	1200	332	200	204
1998	[5]	7169	ST	360.9		0.55	0.82	0.70	0.70		3.9	1.00	100	397	1200	313	200	204
1998	[5]	7186	ST	296.9		0.52	0.87	1.21	0.73		3.9	0.66	100	263	1200	220	0	133
1998	[5]	7190	F	324.1	186.0	1.20	1.45	0.81	1.21	1.04	3.9	0.80	100	315.3	1200	315	150	160
1998	[5]	7202	ST	358.7		0.49	0.72	0.64	0.62		3.9	1.00	100	402	1200	330	200	204
1998	[5]	7203	ST	464.3		0.72	1.06	0.85	0.89		3.9	1.00	100	393	1200	329	200	204
1998	[5]	7209	ST	521.5		0.74	1.06	0.92	0.91		3.9	1.00	100	392.5	1200	329	200	204
1998	[5]	7269	ST	202.3		0.50	0.74	0.80	0.65		3.9	0.66	100	263	1200	234	0	133
1998	[5]	7281	ST	435.3		0.68	1.00	0.80	0.84		3.9	1.00	100	390.5	1200	326	200	204
1998	[5]	7283	F	179.2	66.1	1.11	0.93	0.61	0.82	0.69	3.9	0.50	100	194.5	1200	383	40	100
1998	[5]	7292	ST	456.8		0.71	1.04	0.83	0.87		3.9	1.00	100	389	1200	326	200	204
1998	[5]	7303	ST	471.7		0.62	0.89	0.83	0.77		3.9	1.00	100	390	1200	324	200	204
1998	[5]	7320	F	151.3	55.2	1.10	0.70	0.48	0.59	0.51	3.9	0.50	100	195	1200	409	40	100
1998	[5]	7334	ST	395.9		0.54	0.78	0.68	0.68		3.9	1.00	100	401	1200	332	200	204
1998	[5]	7334	ST	456.8		0.65	0.93	0.81	0.79		3.9	1.00	100	390	1200	323	200	204
1998	[5]	7335	F	207.1	77.8	0.97	0.93	0.69	0.78	0.70	3.9	0.50	100	192.3	1200	382	40	100

Ac	I	S	Strands										Concrete		Steel		
			#1	Dia 1	c1	spl 1	#2	Dia 2	c2	spl 2	#3	Dia 3	c3	spl 3	fcm	fctm	fpu
10 <sup>3</sup> mm <sup>2</sup>	10 <sup>8</sup> mm <sup>4</sup>	10 <sup>6</sup> mm <sup>3</sup>		mm	mm	MPa		mm	mm	MPa		mm	mm	MPa	MPa	MPa	MPa
41.8	4.0	1.7	2	12.5	25	1400									47.95	3.51	1770
150.4	13.8	6.1	8	12.5	25	1400									47.95	3.51	1770
150.4	13.9	6.1	8	12.5	25	1400									47.95	3.51	1770
150.4	14.0	6.1	8	12.5	25	1400									47.95	3.51	1770
54.3	5.0	2.2	2	12.5	25	1400									47.95	3.51	1770
54.3	5.0	2.2	2	12.5	25	1400									47.95	3.51	1770
54.3	5.0	2.2	2	12.5	25	1400									47.95	3.51	1770
54.3	5.1	2.2	2	12.5	25	1400									47.95	3.51	1770
41.8	3.9	1.7	2	12.5	25	1400									47.95	3.51	1770
173.0	15.1	7.6	10	12.5	35	1100									67.8	4.35	1600
173.0	15.1	7.6	10	12.5	35	1100									67.8	4.35	1600
173.0	15.1	7.6	10	12.5	35	950									66.3	4.31	1600
173.0	15.1	7.6	10	12.5	35	950									66.3	4.31	1600
173.0	15.1	7.6	10	12.5	35	1100									69.2	4.39	1600
173.0	15.1	7.6	10	12.5	35	1100									69.2	4.39	1600
173.0	15.1	7.6	10	12.5	35	950									63.4	4.23	1600
173.0	15.1	7.6	10	12.5	35	950									63.4	4.23	1600
173.0	15.1	7.6	10	12.5	35	950									63.4	4.23	1600
173.0	15.1	7.6	10	12.5	35	950									63.4	4.23	1600
173.0	15.1	7.6	10	12.5	35	950									67.8	4.35	1600
173.0	15.1	7.6	10	12.5	35	950									67.8	4.35	1600
216.7	44.1	14.2	13	12.5	35	1100									76.2	4.57	1600
216.7	44.1	14.2	13	12.5	35	1100									76.2	4.57	1600
216.7	44.1	14.2	13	12.5	35	1100									76.2	4.57	1600
216.7	44.1	14.2	13	12.5	35	1100									76.2	4.57	1600
173.0	15.1	7.6	10	12.5	35	950									67.4	4.34	1600
173.0	15.1	7.6	10	12.5	35	950									67.4	4.34	1600
173.0	15.1	7.6	10	12.5	35	1100									62.9	4.21	1600
173.0	15.1	7.6	10	12.5	35	1100									62.9	4.21	1600
216.7	44.1	14.2	13	12.5	35	1100									72.4	4.47	1600
216.7	44.1	14.2	13	12.5	35	1100									72.4	4.47	1600
228.8	46.4	15.0	8	12.5	40	1150		12.5	80	1150					82	4.70	1900
183.8	24.0	9.7	7	12.5	40	1150									82	4.70	1900
183.8	24.0	9.7	8	12.5	40	1150	2	12.5	80	1150					82	4.70	1900
228.8	46.4	15.0	9	12.5	40	1150	3	12.5	80	1150					82	4.70	1900
183.8	24.0	9.7	8	12.5	40	1150	1	12.5	80	1150					82	4.70	1900
228.8	46.4	15.0	8	12.5	40	1150	3	12.5	80	1150	3	9.3	165	1150	82	4.70	1900
228.8	46.4	15.0	8	12.5	40	1150	3	12.5	80	1150					82	4.70	1900
174.0	15.2	7.6	8	9.3	40	1150									82	4.70	1900
228.8	46.4	15.0	8	12.5	40	1150	3	12.5	80	1150	3	9.3	165	1150	82	4.70	1900
183.8	24.0	9.7	10	12.5	40	1150	3	12.5	80	1150					82	4.70	1900
228.8	46.4	15.0	8	12.5	40	1150	3	12.5	80	1150	3	9.3	165	1150	82	4.70	1900
228.8	46.4	15.0	8	12.5	40	1150	3	12.5	80	1150	3	9.3	165	1150	83	4.73	1900
228.8	46.4	15.0	8	12.5	40	1150	3	12.5	80	1150					82	4.70	1900
174.0	15.2	7.6	10	12.5	40	1150									82	4.70	1900
183.8	24.0	9.7	8	9.3	40	1150									82	4.70	1900
228.8	46.4	15.0	8	12.5	40	1150	3	12.5	80	1150	3	9.3	165	1150	83	4.73	1900
228.8	46.4	15.0	8	12.5	40	1150	3	12.5	80	1150					83	4.73	1900
228.8	46.4	15.0	8	12.5	40	1150	3	12.5	80	1150	3	9.3	165	1150	87	4.82	1900
174.0	15.2	7.6	7	12.5	40	1150									84	4.75	1900
228.8	46.4	15.0	8	12.5	40	1150	3	12.5	80	1150					84	4.75	1900
150.9	6.9	4.7	4	9.3	44	1300	4	5	44	1100	4	5	165	1100	84	4.75	1900
228.8	46.4	15.0	8	12.5	40	1150	3	12.5	80	1150					88	4.84	1900
228.8	46.4	15.0	9	12.5	40	1150	3	12.5	80	1150	3	9.3	165	1150	89	4.86	1900
150.9	6.9	4.7	2	9.3	30	1300	6	5	30	1100	3	9.3	165	1100	88	4.84	1900
228.8	46.4	15.0	8	12.5	40	1150	3	12.5	80	1150	3	9.3	165	1150	89	4.86	1900
228.8	46.4	15.0	8	12.5	40	1150	3	12.5	80	1150	3	9.3	165	1150	89	4.86	1900
150.9	6.9	4.7	6	9.3	30	1300	2	5	30	1100	4	5	165	1100	89	4.86	1900

year	Ref.	Test results			Ratio test/theory				loading			Geometry						
		fail. mode	Vu kN	Mcr kNm	F [-]	A [-]	ST [-]	SC [-]	Mcr [-]	span m	a m	s mm	h mm	b mm	bw mm	hct mm	ec mm	
1998	[5]	7368	F	115.5	55.2	1.18	0.89	0.36	0.78	0.85	3.9	0.50	100	195	1200	414	40	100
1994	[6]	S1K01	A	205.0	97.3	0.79	1.56	0.90	0.97	1.04	2.4	0.72	60	200	1200	476	80	100
1994	[6]	S1K02a	ST	156.2		0.40	1.02	0.69	0.58		2.4	0.48	60	200	1200	476	80	100
1994	[6]	S1K02b	ST	220.3		0.28	1.01	0.97	0.41		2.4	0.24	60	200	1200	476	80	100
1994	[6]	S1K03a	A	281.2	55.6	0.36	1.22	1.19	0.52	1.01	2.4	0.24	120	200	1200	476	80	100
1994	[6]	S1K03b	A	245.2	57.1	0.32	1.10	1.06	0.45	1.07	2.4	0.24	80	200	1200	476	80	100
1994	[6]	S1K04	A	252.4	91.7	0.65	1.63	1.09	0.93	1.24	2.4	0.48	80	200	1200	476	80	100
1994	[6]	S1K05	A	249.8	95.0	0.64	1.58	1.05	0.92	1.25	2.4	0.48	120	200	1200	476	80	100
1994	[6]	S1K06	A	203.7	94.7	0.79	1.54	0.88	0.97	1.02	2.4	0.72	80	200	1200	476	80	100
1994	[6]	S1K07	A/F	224.8	99.0	0.87	1.68	0.95	1.07	1.06	2.4	0.72	120	200	1200	476	80	100
1994	[6]	S1K08	A	188.0	101.6	0.88	1.60	0.82	0.99	1.09	2.4	0.88	80	200	1200	476	80	100
1994	[6]	S1K09	A/SC	173.1	96.6	0.81	1.48	0.76	0.91	1.04	2.4	0.88	60	200	1200	476	80	100
1994	[6]	S1K10a	ST	235.6		0.30	1.08	1.04	0.43		2.4	0.24	60	200	1200	476	80	100
1994	[6]	S1K10b	ST/A	210.2	95.3	0.68	1.51	0.92	0.91	1.14	2.4	0.60	60	200	1200	476	80	100
1994	[6]	S1K11a	ST	219.7		0.28	0.99	0.95	0.41		2.4	0.24	80	200	1200	476	80	100
1994	[6]	S1K11b	A	242.2	93.3	0.78	1.72	1.05	1.04	1.11	2.4	0.60	80	200	1200	476	80	100
1995	[6]	S2K01a	ST	235.2		0.30	1.07	1.03	0.43		2.4	0.24	60	200	1200	476	80	100
1995	[6]	S2K01b	SC	199.6	105.7	0.93	1.70	0.88	1.05	1.14	2.4	0.88	60	200	1200	476	80	100
1995	[6]	S2K02a	ST	206.8		0.40	1.18	0.91	0.57		2.4	0.36	60	200	1200	476	80	100
1995	[6]	S2K02b	ST	216.1		0.55	1.42	0.95	0.80		2.4	0.48	60	200	1200	476	80	100
1995	[6]	S2K03a	ST	278.9		0.36	1.25	1.21	0.51		2.4	0.24	80	200	1200	476	80	100
1995	[6]	S2K03b	SC	213.0	107.8	0.99	1.81	0.92	1.12	1.16	2.4	0.88	80	200	1200	476	80	100
1995	[6]	S2K04a	ST	241.6		0.46	1.36	1.05	0.67		2.4	0.36	80	200	1200	476	80	100
1995	[6]	S2K04b	ST	218.5		0.56	1.42	0.95	0.81		2.4	0.48	80	200	1200	476	80	100
1995	[6]	S2K05a	ST	182.4		0.20	0.88	0.80	0.38		2.4	0.24	60	200	1200	476	80	100
1995	[6]	S2K05b	A/SC	170.7	101.6	0.67	1.42	0.74	0.97	1.29	2.4	0.88	60	200	1200	476	80	100
1995	[6]	S2K06a	ST	178.6		0.29	1.09	0.78	0.56		2.4	0.36	60	200	1200	476	80	100
1995	[6]	S2K06b	ST	171.9		0.37	1.17	0.75	0.71		2.4	0.48	60	200	1200	476	80	100
1995	[6]	S2K07a	ST	242.0		0.26	1.15	1.04	0.50		2.4	0.24	80	200	1200	476	80	100
1995	[6]	S2K07b	A	167.8	99.8	0.66	1.39	0.72	0.95	1.27	2.4	0.88	80	200	1200	476	80	100
1995	[6]	S2K08a	ST	213.0		0.34	1.28	0.91	0.66		2.4	0.36	80	200	1200	476	80	100
1995	[6]	S2K08b	ST/A	211.2	99.6	0.45	1.41	0.91	0.88	1.44	2.4	0.48	80	200	1200	476	80	100
1995	[6]	S2K09a	A	133.7	49.7	0.23	0.93	0.67	0.43	1.45	2.4	0.24	60	160	1200	530	50	78
1995	[6]	S2K09b	SC	123.3	79.2	0.78	1.55	0.61	0.91	1.55	2.4	0.88	60	160	1200	530	50	78
1995	[6]	S2K10a	A	143.5	51.4	0.37	1.27	0.72	0.70	1.26	2.4	0.36	60	160	1200	530	50	78
1995	[6]	S2K10b	A	156.3		0.54	1.56	0.78	0.91		2.4	0.48	60	160	1200	530	50	78
1995	[6]	S2K11a	A	179.0		0.31	1.23	0.88	0.58		2.4	0.24	80	160	1200	530	50	78
1995	[6]	S2K11b	A	131.4		0.83	1.64	0.64	0.97		2.4	0.88	80	160	1200	530	50	78
1995	[6]	S2K12a	ST	168.8		0.44	1.47	0.83	0.82		2.4	0.36	80	160	1200	530	50	78
1995	[6]	S2K12b	ST	154.7		0.54	1.51	0.76	0.90		2.4	0.48	80	160	1200	530	50	78
1995	[6]	S2K13a	ST	227.9		0.30	1.04	1.00	0.42		2.4	0.24	60	200	1200	476	80	100
1995	[6]	S2K13b	SC	195.9	96.7	0.95	1.67	0.86	1.03	1.04	2.4	0.88	60	200	1200	476	80	100
1995	[6]	S2K14a	ST	253.7	87.7	0.51	1.45	1.12	0.70	1.40	2.4	0.36	60	200	1200	476	80	100
1995	[6]	S2K14b	ST	217.3	87.8	0.58	1.41	0.94	0.80	1.19	2.4	0.48	80	200	1200	476	80	100
1995	[6]	S2K15a	ST	294.8		0.39	1.32	1.28	0.54		2.4	0.24	80	200	1200	476	80	100
1995	[6]	S2K15b	SC	174.7	91.5	0.85	1.48	0.76	0.92	0.98	2.4	0.88	80	200	1200	476	80	100
1995	[6]	S2K16a	ST	251.0		0.50	1.42	1.09	0.69		2.4	0.36	80	200	1200	476	80	100
1995	[6]	S2K16b	ST	266.0	96.7	0.71	1.72	1.15	0.98	1.31	2.4	0.48	80	200	1200	476	80	100
1999	[7]	HVP-1	A	241.4		0.73	0.81	0.51	0.71		3.9	0.65	50	260	1200	381	80	128
1999	[7]	HVP-2	ST/A	278.9		0.84	0.94	0.59	0.82		3.9	0.65	50	260	1200	381	80	128
1999	[7]	HVP-3	ST	252.3		0.76	0.85	0.54	0.74		3.9	0.65	50	260	1200	381	80	128
1999	[7]	K-1	ST	488.1		0.67	0.87	0.93	0.96		3.9	1.00	50	400	1200	300	200	198
1999	[7]	K-2	ST	476.2		0.66	0.85	0.91	0.94		3.9	1.00	50	400	1200	300	200	198
1999	[7]	K-3	ST	481.4		0.66	0.86	0.92	0.95		3.9	1.00	50	400	1200	300	200	198
1999	[7]	K-4	ST	470.2		0.65	0.84	0.90	0.93		3.9	1.00	50	400	1200	300	200	198
1999	[7]	R-A-1	A	39.7	19.8	0.66	0.85	0.68	0.77	0.85	3.9	0.50	50	200	1200	80	40	100
1999	[7]	R-A-2	A	48.1	21.3	0.78	1.03	0.82	0.93	0.91	3.9	0.50	50	200	1200	80	40	100
1999	[7]	R-A-3	A	51.8	21.0	0.84	1.11	0.88	1.00	0.90	3.9	0.50	50	200	1200	80	40	100



year	Ref.	Test results			Ratio test/theory				loading			Geometry						
		fail. mode	Vu kN	Mcr kNm	F [-]	A [-]	ST [-]	SC [-]	Mcr [-]	span m	a m	s mm	h mm	b mm	bw mm	hct mm	ec mm	
1999	[7]	R-HVP-1	ST	79.6		0.73	0.71	0.49	0.62		3.9	0.65	50	260	1200	130	80	137
1999	[7]	R-HVP-2	A	89.5	48.9	0.82	0.79	0.55	0.70	0.67	3.9	0.65	50	260	1200	130	80	137
1999	[7]	R-HVP-3	ST/A	97.7	51.5	0.89	0.87	0.60	0.76	0.70	3.9	0.65	50	260	1200	130	80	137
1999	[7]	R-K-1	ST	217.6		0.58	0.75	1.01	0.87		3.9	1.00	50	400	1200	140	200	204
1999	[7]	R-K-2	ST	202.0		0.54	0.69	0.93	0.81		3.9	1.00	50	400	1200	140	200	204
1999	[7]	R-K-3	ST	223.5		0.60	0.77	1.03	0.89		3.9	1.00	50	400	1200	140	200	204
1999	[7]	R-VX-1	ST	94.1		0.78	0.87	0.91	0.98		3.9	0.66	50	265	1200	76	0	138
1999	[7]	R-VX-2	ST	92.3		0.76	0.85	0.90	0.94		3.9	0.66	50	265	1200	76	0	138
1999	[7]	R-VX-3	ST	94.6		0.79	0.87	0.92	0.98		3.9	0.66	50	265	1200	76	0	138
1999	[7]	R-VX-4	ST	87.1		0.72	0.80	0.85	0.89		3.9	0.66	50	265	1200	76	0	138
1999	[7]	R-X-1	F	68.8	23.7	1.12	1.33	0.88	1.31	0.92	3.9	0.50	50	200	1200	84	14	100
1999	[7]	R-X-2	F	65.8	22.5	1.07	1.27	0.84	1.25	0.87	3.9	0.50	50	200	1200	84	14	100
1999	[7]	R-X-3	A/F	65.3	23.2	1.06	1.26	0.83	1.24	0.89	3.9	0.50	50	200	1200	84	14	100
1999	[7]	R-XB-1	F	57.4	20.4	0.94	1.19	0.82	1.11	0.84	3.9	0.50	50	200	1200	84	14	100
1999	[7]	R-XB-2	F	60.7	22.3	1.01	1.28	0.87	1.21	0.94	3.9	0.50	50	200	1200	84	14	100
1999	[7]	R-XB-3	A/F	60.4	23.2	0.99	1.25	0.87	1.18	0.96	3.9	0.50	50	200	1200	84	14	100
1999	[7]	VX-1	ST	256.0		0.73	0.94	0.88	0.93		3.9	0.66	50	265	1200	235	0	131
1999	[7]	VX-2	ST	263.5		0.75	0.97	0.90	0.96		3.9	0.66	50	265	1200	235	0	131
1999	[7]	XB-1	F	236.1		0.99	1.27	0.79	1.14		3.9	0.50	50	200	1200	355	14	99
1999	[7]	XB-2	F	228.2		0.95	1.23	0.76	1.11		3.9	0.50	50	200	1200	355	14	99
1999	[7]	XB-3	F	236.1		0.99	1.27	0.79	1.14		3.9	0.50	50	200	1200	355	14	99

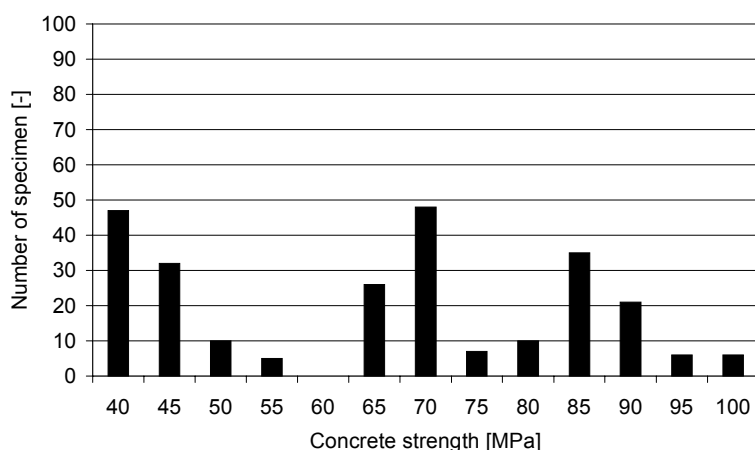


Figure A.1: Frequency histogram of the concrete compressive strength.

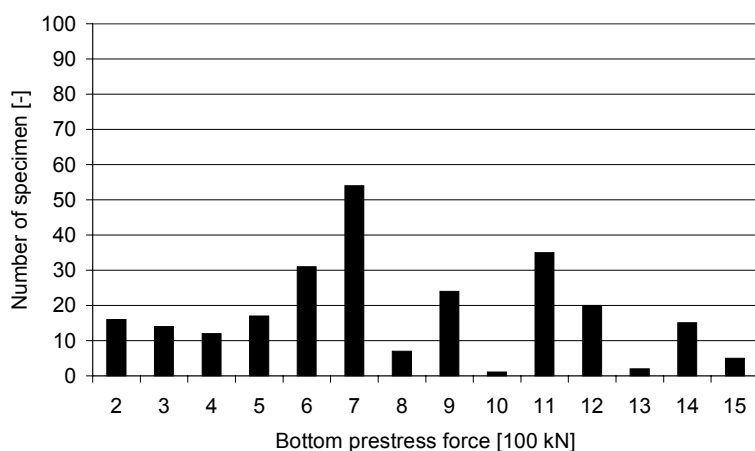


Figure A.2: Frequency histogram of the total prestress force in the bottom strands.

Ac	I	S	Strands									Concrete		Steel			
			#1	Dia 1	c1	spl 1	#2	Dia 2	c2	spl 2	#3	Dia 3	c3	spl 3	fcm	fctm	fpu
10 <sup>3</sup> mm <sup>2</sup>	10 <sup>8</sup> mm <sup>4</sup>	10 <sup>6</sup> mm <sup>3</sup>		mm	mm	MPa		mm	mm	MPa		mm	mm	MPa	MPa	MPa	MPa
64.3	5.3	2.7	1	12.5	40	1150	1	12.5	77	1250	1	9.3	179	1250	97.4	6.00	1900
64.3	5.3	2.7	1	12.5	40	1150	1	12.5	75	1250	1	9.3	179	1250	97.4	6.00	1900
64.3	5.3	2.7	1	12.5	40	1150	1	12.5	77	1250	1	9.3	179	1250	97.4	6.00	1900
129.0	22.9	8.4	2	12.5	44	1300	2	12.5	86.5	1300	4	9.3	44	1300	82.85	5.05	1900
129.0	22.9	8.4	2	12.5	43	1300	2	12.5	86.5	1300	4	9.3	43	1300	82.85	5.05	1900
129.0	22.9	8.4	2	12.5	44	1300	2	12.5	86.5	1300	4	9.3	44	1300	82.85	5.05	1900
68.9	7.0	3.2	2	12.5	39	1150									84.5	5.70	1900
68.9	7.0	3.2	2	12.5	36	1150									84.5	5.70	1900
68.9	7.0	3.2	2	12.5	38.5	1150									84.5	5.70	1900
68.9	7.0	3.2	2	12.5	36.5	1150									84.5	5.70	1900
36.9	1.8	1.2	2	9.3	43.5	1150	1	5	165	1100					89.4	5.84	1900
36.9	1.8	1.2	2	9.3	43.5	1150	1	5	165	1100					89.4	5.84	1900
36.9	1.8	1.2	2	9.3	43.5	1150	1	5	165	1100					89.4	5.84	1900
36.9	1.8	1.2	2	9.3	44.5	1150	1	5	165	1100					85.9	5.21	1900
36.9	1.8	1.2	2	9.3	48	1150	1	5	165	1100					85.9	5.21	1900
36.9	1.8	1.2	2	9.3	45	1150	1	5	165	1100					85.9	5.21	1900
175.0	15.2	7.6	6	12.5	40	1150									84.5	5.70	1900
175.0	15.2	7.6	6	12.5	40	1150									84.5	5.70	1900
144.6	6.8	4.6	8	9.3	45	1150	4	5	165	1150					85.9	5.21	1900
144.6	6.8	4.6	8	9.3	45	1150	4	5	165	1150					85.9	5.21	1900
144.6	6.8	4.6	8	9.3	45	1150	4	5	165	1150					85.9	5.21	1900

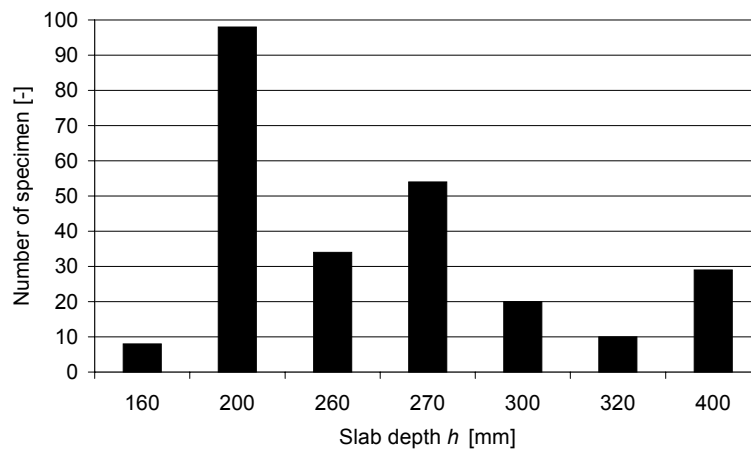


Figure A.3: Frequency histogram of the slab depth.

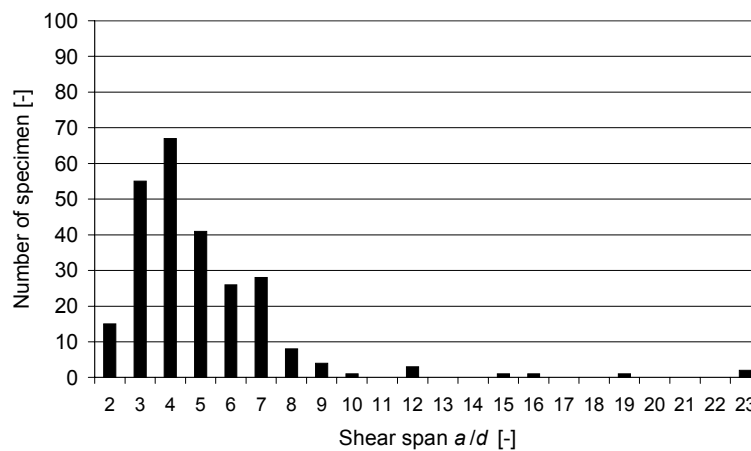


Figure A.4: Frequency histogram of the shear span.

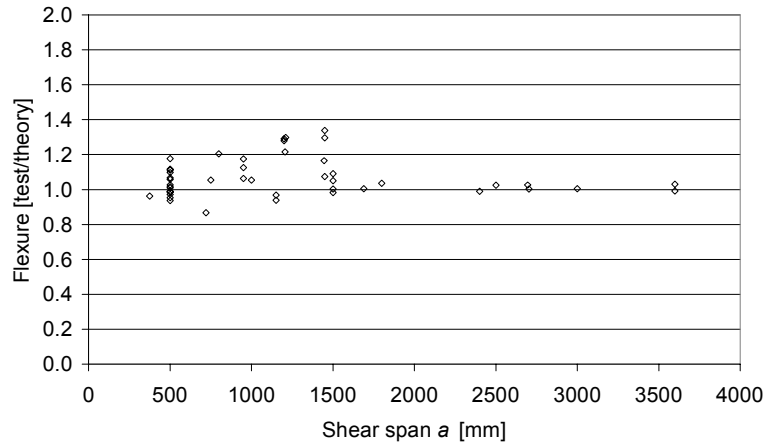


Figure A.5: Test to theory ratio with respect to flexural failure as function of the shear span. It shows that the unsafe values occur at shorter shear spans.

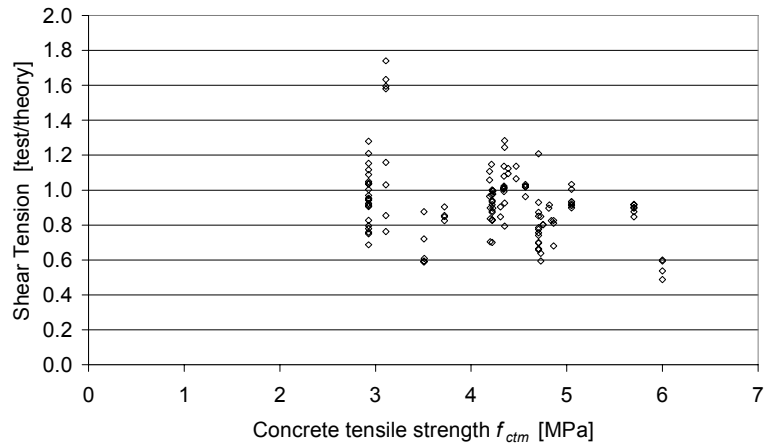


Figure A.6: Test to theory ratio with respect to shear tension failure as function of the splitting tensile strength of concrete. There is a slight tendency of a decreasing ratio for higher tensile strengths.

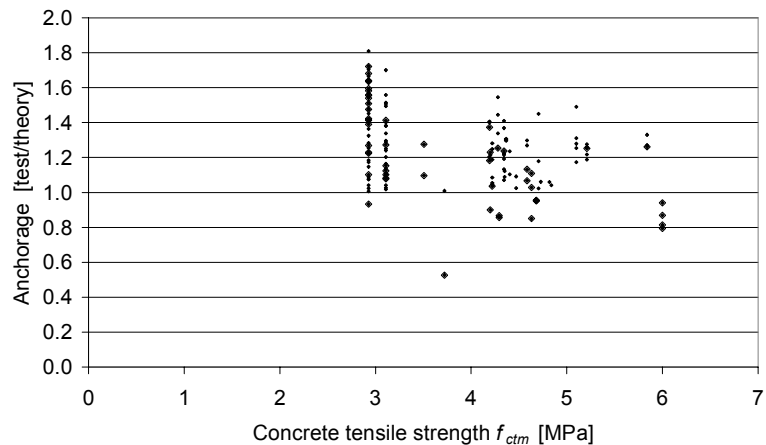


Figure A.7: Test to theory ratio with respect to anchorage failure as function of the splitting tensile strength.

# Appendix B: Transfer and development length

Evaluation of calculation rules according to various codes and researchers for the transfer length and development length of pretensioned strands.

## Transfer length

The increase of the bond stress over the transfer length is considered by most codes. As many different formulations exist, these are compared below, in order to be able to pick an appropriate formulation for the calculation of the anchorage capacity.

The equation of Model Code [CEB-FIP: 1991] is given first, because this relation was used later on for the comparison of the anchorage capacity with the experimental results.

$$\begin{aligned}
 l_t &= \alpha_8 \alpha_9 \alpha_{10} \frac{\sigma_{pi}}{\eta_{p1} \eta_{p2} f_{ctdi}} \frac{A_p}{\pi \Phi} \\
 &= 1 \cdot 0.75 \cdot 0.5 \frac{\sigma_{pi}}{1.2 \cdot 1.0 \frac{0.7 f_{ctmi}}{1.5}} \frac{7}{36} \Phi = 0.130 \frac{\sigma_{pi}}{f_{ctmi}} \Phi \quad \text{7-wire strands} \\
 &= 1 \cdot 0.75 \cdot 0.7 \frac{\sigma_{pi}}{1.4 \cdot 1.0 \frac{0.7 f_{ctmi}}{1.5}} \frac{9}{36} \Phi = 0.201 \frac{\sigma_{pi}}{f_{ctmi}} \Phi \quad \text{wires}
 \end{aligned} \tag{B.1}$$

In this equation  $\alpha_8$  considers the speed of release being 1 for a gradual release and 1.25 for a sudden release. Sawing of the HC slabs should be considered as gradual release.  $\alpha_9$  is the partial safety factor of the model. It considers the scatter of the transfer length and varies between 0.5 (characteristic for the evaluation of splitting failure) and 1.0 (characteristic for anchorage failure). It is assumed that the mean value is in the middle of the two characteristic values at 0.75. The value of  $\alpha_9$  was adjusted to the use of the design tensile strength at time of prestress release  $f_{ctdi}$  rather than the mean tensile strength  $f_{ctmi}$ . Furthermore,  $\alpha_{10}$  and  $\eta_{p1}$  consider the type of tendon, and  $\eta_{p2}$  takes into account the position of the tendon relative to the horizontal during casting. The formula for the transfer length was compared to equations of other codes and researchers. Mitchell et al. [1993] found a very similar relation for the mean value of the transfer length by fitting on experimental results, given by

$$l_t = 0.213 \frac{\sigma_{pi}}{\sqrt{f_{ci}}} \Phi \tag{B.2}$$

With all stresses in MPa. This value was recommended as a design value for anchorage and shear. In order to check the splitting stresses at the slab end, an alternative formulation was proposed that should lead to shorter transfer lengths. However, beyond an initial prestress of 1033 MPa, the alternative leads even to larger transfer lengths. In that case, no safety margin is included.

Zia et al. [1977] derived at a mean value of

$$\left. \begin{aligned} l_t &= 1.3 \frac{\sigma_{pi}}{f_{ci}} \Phi - 58 && \text{gradual release} \\ l_t &= 1.5 \frac{\sigma_{pi}}{f_{ci}} \Phi - 117 && \text{sudden release} \end{aligned} \right\} \text{ in [mm]} \quad \{B.3\}$$

The transfer length for a sudden release was recommended as a design value for both cases. Olesniewicz (1975) came up with

$$l_t = \gamma_M 10 \frac{\sqrt{\sigma_{pi}}}{\sqrt{f_{cci}}} \Phi \quad \{B.4\}$$

With partial safety factor  $\gamma_M$  equal to 1, 0.7 or 1.3 for mean and characteristic lower and upper bound respectively, and the cube compressive strength at time of release  $f_{cci}$  rather than the cylinder strength. For the comparison, the Dutch NEN 6720 relation between the cube compressive strength  $f_{cc}$  and the cylinder compressive strength  $f_c$  was used [NEN 6720: 1995].

$$f_{cc} = 0.85 f_c \quad \{B.5\}$$

In design codes the following relations are given. In Eurocode 2 [PREN 1992-1:2002] the transfer length is independent of the initial prestress  $\sigma_{pi}$

$$l_t = \gamma_M (100 - f_{ci}) \Phi \quad f_c \text{ in [MPa]} \quad \{B.6\}$$

With  $\gamma_M$  equal to 1, 0.8 and 1.2 for mean and characteristic lower and upper bound respectively. The American ACI 318 (1995) prescribes the transfer length as

$$l_t = 0.048 \alpha_2 \sigma_{p\infty} \Phi = 0.048 \sigma_{p\infty} \Phi \quad \sigma_{p\infty} \text{ in [MPa]} \quad \{B.7\}$$

Which is independent of the concrete strength. This is compensated by the requirement that the formula may only be used provided that the strength exceed 24 MPa at the time of the release of the prestress.  $\alpha_2$  depends on the location of the strand, like  $\eta_{p2}$  in the Model Code formulation, and equals 1.3 if the strand is in the upper one-third of the cross section or with more than 305 mm concrete beneath it and 1.0 otherwise. And  $\sigma_{p\infty}$  equals the prestress including time dependent losses. Remarkably, the ACI 318 does not distinguish with some safety factor between favourable and unfavourable effects of the transfer of the prestress.

And the Dutch NEN 6720 prescribes

$$l_t = \gamma_M 0.5 \alpha_1 \alpha_2 \frac{\sigma_{pi}}{\sqrt{0.6 f_{cci}}} \Phi = 0.225 \frac{\sigma_{pi}}{\sqrt{f_{ci}}} \Phi \quad \{B.8\}$$

In which eq. B.5 was used and all stresses are in MPa. Again  $\alpha_2$  depends on the location, equal

to 1.25 for upper bars, and equal to 1 otherwise. The model factor  $\gamma_M$  ranges between 0.5-1.0 depending on the considered design state.

In fig. B.1, the transfer length according to the above mentioned formulae are given on the basis of an assumed prestress of 1200 MPa.

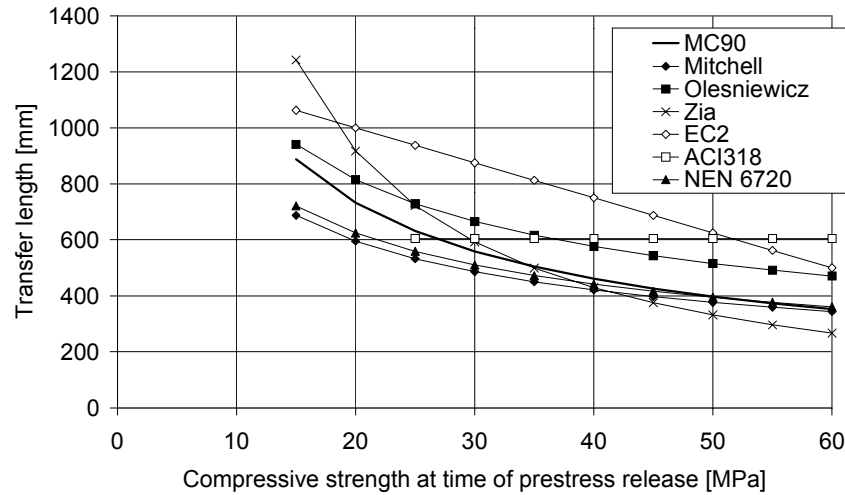


Figure B.1: Mean transfer length  $l_t$  of strand with diameter of 12.5 mm and prestressed with 1200 MPa according to various researchers and design codes, depending on actual concrete compressive strength at time of release  $f_{cr}$ .

As shown in fig 9.8, the bandwidth of the prediction formulae is some 300 mm. The Model Code formulation gives results that are in the middle of the other ones and seems therefore good choice for comparison with the anchorage capacity found in tests.

## Development length

The development length according to various codes and researchers was also compared. All descriptions add a so-called flexural bond length to the transfer length, except for Eurocode.

The Model Code relation reads for wires and strands

$$l_d = l_t + \frac{f_p - \sigma_{p\infty}}{\eta_{p1} \eta_{p2} f_{ctdi}} \frac{7}{36} \Phi = l_t + 0.347 \frac{f_p - \sigma_{p\infty}}{f_{ctmi}} \Phi \quad \{B.9\}$$

In this equation  $f_p$  is the steel strength. In design, obviously, the design steel strength may be used. However, the actual steel strength must be used when comparing with test results.

The development length is only used in the evaluation of anchorage failure, so only a safe upper bound value is required in design. Comparison of the flexural bond length of eq. B.9 with the transfer length of eq. B.1 shows that the model factor  $\alpha_s$  is not included in the flexural bond length, which corresponds to  $\alpha_s$  equal to upper bound value of 1. Furthermore it is noted that the flexural bond length uses the concrete tensile strength at the time of the release of the prestress rather than the concrete tensile strength at time of testing.

Mitchell et al. [1993] derived the following safe upper bound for the development length

$$l_d = l_t + 0.782 \frac{f_p - \sigma_{p\infty}}{\sqrt{f_c}} \Phi \quad \{\text{B.10}\}$$

In this formula,  $f_c$  is the concrete compressive strength at the time of testing.

Eurocode 2 [PREN 1992-1: 2002] states

$$l_d = l_t \frac{f_p}{\sigma_{pi}} = \gamma_M (100 - f_{ci}) \Phi \frac{f_p}{\sigma_{pi}} \quad f_{ci} \text{ in [MPa]} \quad \{\text{B.11}\}$$

As mentioned before, the model factor  $\gamma_M$  ranges from 0.8 to 1.2 for lower and upper bound.

In the ACI code [ACI 318: 1995], the formulation is independent of the concrete strength.

$$l_d = l_t + 0.145 (f_p - \sigma_{p\infty}) \Phi \quad \{\text{B.12}\}$$

And the Dutch NEN code [NEN 6720: 1991] gives the following relation

$$l_d = l_t + \alpha_1 \alpha_2 \frac{f_p - \sigma_{pi}}{\sqrt{f_c}} \Phi \quad \{\text{B.13}\}$$

With  $\alpha_1$  is 0.5 for 7-wired strands and  $\alpha_2$  is 1 for bottom strands and 1.3 for upper strands.

According to the Model Code, the ACI and Mitchell, the transfer length is calculated using  $\sigma_{pi}$  and second term using the stress increment from the prestress including all losses  $\sigma_{p\infty}$  up to the steel strength  $f_p$ . Compare in fig. 2.3 the slope of the steel stress envelop over the transfer length corresponding to release to the slope related to pull out. Bear in mind that the slope is proportional to the bond stress. So, it is assumed that the bond stress that is reached over the transfer length during prestress release, can not be reached again when the strand is pull out. In the author's opinion this assumption is incorrect.

In fig. B.2, the development length is presented depending on the concrete compressive strength at time of testing. In this figure, an initial prestress  $\sigma_{pi}$  of 1200 MPa was assumed, which is reduced to a final prestress value  $\sigma_{p\infty}$  of 950 MPa. This approximated stress loss due to relaxation of the strands and creep and shrinkage of the concrete is obtained from data used by Dutch HC producers. The figure indicates that the Model Code formulation gives results in between the other relations. Therefore, the Model Code was used in calculations of the anchorage capacity.

In order to compare the anchorage capacity of tests with the calculation, the calculation should be based on nominal values, i.e. the mean value of the development length and the mean value of the steel strength. However, the flexural bond length in all formulations of the development length does not distinguish between the mean and the safe upper bound values. Only the Eurocode formulation allows for this distinction due to the different type of formulation. Therefore, the development length was calculated as the sum of the mean value for the transfer length and the safe upper bound values of the flexural bond length, see fig. B.2. (Only Eurocode was calculated as mean value). On the other hand, the formulations are valid up to the characteristic steel strength rather than the actual steel strength. In the calculation of the anchorage capacity, the development length is linearly extrapolated up from the characteristic

steel strength to the actual yield strength of the steel strand. As will be shown below, due to yielding of the strand, the bond stress decreases. So, linear extrapolation of the development length beyond the characteristic steel strength up to the actual steel strength is not conservative.

Again it can be seen that the model code gives reasonable results compared to other codes, which justifies the choice for the model code formulation in the calculation of the anchorage capacity of HC slabs.

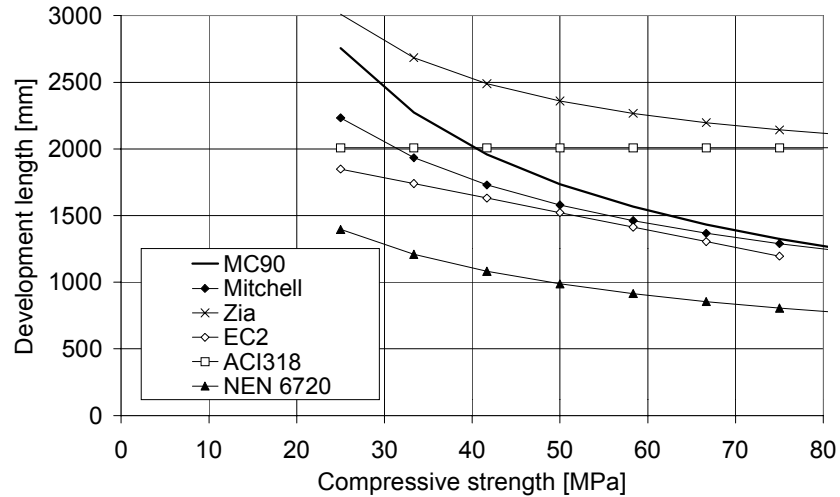


Figure B.2: Development length of 12.5 mm strands, assuming  $\sigma_{pi} = 1200$  MPa and  $\sigma_{p\infty} = 950$  MPa, and an design steel strength of 1740 MPa.



# Appendix C: HC tests at fire conditions

## References of fire tests on HC slabs.

year	reference	test ID	year	reference	test ID
1958	[Gantvoort: 1981]	UL-4130-1	1984	[Loikkanen & Jumppanen: 1984b]	PAL 4450
1958	[Gantvoort: 1981]	UL-4130-2	1984	[Hietanen: 1992]	PAL 4451
1961	[Gantvoort: 1981]	UL-4130-3	1984	[Loikkanen & Jumppanen: 1984c]	PAL 4452
1966	[Johnson & Parks: 1966]	UL-5309-4	1985	[Loikkanen & Jumppanen: 1984d]	PAL 4453
1967	[Brander & Parks: 1968]	UL-5558-1	1985	[Hietanen: 1992]	PAL 4454
1968	[Malhotra: 1968]	FROSI 4904	1985	[Loikkanen & Jumppanen: 1985a]	PAL 566a
1968	[Gantvoort: 1981]	BV-68-98	1985	[Loikkanen & Jumppanen: 1985b]	PAL 556b
1969	[Gantvoort: 1981]	BV-69-79	1985	[Hietanen: 1992]	PAL 556c
1970	[Gantvoort: 1981]	BV-70-03	1985	[Hietanen: 1992]	PAL 566d
1970	[van Elteren: 1972]	BV-72-13	1985	[Hietanen: 1992]	PAL 90228
1970	[Gantvoort: 1981]	BV-77-79	1985	[Hietanen: 1992]	PAL 1126
1970	[Gantvoort: 1981]	BV-78-180	1985	[Hietanen: 1992]	PAL 5308
1971	[Hietanen: 1992]	PAL 1927	1985	[Hietanen: 1992]	PAL 5327
1971	[Hietanen: 1992]	PAL 2892	1986	[Hietanen: 1992]	PAL 5377
1972	[Hietanen: 1992]	PAL 2163	1987	[Peherstorfer & Moser: 1987]	BV 2697
1972	[Hietanen: 1992]	PAL 6710	1990	[Loikkanen & Kajastila: 1990a]	PAL 360a
1974	[Hietanen: 1992]	PAL 7116	1990	[Loikkanen & Kajastila: 1990b]	PAL 360b
1976	[Abrams: 1976]	RD044.01B	1991	[Loikkanen & Kajastila: 1991]	PAL 1127
1977	[Hietanen: 1992]	PAL 1376	1993	[Peherstorfer & Moser: 1993]	BV 3391
1977	[CBR: 1977]	SRP33	1993	[Wesche & Nause: 1993]	3731/5353
1978	[Vermeulen: 1978]	SPG20/9	1993	[Zhao: 1993]	INC93/204
1978	[Vermeulen: 1978]	SPG27/6	1994	[Borgogno & Fontana: 1995]	PTT
1978	[Vermeulen: 1978]	SPG32/16	1995	[Borgogno & Fontana: 1996]	B2-1
1978	[Vermeulen: 1978]	SPK27/10	1995	[Borgogno & Fontana: 1996]	B2-2
1978	[Vermeulen: 1978]	SPG27/6	1995	[Borgogno & Fontana: 1996]	B2-3
1979	[Hietanen: 1992]	PAL 9498	1995	[Borgogno & Fontana: 1996]	B2-4 PL
1980	[Hietanen: 1992]	PAL 1146b	1995	[Borgogno & Fontana: 1996]	B3-1
1980	[Hietanen: 1992]	PAL 1191	1995	[Borgogno & Fontana: 1996]	B3-2 PL
1980	[Hietanen: 1992]	PAL 1350	1995	[Zhao: 1995a]	95-E-467
1980	[Hietanen: 1992]	PAL 1038a	1995	[Zhao: 1995b]	95-E-533
1980	[Hietanen: 1992]	PAL 1038b	1996	[Zhao: 1996a]	96-U-349
1980	[Hietanen: 1992]	PAL 1038c	1996	[Zhao: 1996b]	96-U-350
1980	[Hietanen: 1992]	PAL 1275a	1998	[Teirlinck & Vandevelde: 1999a]	RG 8871
1982	[Hietanen: 1992]	PAL 2480	1998	[Teirlinck & Vandevelde: 1999b]	RG 8872
1982	[Hietanen: 1992]	PAL 2481	1999	[Teirlinck & Vandevelde: 2000a]	RG 9157
1982	[Vandevelde & Odou: 1983]	RG 4514	1999	[Teirlinck & Vandevelde: 2000b]	RG 9158
1983	[Peherstorfer & Moser: 1983]	BV 2311	1998	[Andersen & Lauridsen: 1999]	X52650d
1984	[Hietanen: 1992]	PAL 4248	1998	[Andersen & Lauridsen: 1999]	X52650e
1984	[Loikkanen & Jumppanen: 1984a]	PAL 4337	1998	[Andersen & Lauridsen: 1999]	X52650f
1984	[Hietanen: 1992]	PAL 4448	2000	[Schepper et.al.:2000]	PG10724



# Appendix D: Maturing assumptions for concrete

## Strength and stiffness

The strength and stiffness depend on the aging according to

$$\begin{aligned} f_{ct,t} &= \beta_{cc} f_{ct} \\ f_{c,t} &= \beta_{cc} f_c \\ E_{c,t} &= \sqrt{\beta_{cc}} E_c \end{aligned} \quad \{\text{D.1}\}$$

in which

$$\beta_{cc} = e^{s \left( 1 - \sqrt{\frac{28}{t_T}} \right)} \quad \{\text{D.2}\}$$

where the parameter  $s$  depends on the cement type, see table D.1 and  $t_T$  is the equivalent concrete age in days, which takes into account the effect of temperature on the maturity according to

$$t_T = \sum_{i=1}^n \Delta t_i e^{13.65 - \frac{4000}{273 + \theta(\Delta t_i)}} \quad \{\text{D.3}\}$$

in which the history of the concrete is divided into  $n$  time periods, each of a time increment  $\Delta t_i$ , having a temperature of  $\theta(\Delta t_i)$  in °C during that time period. The maturity of the concrete under curing conditions that deviate from 20 °C equals the maturity that the same concrete would reach at the equivalent concrete age under default curing conditions of 20 °C.

The factor  $\beta_{cc}$  will be larger than unity for concrete older than 28 days. If the strength was measured after more than 28 days, the strength  $f_{ct}$  in eq. D.1 was scaled such that the strength at the testing day, calculated with eq. D.1 to D.3, equals the measured strength.

Fig. D.1 gives an example of the strength development assuming the storage conditions of table D.1 on page 257.

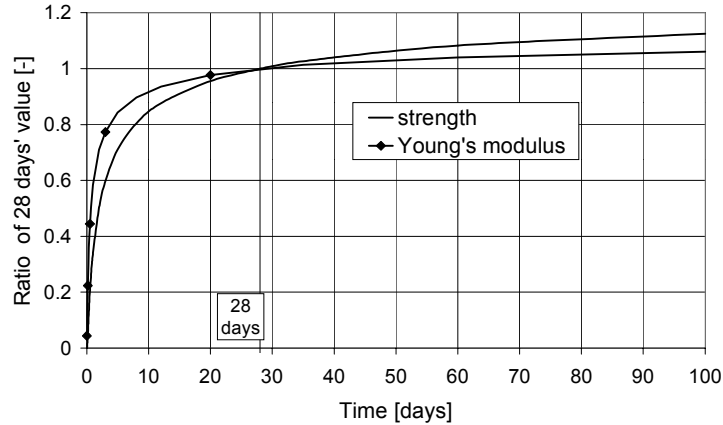


Figure D.1: Strength and stiffness development of concrete containing normal hardening cement.

## Shrinkage

The shrinkage was estimated using the method of the Model Code [CEB-FIB: 1991], including the improvements of the FIB bulletin 1 [FIB: 1999]. The shrinkage was subdivided into an autogenous part and a drying part:

$$\epsilon_s = \epsilon_{auto} + \epsilon_{dry} \quad \{D.4\}$$

The autogenous part does not depend on the relative humidity, but only on the microstructure of the concrete and the time. For the sake of simplicity, the dependency of the microstructure was taken into account only through the compressive strength. As the autogenous shrinkage is caused by the internal hydration process, it is related to the degree of maturity. Therefore, the autogenous shrinkage was calculated using the equivalent concrete age of eq. D.3.

$$\epsilon_{auto} = \epsilon_{cas0} \left( 1 - e^{-0.2\sqrt{t_T}} \right) \quad \{D.5\}$$

In which  $\epsilon_{cas0}$  is the notional autogenous shrinkage strain that depends on the strength, see [FIB: 1999].

The drying shrinkage not only depends on time, temperature, and microstructure, but also on the relative humidity. As temperature effects were explicitly taken into account in the equations of the FIB Bulletin 1 [FIB: 1999], the time should not be corrected for temperature driven accelerated maturity by the use of the equivalent concrete age. The drying shrinkage reads

$$\epsilon_{dry} = \epsilon_{cs} \beta_{RHT} \sqrt{\frac{t - t_s}{\alpha_{sT} + t - t_s}} \quad \{D.6\}$$

in which the concrete age  $t$  and the start time of drying  $t_s$  are expressed in days, and  $\epsilon_{cs}$  depends on the mean compressive strength  $f_{cm}$ ,  $\beta_{RHT}$  depends on the relative humidity and the temperature and  $\alpha_{sT}$  on the temperature [FIB: 1999].

After infinite time, the drying shrinkage reaches a value of

$$\epsilon_{dry}^{\infty} = \epsilon_{cs} \beta_{RHT} \quad \{D.7\}$$

So, the final shrinkage depends on the drying conditions through the parameter  $\beta_{RHT}$ . However, the drying conditions are not always constant during the entire maturing period. The fire test specimens for instance, was stored in a conditioned room at low relative humidity and high ambient temperature after a few weeks of outdoor storage. Once the concrete structure is subjected to varying maturing conditions, it was assumed that the shrinkage starts to develop toward the infinite value corresponding to the current conditions every time the conditions are changed. In order to predict this behaviour, the drying shrinkage was calculated as the sum of the shrinkage at the starting time of new drying conditions and the additional shrinkage that develops during this new period.

$$\epsilon_{dry}^t = \epsilon_{dry}^{t_s} + \left( \epsilon_{dry}^{\infty} - \epsilon_{dry}^{t_s} \right) \sqrt{\frac{t - t_s}{\alpha_{sT} + t - t_s}} \quad \{D.8\}$$

In fig. D.2 a representative shrinkage development is given for a HC slab that was tested under fire conditions. The storage conditions during maturing given in table D.1 were assumed for a concrete with normal hardening type of cement and concrete strength of 85 MPa.

**Table D.1** Assumed storage conditions for HC slabs during maturing.

Description	Start time [days]	End time [days]	Temperature [°C]	RH [%]
Production bench	0	0.68	60	100
Outdoor storage stack	0.68	20	20	80
Indoor conditioning room	20	100	40	50

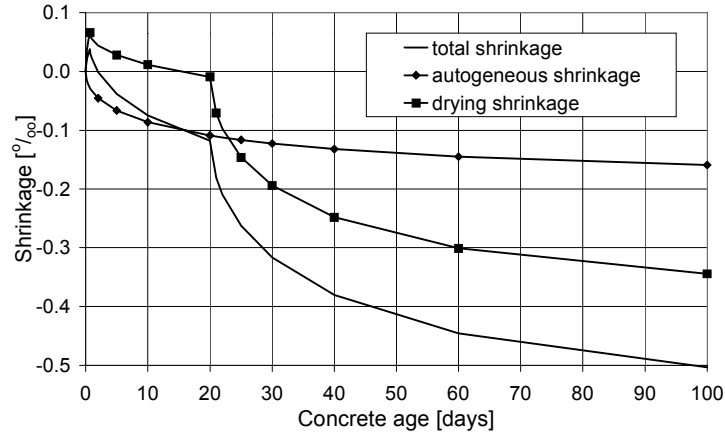


Figure D.2: Shrinkage development of concrete made with normal hardening cement and conditioned during maturing according to table D.1.

## Creep

In the cross sectional model, shrinkage causes large circumferential stresses around the strand up to cracking if no tensile creep would be taken into account. Therefore, in this FE model, the stress releasing effect of the tensile creep effect was taken into account by a reduction of the shrinkage strains in the cross sectional model by a factor  $k_{scr} = 0.5$ .

$$\epsilon_{scr} = k_{scr} \epsilon_s \quad \{D.9\}$$

As a consequence, smaller radial compressive stresses and smaller circumferential tensile stresses around the strand develop than when neglecting the tensile creep.

If concrete is loaded in compression, like in the axial direction of a prestressed HC slab, creep and shrinkage strains must be superimposed to calculate the time dependent loss of prestress. Creep was included for this case by a fictitious transient creep over the maturing period.

$$\varphi_{cr,t} = \frac{\epsilon_{tot}(t, t_0)}{\epsilon_E(t_0)} \quad \{D.10\}$$

The creep coefficient was taken from the FIB Bulletin 1 [FIB: 1999]. The creep coefficient reads It is dependent of the time  $t$ , the time of loading  $t_0$ , the relative humidity and the development of the loading.

The creep factor can be subdivided in a time dependent part and a part that depends on the ambient conditions such as relative humidity and temperature. The creep value corresponding to the load applied at time  $t_0$  reads

$$\varphi_{cr,t} = \varphi_{RHT} \beta_f \beta_{t_0} \beta_t \quad \{D.11\}$$

in which the notional creep factor  $\varphi_{RHT}$  depend on temperature and relative humidity, factor  $\beta_f$  depends on the concrete strength,  $\beta_{t_0}$  on the time of loading  $t_0$  and  $\beta_t$  accounts for the maturing time  $t$  [FIB: 1999].

If the maturing conditions remain constant over the maturing period  $m$ , the final creep factor after infinite time would become

$$\Phi_{cr,t0,\infty}^m = \Phi_{RHT}^m \beta_f \beta_{t0}^m \quad \{D.12\}$$

The effect on the creep development by shifts in temperature during maturing was considered in an approximate way. It is assumed that after a modification of the maturing conditions at the time  $t_m$  from  $m_0$  to  $m_1$  the further development of the creep factor is identical to the development from  $t_m$  on as if conditions  $m_1$  would be present from the time of loading  $t_0$ . However, the starting value at time  $t_m$  corresponds to the value resulting from the maturing conditions  $m_0$  at time  $t_m$ , i.e.

$$\varphi_{cr,t} = \varphi_{cr,tm}^{m_0} - \varphi_{cr,tm}^{m_1} + \varphi_{cr,t0,\infty}^{m_1} \beta_t \quad \{D.13\}$$

Where the subscripts of  $\varphi_{cr}$  are referring to time and the superscripts to the maturing conditions. In fig. D.3 the development of the creep coefficient is presented for the maturing conditions given in table D.1.

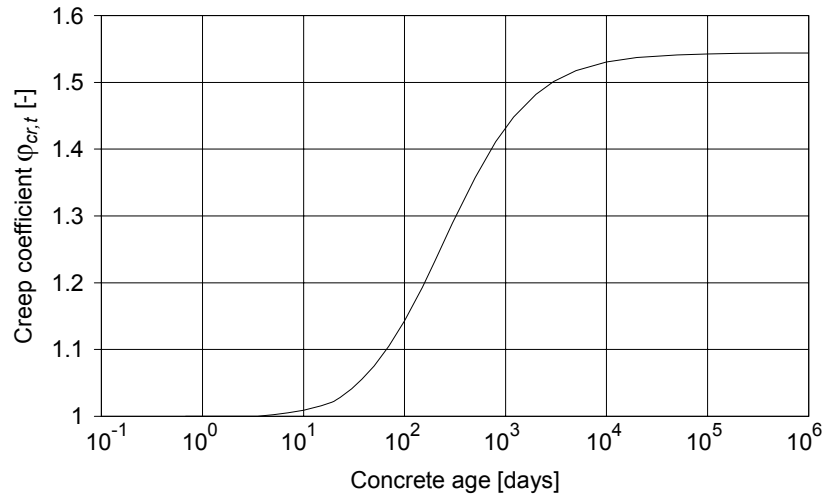


Figure D.3: Development of the creep coefficient for concrete under maturing conditions as given in table D.1.

The creep was taken into account as a transient creep strain by transforming the maturing time  $t$  into a fictitious temperature increase of 100 °C from  $\theta_0 = -80$  to  $\theta_u = 20$  °C, i.e.

$$\gamma\theta_{fic}(t) = \theta_0 + \frac{\theta_u - \theta_0}{t_u - t_0} t \quad \{D.14\}$$

Correspondingly, the thermal expansion coefficient  $\alpha_T$  becomes a fictitious time dependent coefficient of thermal expansion  $\alpha_t$

$$\dot{\epsilon}_{tr,t} = \frac{k_{tr} \alpha_t}{f_{c,20}} \sigma \dot{t} \quad \{D.15\}$$

By increasing the transient creep coefficient  $k_{tr}$  by a factor  $10^3$  from its original value which is

used to calculate actual transient creep during heating beyond 20 °C, and reducing the coefficient of thermal expansion  $\alpha_T$  correspondingly, the thermal expansion during the fictitious temperature increase is negligible but the transient creep strains are considerable. The transient creep, calculated through the latter equation can be equal to the time dependent creep during maturing by further adaptation of the thermal expansion coefficient in the fictitious temperature regime of -80 to 20 °C that represents the maturing time.

From the rate type of formulation of the transient creep in DIANA, it can be derived that the total transient creep at time  $t_u$  depends on all stress increments  $\Delta\sigma_i$  at the begin of each time step  $t_{0i}$  as

$$\varepsilon_{tr,tu} = \frac{k_{tr}}{f_{c,20}} \sum_i^n \Delta\sigma_{t0i} \int_{\theta_{0i}}^{\theta_u} \alpha_T d\theta_{fic} = \frac{k_{tr}}{f_{c,20}} \sum_i^n \Delta\sigma_{t0i} \frac{d\theta_{fic}}{dt} \int_{t_{0i}}^{t_u} \alpha_t dt \quad \{D.16\}$$

The derivative of the fictitious temperature to the maturing time simply equals  $100/t_u$ , see eq. D.14.

According to the Model Code [CEB-FIB: 1991], the time dependent creep  $\varepsilon_{cr}$  at time  $t_u$  can be subdivided into contributions from every load increment at time  $t_{0i}$  before  $t_u$  as

$$\varepsilon_{cr,tu} = \sum_i^n \Delta\varepsilon_{cr,t0i,tu} = \sum_i^n \Delta\varepsilon_{e,t0i} \varphi_{cr,t0i,tu} = \sum_i^n \frac{\Delta\sigma_{t0i}}{E_{c,t0i}} \int_{t_{0i}}^{t_u} \dot{\varphi}_{cr,t0i,t} dt \quad \{D.17\}$$

Combination of eq. D.16 and D.17 results for  $\alpha_t$  in

$$\int_{t_{0i}}^{t_u} \alpha_t dt = \frac{t_u}{100} \frac{f_{c,20}}{k_{tr} E_{c,t0i}} \int_{t_{0i}}^{t_u} \dot{\varphi}_{cr,t0i,t} dt \quad \forall \quad t_{0i} \leq t_u \quad \{D.18\}$$

So, for one given time of loading  $t_{0i}$ , the fictitious coefficient of thermal expansion can be calculated as

$$\alpha_{t0i,t} = \frac{t_u}{100} \frac{f_{c,20}}{k_{tr} E_{c,t0i}} \dot{\varphi}_{cr,t0i,t} = \frac{t_u}{100} \frac{f_{c,20}}{k_{tr} E_{c,t0i}} \varphi_{cr,t0i,\infty}^m \dot{\beta}_t \quad \{D.19\}$$

So, in principle, the fictitious thermal expansion coefficient depends on both the time and the initial time of loading of all load increments. However, in DIANA, the fictitious thermal expansion coefficient can only be dependent on the fictitious temperature which represents the maturing time. So, it can just be given correctly for one unique time of loading  $t_{0i}$  rather than for all possible times of loading. The major load step during the maturing stage is the prestress release. So,  $t_{0i}$  was set to the time of prestress release for the calculation of  $\alpha_t$ .

# Curriculum vitae



Joris Fellingner was born in Didam on June 24, 1970. In 1988 he passed the VWO examinations at the Liemers College in Zevenaar. He studied civil engineering at TU Delft, from which he graduated cum laude in 1994. His master thesis concerned the numerical and experimental evaluation of the fire resistance of steel beams that are integrated in a concrete floor. This study was carried out at TNO Centre for Fire Research. During this study the interest in the fire behaviour of hollow core slabs was aroused. After one year of consultancy work for TNO Centre for Fire Research, he started his Ph.D. study as a research assistant at TU Delft in December 1995. In 1997, he worked again as a consultant for TNO Centre for Fire Research for one year pending the allocation of additional funding for his Ph.D. by the Technology Foundation STW. From 1998 to April 2001, he carried out his Ph.D. study. Since that time he works as a consultant at TNO Centre for Fire Research where he is involved in numerous projects regarding structural fire safety. Fellingner has published his work on several symposia and journals and participates in various committees. Besides, he teaches students at the TU Delft, and gives courses on a regular basis. Being greatly interested in sports, both actively and passively, he also qualified as a volleyball trainer/coach.